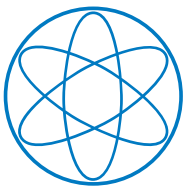


TUM School of Natural Sciences

First measurement of the absorption of $^{3}\overline{\mathrm{He}}$ and $^{3}\overline{\mathrm{H}}$ nuclei in matter and its impact on $^{3}\overline{\mathrm{He}}$ propagation in the galaxy

STEPHAN KOENIGSTORFER



CERN-THESIS-2023-024
23/03/2023



TECHNISCHE UNIVERSITÄT MÜNCHEN

FACHBEREICH: DENSE AND STRANGE HADRONIC MATTER (E62)

2023



TUM School of Natural Sciences

Der Technischen Universität München

Fachbereich: Dense and strange hadronic matter (E62)

First measurement of the absorption of $^3\overline{\mathrm{He}}$ and $^3\overline{\mathrm{H}}$ nuclei in matter and its impact on $^3\overline{\mathrm{He}}$ propagation in the galaxy

Stephan Koenigstorfer

Vollständiger Abdruck der von der TUM School of Natural Sciences der Technischen Universität München zur Erlangung des akademischen Grades eines

Doktors der Naturwissenschaften (Dr. rer. nat.)

genehmigten Dissertation.

Vorsitzende:	Prof. Dr. Alejandro Ibarra
Prüfer der Dissertation:	1. Prof. Dr. Laura Fabbietti
	2. Prof. Dr. Alejandro Ibarra
	3. Prof. Dr. Susanne Mertens (Schriftliche Beurteilung)

Die Dissertation wurde am 31.1.2023 bei der Technischen Universität München eingereicht und durch die TUM School of Natural Sciences am 16.03.2023 angenommen.

Zusamenfassung

Antikerne in Kosmischen Strahlen werden seit langem als eine vielverprechende Sonde fur indirekte Suchen nach WIMP dunker Materie betrachtet, da in diesen Modellen WIMPs Antikerne durch Annihilation zu erzeugen. Sie gelten als so vielversprechende Sonde, weil das erwartete Antikernsignal von dunkler Materie bei niedrigen kinetischen Energien den Hintergrund, der von anderen astrophysikalischen Quellen erwartet wird, um mehrere Größenordnungen übersteigt. Tatsächlich wird nur eine einzige relevante Hintergrundquelle in Betracht gezogen: der Zusammenstoß von Hochenergie-Kosmischen Strahlen mit dem interstellaren Medium. Experimente der aktuellen Generation erreichen Empfindlichkeiten, die optimistische Modelle untersuchen können, und Experimente der nächsten Generation werden in der Lage sein, Signale sämtlicher Modelle vollständig aufzulösen, falls es existiert.
Um aus einem solchen Signal Information zu entschlüsseln, müssen alle Wirkungen, die auf es einwirken, verstanden werden, und die Unsicherheiten jeder dieser Wirkungen bekannt sein. Die relevanten Prozesse sind die Produktion, Ausbreitung und schliesslich die Annihilation dieser Antikerne. Auf der Erde werden Antikerne in hochenergetischen Teilchenkollisionen in Teilchenbeschleunigern produziert. Aufgrund ihrer Seltenheit können traditionelle "fixed-target" Experimente, die zur Messung der Annihilation-Wahrscheinlichkeiten (der sogenannten inelastischen Querschnitt) von Teilchen verwendet werden, nicht fur niedrigenergetische Antikerne verwendet werden. Die in dieser Dissertation vorgestellte Arbeit verwendete eine kürzlich entwickelte neue experimentelle Methode, um erstmals die inelastischen Querschnitte von $^3\overline{\mathrm{He}}$ und $^3\overline{\mathrm{H}}$ zu messen, und verwendete diese Messungen, um den Einfluss der Annihilation auf den erwarteten Antikernfluss in Kosmischen Strahlen zu bestimmen. Daruber hinaus wurde der gleiche Verfahren zur Bewertung des Einflusses von Antikern-Inelastischen Querschnitten auf ihre Ausbreitung auch auf Antideuteronen angewendet. Im Verlauf dieser Arbeit wurden auch die Unsicherheiten bezuglich der Propagation und Produktion von Antinukleonen neu evaluiert.
Der Inhalt meiner Dissertation ist daher die erstmalige Messung des inelastischen Wirkungsqueerschnitts der A=3 Antikerne $^3\overline{\mathrm{He}}$ und $^3\overline{\mathrm{H}}$, sowie die erstmalige Bestimmung der experimentellen Unsicherheiten auf die $^3\overline{\mathrm{He}}$ - und Antideuteronflüsse auf Grund der Annihilation mit dem interstellaren Medium.

Preface

Antinuclei in cosmic rays have long been considered a golden channel for indirect WIMP dark matter searches, since WIMPs are predicted to be able to annihilate to create antinuclei. They are considered such a promising probe because the expected antinuclei signal from dark matter at low kinetic energies exceeds the background expected from other astrophysical sources by sever orders of magnitude. Indeed, only a single relevant background source is considered: the collision of high energy cosmic rays with the interstellar medium. Current generation experiments are reaching sensitivities which can probe optimistic models, and next generation experiments will be able to fully resolve any such signal, if it exists.
In order to decode any information from such a signal, all effects acting on it must be understood, and the uncertainties on each of these effects must me known. The relevant processes are the production, propagation, and finally annihilation of these antinuclei. On earth, antinuclei are produced in high energy particle collisions at particle colliders. Due to their rarity, traditional fixed target experiments employed to measure the annihilation probabilities (called the inelastic cross section) of particles cannot be used for low energy antinuclei. The work presented in this thesis used a recently developed new experimental method to measure the inelastic cross sections of $^3\overline{\mathrm{He}}$ and $^3\overline{\mathrm{H}}$ for the first time, and used these measurements in order to infer the effect of annihilation on the expected antinuclei flux in cosmic rays. Furthermore, the same procedure for evaluating the effect of antinuclei inelastic cross sections on their propagation has been applied to antideuterons. In the course of this work, the uncertainties concerning the propagation and production of antinuclei have also been re-evaluated.
The work carried out as part of my PhD has thus involved measuring the measurement of the inelastic cross sections of the A=3 antinuclei $^3\overline{\mathrm{He}}$ and $^3\overline{\mathrm{H}}$, as well as using them in order to determine the experimental uncertainties on $^3\overline{\mathrm{He}}$ and antideuteron fluxes due to annihilation, both for the first time.

Acknowledgements

I am very happy to be able to write this section, and to thank the many people who played a part in getting me to this point. Not just this thesis, but much of my life has been a group effort, with wonderful people supporting me in different aspects. And while I hope to have helped them as much as they have helped me, it is still a pleasure to have this opportunity to specifically thank them.

Firstly, to the people without whom I would not be me at all. To my parents, Mami and Nico, go the biggest thanks I can give. Mami, not only did you push me to be my best all my life, but you supported me at every stop. This entire thesis is too short to list all the things I am grateful to you for, but fundamentally I want to say thank you for the unconditional love and the needed stern talks to keep things on track when you feel I lost my way. Nico, over the past 13 years you have never imposed your role as a stepdad. But every time I needed help or advice, or just wanted to chat, you were there. I learned so much from your calm way of discussing difficult topics, in particular to listen first and talk later (ok I'm still working on that one). I found a fantastic father figure in you, better than I could ask for. Thank you! And to my siblings, Flo, Elena, Tini and Prince Vince, thank you for all the great times we have together.

Tina – honey – loving you is my great joy, and has been for the past 5 years. Nobody else has listened to my ramblings about science, DnD, and everything else as intensely as you. I love all the times I learn from you, about fliG, and flagella and cryoEM, and about cross stitch, and dance, and the musical ideas behind the How to Train your Dragon theme. I love the geeky science conversations we have about the internal thermodynamics and chemistry of cheese melting, and I love planning our future together. Thank you for being there for me through everything.

To Benni – my very best friend – ours is a friendship which has changed me in many ways. You have been my best friend for almost 15 years, even though for 11 of these we have lived in different countries. You taught me very early on that I should not be so stuck in just my ways, but that other perspectives can have just as much value. Because our friendship is not build on mutual interest like most, but on the appreciation for the different interests we have, and on a foundation of the same base values. You are always there for me. Thank you for everything!

Now on to the people whose contribution was more directly related to my PhD. First and foremost is of course Laura, the boss. I remember the first few meetings we had, looking at plots which I had studied for the better part of the week, and you were able to pick out the critical points where something was wrong in less than

a minute. It took me a long time to realise that it was not just years of experience which made this possible, but the ability to ask critical questions of the information which is presented, to really try and understand the critical points. Out of all the things I learned from you over the last few years, I think this is what will stick with me the most.

Next thanks go all the people in our group, but in particular to the people I worked most closely with on the research which makes up this thesis: Ivan and Laura. Ivan, you taught me pretty much all that I know about antinuclei, and were the perfect discussion partner for all aspects of the analysis. And Laura, we worked together so closely on all the implementations in Galprop, the 100s of extra checks, the antideuteron paper, etc. We worked together through many late nights and got to know and like each other much better than I think either of us expected! We were always in the same boat whenever things were difficult, and managed to make it through together. I came to appreciate your unapologetic brand of honesty, by which you immediately get to the core of any subject. And I am very grateful that we became friends.

Finally, I want to thank my Master thesis supervisor, Prof. Paul Dauncey. You gave me another chance after I had struggled, otherwise I might not be handing in my PhD thesis today at all.

Contents

1 Introduction **1**
1.1 The goal of this work 1
1.2 The standard model of particle physics 1
1.3 Matter and antimatter in the universe 6
1.4 Antimatter-matter annihilations 10
1.5 Antinuclei in the cosmos 17
1.6 Antinuclei on earth 22
1.7 Dark matter and its connection to antinuclei 24

2 Experimental data and experimental method **35**
2.1 ALICE 35
2.2 Identifying antinuclei and building the antiparticle-to-particle ratio . 43
2.3 Extracting the inelastic cross section from the antimatter-to-matter ratio 58

3 Measurement of the $^3\overline{\mathrm{He}}$ inelastic cross section **72**
3.1 Physics motivation and overview of the analysis method 73
3.2 Secondary correction 74
3.3 Results 75

4 Measurement of the antitriton inelastic cross section **77**
4.1 Physics motivation and overview of the analysis method 77
4.2 Accessible momentum range of the measurement 77
4.3 Secondary correction 79
4.4 Results 80

5 Antinuclei in the cosmos **81**
5.1 Sources of antinuclei in the cosmos 83
5.2 Constraining the propagation of antinuclei through the galaxy 103
5.3 The Galprop framework 108
5.4 Annihilations within our galaxy 110
5.5 Antinuclei fluxes for different dark matter masses and annihilation channels 111
5.6 Results for different dark matter profiles 114
5.7 Discussion of the uncertainties on antinuclei fluxes and transparencies 119
5.8 Summary of propagation of antinuclei through the galaxy 120
5.9 Experiments to detect antinuclei in the cosmos 120

6 Final remarks and outlook **126**
6.1 Measurements of the inelastic cross sections of antinuclei 126
6.2 Use of these measurements 126
6.3 Reevaluating physical and experimental effects on the cosmic antideuteron flux and its uncertainties 128
6.4 Outlook 129

7 Appendix **130**
7.1 Current status of the evidence for and against (but mostly against) the existence of anti-stars 130
7.2 Why the statistical hadronization model is not used for calculating (anti)nuclei yields from WIMP dark matter annihilations 130

1 Introduction

1.1 The goal of this work

The main topic of this work in the annihilation of composite antinuclei in nuclear matter. This process – by which one or all of the antinucleons interact and annihilate with nucleons – destroys the antinucleus in the process. Because of these annihilations, antinuclei are some of the rarest stable objects in our matter dominated[1] universe, as once produced they tend to annihilate quickly on cosmic timescales. And only very rare process even create antinuclei in the first place.
But this rarity is why antinuclei have received increased attention in recent years [1, 2, 3, 4], since any process which gives a signal by producing antinuclei does not have to contend with large backgrounds, but can be searched for with hope for a clean signal. In particular, theories which go beyond the current standard model of physics and can produce antinuclei, often hail them as a golden channel for detection. But in order to make any inference from future antinuclei measurements from such processes, their properties must be known, including the chance by which they might annihilate before reaching our detectors. One theory in particular has a vested interest in antinuclei: the weakly-interacting-massive-particle (WIMP) dark matter model. Some versions of this model predict dark matter annihilations into antinuclei, which could enable an indirect channel into unveiling the nature of dark matter.

So this effort to aid the search for new physics thus joins two separate fields of study: high-energy physics, which allows us to produce and study the properties of antinuclei on earth, and the search for signals of dark matter in cosmic rays, in particular antinuclei. The goal of the work carried out during my PhD is the measurement of the inelastic cross sections of the A=3 antinuclei, and the effect of the measured antinuclei inelastic cross sections on an antinuclei signal in cosmic rays near earth.

1.2 The standard model of particle physics

In this section a brief introduction to the standard model of particle physics is given, in order to introduce the terminology and concepts which will be used in this thesis. The standard model of particle physics describes the forces by which elementary particles interact with each other: the strong force, as described by quantum chromodynamics (QCD), the electromagnetic force as described by quantum electrodynamics

[1] It remains of the biggest mysteries of physics why our universe is dominated by matter over antimatter, as the Big Bang should have produced them in equal amounts.

(QED) and the weak force as described by electroweak theory (EWT). The standard model has been incredibly successful in describing the three forces. The forth fundamental force of nature, gravity, completes the description of nature, however, it remains unknown how to incorporate it into the standard model. Additionally, there are phenomena which are currently inexplicable within the standard model, notably dark matter and dark energy. This has prompted many searches for physics beyond the standard model (BSM), in order to complete our understanding of nature. So far however, these searches have remained without success.

In the standard model, there are 4 types of elementary particles: quarks, leptons, gauge bosons and the higgs scalar boson, which are summarized in figure 1. There are 3 generations of quarks and leptons, which differ from previous generations in their mass. Quarks are split into up-like quarks, with a $+\frac{2}{3}$ electric charge[2], and down-like quarks with a $-\frac{1}{3}$ electric charge. Leptons are split between charged leptons with charge $q = -1$ and neutrinos, which carry no electric or color charge, and are very light. There are 4 gauge bosons for the 3 fundamental forces which the standard model describes: the gluon (g) for the strong force, the photon (γ) for the electromagnetic force, and the W and Z bosons for the weak force. The weak bosons couple to all quarks and leptons as well as themselves, while photons couple to electrically charged particles (quarks and charged leptons), and gluons couple to quarks, since they carry a color charge[3]. Additionally, gluons can interact with themselves, since they also carry the color charge of the strong force. Finally, there is the scalar higgs boson, which is responsible for the mechanism which gives particles their mass. All quarks and leptons also have a corresponding antiparticle, with the same mass, spin and lifetime, but with all other quantum numbers inverted according to the charge, parity and time reversal (CPT) symmetry[4].

Quarks always form composite particles made up of either three quarks (baryons) or a quark-antiquark pair (mesons). These two differ in the fact that baryons are fermions (half integer value spin) and mesons are bosons (integer value spin). The baryon number[5] is also conserved in all known reaction of the standard model, which means that the relative number of baryons-antibaryons remains constant.
It is important to note why quarks are never found individually. Quarks carry color charge, which is the charge of the strong force. The shape of the strong force does not allow for isolated color charges to exist, a principle called color confinement. Unlike for example the electromagnetic force, which gets weaker as the distance

[2] Charges of elementary particles are given in multiples of the magnitude of the electron charge e.

[3] Color charge is the QCD equivalent of the electric charge.

[4] Further information about CPT symmetry can be found in any university level physics textbook, such as [5], and in section 1.2.1.

[5] The baryon number is a quantum number where baryons have 1 and antibaryons have -1.

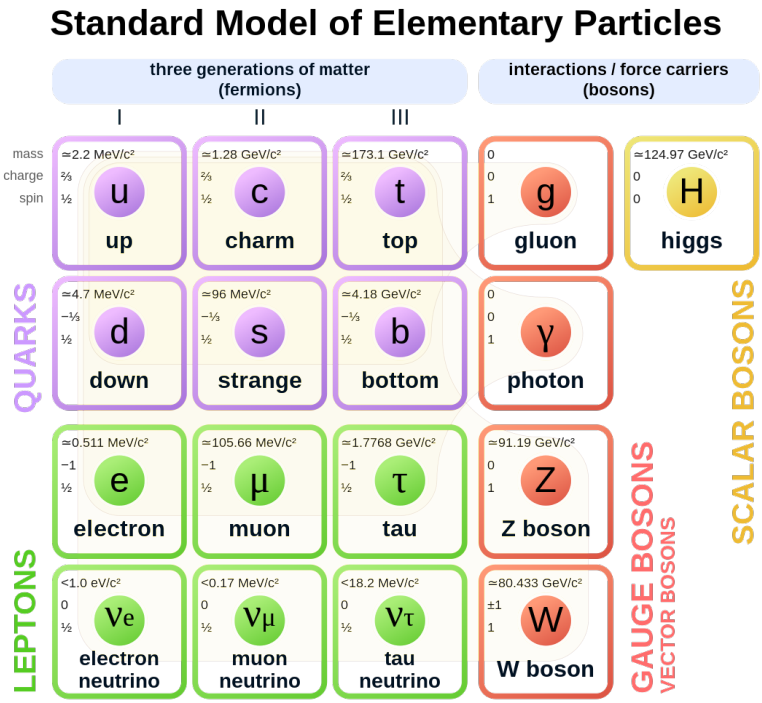


Figure 1: The particles of the standard model of particle physics. There are 3 generations of quarks and leptons, which differ from previous generations only in their mass. Quarks are split into up-like quarks, with a $+\frac{2}{3}$ charge, and down-like quarks with a $1\frac{1}{3}$ charge. Leptons are split between charged leptons with charge $q=-1$ and neutrinos, which carry no electromagnetic or color charge, and are very light. There are 4 gauge bosons for the 3 fundametal forces which the standard model describes: the gluon (g) for the strong force, the photon (γ) for the electromagnetic force, and the W and Z bosons for the weak force. Additionally, there is the scalar higgs boson, which is responsible for the mechanism which gives other particles their mass.

between two particles grows, the strong force remains constant. The potential of the strong force can thus be phenomenologically described by the Cornell potential [6], as given in equation 1:

$$V(r) = -\frac{4}{3}\frac{\alpha_s}{r} + \kappa r, \tag{1}$$

where κ is constant. The second term of equation 1 dominates at large radii (>1 fm), and is thus responsible for the long distance behavior of the strong force. The energy stored in the field between two particles can be found by $\delta E(r_1 - r_0) = V(r_1) - V(r_0) = \int_{r_0}^{r_1} \vec{F}.d\vec{r}$, i.e. the path integral of the force along the separation between the particles.

If the force decreases enough[6] as the distance grows, this allows potential energy to be stored in the field between two particles, without this energy becoming infinitely large at large distances. However, if the force remains constant even with larger distances, the energy stored in the field increases proportionally to the distance between particles. For the strong force, this gluon field between two particles which are being separated is often called a string. Eventually, enough energy is stored in the string that a new antiquark-quark pair can be created, isolating the color charges at each end of the string, thus splitting the string in two. The mount of energy stored in gluon strings is estimated to be roughly 1 GeV/fm [7]. This mechanism, which is shown in figure 2, is called string fragmentation, and is an intuitive explanation for why the color charges of the strong force cannot be isolated.

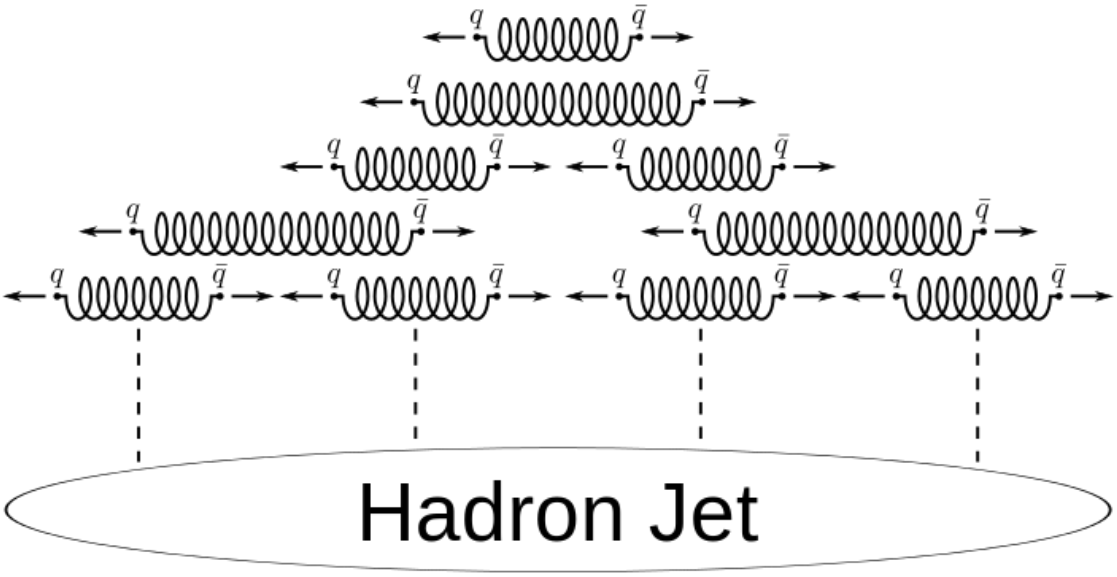


Figure 2: Color confinement by string fragmentation. As the antiquark-quark pair moved away from each other, more and more energy is stored in the color flux tube between them. Eventually, there is sufficient energy to create a new quark-antiquark pair, and thus truncate the flux tube. This process continues until the (anti)quarks run out of sufficient energy to create new quark-antiquark pairs. The quarks can then hadronise. The figure is taken from [8].

[6] If the force decreases as $1/r$, the integral of $\int_{x_0}^{\inf} \frac{1}{\vec{r}}.d\vec{r} \propto \ln(r)$ will go to infinity at infinite distances, therefore the force simply decreasing is not sufficient. However, if the force decreases as $1/r^2$ – as it does for the electromagnetic and gravitational forces – the integral is finite at infinite distances.

1.2.1 Symmetries and symmetry breaking within the standard model

Symmetries are a fundamental aspect of the standard model. A symmetry can be defined as a global operation under which the laws of physics remain the same, and they can be deceptively powerful. In fact, something as fundamental as conservation of energy can be shown to be equivalent to a symmetry to translations in time. Other continuous symmetries such as spatial translation and spatial rotation give rise to conservation of momentum and angular momentum, respectively[7]. But there are also symmetries which are not continuous, but discrete[8]. The standard model of particle physics contains three important and related discrete symmetries [5]. Under these symmetries, the laws of physics are expected to behave the same. C-symmetry, which stands for charge and represents replacing particles with their antiparticles. P-symmetry, which stands for parity symmetry, which represents spatial inversion along the 3 physical axes. And finally T-symmetry, which stands for time-inversion symmetry, which represents inversion of the direction of time.

They are called near symmetries, because each of them is individually broken within the standard model. A symmetry can be broken in two ways: explicitly or spontaneously. Explicit symmetry breaking is when the Lagrangian corresponding to an interaction does not itself respect the symmetry, while spontaneous symmetry breaking is when the Lagrangian respects the symmetry, but its ground state solution does not. The most famous individual violation is the breaking of P-symmetry of the weak force, which couples only to left-handed fermions and right-handed antifermions. In other words, a system of fermions and antifermions inverted under P-symmetry would no longer couple to the weak force, as the fermions are now right handed and the antifermions left handed. It is then obvious that replacing particles by their antiparticles would restore this symmetry. This combined symmetry is called CP-symmetry, and is thought to be respected by the strong and electromagnetic forces, however, there is a degree of CP violation in the mixing of different quark generations by means of the weak force, as described by the Cabbibo-Kobayashi-Masakawa (CKM) matrix. Introducing a complex phase in the quark mixing allows for the weak force to violate CP symmetry [10].

This can be exemplified by the following consideration. Consider a process $a \to b$, and the corresponding process with the antiparticles $\bar{a} \to \bar{b}$ and denote

[7] The relations between physical symmetries and conservation laws was established by Noether's first theorem [9].

[8] In order to distinguish between a continous and discreet symmetry, consider the difference between spatial translations and spatial inversions. The first is an operation which moves a system to a different point in space. It does not matter if the movement happens by 1m or 1km, the symmetry should hold all the same and is thus considered continous. Meanwhile, spatial inversion inverts the direction of the axes, similar to how a mirror inverts one axis. This is not a continuous operation, since it is impossible to "half-mirror" an object.

the amplitudes with M and $\bar{M}$. By CP symmetry (i.e. before the violation), these numbers must be the same. We can separate them into a magnitude and a phase as $M = \bar{M} = |M|e^{i\theta}$. If there is a complex phase term introduced (for example by the CKM matrix) the amplitudes become $M = |M|e^{i\theta}e^{i\phi}$ and $\bar{M} = |M|e^{i\theta}e^{-i\phi}$. Since measurable rates are proportional to $|M|^2$, CP symmetry is still conserved. However, now consider the case where the reaction can take two different routes, $a \to 1 \to b$ and $a \to 2 \to b$ and the amplitudes become: $M = |M_1|e^{i\theta_1}e^{i\phi_1} + |M_2|e^{i\theta_2}e^{i\phi_2}$ and $\bar{M} = |M_1|e^{i\theta_1}e^{-i\phi_1} + |M_2|e^{i\theta_2}e^{-i\phi_2}$. This allows the calculation of the differences in amplitudes as $|M|^2 - |\bar{M}|^2 = -4|M_1||M_2|\sin(\theta_1 - \theta_2)\cos(\phi_1 - \phi_2)$. Thus, the introduction of a complex phase causes a violation between matter and antimatter.
CP violation was first observed in the decays of neutral Kaons [11] in 1964, and was confirmed in 1999 [12]. Since then it has also been observed in the decays of B and D mesons [13, 14]. CP violation is also necessary (but not sufficient) in order to produce the matter-antimatter asymmetry, as is elaborated in section 1.3.3. Even though the CP symmetry is being violated, the combined CPT symmetry is expected to be conserved in all standard model processes [15, 16].

Lastly, let us consider what is known as the strong CP problem. The QCD Lagrangian must include a CP violating term in order to account for the difference between the pion and η masses [17], which is characterised by a free parameter $0 < \bar{\theta} < 2\pi$. But by measurements of the neutron electric dipole moment it has been shown that $\bar{\theta} \lesssim 10^{-10}$. This represents a fine tuning problem: there must be a CP violating term in QCD, but it must also be set to be almost 0. So far, only one convincing solution has been introduced: the Peccei-Quinn (PQ) model. This model introduces a new global symmetry to the QCD Lagrangian, and a corresponding scalar field. This symmetry is then spontaneously broken at low energies, creating the axion[9], a promising alternative dark matter model. For a more detailed mathematical description of the axion see [18].

1.3 Matter and antimatter in the universe

1.3.1 Origin of baryonic matter

The majority of the baryonic matter we see in the universe was created within the first instances after the Big Bang. Initially, the universe was in a hot dense state, with temperatures much higher than the masses of the elementary particles. In fact, the temperature was so high that the higgs mechanism did not yet provide mass to particles [19] ($T \gtrsim 150$ GeV). During this time, quarks, leptons and bosons were in a thermodynamic equilibrium. As the universe underwent inflation, it became colder and colder, until eventually the higgs mechanism started to make particles massive

[9] The name axion comes from a brand of laundry detergent, and was chosen because the axion "cleans up" the strong CP problem.

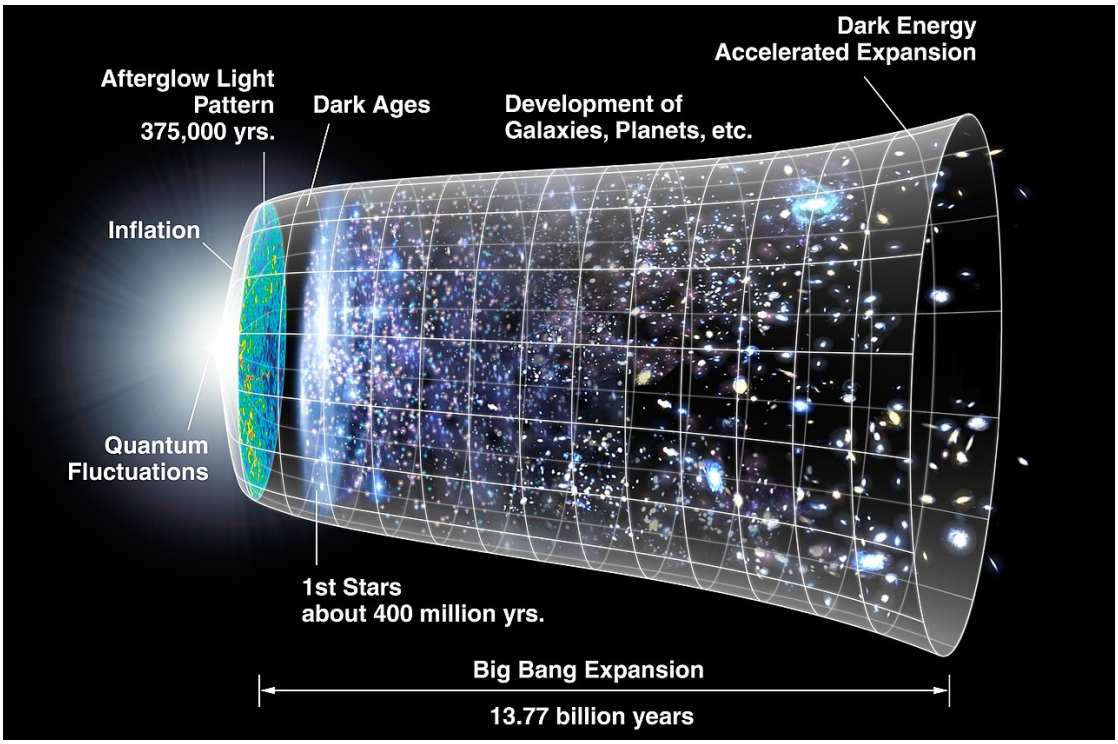


Figure 3: Timeline of the universe, starting from the Big Bang [22].

[19] (see section 1.3.4 for more details). This phase transition of the universe is one option for the source of the matter excess in the universe. As the universe continued to evolve and temperatures cooled, quarks and gluons first formed a quark-gluon plasma – a state of matter in which color charges can move freely [20, 21] – and eventually hadrons, which decay leaving only the most stable hadrons (protons and neutrons) behind. At this point about 1s had passed since the Big Bang. From about 10s to 20 minutes after the Big Bang, the temperatures enabled nuclear fusion. It was during this time that most of the deuterium, helium-4 and lithium in the universe were formed.

The immediate period after the big bang shaped our universe in more ways than simply creating an excess of matter over antimatter. The gravitational collapse of dark matter during this time is thought to be responsible for the formation of galactic structures [23]. The creation of nuclear matter determines the majority of the make up of the universe to this day. The timeline of the evolution of the universe is shown in figure 3.

1.3.2 A matter dominated universe: antimatter-matter asymmetry

To the best of our knowledge our universe is entirely dominated by matter over antimatter. This observation is staggering, because in all the reactions we can observe in particle physics experiments near earth, whenever new matter is produced the same amount of antimatter is produced as well. So the a priori assumption is that the universe houses as much antimatter as it does matter. And at first glance, this doesn't seem to impose any impossible constraints, as from a distance matter and antimatter are indistinguishable[10]. So while our solar system might be made of matter, what is to keep other solar systems, or even other galaxies from being made of antimatter? The issue arises when we look at the surroundings of solar systems or galaxies. Interstellar/intergalactic space is not completely empty, but populated at very low densities by protons and helium-4 from surrounding stars/galaxies. We know the density of protons in these regions to be about $n_{\mathrm{H}} \approx 1\ \mathrm{cm}^{-3}$ for interstellar space [24], and $n_{\mathrm{H}} \approx 1\ \mathrm{m}^{-3}$ for intergalactic space [25]. And when a matter dominated region and an antimatter dominated region are next to each other, then in this vast space of low density matter, plenty of annihilations would occur. These annihilations would produce distinctive signals in gamma ray searches, due to high energy photons emitted from e^+e^- annihilations or from the decay of π^0s produced in $\mathrm{p\overline{p}}$ annihilations [26]. The lack of any such signals places stringent limits on any large areas of antimatter within the observable universe, and leads us to believe that our universe is indeed dominated by matter. The source of this matter-antimatter asymmetry is one of the big remaining mysteries of physics.

It isn't known exactly how the different populations of matter and antimatter came to be. Perhaps only a minute difference between the two caused a tiny fraction more matter to be produced than antimatter. And since the majority of both annihilated, what we see today might by this tiny leftover fraction. For this reason, searches for differences between matter particles and their antimatter counterparts are looking to find even the tiniest discrepancy between the two [27, 28].

1.3.3 Sakharov condition

Given the a priori assumption that the same amount of matter and antimatter would be produced, it is necessary to clarify the conditions under which this could be altered. In [29], the necessary conditions for the creation of a baryon excess were shown to be:

- Some interactions of elementary particles must violate baryon number conservation, since the net baryon number of the universe must change over

[10] This means to say that matter atoms would produce the same spectral lines as antimatter atoms, and undergo the same fusion reactions we see in stars.

time

- C and CP must be violated so that there is no equality in the forward and backward rates of the baryon number violating processes.
- The net flux must be created in out-of-equilibrium conditions, since otherwise CPT symmetry would assure compensation of the effect.

The first condition is trivial. The second condition means that there must be a reaction which differentiates between the matter and antimatter, in order to give rise to a process which would preferably create baryons over antibaryons. The third condition requires some more explanation. It is based on the fact that we believe the CPT symmetry to be exact. Therefore, there must be a process which only happens in one direction in time. This cannot occur in an equilibrium condition, since in equilibrium all reactions occur in both the forward and backward directions. Therefore, it must be a reaction linked to out-of-equilibrium processes.

1.3.4 Baryogenesis within the standard model

It is possible to account for the matter-antimatter asymmetry in the universe through standard model processes. One such process was outlined in [30]. The main arguments of this paper are reproduced here, to exemplify how the Sakharov condition above can be applied.

The main idea of the mechanism is threefold: i) the existence of a first order phase transition as the universe cools below the electroweak phase transition. The phase transition satisfies the out-of-equilibrium part of the Sakharov conditions. ii) quarks and antiquarks scattering of the phase boundary in an asymmetric fashion, due to CP-violating effects. This results in a net baryon flux through the phase boundary. And iii), the excess antiquarks in the hot medium are removed by an effect which does not conserve baryon number, before the phase transition is complete in the entire universe.
In the standard model, particles get their mass by their Yukawa coupling to the higgs vacuum expectation value [31]. The vacuum expectation value of the higgs field vanishes at temperatures above the electroweak phase transition, such as were present during the early universe [19]. If this phase transition is treated as a first order phase transition, with bubbles of the colder phase forming out of the hot medium, then the vacuum expectation value of the higgs will change while crossing the phase boundary. This will change the masses of fermions as they move across this phase boundary, which thus acts as a potential barrier. This causes both quarks and antiquarks to scatter from this barrier. However, due to the CP-violating nature of the weak interaction, the transmission through the barrier can be different for quarks and antiquarks, resulting in a baryon flux through the phase boundary. Excess antiquarks in the medium are then removed by sphalerons. A sphaleron is a solution

to the electroweak field equations, geometrically represented by a saddle point which connects a 3 baryon system to a 3 antilepton system[11] [32]. Sphaleron effects are expected to be frozen out below about 10 TeV. Since the temperature is higher on one side of the phase transition than the other, the baryon number symmetry violating process is hypothesised to occur only on the hot side, and thus leave a net baryon number.

While sphalerons are currently hypothetical, it is expected that the high luminosity upgrade of the LHC will be able to start the experimental search for sphalerons [33].

1.4 Antimatter-matter annihilations

The lightest quarks – u and d – make up normal nuclear matter, i.e. protons uud and neutrons udd, which are the two lightest baryons with masses of 938 MeV/c^2 and 939 MeV/c^2, respectively. Since the proton is the lightest baryon, and the baryon number must be conserved, any reaction of the proton with other matter must leave an intact proton at the end, thus never making the energy stored in the proton's mass available to create new particles. When baryons interact with their antibaryons, they annihilate, releasing their entire mass as available energy to create new particles. This is because by definition, the total baryon number of such a reaction is 0. The same is true for the annihilations of leptons and lepton number conservation, and for the conservation of electric charge in the annihilations of leptons and baryons. In principle, if a quantum number is antisymmetric under the C symmetry, it will be conserved by construction in antimatter-matter annihilation events and thus will never limit the available phase space of reactions.

1.4.1 Annihilation of $q\bar{q}$ and $l\bar{l}$ pairs

It is simplest to start with the Feynman diagrams for the annihilations of elementary quarks and leptons. The lowest order diagrams are given in figure 4. Their relative contribution is proportional to the force's interaction strength to the exponent of the number of vertices, so α for the electromagnetic force, α_w for the weak force and α_s for the strong force. At low energies, the three parameters have an ordering α_s»α»α_w[12]. Essentially, quark and leptons can annihilate with their antiparticles through electromagnetic and weak channels, which can also convert from quarks to

[11] And equivalently 3 antibaryons to 3 leptons.

[12] The couplings depend on the energy scale, as all of them are running coupling constants. At high energies, the weak force is actually stronger than the electromagnetic force. This difference is due to the mass of the weak bosons.

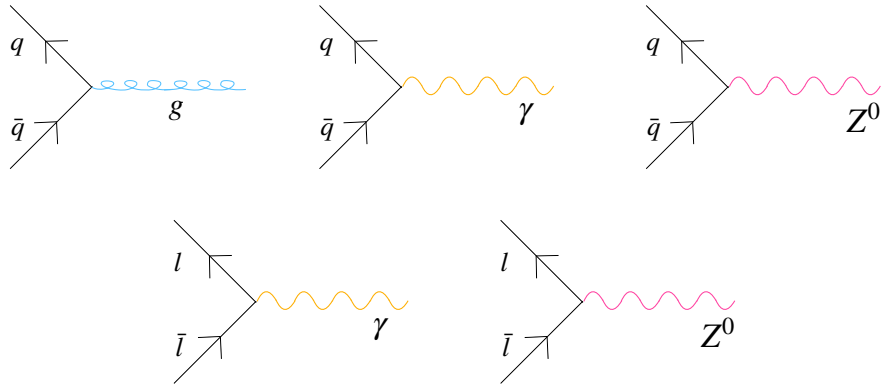


Figure 4: First order Feynman diagrams showing the annihilations of elementary particles. Top row: quark-antiquark annihilation through the strong (left), electromagnetic (middle) and weak (right) force. Bottom row: lepton-antilepton annihilation through the electromagnetic (left) and weak (right) force.

leptons and vice versa. Quarks can additionally annihilate via a gluon into either another quark-antiquark pair or into hadron jets. For quarks, annihilation through the strong force should outweigh annihilation through the electromagnetic force by a factor $\alpha_s^2/\alpha^2 >> 1$, which means that the strong channel should dominate.

1.4.2 Antiproton-proton annihilations

It is important to note at the start of this chapter that there is currently no theory or even model which can describe the available data for antiproton-proton annihilations, or offer up an explanation for the underlying mechanism [34]. This is in stark contrast to quark-antiquark annihilation, which is just a first order QCD process. In this section I shall attempt to give an overview of the difficulties in describing this process, and thereby offer up a qualitative picture of the possible annihilation mechanisms.

It is tempting to assume that in order to scale up an annihilation event, one might just be able to scale up the single Feynman diagrams for quark-antiquark annihilation in order to get a description for antiproton-proton annihilation. However, the picture is far more complicated. This can be intuitively understood by the fact that (anti)protons are made up of 3 valence (anti)quarks, but in the annihilation

of (anti)proton pair, some of their valence (anti)quarks may well survive. In fact, consider the following reaction $p\bar{p} \rightarrow 3M$, where M denotes a meson. This reaction can occur by simply rearranging the quark content of the proton and antiproton, which is illustrated in figure 5. Such a rearranging of the quarks can happen if the quarks can feel each others strong potential, which can be mediated through pion exchange. This can be seen as equivalent to nucleon-nucleon interactions through pion exchange, at distances beyond the confines of color confinement. This effectively allows the potential for quark rearranging to be felt at further distances than the potential for quark-antiquark annihilation. The annihilation potential between an antiproton-proton pair therefore can have a long range ($\gtrsim 1$ fm) and a short range ($\lesssim 1$ fm) term, where the long range term is dominated by the rearrangement of quarks and antiquarks into mesons, and the short range term is dominated by quark-antiquark annihilation. The common notation of these processes is An and Rn for annihilation (A) and rearrangement (R) into n mesons.

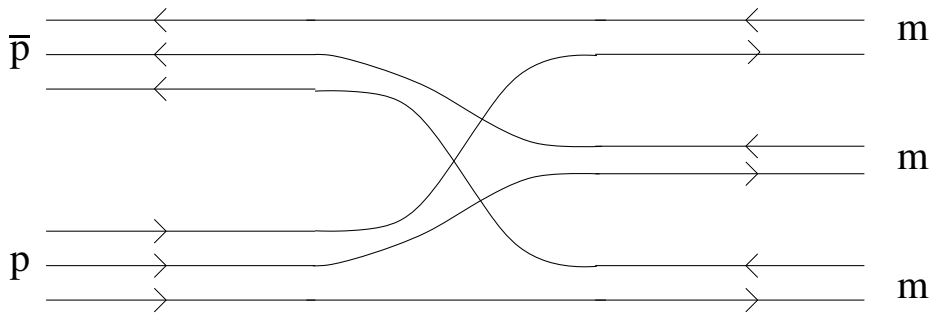


Figure 5: Schematic of $p\bar{p}$ annihilation into 3 mesons, done by rearranging the valence quarks but without annihilating any quark-antiquark pair.

One important observable to distinguish between these two different annihilation mechanisms is the production of strangeness, i.e. by the reaction $p\bar{p} \rightarrow 2K+XM$. This reaction cannot occur with a simple rearrangement of quarks[13], as a new $s\bar{s}$ pair has to be created. If antiproton-proton annihilation would be dominated by the rearrangement of quarks, we would expect to see almost no produced kaons, while if

[13] Neglecting quark-antiquark creation by string fragmentation.

the quark annihilation channel would dominate, we would expect to produce Kaons almost as much as pions. In fact we observe about 5% of final states which include kaons [34, 35], which suggests that the annihilation channel is suppressed compared to the quark rearrangement channels.

Given these considerations, the antiproton-proton annihilation cannot easily be described by perturbative QCD, and we are still missing an effective model capable of explaining the data. This is why a quantitative description of this interaction so difficult. Instead, an empirical parameterization is commonly used to describe the antiproton-proton inelastic cross section. A description accurately fitting the available data has been proposed by Tan et al. [36], and is reproduced in equation 2, where $T_{\bar{p}}$ is the antiproton kinetic energy in the proton rest frame.

$$\sigma_{\text{inel}}^{p\bar{p}} = 24.7(1 + 0.584 T_{\bar{p}}^{-} 0.115 + 0.856 T_{\bar{p}}^{-0.566})\text{mb}. \tag{2}$$

Another description – which is implemented in the propagation code Geant4 – is based on attempting to assign cross sections to each individual process which might occur and is explained in [37]. In their model, they split the antiproton-proton annihilation into the sub processes laid out in figure 6. The momentum dependence of these processes is given by Regge theory [38, 37, 39]. This method works for determining the cross sections of particular channels, which is necessary for an accurate description of particle propagation, as is shown in figure 7. However, this model does not match experimental data better than within a factor two. This highlights the difficulties in accurately predicting the inelastic cross section of antiproton-proton annihilations.

An overview of available data on the antiproton-proton annihilation data is given in [35, 41, 40].

1.4.3 Antiproton-nucleus annihilation: the Glauber model

In the previous section it has been established that while the antiproton-proton inelastic cross section has been well measured, a theoretical model is still lacking. In this section we therefore focus on the experimental results for antiproton-matter annihilations, and how we can use them to infer the annihilation mechanism.

When moving from antiproton-proton to antiproton-nucleus annihilations, several new effects come into play. The question is if only one nucleon in the nucleus interacts in the initial annihilation, and then how the antinucleus acts after the annihilation occurs. Thankfully, while those points certainly raise additional difficulties in finding a theoretical description, we can benefit from measurements of antiproton

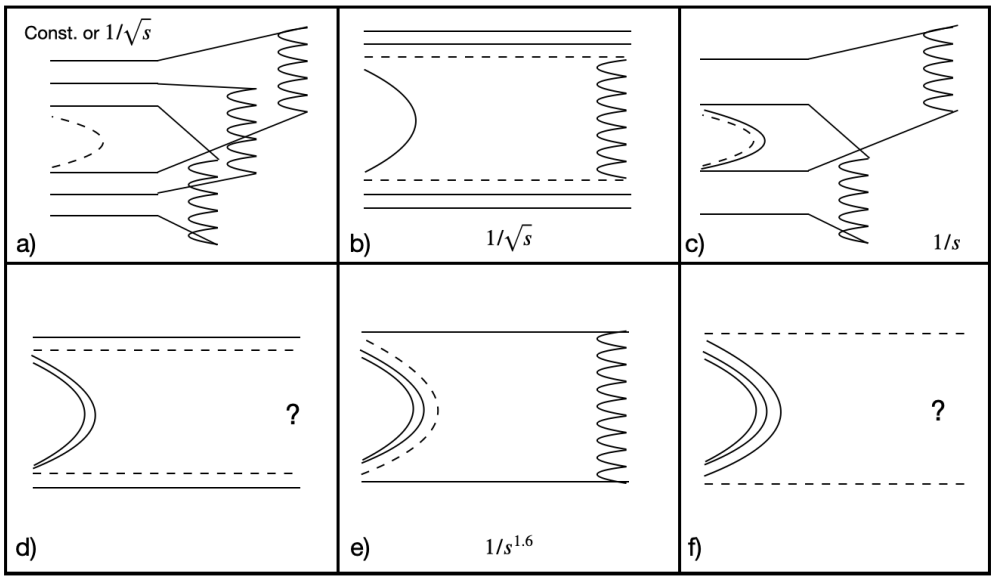


Figure 6: Annihilation channels for antiproton-proton. The solid lines represent quarks and the dashed lines represent a gluonic string (which can then decay via string fragmentation, as shown in figure 2). Curled lines represent $\bar{q}q$ annihilations. The diagrams thus represent: a) 3 antiquark-quark annihilations; b) a single antiquark-quark annihilation into 2 mesons and a gluon string; c) corresponds to a quark-antiquark and string annihilation, with the creation of 2 quark-antiquark strings. Diagrams e) and f) can produce exotic mesons. Figure taken from [38].

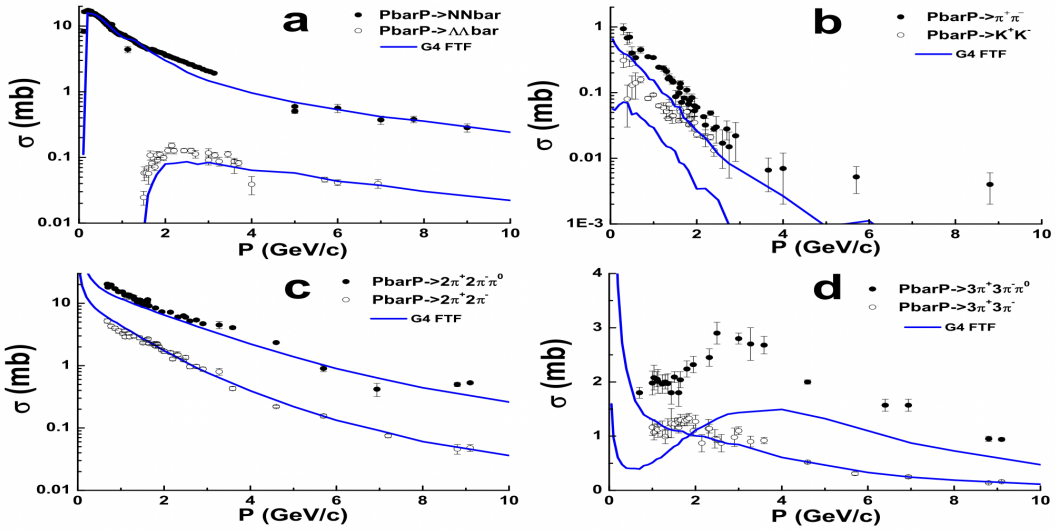


Figure 7: A comparison of antiproton-proton inelastic cross section data with the model used in Geant4 [37]. Points are experimental data as described in [40], the blue line represents the model. See text for details.

absorption. These are parameterised according to the Glauber model [42, 43, 44]. The Glauber model parameterises the inelastic cross section of antiprotons on nuclei as a geometric scaling of the antiproton-proton cross section, according to equation 3, where R_A is a free parameter which can be roughly understood as the target nucleus' radius, and characterised as $R_A = r_0 A^{1/3} f(A)$. $r_0 = 1.1$ fm, and $0.8 < f(A) < 1.1$ is a correction factor as a function of A. h denotes the hadron in question, A is the mass number of the target nucleus and σ_{hN}^{tot} is the total antiproton-nucleon cross section

$$\sigma_{hA}^{in} = \pi R_A^2 \ln\left[1 + \frac{A\sigma_{hN}^{tot}}{\pi R_A^2}\right]. \tag{3}$$

1.4.4 Antinuclei-matter annihilations: the Glauber model and geometric scaling

Having established the details of the antiproton inelastic cross section, we can now start to consider the process of antinuclei annihilation. All the considerations made for the antiproton inelastic cross section still hold true, but additionally there is also the potential between the antinucleons to consider. This means that one not only has to consider the breakup of the matter nucleus, but also the breakup of the

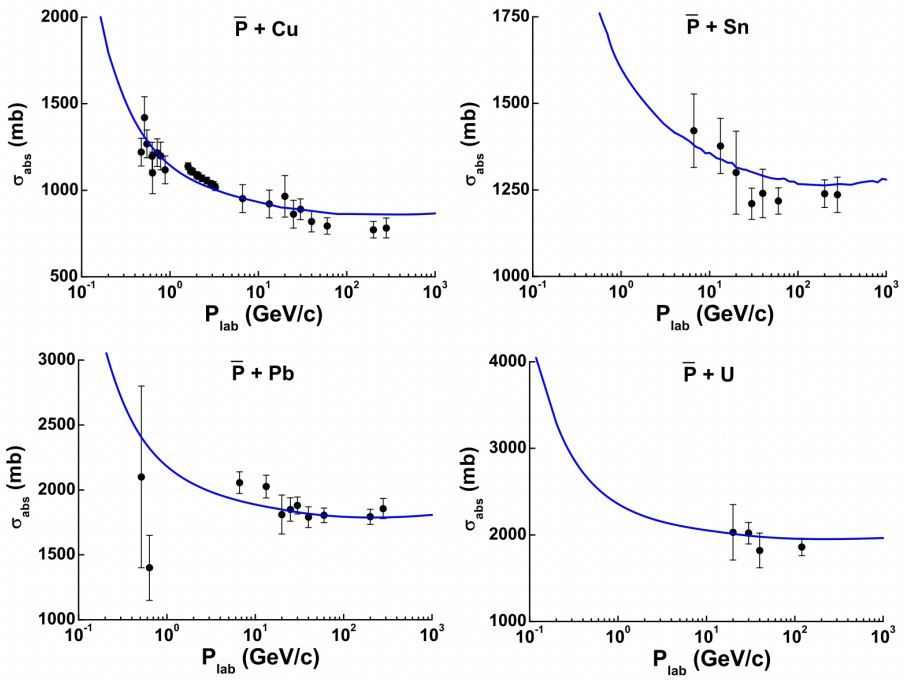


Figure 8: Antiproton-nucleus annihilation for different materials, taken from [44].

antimatter nucleus, leaving a smaller antinucleus behind. This has been observed for antideuterons in the reaction $\overline{\mathrm{d}} + A \rightarrow \overline{\mathrm{p}} + X$ [45, 46]. However, it is not clear if the antiproton which was measured survived the initial collision or if it was created from the annihilation of the antideuteron.

In order to scale up the cross sections from antiproton-nucleus to antinucleus-nucleus annihilations, we can also employ the Glauber model. The full mathematical treatment can be found in [47], however, due to the computational effort required to do real time Glauber calculations, Geant4 uses a parameterization to approximate the result of Glauber calculations. This parameterization is based on extending 3 to light antinuclei, according to equation 4, where B is the mass number of the antinucleus

$$\sigma_{BA}^{in} = \pi(R_A^2 + R_B^2)\ln\left[1 + \frac{BA\sigma_{hN}^{tot}}{\pi(R_A^2 + R_B^2)}\right]. \tag{4}$$

R_A is then used as a fit parameter to tune the simplification to the expected value of full Glauber calculations. The form of R_A is given by equation 5

antinucleus	c_1	c_2
$\overline{\mathrm{p}}$	1.31	0.9
$\overline{\mathrm{d}}$	1.38	1.55
$^3\overline{\mathrm{He}}$/ $^3\overline{\mathrm{H}}$	1.34	1.51
$^4\overline{\mathrm{He}}$	1.30	1.05

Table 1: Constant values for determining the fir parameter R_A used in the Geant4 Glauber approximation for antinucleus-nucleus collisions [44].

$$R_A = c_1 A^{0.21} + c_2 A^{1/3}, \tag{5}$$

where c_1 and c_2 are constant whose exact value depends on the antinucleus on question. The values are given in table 1 for the antinuclei up to $A = 4$.

1.5 Antinuclei in the cosmos

1.5.1 Why producing antinuclei is so difficult: production mechanisms of antinuclei

The difficulty in producing antinuclei is not just to the necessary energy to create them, but also due to their production mechanism.

The exact production mechanism for composite antinuclei in high energy particle collisions is still unknown. There are currently two models aiming to describe this phenomenon. The first is the statistical hadronization model, which models the production of the nuclei as a statistical process with a characteristic temperature (at heavy ion collisions at the LHC this temperature is 156 MeV [48]). This model has had great success by describing particle yields over 9 orders of magnitude in yield, as is shown in figure 9. The SHM is a grand canonical ensemble, since new particles can be created through in hard scatterings.

The problem with the statistical hadronization model is that it predicts a the production of nuclei from a thermalized medium, when the binding energy of the nuclei is far below the temperature given by the model. For example, the deuteron binding energy is ≈ 2.2 MeV, compared to the temperature of 156 MeV predicted by the model. This has been dubbed the "snowball forming in hell" problem. Additionally, the statistical hadronisation model says nothing about the underlying mechanism by which the nucleons form antinuclei.

The second model is the coalescence model. This model considers the relative momenta of nucleons produced in the collision, and if they are close enough together,

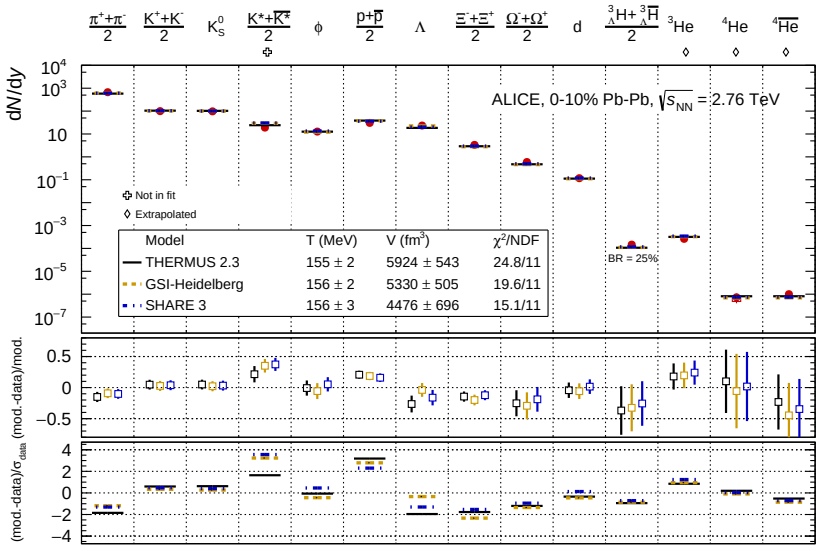


Figure 9: Statistical hadronisation model fits, with three different implementations, to the light flavour hadron yields in central (0-10%) Pb–Pb collisions at $\sqrt{s_{NN}}$= 2.76 TeV. The upper panel shows the fit results together with the data, whereas the middle panel shows the difference between model and data normalised to the model value and the lower panel the difference between model and data normalised to the experimental uncertainties. Figure and caption taken from [48].

assigns them a chance to bond together and form a nucleus. The advantage of this is then that given a set of space and momentum coordinates[14], the coalescence model can predict the nuclei spectra from the spectra of protons and neutrons. This relation is then experimentally characterized by equation 6:

$$B_A = E_A \frac{d^3N_A}{dp_A^3} \left[\left(E_{p,n} \frac{d^3N_{p,n}}{dp_{p,n}^3} \right)^A |_{\vec{p}_p=\vec{p}_n=\vec{p}_A/A} \right]^{-1} \tag{6}$$

, where B_A is the coalescence parameter. While this model also requires fits to experimental data in order to give predictions of the yields and spectra of antinuclei, it gives an explanation for the mechanism of how nucleons bond together. Several versions of the coalescence model exist, which differ mostly in the criteria for when two nucleons coalesce. The simplest form – often called "hard sphere" coalescence – is to consider a threshold relative momentum in the pair rest frame, and any pair below this threshold will coalesce. This model is not very predictive, since it requires fits to data of each energy of interest in order to determine this threshold value p_0. Expanding on this approach, the wave functions of the nucleons and the resulting nucleus can be considered. This is called "Wigner function coalescence"; it is outlined in [49, 50] and was recently tested against data in [51]. This approach considers both momentum and space coordinates, and therefore can take the system size into account. The size of the system is important, since a priori it is expected that if particles are further apart, they are less likely to coalesce. For a more comprehensive review of the coalescence model, see [52, 53].

What can we infer from these models on the production of antinuclei? The important takeaway for this thesis is that their production relies on significant amounts of available energy, and on producing two nucleon close in both space and momentum. These restrictions limit the production of antinuclei to high energy collisions or exotic production channels.

1.5.2 Why to we care: antinuclei as a golden channel for new physics

The main reason why cosmic ray antinuclei make such an interesting probe for new physics is twofold: i) the rarity of the standard model processes which produce them means that any signal does not have to contend with a copious background and ii) that there are already viable theories of new physics – namely WIMP dark matter –

[14] Traditionally coalescence models neglect the spatial correlation part, assuming that the nucleons are close enough together in space to coalesce. And any difference between the sizes of collision systems is then accounted for by a different coalescence parameter.

which predict a detectable antinuclei signal. This has led to the coining of cosmic ray antinuclei as a "smoking gun" for new physics.

The first discovery of antimatter in cosmic rays was also the first discovery of antimatter in general: the discovery of the positron in charged particle showers from cosmic rays, in 1932 [54]. The discovery of antiprotons in cosmic rays would take almost half a century more, finally being observed in 1979 [55, 56]. During this time, antiprotons in cosmic rays were a probe into the matter-antimatter asymmetry of the universe, as their abundance could give a hint to the presence of antimatter dominated regions in our galaxy. Their discovery and study to the present day are consistent within uncertainties with production from high energy collisions of cosmic rays with the interstellar medium, providing no evidence for any antimatter dominated regions[15]. The antiproton to proton ratio in cosmic rays is roughly 10^{-4}.

Nowadays, the focus is on the search for antinuclei as a probe of new physics. The expected production from high energy cosmic ray collisions is very low, particularly at low energies (see section 5 for exact values), while several dark matter models predict an antinuclei flux within reach of current or next generation detectors [57]. The antinuclei of interest are antideuterons ($\overline{\mathrm{d}}$) and anti Helium-3 $^3\overline{\mathrm{He}}$. $\overline{\mathrm{d}}$s are expected to be produced in greater amounts than $^3\overline{\mathrm{He}}$, since they only consist of 2 antinucleons rather than 3. However, since $\overline{\mathrm{d}}$ have the same charge as the antiproton, which exist far more copiously, they are more difficult to detect experimentally. This is because the signal for $\overline{\mathrm{d}}$s can overlap with the tail of the antiproton signal. $^3\overline{\mathrm{He}}$ on the other hand is much easier to detect experimentally, due to its double charge, and the associated quadrupled specific energy loss (see equation 12). For both, the background in the low energy region (below a few GeV/nucleon) is expected to several orders of magnitude below the expected signal strength. This is in strong contrast to searches involving gamma rays [58], or antiprotons [59, 60], where the signal to background ratio is expected to be on or below the % level. Thus, an observation of a low energy antinuclei flux would be a sign for new physics.

1.5.3 What affects antinuclei in cosmic rays: production, propagation and annihilation

As explained in the previous section, low-energy antinuclei in cosmic rays provide a uniquely background free probe into new physics. But in order to interpret any future observation, it is necessary to understand what affects their abundance and spectral shape. These factors can be summed up as 3 things: their production, propa-

[15] Nowadays constraints on antimatter dominated regions are more stringently set by gamma ray searches.

gation and annihilation. While a more detailed description of each is given in section 5, this section aims to give a brief introduction on the importance of the three aspects.

The production of antinuclei in cosmic rays can be classed into two categories: i) production in high energy collisions of cosmic rays with the interstellar medium and ii) new, exotic sources. This is different to light nuclei in cosmic rays, whose production is dominated by their production in the stellar cycle. Their production in high energy cosmic ray collisions can be somewhat constrained by experiments at accelerators, which probe fundamentally the same reaction of $p + p \rightarrow \overline{\mathrm{d}}/^3\overline{\mathrm{He}} + X$. However, the energies and rapidities at which production mostly occurs are usually at much lower energies than the ones probed by acclerators, e.g. for antideuterons the most important centre-of-mass energy for production in high energy cosmic rays is $\sqrt{s} \approx 25$ GeV (see figure 55). For a more detailed and quantitative discussion of the relevant energies please see section 5. Furthermore, the experiments most capable of studying antinuclei, the ALICE (A Large Ion Collider Experiment) experiment at the LHC and the STAR experiment [61] at the Relativistic Heavy Ion Collider, probe their production at midrapaidity, rather than at the highly forward rapidities relevant for production in cosmic ray collisions. This means that for much of the relevant parameter space for production, extrapolation from experimental data is necessary. On the other hand, production from new physical processes – such as the annihilation of WIMP dark matter which is discussed in detail in this thesis – is even less constrained, and has to be probed by letting Monte Carlo simulations run from an assumed standard model state in the annihilation.

Once the antinuclei are produced, they travel through the galaxy until they eventually reach earth. On this journey they are affected by magnetic fields, bulk motion (i.e. diffusion and convection effects), as well as other effects. The good thing is that these affects are the same for all cosmic rays, and can therefore be constrained by observations of more abundant cosmic ray species. Recent work on the topic was done in [62, 63], and is explained in more detail in section 5.

On their journey, antinuclei do not merely travel through empty space; the space between stars is filled with the diffuse interstellar medium (ISM), which is made up of about 0.9 protons per cubic centimeter [24]. As antinuclei traverse this matter, they might interact and annihilate with it. To account for this loss it is necessary to quantify the inelastic cross section of antinuclei down to low energies. The measurement of these cross sections and the quantification of their effect on antinuclei losses is the topic of this thesis.

1.6 Antinuclei on earth

On earth, we have the ability to artificially produce antinuclei at high energy physics facilities, like the LHC. In fact, antideuterons were first observed in 1965 in collisions of protons on Beryllium at the Proton Synchrotron [64]. Since then, antinuclei have been observed in higher energy collisions in much larger amounts, both at CERN facilities [65, 66, 67, 68], and heavy ion facilities [69]. The ALICE experiment in particular, has published spectra of antinuclei up to $^4\overline{\mathrm{He}}$ [65, 66, 67, 68] in both pp and Pb-Pb collisions. This section aims to give an overview of the studies of antinuclei on earth.

1.6.1 Production at accelerators

Production at accelerators can be classed by energy, and by collisions system. Energy affects the barychemical potential [16], while the collisions system determines the penalty factor for producing heavier (anti)nuclei. The penalty factor – which describes the amount by which the production of (anti)nuclei is suppressed for each additional nucleon – is roughly 1/300 in Pb–Pb collisions at 5.02 TeV, while being roughly 1/1000 in pp collisions at 13 TeV [72]. The relative p_T integrated yields of nuclei are shown in figure 10.

1.6.2 Annihilation at accelerators

Traditionally, annihilations have been studied in fixed target experiments [46, 45, 40]. In those experiments, a beam of antiparticles is produced and then fired at a target. The number of particles before and after the target are measured, and the resulting disappearance probability is used to calculate the inelastic cross section. However, this method relies on the ability to produce a clean beam of antiparticles, with sufficient statistics to conduct such an experiment. This comes with two challenges: i) the difficulty of producing antinuclei due to the required energy thresholds and ii) producing the antinuclei in a focused direction, so that they can be captured directed towards a target. These two constraints are unfortunately counterproductive. In order to compensate the difficulty of meeting the energy requirement for the collisions, it is far more energetically favourable to collide in the particles rest frame, however, this produces particles in all directions, not focused towards the beam direction. This makes such measurements increasingly more difficult for higher

[16] The baryochemical potential is a measure of how much more energy is required to produce antibaryons to baryons. A value of 0 means that they are produced in equal amounts, and is found at LHC energies at mid-rapidity [70, 71].

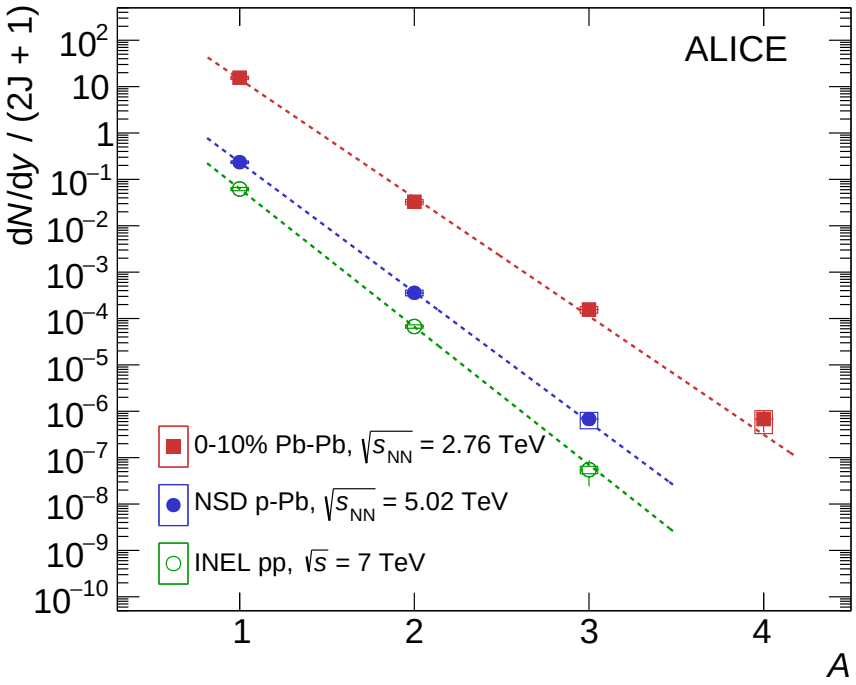


Figure 10: Production yield $\mathrm{d}N/\mathrm{d}y$ normalised by the spin degeneracy as a function of the mass number for inelastic pp collisions, minimum-bias p-Pb and central Pb-Pb collisions. The empty boxes represent the total systematic uncertainty while the statistical errors are shown by the vertical bars. The lines represent fits with an exponential function. Figure taken from [72].

mass antinuclei.

However, since antinuclei up to $A = 4$ have been observed in heavy ion collisions [48], they also have to annihilate in the detector. But it is far more difficult to find an equivalent observable to the fixed target experiment within such an experiment, because it is a priori not possible to know how many particles get produced, and therefore the "loss" of particles is not trivial to measure. The methods developed to measure this loss are the topic of this thesis and will be explained in section 2, so just a brief introduction is given here. The first method is based on using the knowledge of nuclei production and the baryochemical potential to calculate how many antinuclei should have been produced. The second is based on measuring the particles individually in two different detector systems, and to calculate the loss between the two.

1.7 Dark matter and its connection to antinuclei

In this section a brief introduction into the motivation and evidence for dark matter is given, several prominent dark matter models are discussed, with a particular focus on WIMP dark matter. Furthermore, the connection with WIMP dark matter and antinuclei is discussed.

1.7.1 The evidence for dark matter

The first evidence for dark matter was observed by Zwicky [73] in 1933, who realised that the rotation curves in galaxy clusters could not be caused solely by the luminous matter observed. His conclusions were not taken seriously until almost 40 years later, when the search for missing mass caused by the advent of cosmology made his theory of dark matter attractive. During this time, the big bang cosmology had prevailed, but left open the question of the ultimate fate of universe. Within big bang cosmology, there are three option. The first is that the universe expands forever, with the gravitational pull merely slowing down the expansion over time, never stopping it. The second is a closed universe, where the density of matter is bigger than some critical density, and therefore will eventually outperform the expansion, causing a collapse of the universe back towards a hot dense medium. And finally, a flat universe, where the density is exactly this critical density, such that eventually the gravitational pull of galaxies will exactly counterbalance the expansion, asymptotically reducing the expansion to 0. From Einstein's theory of general relativity, it can be shown that these fates correspond to the geometry of the universe, and are characterised by a density Ω, where the critical density leading to a flat universe is given by $\Omega_c h^2 = 1$ [74, 75]. It was expected that the geometry of the universe is flat[17], but observations from galaxy clusters showed that luminous matter only made up a fraction of this density [75]. Cosmologist turned back to Zwicky's discovery [76, 77], claiming that dark matter made up the missing mass.

More evidence of dark matter was soon to follow. Tracking the rotation curve in galaxies provided evidence for dark matter bound in galaxies [78, 79, 76]. Measuring the dispersion velocities of galaxies around either other galaxies (such as the

[17] This means that the local geometry of spacetime is euclidean, which means that all the angles in a triangle in this space add up to 180 degrees. As a counterexample to euclidean space, consider the surface of a sphere, like the surface of earth. It seems locally euclidean, when you lay a triangle on flat ground and add up the angles, they come out to 180 degrees within the measurement uncertainties. But now consider an airplane which starts at the equator flying due north to the north pole. Once it reaches there it makes a 90 degree turn, and flies due south until it once again reaches the equator. It then turns 90 degrees again so it flies along the equator back towards its original destination. The triangle made by the airplane consists of 3 90 degree angles, or 270 degrees. As such, the surface of a sphere like earth is not a euclidean space.

velocities of dwarf galaxies around a more massive one) or around galaxy clusters provided evidence for dark matter trapped in larger gravitationally bound structures, as did gravitational lensing [80]. For a comprehensive review of the evidence for dark matter see the particle data group [74]. Each piece of evidence points to a type of matter which does not interact electromagnetically (hence "dark"), and makes up the majority of the mass found in cosmic structures.

Further evidence for dark matter can be found in structure formation in cosmology. From anisotropies in the cosmic microwave background (CMB), it can be inferred that at the time of CMB decoupling the baryonic density fluctuations were of order $\delta\rho_{\text{rec}}/\rho \approxeq 10^{-5}$. Since these fluctuations scale linearly with the expansion of the universe, today's baryonic density anisotropies can be calculated as $\delta\rho_b/\rho|_{\text{today}} \approxeq 10^{-2}$ [74]. Since matter is highly concentrated into galaxies in the present day universe, fluctuations are $\delta\rho_b/\rho|_{\text{obs}} >> 1$. This discrepancy can be solved by adding a dominant non-relativistic, collisionless component the mix, which decoupled from thermal equilibrium well before the CMB. In other words, in order to explain structure formation from the early universe, one needs a dominant component of the mass to be in a form which does not interact electromagnetically, and does not heavily self-interact, which is also what is needed in order to explain the present-day observations of galactic motion.

Finally, it is important to discuss the difference between hot and cold dark matter. Dark matter which was thermally produced in the early universe – called a thermal relic – can be split into two categories: hot relics, which were still ultra-relativistic when they decoupled from thermal equilibrium, and cold relics, which were no longer relativistic, or cold enough to significantly cool from the expansion of the universe. Due to the different velocities of these relics, hot relics are expected to cause sharp features in the large scale structure of the universe, while cold dark matter is expected to cause a smooth large scale structure. This can be understood as how easily a particle is trapped in a gravitationally collapsed structure. After an initial overdense region forms and a gravitational well builds, slow (cold) particles will be trapped in the well first, while fast (hot) particles will not be trapped in the well until the gravitational well becomes much deeper. To get an idea of the order of magnitude of velocities, consider the escape velocity of our galaxy, which lies around 600 km/s [81], which is equivalent to $\beta \approxeq 2\times 10^{-3}$. Thus, relativistic particles would provide a counterbalance to the formation of gravitationally collapsed structures, and thus require deeper wells for large scale structures to form. This feature can be seen in 11, which shows that the large scale structure of our universe prefers the cold dark matter model.

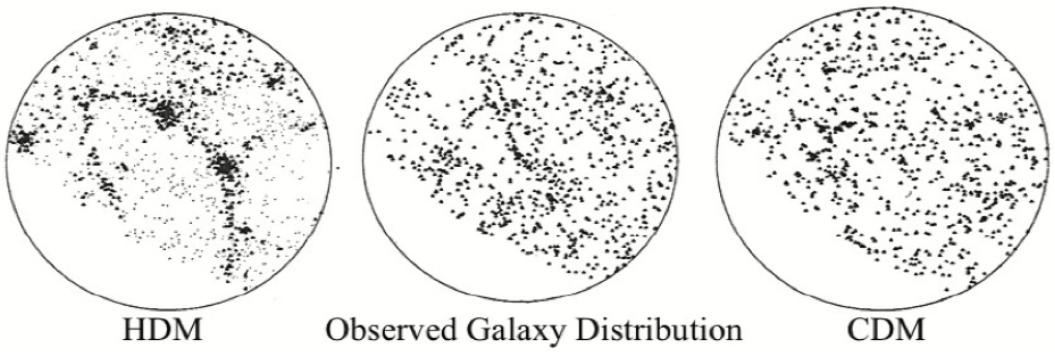


Figure 11: Computer simulations of the distribution of galaxies within our universe, with hot dark matter (left) and cold dark matter (right), compared to the observed distribution (middle). Figure is taken from [23].

1.7.2 WIMP dark matter and the WIMP miracle

WIMP dark matter is a candidate model for dark matter, which explains dark matter as heavy particles which only interact gravitationally an through the weak force. WIMPs are a tempting choice for dark matter, since their properties could explain all the observed phenomena (galactic motion and structure formation). A WIMP is a stable particle[18], with a mass from a few GeV to a few TeV. At their inception there were several promising WIMP candidates from supersymmetric expansions to the standard model, although since then the parameter space available for WIMPs has been probed and become far more constrained. But the real allure of the WIMP is the WIMP "miracle".

The WIMP miracle is well known to be the fact that when one considers a particle of the weak mass scale with a self annihilation cross section close to the weak interaction strength (on the pb level), the present day dark matter relic density can be obtained. Additionally, in many versions of supersymmetry, the lightest supersymmetric particle is indeed a weakly interacting heavy particle, the ideal scenario for the WIMP [82]. In the following section the derivation of the WIMP abundance is shown, which is reproduced here from [83]. The WIMP is denoted as χ, and it is assumed be in thermal equilibrium with other matter while the temperature is $T > \mathrm{m}_\chi$ During this time, the WIMP density n_χ evolves according to the Boltzmann equation, shown in equation 7

$$\frac{dn_\chi}{dt} = -3Hn_\chi - <\sigma_{ann}v>(n_\chi^2 - n_{eq}^2), \tag{7}$$

[18]The WIMP lifetime must be greater than the current age of the universe, since otherwise most would have decayed by now.

where H is the Hubble constant at that time, which in a radiation dominated universe[19] is given by $H^2 = \rho_{rad}/3M_P^2$, where M_P is the Plank mass. While the system is in equilibrium, the number density tracks the equilibrium density n_{eq}. n_{eq} is number density of dark matter where it is in equilibrium with the thermalised medium. In a radiation dominated universe, this depends dominantly on the radiation density, which scales with the expansion of space with a different dependence than the matter density [84]. Subsequently, at some temperature T_f<m$_\chi$, the expansion rate will exceed the annihilation rate, and dark matter will freeze out, and their comoving number density (i.e. the number density accounting for the volumetric expansion of the universe) will remain constant from this point on. An approximate solution to the Boltzmann equation at this point gives equation 8, where $\Omega_\chi h^2$ is the dimensionless dark matter density in the universe[20], s_0 is the present day entropy density of the Universe, g_* is the number of relativistic degrees of freedom of the particle χ at freeze out, and $x_f = T_f/m_\chi \approxeq 1/25$ is the freeze out temperature scaled to the dark matter mass. The value for $x_f = 1/25$ is obtained from solving the Friedmann equation[21] numerically for the freezeout temperature (see [83] for more details). This means that WIMPs would have still moved at relativistic speeds at freezeout, with velocities $< v > \approx c/3$

$$\Omega_\chi h^2 \approx \frac{s_0}{\rho_c/h^2}\left(\frac{45}{\pi^2 g_*}\right)^2 \frac{1}{x_f M_P} \frac{1}{<\sigma_{ann} v>}. \tag{8}$$

Plugging in the known values for the parameters [75] and setting $\Omega_\chi h^2 = 0.12$ from the latest Planck Collaboration results [75], one obtains equation 9

$$\frac{\Omega_\chi h^2}{0.12} = \frac{1}{\frac{<\sigma_{ann}>}{10^{-36} c\, m^2} \frac{v/c}{0.1}}. \tag{9}$$

Thus, setting the thermally averaged annihilation cross section to a value of 1pb * c, and using average velocities of the order one would expect from a WIMP at freeze-out, the current dark matter abundance is recovered. A schematic representation of this process is shown in figure 12, where the decoupling temperature T_{dec} and the freezeout temperature T_f are shown separately. The decoupling temperature is the temperature at which the dark matter and luminous matter stop being in thermal equilibrium, while the freeze out temperature the point where the expansion rate becomes the dominant term for the density change for dark matter, over the annihilation term.

[19] The universe was dominated by radiation until roughly 47ky after the Big Bang, which is many orders of magnitude longer than the dark matter decoupling time, which is at $\lesssim 1$ s.

[20] Ω_χ can be interpreted as the curvature of space which dark matter is responsible for.

[21] This is the solution to Einstein's field equations for an open, closed or flat universe.

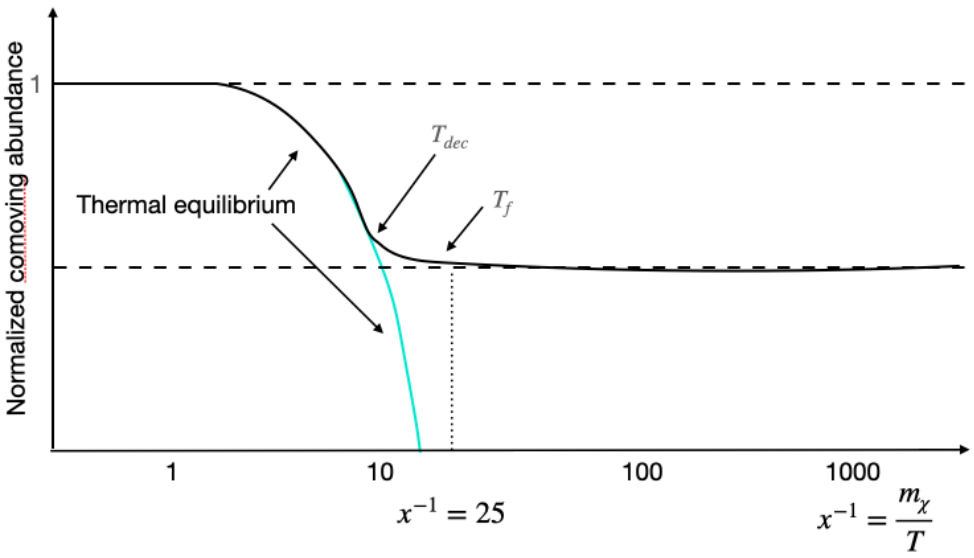


Figure 12: Transition of dark matter from thermal equilibrium to freeze out. Both the decoupling temperature (where dark matter stops being in thermal equilibrium with luminous matter) and the freeze out temperature (when the rate of expansion has dropped the annihilation rate to negligible amounts, so that the comoving density can be considered constant) are indicated on the schematic. Figure is based on the figure in [83].

1.7.3 Other dark matter models

WIMP dark matter is not the only dark matter model on the market, indeed, dark matter models span over ≈ 30 orders of magnitude in mass. A collection of models and their mass ranges is shown in figure 13. Notable other dark matter candidates are neutrinos, sterile neutrinos, axions and primordial black holes (not shown in figure 13). In this section we shall briefly discuss their main concepts, advantages and disadvantages. Promising candidates usually share the quality that they solve not just the nature of dark matter, but also another problem in physics. As discussed earlier, the WIMP neutralino was considered the supersymmetric extension to the standard model at its inception.

Let us first consider axion dark matter. Axions arise naturally in the Peccei-Quinn (PQ) solution to the strong CP problem [85, 86] (see section 1.2.1 for more details), by arguing that the CP violating term $\bar{\theta}$ of the QCD Lagrangian is relaxed to 0 due to an additional PQ symmetry. This symmetry is accompanied by a scalar field which

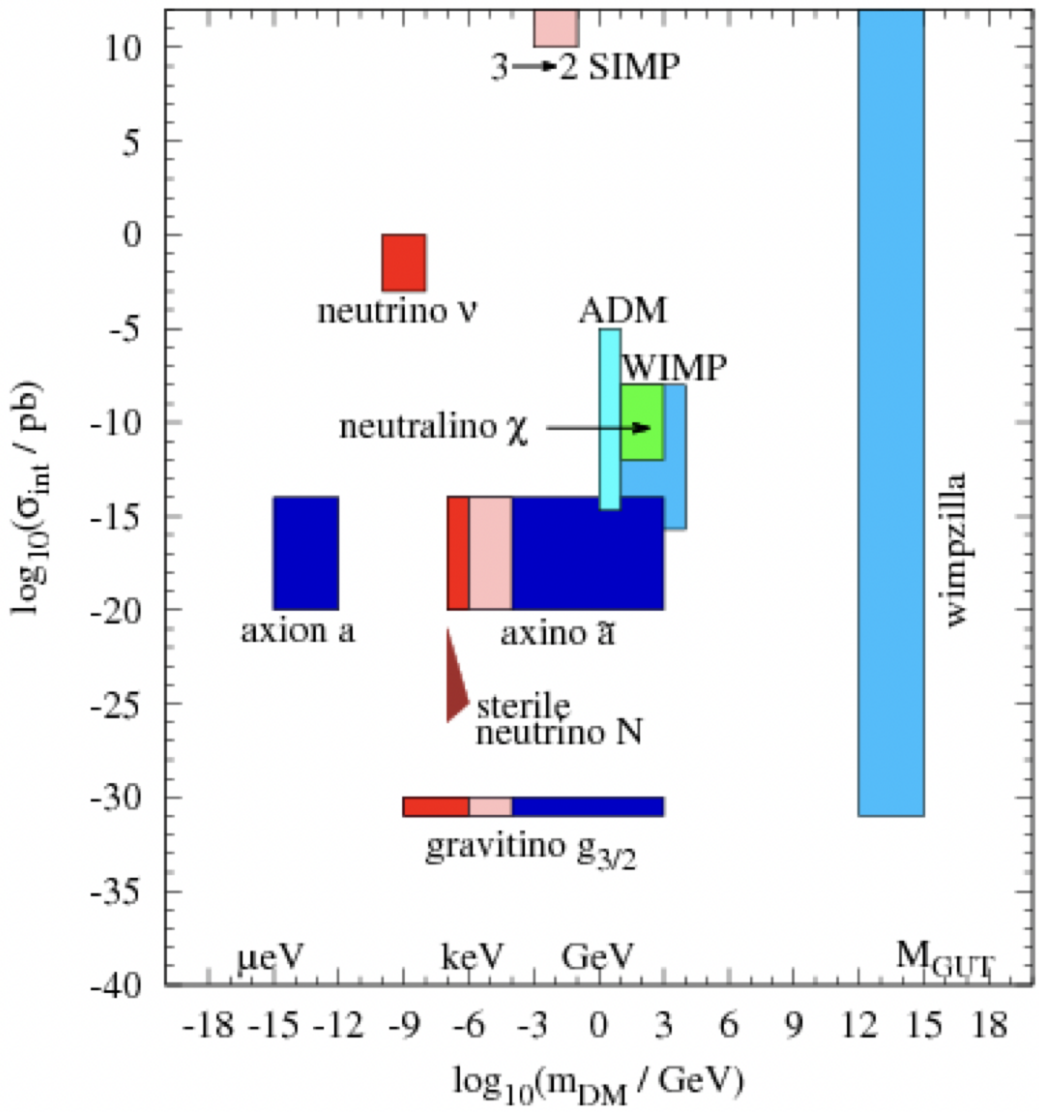


Figure 13: Collection of candidate dark matter models over a wide mass range. The most prominent candidates are WIMP dark matter, axion dark matter and sterile neutrinos. Primordial black hole dark matter is not shown on this plot. Figure taken from [83].

spontaneously breaks the symmetry at low energy, giving rise to the axion. While the initial model, which predicted axion masses of order O(100keV) has long since been experimentally ruled out, it has been replaced by models using the same mechanism to dynamically solve the strong CP problem. Axions of such fields are expected to

have masses in the μeV range. As a side effect, the scalar field would populate the universe with axions, which – since they are produced non-thermally at rest [1] – would be considered cold dark matter even though they have such low masses. As such, a dark matter theory which is not at least partially made up of axions has to provide an alternate solution to the strong CP problem.

Out of all the standard model particles, the neutrino is the only particle which does not interact through either the strong or electromagnetic forces. This makes it a promising initial candidate for dark matter. However, the present-day abundance of neutrinos would be given by equation 10 (further details can be found in [83]). Current constraints on the sum of the neutrino masses $\sum m_\nu$ limit the amount of dark matter in the form of neutrinos to about 0.5%-1.6% [74]. These constraints come from neutrino mixing experiments, as well as from cosmological bounds. This is because neutrinos – being hot dark matter – have a direct impact on large scale structure formation. A related dark matter model is that of sterile neutrinos. This group of models postulates that the right handed neutrinos (and left-handed antineutrinos), are far more massive than their chiral partners. Since they interact only gravitationally (neutrinos carry no electromagnetic or color charge, and the weak force couples only to left-handed neutrinos and right-handed antineutrinos), they would constitute a viable candidate for dark matter [87]. Recent observations of neutrino mixing [74], show that neutrinos are not massless but have a finite mass. The higgs mechanism responsible for giving SM particles their mass requires both left-handed and right-handed fermions, and thus suggests the existence of the neutrinos' chiral partners. Their mass also means that their chirality is not relativistically invariant, since their velocities are slower than the speed of light; i.e. it is possible for an observer to travel faster than the neutrinos and thus observe them with a different chirality. However, it is not known why the couplings to for the left- and right-handed neutrinos would be so different

$$\Omega_\nu h^2 = \frac{\sum m_\nu}{91.5\text{eV}}. \tag{10}$$

The final dark matter candidates to consider are primordial black holes. They are discussed more closely in section 5.1.4, but a brief overview is given here for completeness. Very shortly after the big bang ($O(10^{-23})$s), overdense regions in the universe might have collapsed into black holes. Depending on the time of their formation, they would have consumed most the of available mass within their observable universe at the time, i.e. within their horizon. Such black holes would have expected masses today ranging over many orders of magnitude, well below the critical mass for a stable black hole [88]. Black holes below this mass tend to radiate energy off at a rate faster than their mass accretion, via Hawking radiation [89, 88]. The rate

at which such small black holes radiate off energy is higher the smaller they are, meaning towards the end of their lifetime they disappear via runaway evaporation. During such a process, new antiparticles and particles can be produced. Such primordial black holes fit the required properties of dark matter, being colissionless uncharged matter which interacts gravitationally. However, due to null observation of the particles expected to be released from the evaporation of black holes, their abundance can be tightly constrained. As such, they can at most make up a tiny fraction ($\approx 10^{-11}$) of the observed dark matter in our galaxy.

1.7.4 Dark matter annihilations into antinuclei

The null results from searches for direct detection of WIMPs, either from evidence for supersymmetry at the LHC or from direct detection experiments [90, 91], have motivated other probes for WIMPs. Antinuclei observations from WIMP annihilations have become one of the most promising of such probes, since many WIMP candidates are expected to produce a detectable flux of low energy antinuclei [4, 2]. By definition WIMPs can couple weakly to standard model particles, and their wide plausible mass range leaves open a large parameter space with sufficient energy to create antinuclei. Additionally, since dark matter is expected to be cold, the production of antinuclei occurs in the galactic rest frame, providing no boost to artificially increase their momentum. Thus, considering WIMP annihilations into an initial standard model state, the production of antinuclei is plausible. In a given point in space, the amount of antinuclei produced is then dependent on the number of dark matter annihilations times the spectrum of produced antinuclei in such annihilations, as given in equation 11

$$q(\vec{r}, E) = \frac{1}{2}\left(\frac{\rho_\chi(\vec{r})}{m_\chi}\right)^2 < \sigma v > (1+\epsilon)\frac{dN}{dE}, \tag{11}$$

where ρ_χ is the measured dark matter density at a given point, and $(1+\epsilon)$ accounts for the contribution from other annihilation products which later decay into the antinucleus in question. This process is discussed in more detail in section 5.

1.7.5 Majorana vs. Dirac dark matter

To current knowledge, every fermion in the standard model has an antiparticle, with the same mass and quantum numbers, but opposite charge. This was first predicted by Paul Dirac, who realised that the wave equation he developed to account for special relativity in the motion of electrons implied a second solution, corresponding to a particle with opposite charge [92]. This particle, the positron, was subsequently

discovered, and was the first discovery of antimatter [54].

However, it is mathematically possible for a particle to be its own antiparticle; such particles are called Majorana particles. Out of the fermions in the standard model, only the neutrino could be a majorana particle, since all other fermions have known antiparticles. The majorana nature of the neutrino is being investigated by searching for neutrinoless double beta decay, a process by which two beta decays happen almost simultaneously, the produced neutrinos annihilate and thus provide additional energy to the electrons. The GERDA experiment is currently looking for such an effect [93], but has so far found no signal.

WIMP dark matter is often assumed to be a majorana fermion. Given the lack of any known majorana particles, this seems somewhat unintuitive. The reason is mainly historical, since the original motivation for the WIMP was the supersymmetric neutralino, which is a hypothetical Majorana particle [82]. The reason this convention is still used, is that the effects of the assumption on the Dirac or Majorana nature of a WIMP are degenerate with the assumed WIMP self-annihilation cross section and therefore they produce the same signal. To show this, let us consider equation 11, which describes the source term for antinuclei from Majorana dark matter annihilations. The Dirac nature of the WIMP enters the equation in two ways. First, the density considered. Since the total gravitational effect of dark matter is known, the total measured dark matter density is the sum of the densities of dark matter and anti dark matter $\rho_{\mathrm{DM}}^{\mathrm{meas}} = \rho_{\chi} + \rho_{\overline{\chi}}$.Thus – assuming symmetric populations of dark matter and anti-dark matter – the density term in equation would be $\rho_{\chi}\rho_{\overline{\chi}} = \frac{\rho_{\mathrm{DM}}^2}{4}$. This is a factor of 2 lower than original density term (the symmetry factor of $1/2$ in equation 11 is due to the Majorana nature and thus falls away). However,the second effect is on the thermally averaged annihilation cross section $<\sigma v>$. When predicting the value of $<\sigma v>$ required for the currently observed abundance (as was done in section 1.7.2) the same density alteration is required, which means that the prediction for the thermally averaged cross section remain the same. This is shown in figure 14. Thus, these two effects cancel, yielding the same results for Dirac or Majorana dark matter.

The only possible difference between the two models would come from an asymmetry in the population of dark matter and anti dark matter, and only if this was created after decoupling. If the asymmetry was caused prior to decoupling, the derivation for the expected WIMP cross section would account for this. Thus, such an asymmetry would have had to be caused by a process after dark matter decoupled from thermal equilibrium, which suggests it would have had to form through purely dark matter interactions. It is therefore difficult to suggest any process which

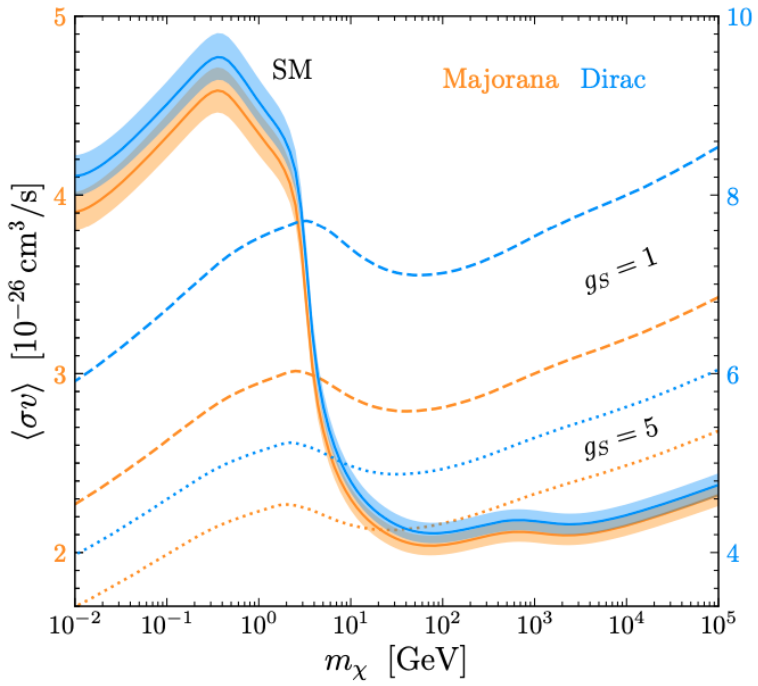


Figure 14: Thermally averaged annihilation cross section for WIMP dark matter as a function of the dark matter mass as it is required to reproduce the measured present-day abundance of dark matter. The left y-axis shows the values for Dirac dark matter, while the right y-axis shows the values for Majorana dark matter, showing the difference of a factor 2. Taken from [94].

would cause such an asymmetry. However, assuming an asymmetry was formed, the number of annihilation would be reduced by the factor $4x(1-x)$ in respect to the case of symmetric Dirac dark matter, where $x = \rho_\chi/\rho_{\chi+\overline{\chi}}$ is the asymmetry factor. For further discussion of asymmetric dark matter, see section 4D in [83].

1.7.6 The search for dark matter: the link between WIMP dark matter and antinuclei

Searches for dark matter can be classed into 3 categories: production searches, direct detection experiments and astrophysical searches. Production searches look to detect the production of dark matter particles in high energy collisions at accelerators. Technically, if WIMP dark matter is weakly interacting and within a mass range which can be produced at accelerators, it might be detectable. However, there is currently no evidence for the production of dark matter at accelerators. Such production searches usually constitute only a small part of the physics programs of accelerator

797 experiments. The second category of experiments are direct detection experiments.
798 These experiments look for WIMP-nucleon interactions and the corresponding re-
799 coil, and include the XENON [95, 90] and LUX collaborations [91]. These will be
800 discussed in more detail in section 5.
801
802 The final probes are astrophysical searches. These focus on signals produced
803 by potential WIMP dark matter which can be differentiated from standard model
804 sources. These signals can come either from annihilations or decay of WIMP dark
805 matter[22], and we have to chose detection channels in which we could both get a
806 reliable signal and differentiate it from other cosmic sources. The most promising
807 searches are gamma rays and antinuclei [96], both of which could be produced in
808 the annihilation of many WIMP candidates, and would produce signals which are
809 expected to be distinguishable from common astrophysical backgrounds. This thesis
810 focuses on measuring antinuclei inelastic cross section and their effect on such an
811 antinuclei signal, in order to help interpret any future antinuclei measurements in
812 cosmic rays.

[22]Technically WIMP dark matter could also scatter of baryonic matter, but this would be much easier to observe in direct detection experiments than in space.

2 Experimental data and experimental method

2.1 ALICE

This section aims to highlight the capabilities of the ALICE detector, in particular in the context of identifying antinuclei and measuring their inelastic cross sections. Measuring antinuclei inelastic cross section was not considered in the design of the ALICE detector. Rather, the excellent tracking and particle identification capabilities of the detector enable these measurements, which go beyond the scope originally envisioned for the detector. We shall therefore discuss the full chain of experimental methods, starting from the particle identification in each of the detectors, to the ALICE data structure and how they are used to obtain the antiparticle-to-particle ratios.

2.1.1 Overview

ALICE is one of the four major experiments at the large hadron collider (LHC) near Geneva, Switzerland. It is the only dedicated heavy-ion experiment at the LHC, with its main physics motivation being the study of the quark-gluon-plasma (QGP). The experiment has 19 subdetector systems [97], of which the most important for this analysis are the Time-Projection-Chamber (TPC), the Inner Tracking System (ITS) and the Time-of-Flight detector (TOF). In particular the TPC sets ALICE apart from the other major LHC experiments, by enabling very precise tracking of particles, good particle identification via momentum and specific energy loss measurements, and its sensitivity low momentum particles (down to $p_T \approx 0.2$ GeV/c). In particular the TPC is special because it maintains the capability to do all this in an environment with more than 10k charged tracks at mid-rapidity in central Pb–Pb collision. The momentum measurement is enabled by a solenoid magnetic field, which is usually operated at 0.5 T[23]. The central detector systems are constructed in a cylindrical shape, providing full azimuthal coverage. The coverage in the forward and backward direction can conveniently be described using the measure of pseudorapidity (η), which is defined as $\eta(\theta) = -\ln[\tan(\theta/2)]$, where θ is the angle which the emitted particle has to the beam axis. This measure is anti-symmetric around $\theta = \pi/2$, i.e. the angle normal to the beam axis, and is 0 at this angle. The central detectors of ALICE cover the midrapidity range of $|\eta| \lesssim 1$. A schematic representation of ALICE with all its subdetector systems can be found in figure 15. It is important to note that the detector discussed in this section is the ALICE detector as it existed during the Run 2 data taking period (2015-2018). The main limitation of this version of the ALICE detector was its moderate interaction and data readout rates, the latter of which was limited to about 1kHz in Pb–Pb collisions and 200kHz in pp collisions.

[23] There are also dedicated low B field runs, where the field is set to only 0.2 T.

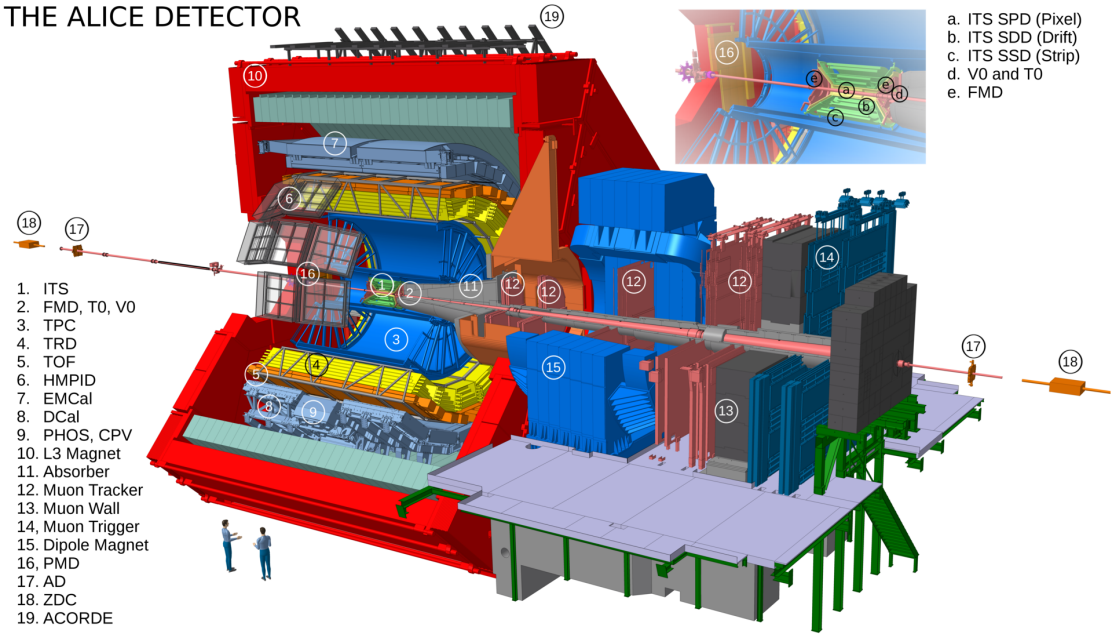


Figure 15: Schematic representation of the ALICE detector and its subdetector systems, during the Run 2 data taking period (2015-2018).

This is due to the $1\mu s$ timespan required for reading out a single event, dead-time for the detector. The ALICE upgrade for LHC Run3 which has started in 2022 will instead be able to read out data at rates up to 50 kHz, and provide a significant boost to the statistics which the ALICE detector can provide.

2.1.2 The ALICE Trigger System

The ALICE detector cannot read out all events which occur, both due to the detector dead-time when reading out an event and due to the data rates which would be involved. Instead, interesting events are selected by predefined criteria, and then triggered upon. This trigger system then initiates the entire read-out sequence of the detector. The most basic trigger is the so called minimum bias (MB) trigger, which should trigger in the presence of any beam–beam collisions and not introduce any bias based on the occurring physics. This is an important data sample to check against, however, it is interesting to bias the selected events in favor of "more interesting" physics. Such triggers look for less common conditions more favorable to rare physics events, such as e.g. the presence of more charged particles. These triggers exploit the fact that data acquisition is limited by the ALICE read-out rate – not by the occurrence rate of rare events – in order to collect data for rare events at the same 200kHz (1kHz) rate in pp (Pb–Pb) collisions at which MB data can be

collected.

For pp collisions, the trigger-criterion used in the analyses presented in this thesis is the multiplicity in the V0 detectors (V0A and V0C), which is correlated with the charged particle multiplicity at midrapidity. The V0 detectors are plastic scintillator arrays in the forward and backwards regions, covering a pseudorapidity range of $2.8 < \eta < 5.1$ and $-3.7 < \eta < -1.7$, respectively. They are located 3.4 m and 0.9 m from the interaction point. The high multiplicity trigger is configured so that the highest 0.17% of multiplicity events are selected by the V0 detectors, while also requiring a minimum of 1 charged particle at midrapidity. This proxy works well for high multiplicities also at midrapidity, as this selection results in an average of 30-40 charged particles at mid-rapidity, as opposed to ≈ 7 particles for MB collisions.

2.1.3 Inner Tracking System (ITS)

The Inner Tracking System (ITS) is the innermost detector in ALICE, staring at a radius of just 3.9 cm from the interaction point and reaching a radius of 43 cm. It consists of 3 lightweight silicon bases sub-systems, called the Silicon Pixel Detector (SPD), the Silicon Strip Detector (SSD) and the Silicon Drift Detector (SDD). The ITS covers a pseudorapidity range of $|\eta| < 0.9$[24]. A schematic of the ITS is shown in figure 16. Since the ITS is the closest detector to the interaction point, it plays a vital role in determining the position of the initial vertex of the collision, called the primary vertex. Indeed, its ability to accurately reconstruct particle trajectories enables the reconstruction of the primary vertex to a precision of 100 μm, and constrains the particles' distributions of their distance-to-closest-approach (DCA). This is particularly important when analysing nuclei at low momenta, since for deuterons, ^{3}He and ^{3}H the contribution from secondaries from material spallation is the dominant contamination in the nuclei signal. The requirement of a cluster in the first ITS layer (SPD), removes any tracks from particles which get created from material interactions at larger radii, unless there is a matchable cluster on their trajectory by chance. The ITS also allows the rejection of pile-up events[25]. The particle identification capabilities of the ITS become less reliable for very large specific energy loss (dE/dx) due to saturation effects, which makes the ITS less useful for PID of doubly charged particles such as ^{3}He.

[24] The SPD can detect particles with a wider range, up to $|\eta| < 1.95$.

[25] Pile-up is what happens when tracks from a different physical collision are incorrectly matched to the same event.

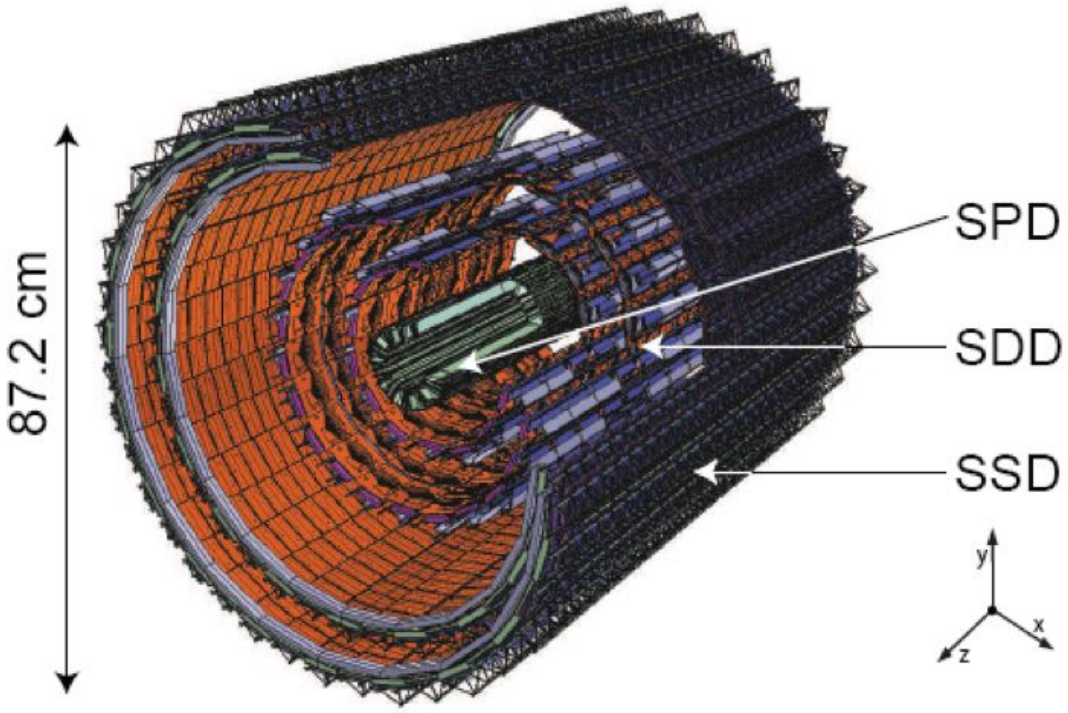


Figure 16: A schematic of the ALICE Inner Tracking System. The three layer groups (SPD, SSD, SDD) are marked.

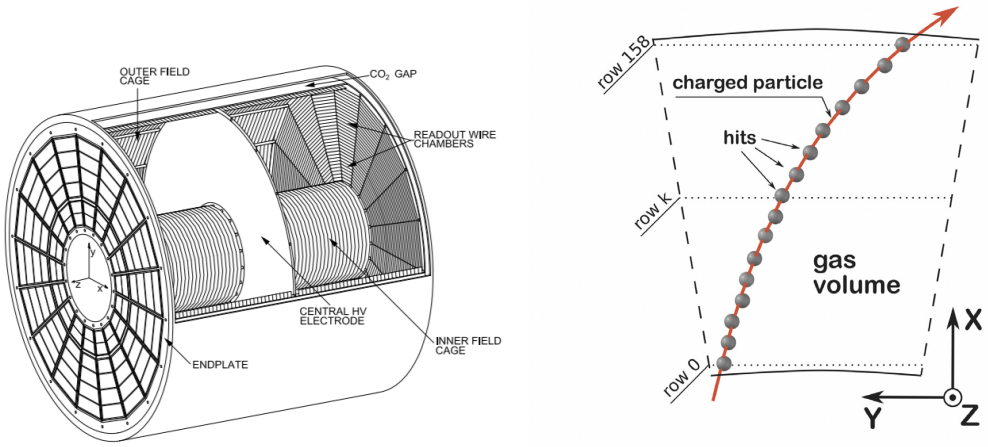


Figure 17: Left: Schematic of the field cage of the TPC detector [98]. Right: Schematic of the reconstruction mechanism for tracks in the TPC [99].

2.1.4 Time Projection Chamber

The Time Projection Chamber (TPC) is the main tracking detector of the ALICE experiment. It follows the ITS in the central barrel, at radii from 85 cm to 247 cm from the interaction point, covering a pseudorapidity range of $|\eta| < 0.9$. The schematic layout of the TPC is shown in figure 17. It consists of a gas filled field cage, which can measure the ionisation caused by charged particles travelling through the gas. Due to the applied electric field, the electrons created from ionisation drift towards the read out cathodes of the field cage. The amplitude of the measured signal then gives a measure of the specific energy loss of the particles (dE/dx), while the position of the clusters at the readout cathode gives the 2-dimensional (x and y) position of the tracks of the particles. Finally, by measuring the time of arrival of the electrons relative to the timing of the initial collision, the z position of the clusters can be calculated. This method is shown on the right of figure 17. Measuring the position and therefore the curvature of the track allows the determination of the momentum of the particles.

Due to the combination of a momentum and a specific energy loss measurement, the TPC has excellent particle identification abilities. The energy loss of relativistic particles[26] is given by the Bethe-Bloch formula, which is reproduced in equation 12

$$-\frac{dE}{dx} = \frac{4\pi n z^2}{m_e c^2 \beta^2}\left(\frac{e^2}{4\pi\epsilon_0}\right)^2\left[\ln\left(\frac{2m_e c^2\beta^2}{I(1-\beta^2)}\right)-\beta^2\right], \tag{12}$$

[26] At very low energies below $\lesssim 0.5$MeV and at very high energies > 100GeV, the Bethe-Bloch formula does not apply.

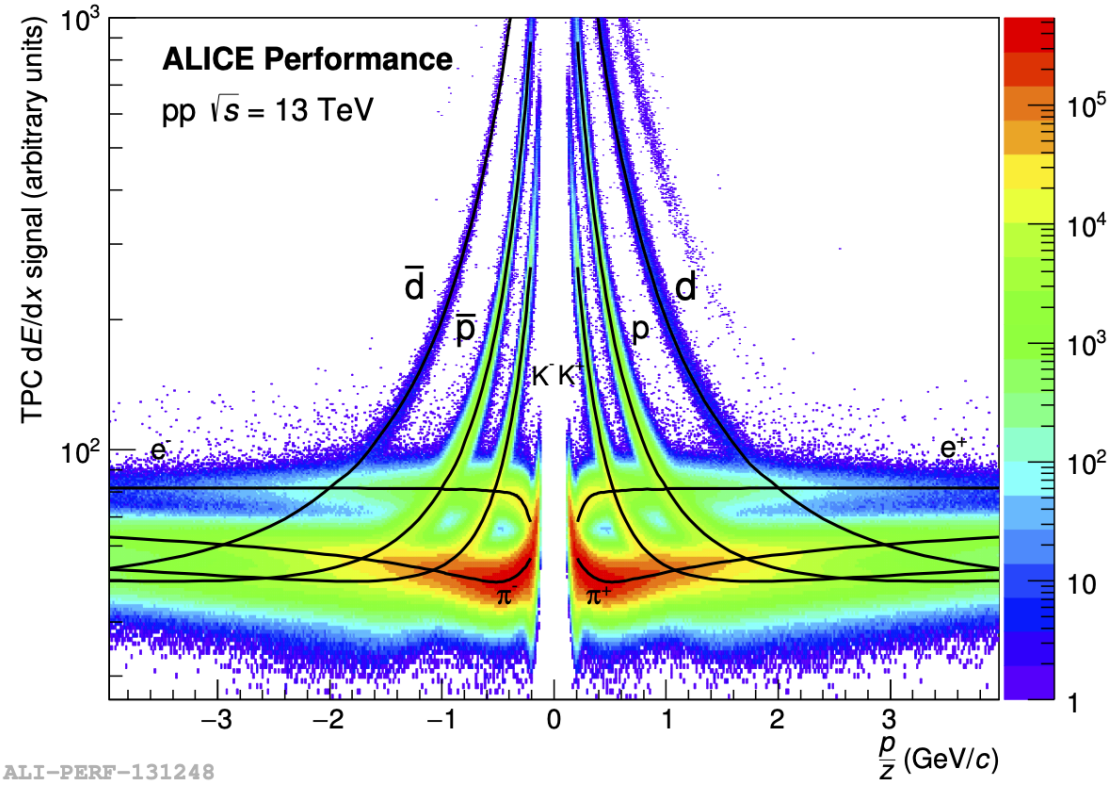


Figure 18: Specific energy loss in the TPC as a function of the rigidity p/z. Due to their masses, particles can be differentiated according to equation 12. This shows the identifying power of the TPC for low momentum particles.

where n is the electron density of the material, I is the mean excitation energy of the material, and the other symbols have their usual meaning. Since equation 12 is a function of only β and z for a given material, a measurement of both the momentum $p = \frac{\beta}{\sqrt{1-\beta^2}} m$ and the energy loss will differentiate particles of different masses. This separating power of the TPC is shown in figure 18, which shows that at low momenta, particles are very well identified by the TPC alone.

The TPC Particle identification (PID) response can be be expressed as the variable $n\sigma_{\mathrm{TPC}}$, which is a measure of how close a track follows the Bethe-Bloch curve of a given particle hypothesis, according to equation 13

$$n\sigma_{\mathrm{TPC}} = \frac{(\frac{dE}{dx})_{meas} - <\frac{dE}{dx}>_{exp}}{\sigma_{resolution}}, \tag{13}$$

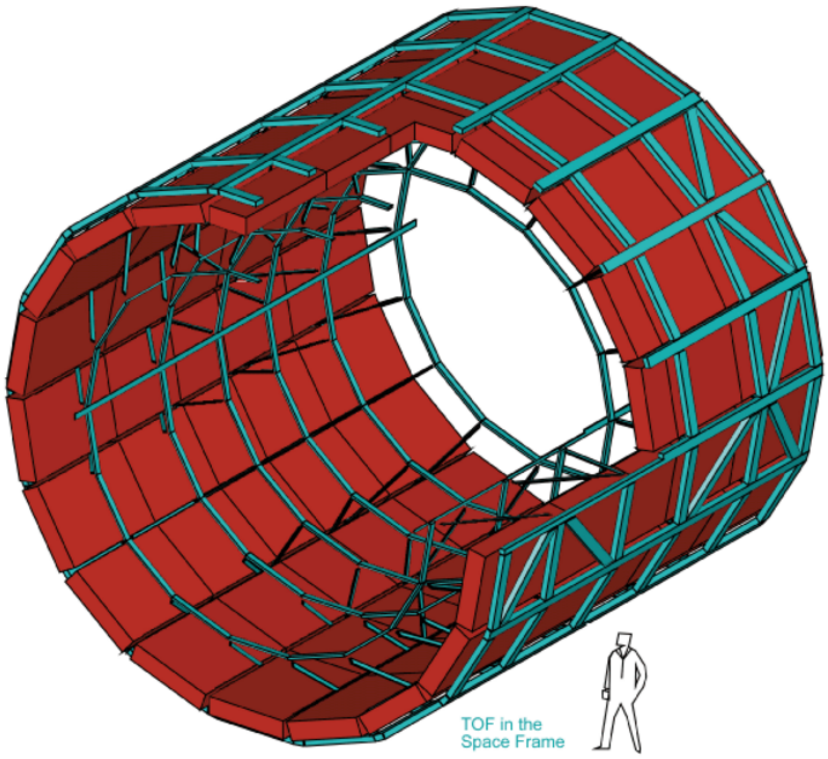


Figure 19: The TOF detector of the ALICE experiment.

where $\frac{dE}{dx}$ is the specific energy loss at a given momentum and $\sigma_{resolution}$ is the resolution of the TPC.

2.1.5 Time-of-flight detector (TOF)

As can be seen from figure 18, the differentiating power of the TPC decreases drastically at higher momenta, as the energy loss of particles tends towards the value for a minimum ionising particle (MIP), and their bands thus start overlapping with each other. In order to distinguish between particles of different masses at higher momenta, an additional information is required. The detector used for this purpose in ALICE is the Time-of-flight (TOF) detector. The TOF is a detector based on multi-gap resistive plate chambers [100], which measures the time difference between the initial collision and the formation of a cluster in one of its readout pads. It is arranged in a cylindrically symmetric structure between 370 cm and 399 cm from the interaction point and has the same coverage in pseudorapidity as the TPC ($|\eta| < 0.9$). The TOF is mounted in a steel structure called the space frame [100, 97]. A schematic representation of the TOF detector is shown in figure 19.

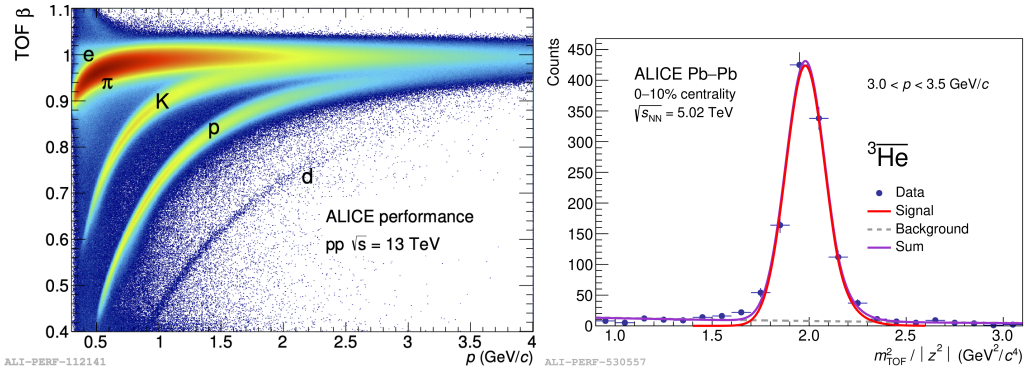


Figure 20: Left: Measurement of the track velocity β_{TOF} as a function of the reconstructed momentum of the particle associated to the track, from the TOF detector in pp collisions at $\sqrt{s} = 13$ TeV. β_{TOF} is classically measured as length of the track divided by the time-of-flight. Right: Performance figure showing the TOF used for the identification of $^3\overline{\mathrm{He}}$ nuclei.

The time resolution of the TOF readout pads is ≈ 50 ps[27]. In order to measure the time-of-flight, the initial time of the collision must be known. This can be done by the TOF itself with large enough multiplicities, and for lower multiplicities it is done with the T0 detector, which consists of Cherenkov arrays [101]. Thus, a measure of the particle velocity, called the TOF beta, can be measured as $\beta = L/t$, where L is the length of the track on its curved trajectory through the TPC, and t is the measured time-of-flight. From the relation $p = \gamma\beta mc$, equation 14 can be derived, which relates the measured β_{TOF} to the tracks mass. The factor $1/Z^2$ cannot be neglected here since the detector cannot know the particles mass a piori. Thus, when analysing multicharged particles such as $^3\overline{\mathrm{He}}$, the observable from the TOF is m_{TOF}/Z^2

$$m^2/Z^2 = \frac{p^2}{c^2Z^2}\left(\beta_{\mathrm{TOF}}^2\gamma^2\right) = \frac{p^2}{c^2Z^2}\left(\frac{c^2t^2}{L^2} - 1\right). \tag{14}$$

The performance of the TOF detector is shown in figure 20. A clear separation between particles can be seen up to much higher momenta than in the TPC. This is particularly true for higher mass particles. The deuteron line can be seen below the marked proton line, and is well differentiable well beyond the merging of the proton and pion lines.

[27] In order to get an idea of this resolution, a particle travelling at the speed of light will travel roughly $c * 50\mathrm{ps} = 1.5$ cm.

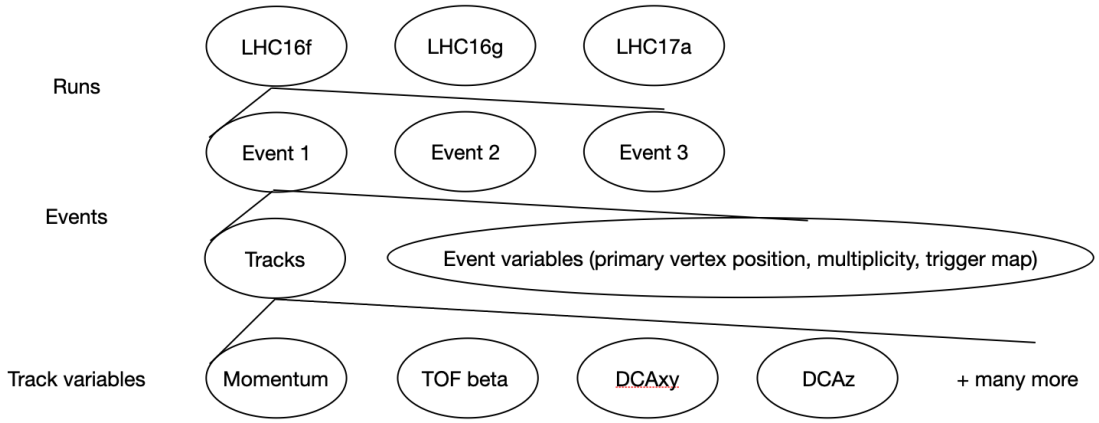


Figure 21: Schematic of the data structures within ALICE. The data is split by run periods, then by event, and within the event by tracks.

2.1.6 Basics of ALICE data structure

ALICE data is split by periods, which in turn consist of runs, then by events, and within the event by tracks, as is shown in figure 21. Runs are the periods of time during which collisions occurred under the same conditions, which means that the data taking is started and kept up until either the LHC beam cycle comes to an end or there is some problem which requires the run to be ended. This means that runs are of arbitrary length. Once the raw data is taken, the Data Preparation Group (DPG) is responsible for doing a reconstruction pass over the data, which means to build the tracks from the individual detector hits, correcting for any calibration or distortion effects. The data structure one is left with is a list of events, each of which contain a list of tracks. This is what is subsequently used by analysers[28]. This hierarchy is shown in figure 21.

2.2 Identifying antinuclei and building the antiparticle-to-particle ratio

This section described the process to identify (anti)nuclei using the ALICE detector, and the method by which the antiparticle-to-particle ratio is then reconstructed. For this purpose, 10^9 high multiplicity pp events at $\sqrt{s} = 13$ TeV were analysed.

[28]There are two files available for runs: ESD and AOD files. The difference is the level of lossy compression in each track. ESD files keep more information – such as a track's momentum at different points in the TPC – while AOD files are faster to analyse due to the smaller memory required.

2.2.1 Collision system and event selection

The data provided in ALICE by necessity includes a large range of particles. For analyses which do not want all charged particles, these act as impurities. Therefore, cuts are applied at the analysis level, to provide a much cleaner environment for the actual analysis. Within the analysis, these cuts happen on both an event and a track level, leaving a subset of tracks which can be analyzed. The goals of these cuts are: i) to cut bad quality tracks, such as ones where the PID is not certain, ii) to cut tracks of uninteresting particles for the specific analysis, e.g. particles produced by material spallation in the analyses in this thesis and iii) to reduce the background, such as from secondary particles from weak decays. These cuts also vary between collision systems, which is necessitated by their different properties. To exemplify this, lets compare a relevant difference between high multiplicity pp and Pb–Pb collisions. In HM pp collisions the mean multiplicity is 34, while in central Pb–Pb collisions it is about 1000. This means that the mean occupancy of the detectors is much greater in Pb–Pb collisions, which in turn means that the tracking algorithm has a higher chance to assign a wrong cluster to a track. In order to reduce this effect, the matching window for the TOF detector is reduced in Pb–Pb collisions, from 10 cm to 3 cm. For the analysis method explained in section 3.1.2, this introduces an uncertainty, as some tracks could be elastically scattered in the TRD or space frame, causing them to miss the matching window without having interacted inelastically. To evaluate and counteract this, a special reconstruction of the Pb–Pb data was used, where the matching window was set to 10 cm instead of 3 cm. The effect of this change is explained in section 3.1.2.

2.2.2 Reconstruction of raw (anti)nuclei spectra

In order to obtain the raw antinuclei spectra, the tracks first have to be identified as antinuclei. This particle identification (PID) occurs on the basis of two main detectors: the TPC and the TOF. Due to the distinct masses of antinuclei (they are heavier than most other long lived particles), they leave a distinct signal in each detector. In the TPC, antideuterons are clearly separated by their energy loss up to a momentum of about 1.4 GeV. $^3\overline{\mathrm{He}}$ is well separated from lighter particles in the TPC for all momenta, due to its double charge[29]. Since the energy loss rises with Z^2, the energy loss of $^3\overline{\mathrm{He}}$ is characteristically much higher than those of singly charged particles. The particle identification of $^3\overline{\mathrm{H}}$ uses the TOF for all considered momenta.

[29] This means that $^3\overline{\mathrm{He}}$ has to contend with impurities from $^4\overline{\mathrm{He}}$, which is also doubly charged. However, given that for each additional nucleon a penalty factor is introduced for the production (as shown in figure 10), this contribution is below the % level and therefore negligible with the uncertainties of this analysis.

In the TOF, the time of flight measurement combined with the track length and curvature gives a measurement of the particles mass, according to equation 14. This allows a clean signal for $^3\overline{\mathrm{H}}$ and $^3\overline{\mathrm{He}}$. For antideuterons, there is still a significant contamination from the tail of the proton distribution at those masses, which requires a fit to the signal and the background to extract the antideuteron yield. Figures 22 and 23 show the extraction procedure in the TPC and TOF for $^3\overline{\mathrm{He}}$. Figure 24 shows the extraction for $^3\overline{\mathrm{H}}$. The particle and antiparticle $n\sigma_{\mathrm{TPC}}$ distributions are fit with a gaussian function. For $^3\overline{\mathrm{He}}$, a second gaussian is used to account for the background from (anti)triton[30]. Both the $^3\overline{\mathrm{He}}$ and $^3\overline{\mathrm{H}}$ signals in the TOF detector are very clean, as is shown in figures 23 and 24, therefore, the TOF signal is used by applying a cut on the m^2_{TOF}. The combination of these measurement allows the extraction of the (anti)nuclei spectra, which are shown in 25.

It is important to note that the histograms in this analysis are low statistics histograms, i.e. they have many bins with 0 counts towards their sidebands. This presents challenges when using the default implementations of χ^2 fitting algorithms, since those tend not to treat empty bins rigorously, if they are included in the fit at all. Therefore, a minimised log-likelyhood fit was done, using proper Poisson errors on empty bins (i.e. empty bins are assigned an uncertainty of ±1.14, for further information see the statistics chapter in [74]).

2.2.3 Correction for secondaries from material spallation

In order to obtain pure samples of nuclei, any secondary nuclei not created in the initial collision need to be subtracted from the obtained raw spectrum. Two sources of secondary particles exists: weak decays and material spallation. For $^3\overline{\mathrm{He}}$ and $^3\overline{\mathrm{H}}$ weak decays are negligible, since the amount of $^3\mathrm{H}_\Lambda$ measured in pp collisions is much less than the amount of $^3\overline{\mathrm{He}}$. The branching ratio of $^3\mathrm{H}_\Lambda \rightarrow {}^3\overline{\mathrm{He}}$ is expected to be 25% [74]. Thus, secondary nuclei (both ^{3}He and ^{3}H) from material spallation remain, which shall simply be referred to as secondaries hereinafter. Since these secondaries are created by essentially "knocking out" these nuclei from larger nuclei in the ALICE detector material and in the beampipe, no secondary antinuclei exist. In order to differentiate between secondaries and primaries, we make use of the fact that all primaries have a common origin (the primary vertex), while the distribution of secondaries should not point to the primary vertex. The measure of how close

[30] The reason why the contamination shows up in the low momentum bins for helium but not for tritons is due to the double charge of $^3\overline{\mathrm{He}}$. This means that by grouping particles in bins of measured momentum, we are actually grouping them in bins of p/Z. Thus, when looking at a given bin in p/Z, tritons have half the momentum of $^3\overline{\mathrm{He}}$. Since this contamination is at values of p/Z before the start of the triton analysis, the inverse contamination does not need to be corrected for in the $^3\overline{\mathrm{H}}$ measurement.

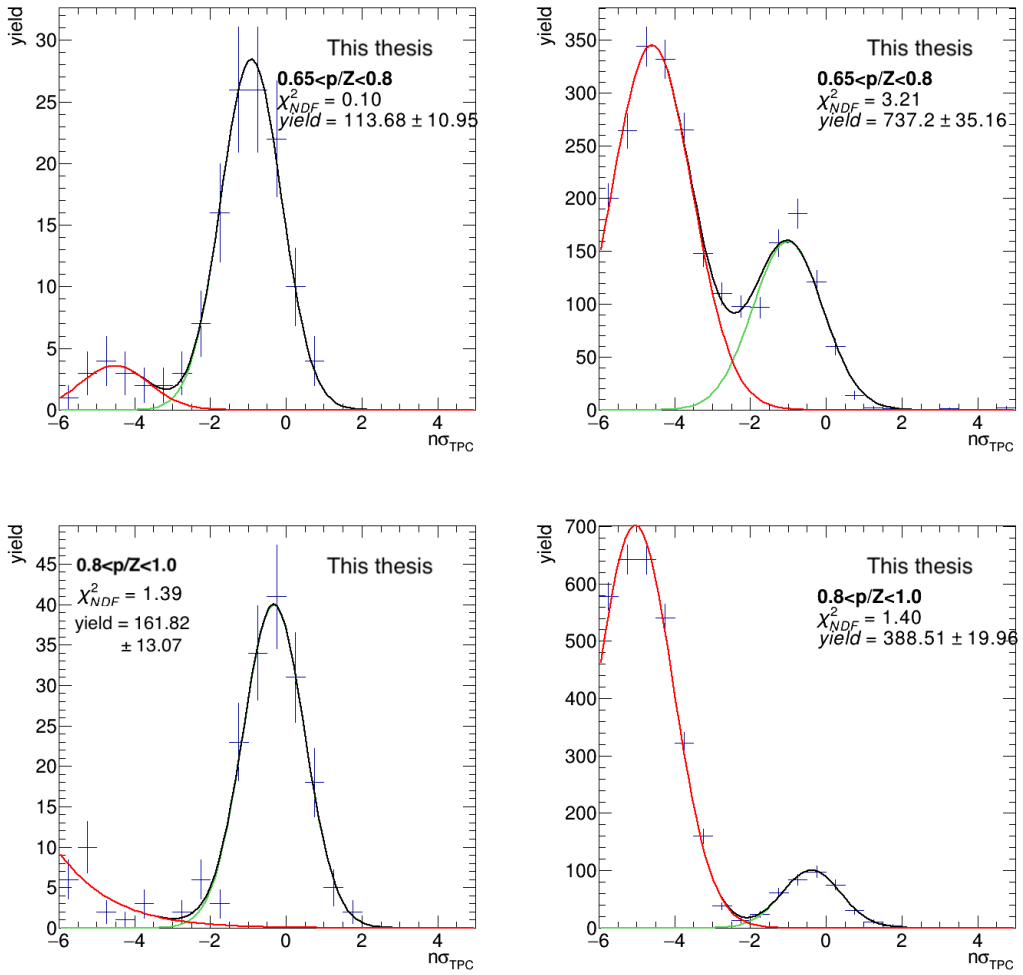


Figure 22: Particle identification procedure for $^3\overline{\text{He}}$ (left) and ^{3}He (right), showing the distribution of $n\sigma_{\text{TPC}}$ for the momentum bins in the TPC only part of the analysis. The green line is the fitted signal, the red line is to fit the contamination towards negative $n\sigma_{\text{TPC}}$. The black line shows the combined fit.

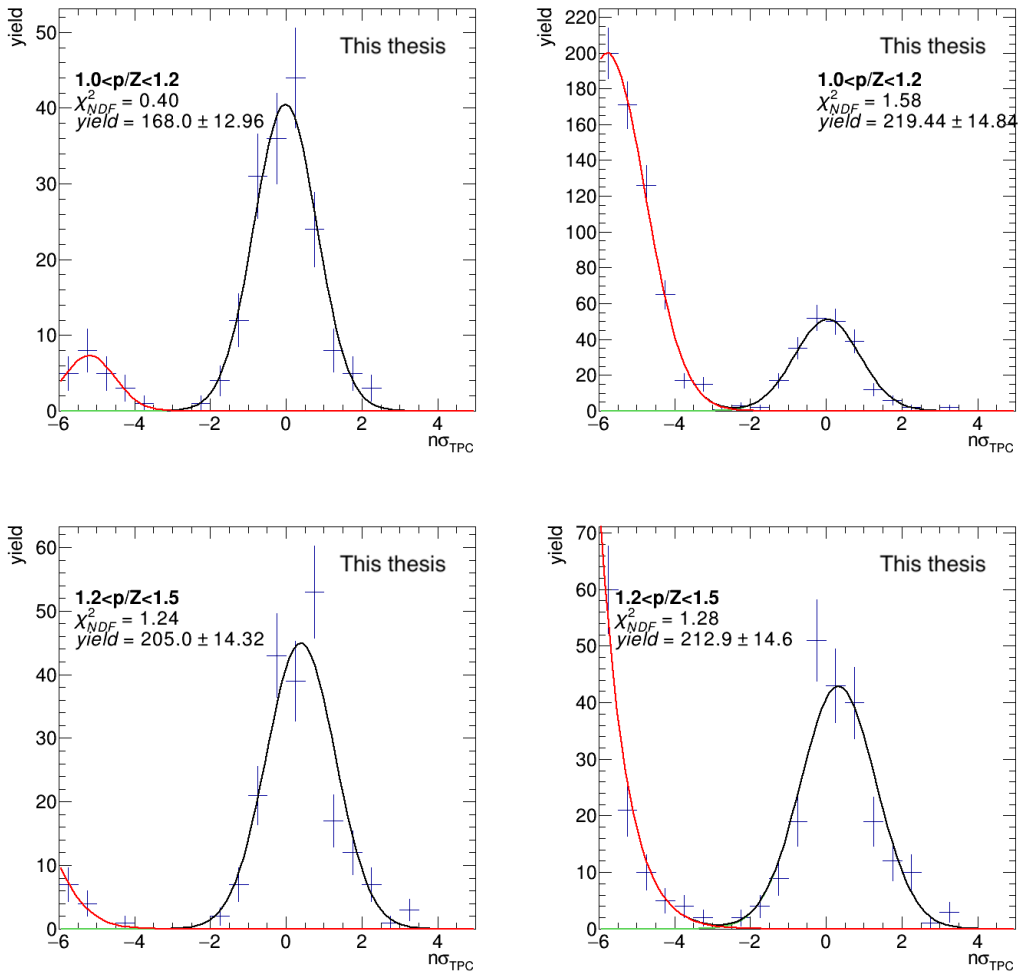


Figure 23: Plots of the $n\sigma_{\mathrm{TPC}}$ distribution for $^3\overline{\mathrm{He}}$ (left) and ^{3}He (right), for the momentum bins in the TPC+TOF only part of the analysis, i.e. after a cut on m^2_{TOF} is applied. The green line is the fitted signal.

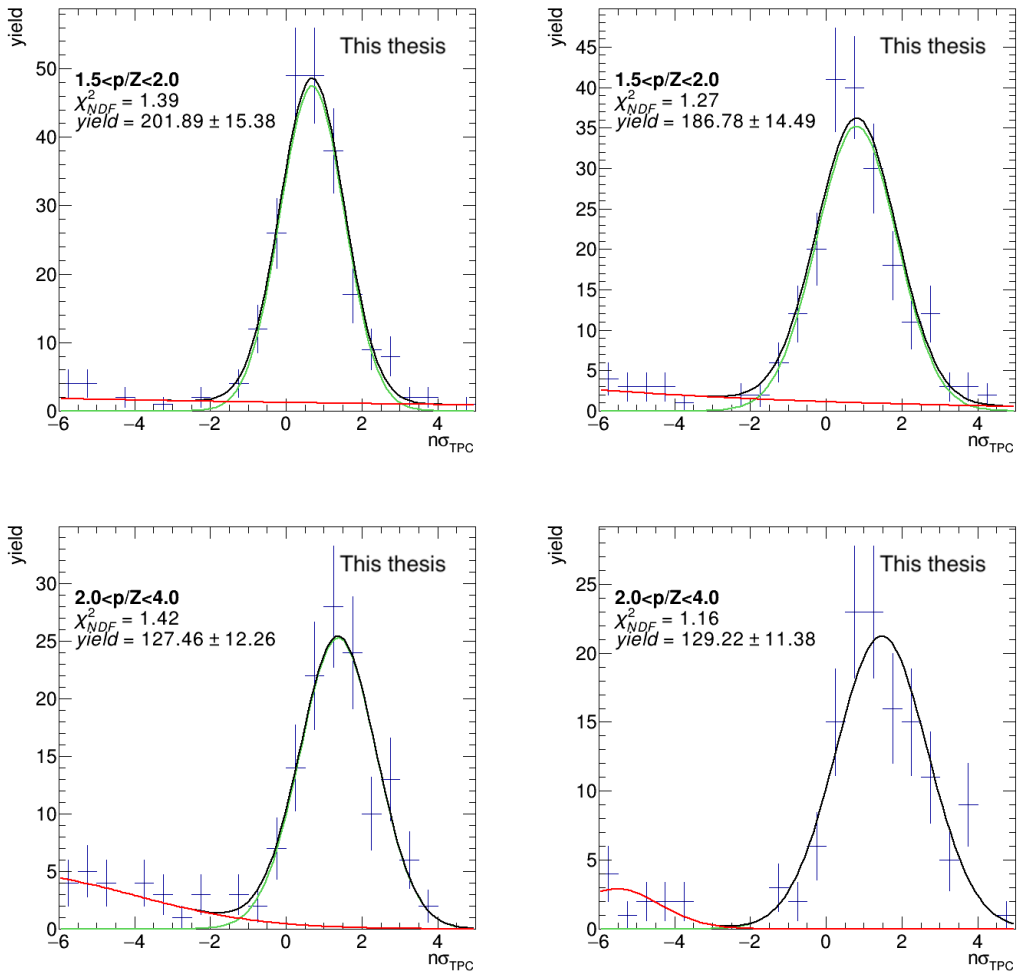


Figure 23: (Continued) Plots of the $n\sigma_{\mathrm{TPC}}$ distribution for $^3\overline{\mathrm{He}}$ (left) and ^{3}He (right), for the momentum bins in the TPC+TOF only part of the analysis, i.e. after a cut on m^2_{TOF} is applied. The green line is the fitted signal.

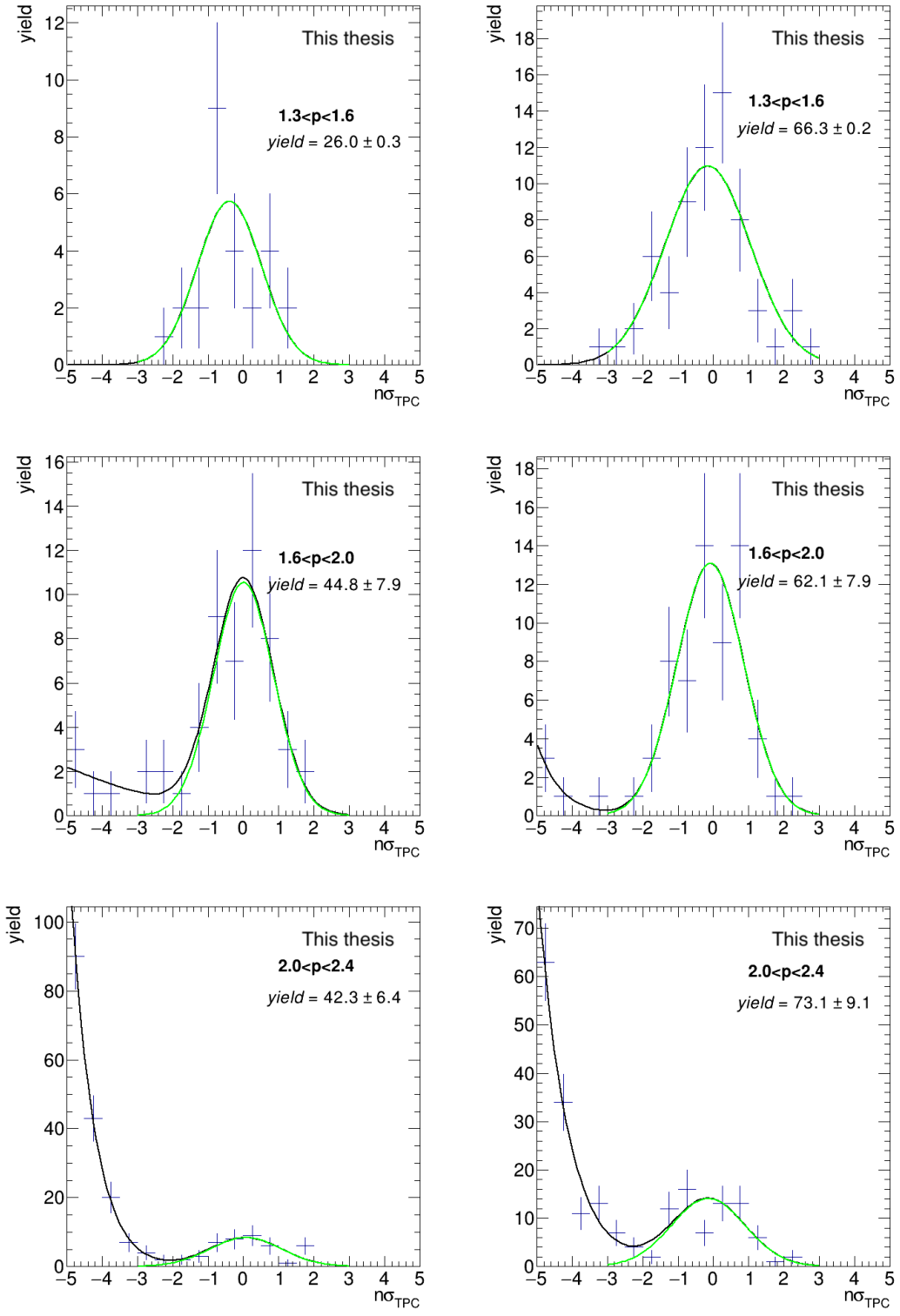


Figure 24: Particle identification procedure for $^{3}\overline{\mathrm{H}}$ (left) and $^{3}\mathrm{H}$ (right), showing the $n\sigma_{\mathrm{TPC}}$ distribution for each momentum bin, after a cut on m^2_{TOF} is applied. The green lines represent the fitted signal, and the black lines the fitted signal+background.

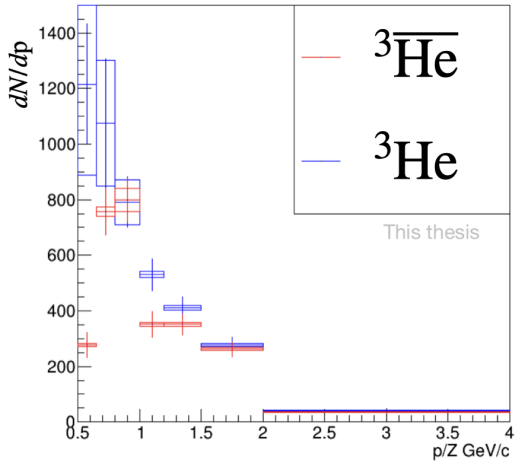


Figure 25: (Anti)nuclei spectra for ^{3}He $^3\overline{\mathrm{He}}$. Blue points show ^{3}He while the red points show $^3\overline{\mathrm{He}}$. Statistical uncertainties are shown as errorbars while systematic uncertainties are shown as boxes. These spectra are not yet corrected for secondary particles from material spallation.

a particle's track reaches to the primary vertex is known as the distance of closest approach (DCA), and within ALICE is resolved in both the xy and the z planes. In order to fit these distributions, they have to be projected onto one of the two directions, which involves cutting on the other. The DCA$_{xy}$ distributions were used for the fits described later in this chapter. The resulting changes in the primary ^{3}He yields depending on the values of DCAz which are selected is shown in figure 26. An uncertainty of 8% is applied to the first bin as a result of this cut.

We expect the primary DCA distribution to be peaked sharply at 0, while the distributions for secondaries should be mainly flat. Example distributions from Monte Carlo Simulations are shown in figure 27.

Figure 27 shows that while the distribution for primaries is indeed sharply peaked at 0, the distribution of secondaries is not flat, but also peaks around 0. This is an experimental effect due to the tracking algorithm, which prefers reconstructing tracks pointing towards the primary vertex. This is exacerbated by the possibility to assign a wrong ITS cluster to the track. Several cuts can be made on the tracks to minimize this effect, which are outlined in section 2.2.2. The most important cut is on the number of clusters in the first ITS layer, which reduces the number of secondary tracks by $\approx 85\%$, as is shown in figure 28.

The biggest challenge with secondary corrections is to get reliable templates for secondary nuclei from material. For a combinatorial background, a side band analysis can be done, since no deviating behaviour in the signal region is expected,

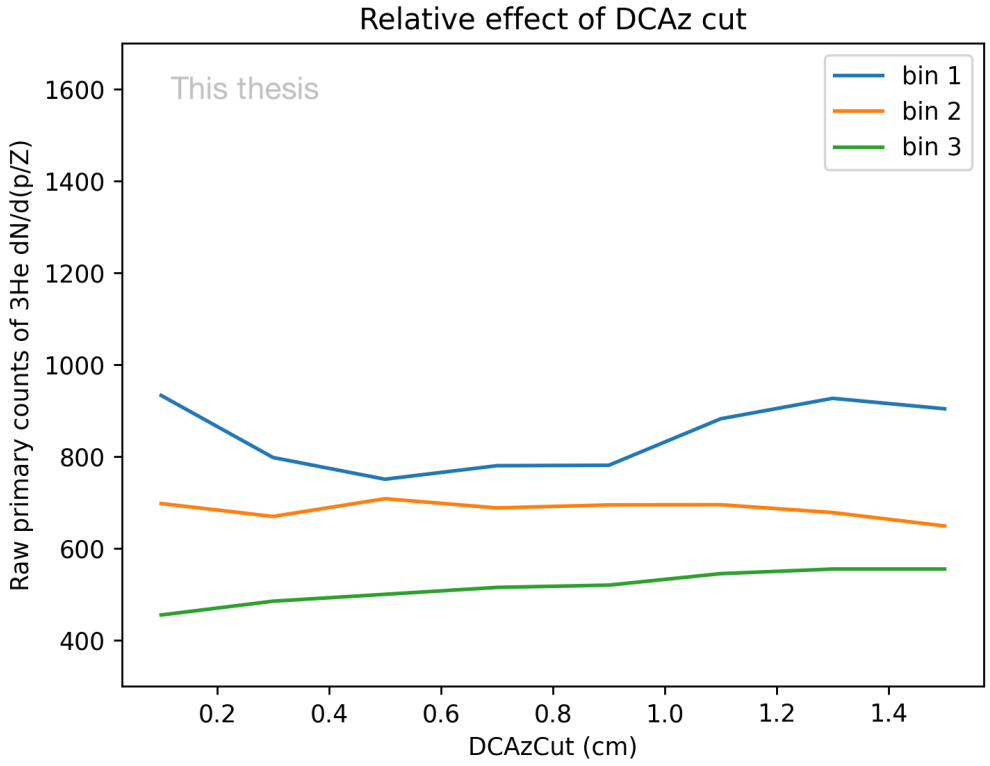


Figure 26: Extracted primary ^{3}He yields in each analysis bin as a function of the value of the cut on |DCAz|. Due to the variations in the first bin, an 8% uncertainty was assigned.

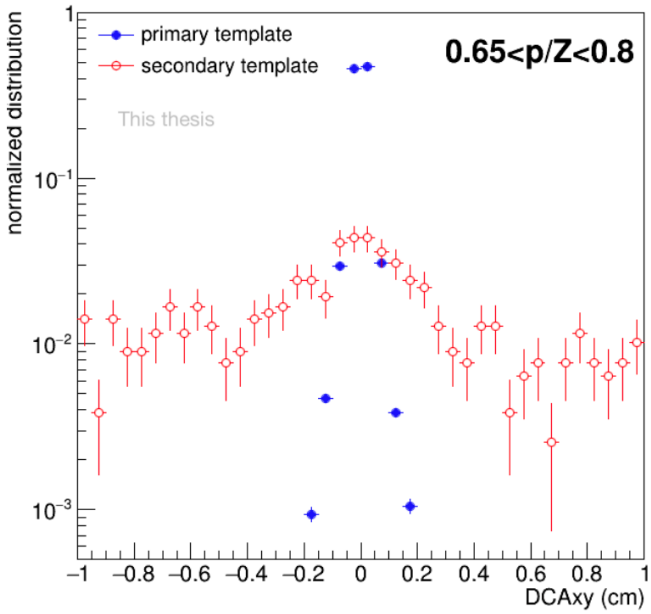


Figure 27: Example DCA_{xy} distributions of particles from primary and secondary particles in Monte Carlo simulations. The particle shown here is $^3\overline{\text{He}}$ with a $|DCA_z|<1$ cm requirement.

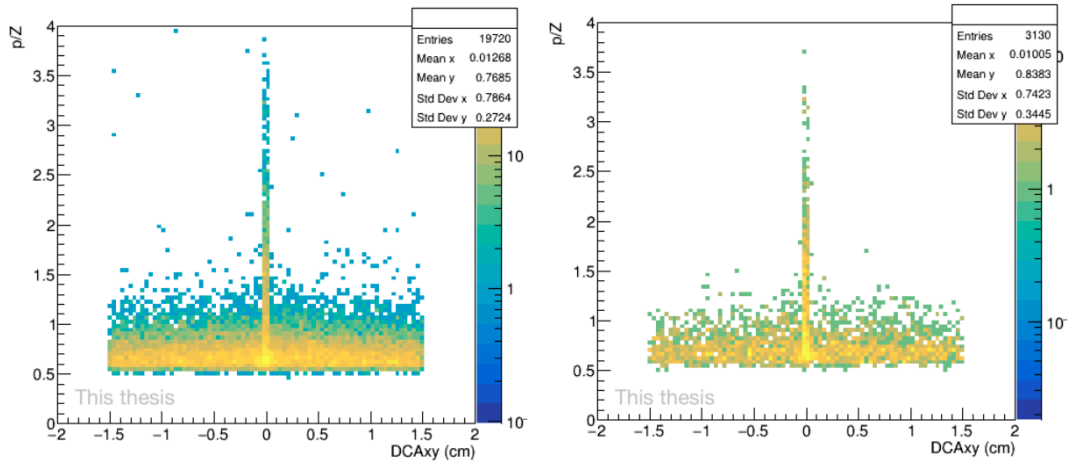


Figure 28: DCA_{xy} distributions of ^{3}He candidates without any cut on ITS hists (left) and after a hit in one of the two first layers of the ITS is required (right). The reduction in the number of candidates is mainly in the sidebands, and therefore from secondaries.

but since we have already seen in figure 27 that secondary tracks are also peaked towards the primary vertex, the sideband analysis cannot help us account for this. It is however also impossible to extract a pure secondary distribution from data, since the peak region always necessarily includes the particles produced in the initial collision. Thus, we need to simulate the distribution with Monte Carlo simulations. This means that we rely on the assumption that the angular distribution of the spallation processes are accurately reproduced in Monte Carlo[31]. The advantage of this method, is that in full ALICE Monte Carlo simulations, the same tracking algorithm is used as in data reconstruction, which means that if the spallation processes are accurately simulated, the distribution will match the true distribution. Also, these simulations rely on the correct underlying event, i.e. for high multiplicity pp collisions, such collisions need to be accurately simulated. This is due to the fact that the spallation is triggered by particles produced in the primary collision. A final challenge to obtaining the template fits is the rarity of these spallation processes in MC simulations.

In order to extract the secondary fraction from the DCA distributions, template fits are used. These fits take the shape of input templates (in this case from primaries and from secondaries) and try to match their relative contribution in order to reproduce the shape in data. Two different fitting algorithms were investigated: the TFractionFitter and Roofit. The main difference between the two is that the TFractionFitter can change the shape of the templates within uncertainties in order to better reproduce the data. In the limit of infinite statistics, both of these methods should produce the same result. In the analyses shown in this thesis, the TFractionFitter was used as the default method, and Roofit was used to crosscheck these results. Additionally, a sideband analysis of the templates was performed as an additional crosscheck. A comparison of the template fits obtained using these three methods is shown in figure 29. As can be seen, the uncertainty introduced by the scaling of the histogram (the comparison of the left and central panels in figure 29) is smaller than the uncertainty returned by the fit. The detailed fits and corresponding primary fraction are shown in sections 3 and 4.

One could also ask the question of which primary particles are responsible for the largest amounts of nuclei secondaries from spallation. In order to investigate this question, a toy Monte Carlo simulation was used, where beams of primary particles were fired on layers of beryllium and beryllium + carbon, corresponding to the materials of the beampipe and the support structure of the first ITS layers. This

[31] The absolute value of the cross section is not important for the accuracy of the templates, since the relative weight is later determined by the template fits. However, too low a cross section means that far more events have to be simulated in order to gain sufficient statistics to obtain the template.

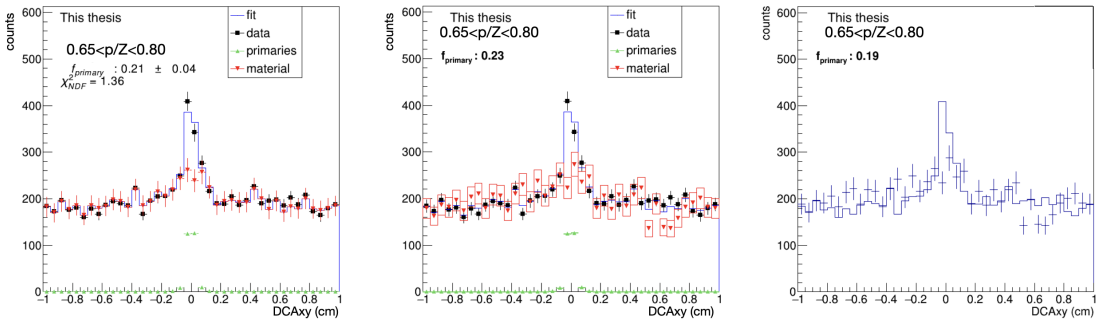


Figure 29: Comparison of different methods for determining the primary fraction from the template fits, shown in the second bin of the $^3\overline{\text{He}}$ analysis, with a $|\text{DCA}_z|$<1cm cut. (Left) Fit using the TFractionFitter. (Middle) Default templates scaled according to the weights assigned by the TFractionFitter, but without changing their shapes. (Right) Fits performed by scaling the material templates to the region outside $|\text{DCA}_{xy}| < 0.1$ cm. The solid line represents the data and the histogram points are the fitted material template. See text for more details.

configuration was chosen since if the spallation occurs later, the missing hit in the first ITS layer allows a large degree of rejection[32]. An exponential energy spectrum was used for the primary particles, tuned to the proton spectrum measured by ALICE [102]. Geant4 was employed for this simulation [103, 104]. The resulting yields of secondary deuterons and ^{3}He are shown in figure 30. Interestingly, the primary antiparticles produce a larger portion of the secondary nuclei than their primary particles. Also, while antideuterons produce a larger amount of secondary nuclei than antiprotons (by roughly 2x), given that their relative abundance in pp collisions is 1000x less, their contribution is expected to be on the sub % level. This leads to the conclusion that it is mainly (anti)protons and pions which are responsible for creating secondary antinuclei. Therefore, when using ALICE Monte Carlo simulations, it is not necessary to employ a coalescence afterburner with the underlying event in order to accurately simulate the secondary distributions. A caveat to this is that the simple toy Monte Carlo simulation only probed absolute yields, rather than the angular distribution, and as already noted above, the latter is the important factor. However, given that the contribution to the yields is on the sub % level, any difference in the distribution is expected to be negligible.

[32] This is somewhat less true in Pb-Pb collisions, since the multiplicities are so much higher and therefore a wrongly associated ITS cluster is far more likely.

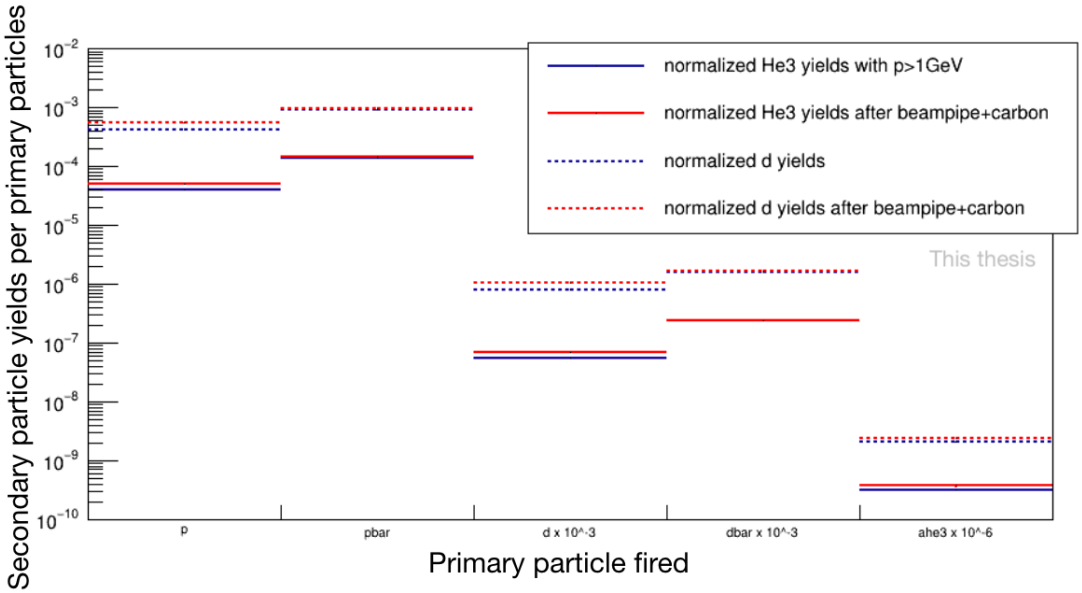


Figure 30: Normalized secondary particle yieds as a function of primary particles fired obtained from a toy Monte Carlo simulation of a particle beam on materials mimicking the LHC beampipe in ALICE and the beampipe + ITS support structure. The resulting secondary deuterons and ^{3}He are shown as a function of the primary particle fired, where the results are roughly scaled by the primary particles relative abundance.

2.2.4 Annihilations within the detector

Annihilations within the detector material can occur at any point within the detector, but are of course more likely in denser materials. For the purpose of this discussion we shall differentiate between 3 different scenarios: i) annihilations before the middle of the TPC, since such tracks cannot be identified and will therefore not be reconstructed in our spectra. ii) annihilations between the middle of the TPC and the TOF, since these annihilations can be directly probed by the comparison of the yields in the TPC and TOF. And finally annihilations outside of the TOF detector, which for the purposes of this analysis is not seen at all, i.e. such annihilations are not measured.

Let us first consider the case where the annihilation occurs before the middle of the TPC. A track with less than half of the TPC clusters will be removed by the track cuts, therefore this track will not show up in our analysis, and will never even be identified as an antinuclei candidate track. The situation is slightly different when considering tracks which annihilate between the TPC and the TOF. Those tracks can be identified in the TPC. For $^3\overline{\mathrm{He}}$ this identification can occur over the whole momentum range ($0.5 < p/Z < 4$ GeV/c in HM pp collisions), while for antideuterons this identification only works up to $p < 1.4$ GeV/c and for $^3\overline{\mathrm{H}}$ it only works up to $p < 1.5$ GeV/c. However, since the antinucleus does not reach the TOF, the TOF hit will either be missing, or at a wrong time (i.e. giving an incorrect TOF mass). This allows for two options in these analyses: in the case where the TPC is sufficient to clearly identify the antinucleus, and it is within the acceptance of the TOF, the difference between the TPC and TOF yields can be used in order to probe the antinuclei inelastic cross section without being reliant on the corresponding nuclei yields. The second option is to use the TOF information in order to increase the amount of material which the particles need to traverse before being considered in the analysis, which makes the ratio more sensitive to the inelastic cross section. This increase is rather drastic, since the material budget increases by a factor of ≈ 5 when switching between a TPC only analysis and one which includes the TOF. This can be seen in figure 31, which shows the cumulative material budget in ALICE as a function of radius.

We are thus left with the two possible methods for measuring annihilations within our detector. The first is based on quantifying the loss of antiparticles as they move through the detector, by comparing them to their particle counterparts. This method works for any particles and momentum range which the detectors can probe a priori[33]. As part of this thesis, this method was performed for $^3\overline{\mathrm{He}}$ and $^3\overline{\mathrm{H}}$. The second is based on comparing the yields in the TPC and the TOF, in regions where

[33] As we have seen in section 2.2.3, the unreliability of the secondary correction at low momentum limits the low momentum reach of this method.

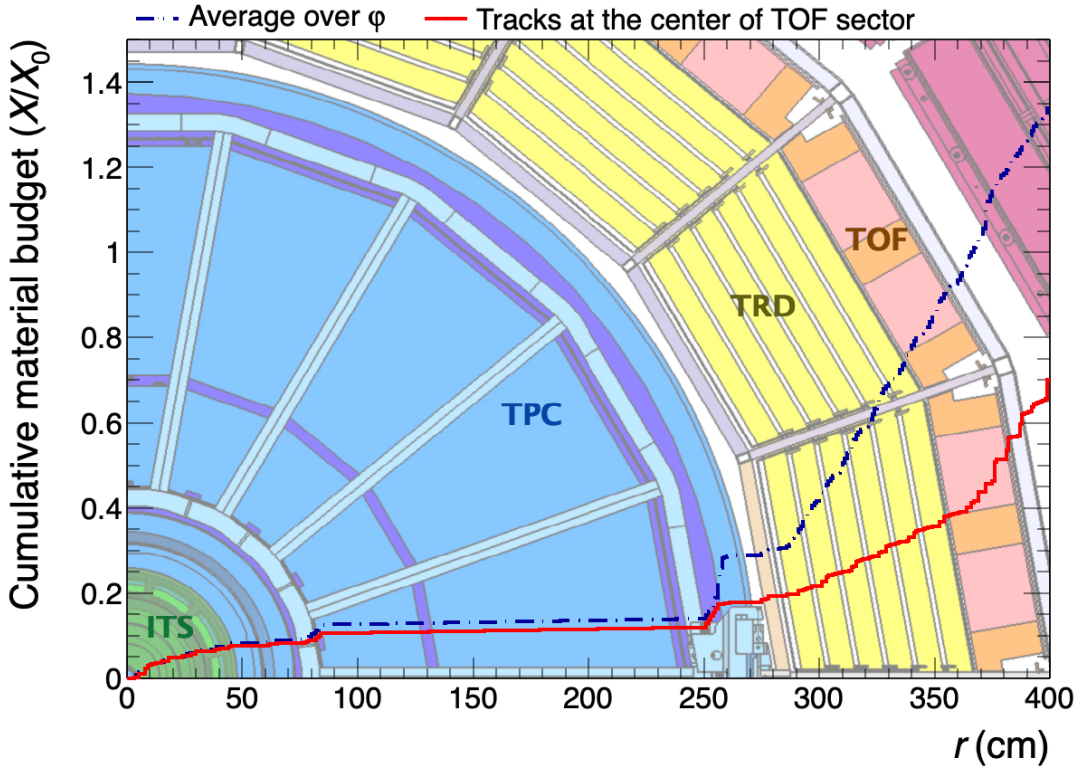


Figure 31: Cumulative material budget of the ALICE detector, as a function of radius from the beampipe, taken from [105]. The solid red line is the value for straight tracks which hit the centre of the TOF sector, while the dashed blue line is the average value over azimuthal angle.

the antinucleus can be clearly identified in the TPC alone, and which include the acceptance of the TOF.

The analyses utilising the TOF-to-TPC method for the measurement of the inelastic cross sections of $^3\overline{\mathrm{He}}$ and $^3\overline{\mathrm{H}}$ were performed by others, and are reproduced in this thesis since they are closely related to the results shown in this thesis. The measurement of the antideuteron inelastic cross sections in pp and p–Pb collisions were also not done as part of this thesis, however the comparison of the two results to show the independence of the antiparticle-to-particle ratio on the chosen collision system was performed as part of this thesis.

2.3 Extracting the inelastic cross section from the antimatter-to-matter ratio

The idea behind using the antimatter-to-matter ratio as the observable to measure the antinuclei inelastic cross section, is that antinuclei will annihilate in the detector material, and therefore disappear from our measurement[34]. In order to quantify the inelastic cross section we thus need to know how many particles were originally produced, i.e. we need to normalise the antinuclei spectrum to the number of originally produced antinuclei. However, we cannot use theoretical predictions tuned to this data, since that would be a circular argument, i.e. we would get out the same inelastic cross section as we put in. Therefore, the matter nuclei are used as a proxy instead. This works very well for a few reasons. First, the matter inelastic cross section can be easily measured, and have been measured for deuterons [106], ^{3}He [107]. For ^{3}H, the inelastic cross section could be measured with the same method, but has not been measured yet. Second, other effects on the acceptance or efficiency will largely cancel between the nuclei and antinuclei counterparts, since the two only differ in their charge sign. Third and perhaps most important, is the fact that at LHC energies, the primordial ratio is very close to unity, and has been accurately measured for antiprotons [108]. This means that we know to a very high degree of accuracy how many antinuclei are produced relative to the produced nuclei, and the other processes by which both might be lost within the detector are also well understood. Thus, the antimatter-to-matter ratio is sensitive to the antinuclei inelastic cross section, and other variables it is sensitive to are well understood and under control. This makes this ratio such a promising probe to measure the inelastic cross section.

Having established that the antimatter-to-matter ratio is sensitive to the inelastic cross section, it is still not trivial to extract the inelastic cross section from this observable. This difficulty is due to having to account for many processes. One example is the path which the particles take through the detector. In the magnetic field, (anti)nuclei travel on curved tracks, so the amount of matter they interact with will depend on their initial trajectory. This thus needs to be averaged over the η distribution of the antinuclei. This is just one of many similar effects which make an analytical relationship between the antimatter-to-matter ratio and the antinuclei inelastic cross section difficult to achieve. Fortunately, detailed simulations of the ALICE detector using Geant4 account for all pertinent interactions of (anti)nuclei. We therefore compare our measured ratios to ones obtained using Geant4 simulations,

[34] Annihilation of antinuclei is the dominant inelastic process at low energies, however, it is not the only process we observe. Antinuclei – being composite objects – may also break apart in inelastic reactions which leave the antinucleons intact. The measurement techniques described in this section measure the total inelastic cross section, which includes all inelastic processes.

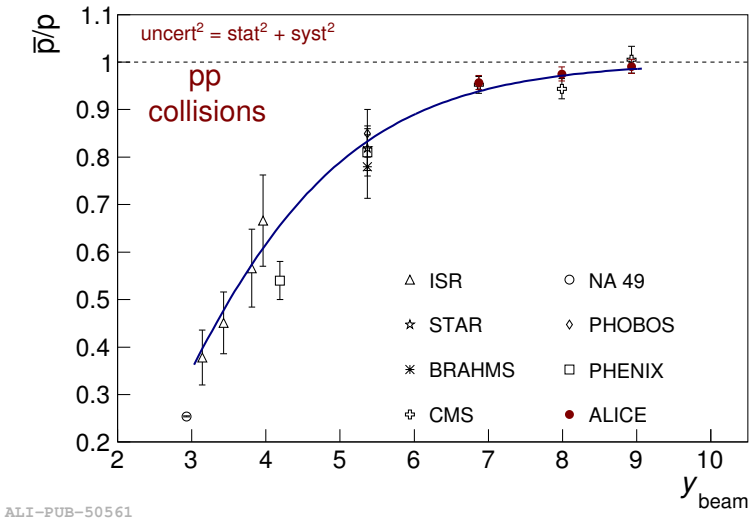


Figure 32: Ratio of antiprotons to protons produced at mid-rapidity as a function of beam rapidity. At LHC energies the value approaches unity, demonstrating that at such high energies antimatter and matter are produced in almost equal amounts. Figure taken from [108].

in order to obtain our results on the inelastic cross section. In order to probe the relationship of the antinuclei-to-nuclei ratio to the inelastic cross section, the Geant4 code was modified to vary the inelastic cross section, keeping all other interactions the same.

2.3.1 Using the antipartilce-to-particle ratio from Monte Carlo simulations

In order to fairly compare the Monte Carlo simulations to the produced data, it is vital to account for the primordial ratio[35] at such high energies. The relevant ratio of antiprotons-to-protons is shown in figure 32. Based on the same arguments as the formula for the coalescence parameter 6, the effect on the ratio of antinuclei will be the same as to the antiproton-to-proton ratio taken to the exponent of the mass number of the antinucleus.

2.3.2 Ratios as a function of the inelastic cross section scaling factor

In order to extract the inelastic cross section measurement from the antiparticle-to-particle ratio, we have to compare the measured ratio in each bin to values from

[35] In other words: how much more antimatter particles we have for each matter particle. Given that we collide purely matter particles, there is a penalty for producing antimatter, even though at such high energies it is vanishingly small.

MC simulation with varied values of the inelastic cross section. The use of MC is necessary in order to obtain the dependence of the inelastic cross section on the antiparticle-to-particle ratio. This then allows the bin-by-bin extraction of the inelastic cross section by comparing the dependence in MC to the measured value of the ratio in the data [36]. These plots are shown for the $^3\overline{\mathrm{He}}/^3\mathrm{He}$ and $^3\overline{\mathrm{H}}/^3\mathrm{H}$ ratios in figures 33 and 34, respectively. These plots also show fit lines to the Monte Carlo points, which were with with an exponential according to the Lambert-Beer absorption law [109], which is reproduced in equation 15

$$N_{\mathrm{surv}} = N.\exp\left(-\sigma.\rho.L\right), \tag{15}$$

where L is the distance travelled through a medium, σ is the absorption cross section and ρ is the density of the medium. The only difference between the different Monte Carlo simulations is the implemented inelastic cross section, $\sigma = \sigma_{\mathrm{inel}}$. Thus, by mapping the measured antiparticle-to-particle ratio onto the fitted dependence to find the intercepts, the corresponding value of the scaling factor on the inelastic cross section is found from the x values of the intercepts. In order to reconstruct the values of the inelastic cross section corresponding to the values of the scaling factor, 2 things are necessary: the average material of the ALICE detector (to pick the corresponding cross section implemented in Geant4) and the average energy loss of antinuclei before annihilation occurs (in order to multiply the correct momentum values). These two factors are discussed below in sections 2.3.4 and 2.3.3, respectively.

For the TPC/TOF method, a similar method is used in order to extract the measurement of the inelastic cross section from the TPC/TOF ratio. However, due to the increased amount of material budget which particles have to traverse and the much reduced statistical uncertainties provided by the Pb–Pb data set, the exponential functions are much less steep in the area of interest. An example of such a fit is shown in figure 35.

2.3.3 Accounting for energy losses between the primary vertex and the point of annihilation

We collect the histograms leading to the antiparticle-to-particle ratio as functions of the momentum these particles have at the primary vertex p_{Vtx}. However, the

[36] This is a proxy for the actual inelastic cross section measurement. However, the mapping from the scaling factor to the inelastic is not exact, but is subject to the uncertainty from any energy loss before annihilation occurs, as will be discussed in section 2.3.3.

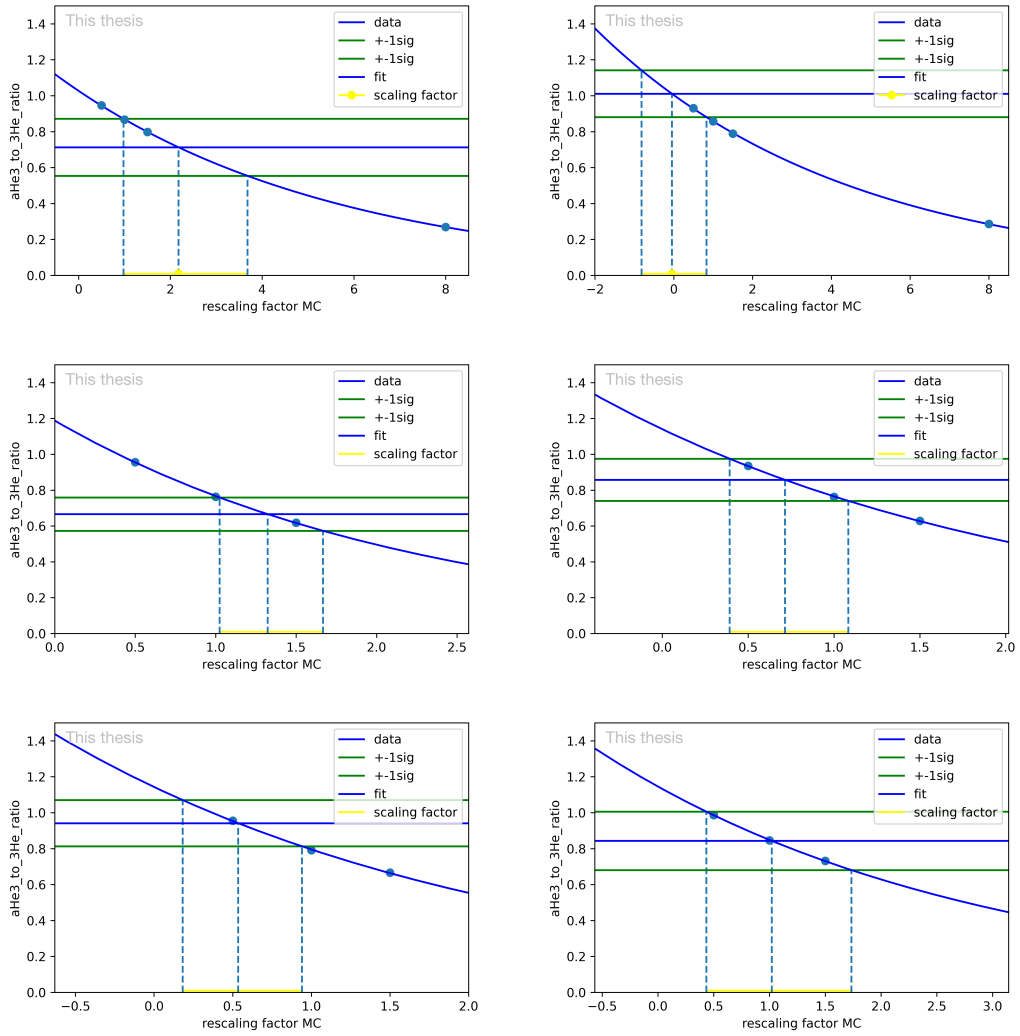


Figure 33: Bin by bin plots of the $^3\overline{\mathrm{He}}/^3\mathrm{He}$ ratio as a function of the varied inelastic cross section in Monte Carlo simulations, together with the one measured in data. The fitted line is an exponential fit according to the Lambert-Beer law 15, and is used to extract the cross section scaling factor.

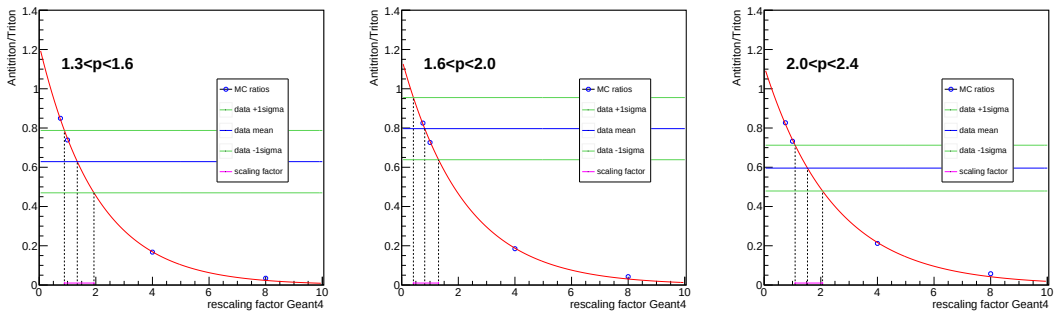


Figure 34: Bin by bin plots of the $^3\overline{\mathrm{H}}/^3\mathrm{H}$ ratio as a function of the varied inelastic cross section in Monte Carlo simulations, together with the one measured in data. The fitted line is an exponential fit according to the Lambert-Beer law 15, and is used to extract the cross section scaling factor.

cross section should be given as a function of the momentum which the particles have during annihilation, $p*$. This means energy losses which occur before annihilation need to be accounted for. Since we do not see tracks for particles which annihilate, this cannot be done on a case-by-case basis, but must be done statistically.

In order to correct for this, let us consider 2 extreme scenarios for where the annihilation might occur. If the annihilation occurs immediately when the particle is produced and meets the beampipe, then it will still have its initial momentum p_{Vtx}. The latest point at which a particle can annihilate and still be included, is just before it would get recognized by the detector. This can be denoted as p_{TPC} and p_{TOF}, for the TPC and TOF regions of the analysis, respectively. p_{TPC} can be determined very accurately in data, since the tracking of the TPC allows the determination of the momentum. Since the annihilation must occur somewhere between these two momenta, we can assume a mean value of $p* = \frac{p_{\mathrm{TPC}}+p_{Vtx}}{2}$, and evaluate the uncertainties by evaluating the cross section using the 3 different scenarios MIN $p* = p_{Vtx}$, MEAN $p* = \frac{p_{\mathrm{TPC}}+p_{Vtx}}{2}$ and MAX $p* = p_{\mathrm{TPC}}$. A schematic representation of how this uncertainty is then applied to the inelastic cross section is shown in figure 36. The uncertainty from this correction is less than 3% for $^3\overline{\mathrm{He}}$ and 2.5% for $^3\overline{\mathrm{H}}$. p_{TOF} can similarly be found from the measurement of β_{TOF}.

2.3.4 Evaluating the average ALICE material budget

The annihilations in the ALICE detector can occur on any of the materials in the detector. Therefore, the inelastic cross section can only be shown on an average material. In order to obtain the average detector material, a weighted average is evaluated, based on the density of a given material ρ. This was calculated over 1 cm

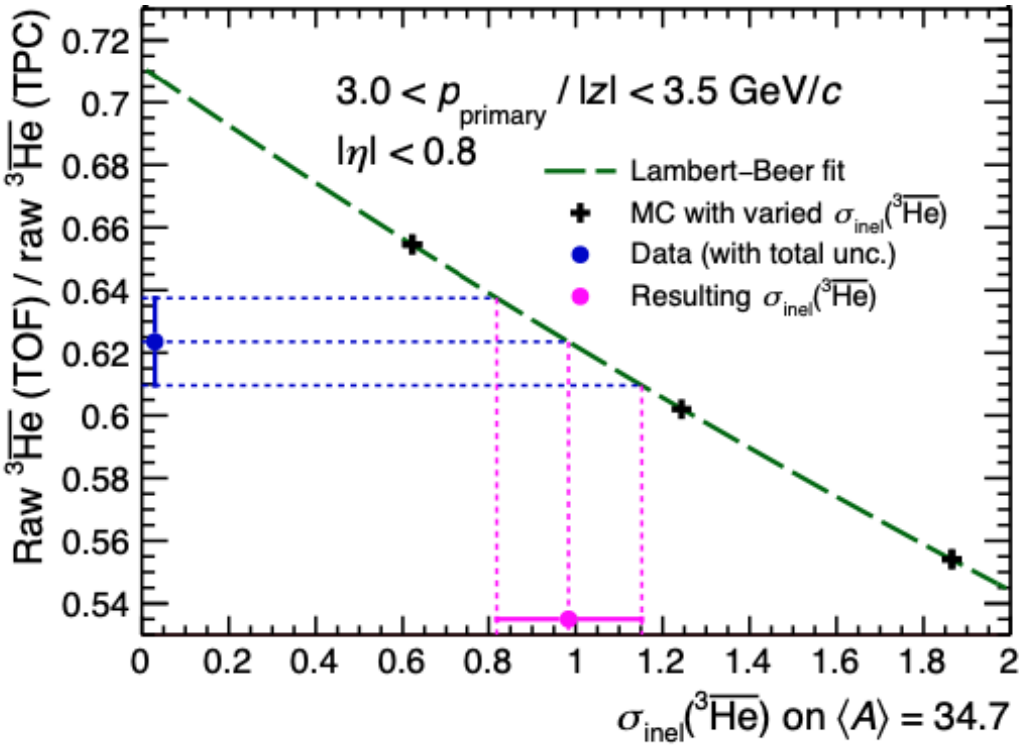


Figure 35: TPC/TOF ratio for $^3\overline{\text{He}}$ as a function of the varied inelastic cross section, for one momentum bin. Figure taken from [110]. The dashed green curve is the a fit of the Lambert-Beer law (equation 15) to the values of the TPC/TOF ratio obtained from MC simulations with varied inelastic cross section (black crosses). The blue datapoint is the ratio in data, and the pink point is the corresponding measurement of the inelastic cross section.

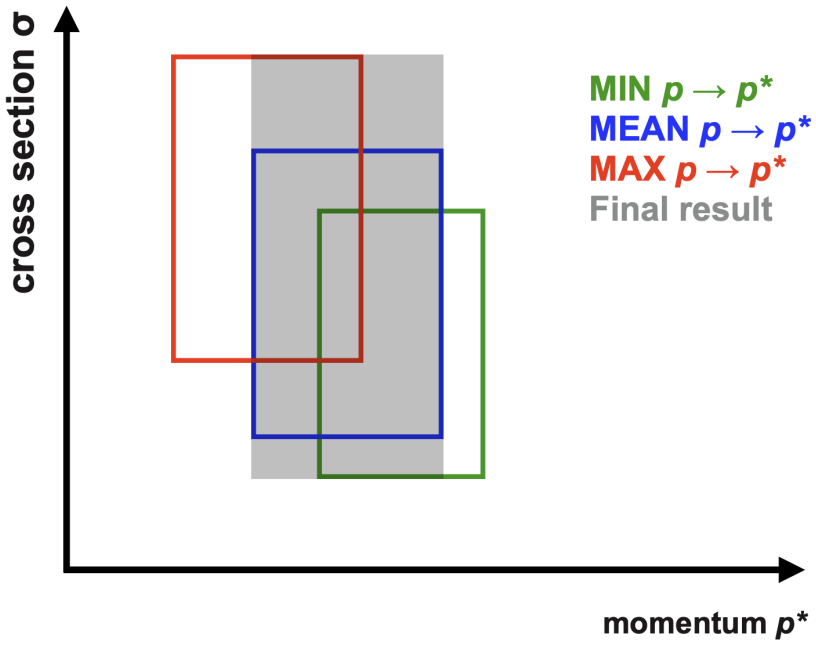


Figure 36: Schematic representation for how the correction for the energy loss of antinuclei – and the corresponding systematic uncertainty – is applied to the measurements of the inelastic cross sections. In order to map from the scaling factor to the inelastic cross section, the default parameterization used in Geant4 is employed.

Average mass number	TPC only	TPC + TOF	TPC/TOF matching
$< A >$	17.4	31.8	34.7

Table 2: Values for the average atomic mass number of the ALICE detector material $< A >$, for different analysis methods. They are evaluated according to equation 16.

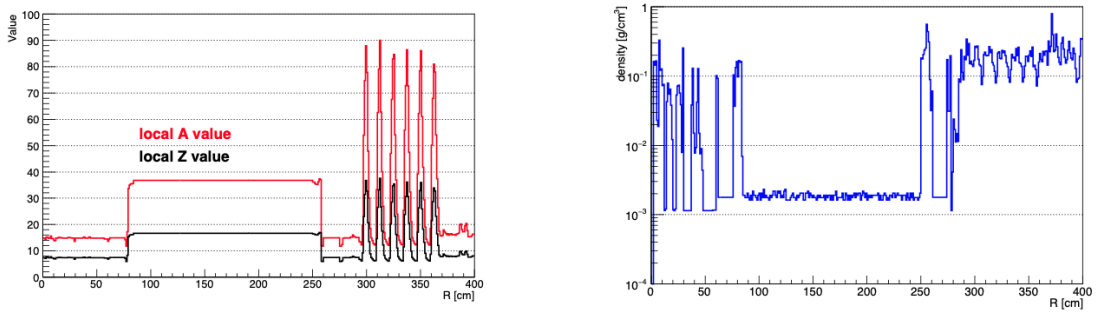


Figure 37: Local A and Z values (left) and density (right) of the ALICE detector material ad mid-rapidity as a function of the radial distance from the interaction point.

steps (which are denoted as i) from 0 cm up to a radius R, which is the last position in the detector at which the particles could be identified. This means that annihilations before this point are accounted for in the inelastic cross section measurements. Since the distribution of the ALICE detector is non-uniform in azimuthal angle ϕ, the material values were averaged over many random azimuthal angles (denoted as j). This is shown in equation 16

$$< A >= \frac{\sum_{i=1}^{R} \rho_i A_i}{\sum_{i=1}^{R} \rho_i} = \frac{\sum_{i=1}^{R} \sum_{j=1}^{N} \rho_{ij} A_{ij}}{\sum_{i=1}^{R} \sum_{j=1}^{N} \rho_{ij}}. \tag{16}$$

The local A and Z values of the ALICE detector, as well as its density, as a function of radius is shown in figure 37. This yields different values for different measuring methods, depending on the range of radii in which the annihilation can occur. If only the TPC is used for determining the antiparticle-to-particle ratio, then only the distance between the beampipe and the middle of the TPC (ca. 168 cm from the beampipe) is considered. When the TOF detector is also used, distances up to the TOF detector (370 cm) are considered. Finally, for the TOF/TPC method, the radii from the middle of the TPC (168 cm) to the TOF detector (370 cm) are evaluated.

Once the scaling factors are extracted by comparing the ratios in data to the ones obtained in MC, they need to multiplied by the inelastic cross sections used

in MC in order to obtain the measured value for σ_{inel}. Since Geant4 only has cross sections implemented on existing materials, the one with the closest mass number A was chosen, and then scaled according to the parameterizations used in Geant4, as described in equations 3 and 4 in section 1.4.3.

2.3.5 Uncertainty coming from the material budget

The measurement outlined in this thesis relies on the accurate knowledge of the ALICE material budget. This is because the loss of antinuclei is proportional to $e^{-\sigma_{\text{inel}}\rho l}$, where ρ is the density of the material traversed and l is the path length of the antinucleus through the material. Thus, the material budget can be quantified as the sum of $\rho_i l_i$, over all the materials i in the detector. This means that the constraints on the cross section are actually on the product of the cross section and the material budget, and thus any uncertainty on the material budget is 1:1 applied to the inelastic cross section measurement.

Originally, the uncertainty on the material budget was quantified to be about 5% using photon conversions [111], up to the middle of the TPC (since later conversions would result in tracks which have less than half of the TPC clusters and thus cannot we well identified). However, this method left out the bulk of the material budget considered in any analysis using the TOF, as can be seen from figure 31. Therefore, the material between the TPC and TOF detectors needed to be validated using a different method. In order to to this, the same underlying idea as the TPC/TOF analysis was used, but rather than assuming a well known material budget and measuring the cross section, a particle with an accurately measured cross section was used in order to probe the material budget. The trick was to find a particle which could be identified cleanly enough in the TPC alone. For this purpose, π^+ and π^- from $\mathrm{K}^0_s \rightarrow \pi^+ + \pi^-$ decays and protons from Λ or $\overline{\Lambda}$ decays were used [112]. Due to their decay topology, they could be cleanly identified in the TPC alone, and their cross section was very accurately known. The measured ratio was then compared to ratios from simulation with varied ALICE material budget, in order to ascertain the uncertainty on the material budget between the TPC and TOF. The resulting uncertainties are shown in figure 38. It can be seen that an uncertainty of $\approx 5\%$ is achieved using this method.

Therefore, a global uncertainty of about 5% is assumed on the material budget. This uncertainty is included in the total uncertainty calculated on the the primordial ratio, which is the ratio of how many antiparticles are produced in respect to their particle equivalents, at the energies probed. This measurement is based on the $\bar{\mathrm{p}}/\mathrm{p}$ ratio as measured by ALICE [70, 71, 108]. The uncertainty on this ratio is 1.5%, which is applied for each nucleon in question for both analyses, i.e. 3% for antideuterons

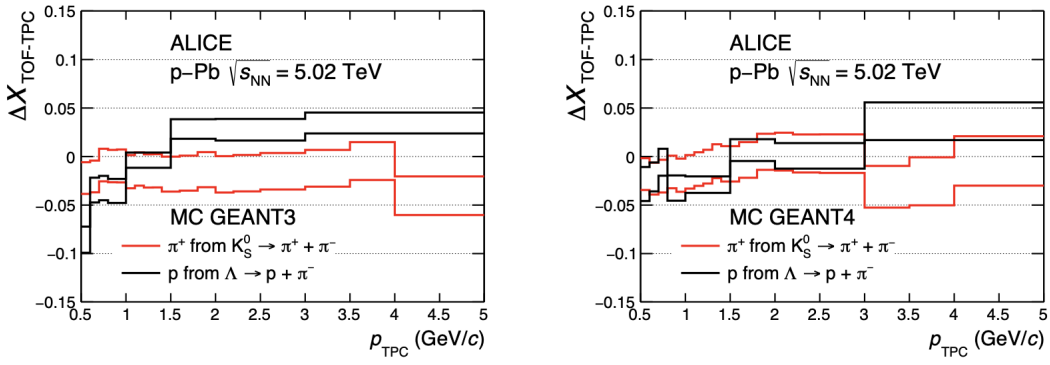


Figure 38: Uncertainty on the ALICE material budget between the TPC and TOF detectors, as found by comparing the yields in the TPC to the ones in the TOF for pions from K^0_s decays (red) and protons from Λ decays (black). The uncertainty is determined by comparing the measured ratio to ones obtained from detailed Monte Carlo simulations of the ALICE detector with varied material budgets, using Geant3 (left) and Geant4 (right). Figures taken from [113].

and 4.5% for $^3\overline{\mathrm{He}}$ and $^3\overline{\mathrm{H}}$, which therefore includes the uncertainty on the material budget.

2.3.6 Non-linear error propagation

The experimental observable is the antiparticle-to-particle ratio, which is then used to calculate the inelastic cross section. Thus, it is necessary to propagate the errors from the former to the latter. This is however non-trivial, since the two are related via an exponential as described in the previous section. Thus, the initially symmetric uncertainties on the ratio become asymmetric when propagated to the inelastic cross section. Additionally, the systematic and statistical uncertainties – which are independent on the ratio and thus sum up in quadrature – can no longer be summed in quadrature on the inelastic cross section, since the scaling between them is no longer linear but exponential. Indeed, as the slope of the exponential is not known a priori, the uncertainties cannot be added at all without knowledge of the dependence of the antiparticle-to-particle ratio in a given bin on the inelastic cross section. This leaves two options for the representation of uncertainties on the inelastic cross section: i) show the statistical and systematic uncertainties separately, and give the parameterization of the exponential curve used to add them together for each bin or ii) sum the two uncertainties on the ratio and then propagate the total uncertainty. The second option is significantly more practical since it gives the reader immediate access to the total uncertainty, and does not require extra explanation. The separate

uncertainties can be recovered using the fits shown in figures 33 and 34.

An important note is that this asymmetry arises far more prominently in the antiparticle-to-particle analysis than in the TOF/TPC analysis. This is due to 2 factors: the much reduced statistical uncertainties for the TPC/TOF analysis and the increased material budget required (as opposed to the TPC only part of the antiparticle-to-particle analysis). This results in the fact that within the uncertainties, the effect of the inelastic cross section on the TPC/TOF ratio is well approximated with a linear function. Thus, the error propagation from the TPC/TOF ratio to the inelastic cross section has only barely noticeable asymmetries.

2.3.7 Systematic uncertainties

In this section we will discuss the sources of systematic uncertainties on the inelastic cross section measurements using the antiparticle-to-particle method for A=3 antinuclei. The uncertainties are dominated by statistical uncertainties at high momenta, while at low momenta the uncertainties are dominated by the correction for secondary nuclei.

The systematic uncertainties can be categorised into two camps: 1) accounting for explicit biases in the analysis techniques or 2) uncertainties coming from a lack of knowledge on one or more involved quantities.
An example of an explicit bias is the selection of bin sizes in the histograms used for particle identification. The size chosen was 0.5 $n\sigma_{\mathrm{TPC}}$, but in essence this could have been any continuous value able to resolve the peak structure. In the limit of infinite statistics, the choice would not matter, but for the limited statistics present in this work, such choices can introduce a bias to the extracted (anti)nuclei yields, since the distributions are fitted in order to extract the yields. To account for this, variables which might introduce an difference to the results were investigated by varying them around the chosen value until the extracted yields changed by ± 10%, and the variance of the results were used to assign them an uncertainty. Finally, before applying this uncertainty to the final results, a Barlow check was performed [114]. A Barlow check is a statistical test which evaluates if the variance seen by changing a parameter is what is expected within statistical uncertainties, and ensures that an uncertainty is not doubly counted (once in the statistical uncertainty of the data, and once in the systematic uncertainty). There were two relevant uncertainties of this kind in the $^3\overline{\mathrm{He}}$ and $^3\overline{\mathrm{H}}$ analyses: track cuts and the PID procedure. The evaluation of the PID procedure is explained above, with the additional evaluation of the effect of the fit ranges, with the same method. The uncertainty due to the track cuts was slightly more complicated, due to the possible interdependence of different parameters. The track parameters on which cut were performed were each assigned

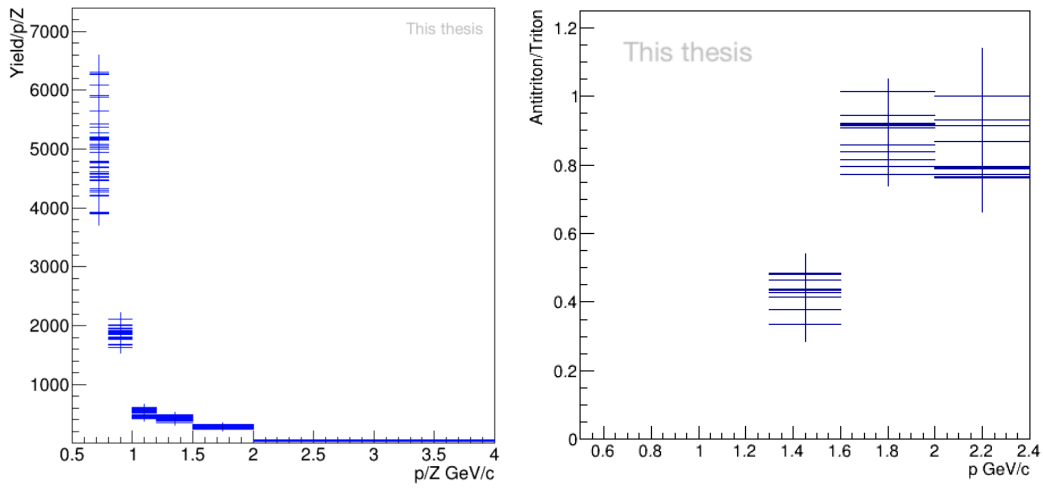


Figure 39: Evaluation of the systematic uncertainty due to track cuts, for $^3\overline{\mathrm{He}}$ (left) and $^3\overline{\mathrm{H}}$ (right). The same analysis was re-performed over 100 times with random permutations of "tight", "default", and "loose" cuts on each considered parameter.

a "tight", "default", and "loose" value, and the analysis was checked with random permutations of these cuts over 100 times, as shown in figure 39. The standard deviation of these results was thus taken as the uncertainty.

The second type of systematic uncertainty is due to lack of knowledge on a given parameter. An example of this is uncertainty on the material budget, which is only known to a precision of 4.5% . This effect is evaluated on the primordial antiproton-to-proton ratio, causing an uncertainty of 1.5% . Since the relationship between the antiproton-to-proton ratio and the antiparticle-to-particle ratio for nuclei goes to the exponent of A (see equation 6), the resulting uncertainty on $A=3$ ratios is 4.5% . The next uncertainty is due to the correction for secondary nuclei. This uncertainty is due to the limited statistics of both the templates and the data, making a fit between them difficult. This uncertainty is also applied on the antiparticle-to-particle ratios. Another uncertainty is the uncertainty on the measured matter inelastic cross section[37] on the antiparticle-to-particle ratio. This uncertainty was evaluated by varying the cross section in Monte Carlo simulations using Geant4, and was found to be 0.75% for $p < 1$ GeV/c, and 2.3 % for $p > 1$ GeV/c. This is the same for $^3\overline{\mathrm{He}}$ and $^3\overline{\mathrm{H}}$. The effect of the elastic cross section of both matter and antimatter were also studied, with an effect < 1% for both $^3\overline{\mathrm{He}}$ and $^3\overline{\mathrm{H}}$ in all momentum bins. This is shown in figure 40.

[37] Inelastic processes for matter can be hard scattering events which lead to breakup. The result is the same: a loss of the track in the analysed data.

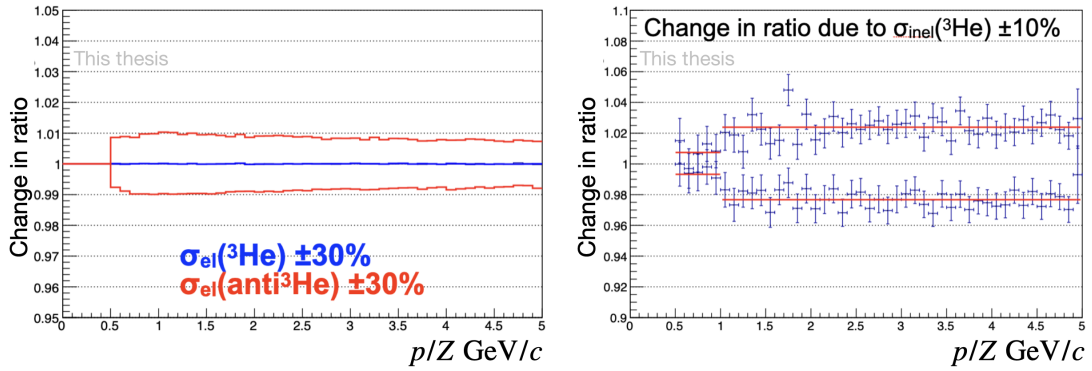


Figure 40: Uncertainty on the antiparticle-to-particle ratio introduced by varying the elastic cross sections by 30% (left) and the inelastic matter cross section by 10% (right). Since the cross section for $^3\overline{\mathrm{H}}$ and $^3\overline{\mathrm{He}}$ are the same in Geant4, these values are valid for both species.

Finally, the uncertainty coming from the energy loss correction, which is due to our lack of knowledge at what momentum the annihilation occurs. It is applied during the extraction of the inelastic cross sections from the ratios, as described in section 2.3.3.

2.3.8 Bench-marking the method on the antiproton inelastic cross section

In order to be sure that the antiparticle-to-particle methods gives an accurate measurement of the inelastic cross section, the method first had to be benchmarked by evaluating it using a particle for which the inelastic cross section was well known. This was done using antiprotons in [105]. The resulting inelastic cross sections are shown in figure 41. They match the parameterization implemented in Geant4 very well.

Since the antiproton inelastic cross section has been well measured, reproducing it with the antiparticle-to-particle method benchmarks the validity of the method. This allows its application to previously unmeasured quantities: the inelastic cross sections of $\overline{\mathrm{d}}$, $^3\overline{\mathrm{He}}$ and $^3\overline{\mathrm{H}}$. For $^3\overline{\mathrm{He}}$ and $^3\overline{\mathrm{H}}$ the TOF-to-TPC method was in addition to the antiparticle-to-particle method, to take advantage of the increased statistics available in Pb–Pb collisions. The validity of this new method had to be established by comparing it to the measurements using the already benchmarked antiparticle-to-particle method, showing not just the complementary nature of these two measurements, but also the necessity for both to be used in parallel.

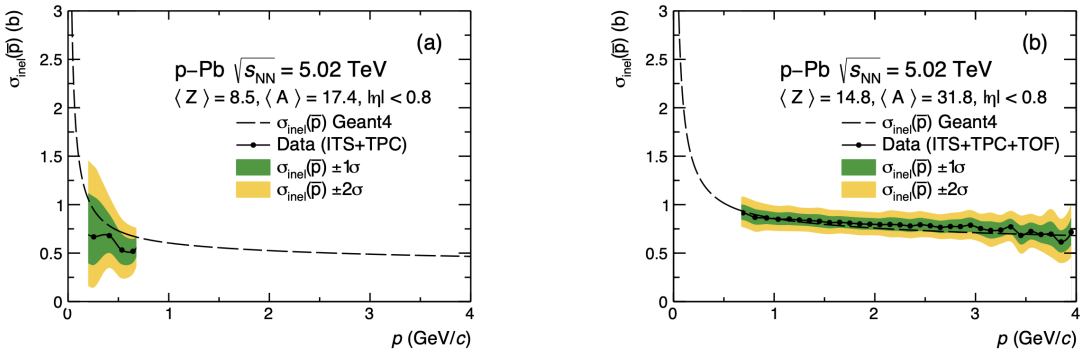


Figure 41: The antiproton inelastic cross section on the average ALICE detector material, taken from [105]. The black line and dots show the datapoints, while the green and yellow bands show the 1 and 2 sigma total uncertainties (stat^2+syst^2). The dashed line is the parameterization for this cross section in Geant4, which is fitted to data.

2.3.9 Independence of collision system

The antimatter-to-matter ratio method's dependence on collision system has been investigated by applying the same analysis method employed in pPb collisions in [105] to high multiplicity pp collisions. The dependence on the collision system is due to the differences in the collision energy, and the resulting difference in the primordial ratio is discussed in section 2.3.1. By taking the antiproton-to-proton ratio for the different collision systems and comparing them, the predicted difference between the antideuteron-to-deuteron ratio was obtained. The results are shown in figure 42, which show that the differences between collisions systems are consistent with the expected deviation. Thus, the inelastic cross section measurements for the two are consistent. This independence of the inelastic cross section on the collision system is expected, since the inelastic cross section is completely independent on the collision system. This becomes especially self-evident when considering that the annihilations do not occur in the initial collisions, but rather as the antiparticles travel through the detector material.

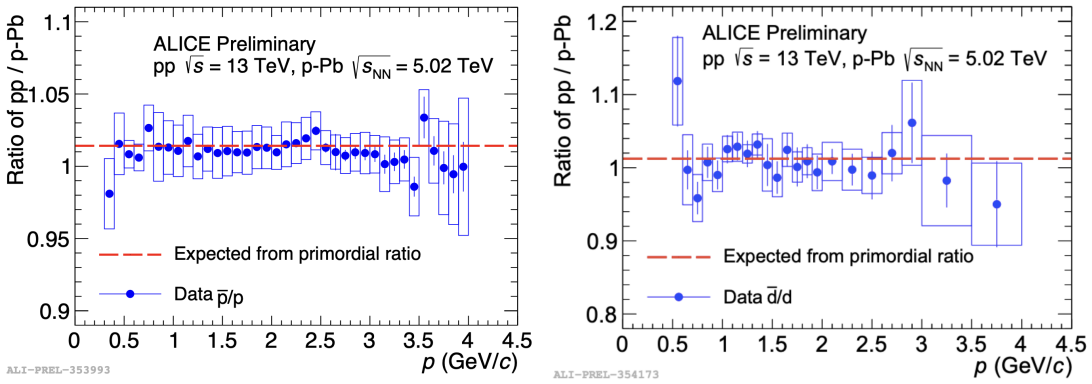


Figure 42: Ratio of the antiproton-to-proton ratios (left) and antideuteron-to-deuteron ratios (right) as a function of momentum, obtained in high multiplicity pp collisions and in pPb collisions, compared to the expected difference from the different collision energies (dashed red line). The agreement with the red line shows that this analysis technique is consistent across different collision systems, as expected.

3 Measurement of the $^3\overline{\mathrm{He}}$ inelastic cross section

The measurement of the $^3\overline{\mathrm{He}}$ inelastic cross section is one of the main results of this thesis. This is the first measurement of this inelastic cross section, which is important not just for nuclear physics, but also for astrophysical searches for physics beyond the standard model, as discussed in section 1.5.2. Historically, inelastic cross section measurements were performed using fixed target experiments: a beam of the particle of interest with well-determined momentum was isolated, and then fired on a material target with known properties. By measuring the abundance of the particle before and after the target, the cross section could be measured. The difficulty in doing this for antinuclei lies in the production and isolation of an antinuclei beam, since antinuclei production is so rare and has a high $\sqrt{s}$ threshold. Even at the places where antinuclei are produced (at the LHC and at the relativistic heavy ion collider (RHIC) [115]), further isolating a beam of such particles is not feasible within current experimental constraints. In fact, out of all antinuclei (A>2), this method has only been applied to high energy antideuterons [46, 45], at the U-70 proton synchrotron in the 70s, for particles at very high momenta of 13 GeV/c and 25 GeV/c. Recently, roughly half a century later, the new measurement technique using the antiparticle-to-particle ratio has been shown to be able to measure the antideuteron inelastic cross section down to 500 MeV/c [105]. This measurement has now been expanded to $^3\overline{\mathrm{He}}$ [110] and $^3\overline{\mathrm{H}}$, and a separate complementary method (TPC/TOF method) has enabled the use of the high statistics Pb–Pb data to boost the measurements' precision. Both these new methods rely on quantifying the absorption of antinuclei

as they travel through the detector material, rather than a dedicated target. The disadvantage of this approach is that the detector material is optimised to have little material budget as possible, as to not interfere with the particles of interest. Nevertheless, these methods allow us to further our knowledge of antinuclei inelastic cross sections for the first time in half a century.

3.1 Physics motivation and overview of the analysis method

$^3\overline{\mathrm{He}}$ nuclei are a promising probe for indirect dark matter searches, but in order to understand any potential signal, it is necessary to know their disappearance probability as they travel to earth from their cosmic sources, as is extensively discussed in sections 1.5.2 and 5.1.2. While this is the astrophysical motivation for this measurement, it also has applications in nuclear physics, in particular for improved modelling of antinuclei propagation through the detector material using Geant4. This is particularly important in the low energy region ($lessim$ 2 GeV/c), where Glauber model calculations are less reliable. Measurements of (anti)nuclei production rely on efficiencies to be well reproduced by Monte Carlo simulation, which requires the inelastic cross sections as input.
The analysis methods used to measure the inelastic interaction cross section are laid out below.

3.1.1 Antiparticle-to-particle ratio method

The detailed steps of this method are described in section 2.
The antiparticle-to-particle method is based on using the ratio of antiparticles to particles as an observable for the cross section. This works since at LHC energies, the relative amounts of matter and antimatter which are produced are well known. They are produced in almost equal amounts, and therefore dividing the number of antiparticles by the number of particles acts as a normalization of the number of antiparticles produced[38]. The detector material itself acts as a target. Since antiparticles and particles have the same interactions with the detector material apart from annihilation, uncertainties due to particle identification and tracking cancel to a large extent.

3.1.2 TOF-TPC matching method

The second method for measuring $\sigma_{\mathrm{inel}}(^3\overline{\mathrm{He}})$ uses the fact that over a wide momentum range, $^3\overline{\mathrm{He}}$ can be clearly identified in both the TPC and the TOF detectors. We can therefore check the amount of $^3\overline{\mathrm{He}}$ nuclei present in the TPC, and how many

[38] This method does not in principle require equal amounts of matter and antimatter, merely a very precise knowledge of the ratio of antimatter to matter which is produced.

of those make it all the way to the TOF detector. This method works akin to a fixed target experiment, in that a "beam" is identified by measuring $^3\overline{\mathrm{He}}$ in the TPC, this beam is then fired upon the "target", which in this case is the space frame and the TRD. Some of the nuclei will annihilate, while the others which make it through will generate a matching TOF hit, thus allowing us to quantify the "beam" loss between two detectors.
The advantage of this method is that only the antiparticles are required; no specific assumptions about the antimatter-to-matter ratio need to be assumed and tested. This also means that no correction for secondary nuclei from material spallation needs to be applied, since the origin of the $^3\overline{\mathrm{He}}$ has no impact on the result[39]. The disadvantage is that the acceptance of the TOF detector limits the applicability of this method to higher momenta, so it is more difficult to measure the low energy rise of the inelastic cross section.

The measurement of $\sigma_{\mathrm{inel}}(^3\overline{\mathrm{He}})$ using the TPC-TOF matching method is thus complementary to the antiparticle-to-particle method described above. This analysis was not carried out as part of this work, but ties in closely with the results shown both in this chapter and in chapter 5, and is thus described here. The measurement is also shown together with the measurement using the antimatter-to-matter inelastic cross section. More details about the analysis can be found in [116, 110].

3.2 Secondary correction

In order to extract the cross section from the antiparticle-to-particle ratio, only particles produced at the primary vertex must be considered. Thus, secondary particles need to be accounted for by using template fits, as described in section 2.2.3.

The template fits done for the secondary correction of ^{3}He are shown in figure 43. The cut on $|\mathrm{DCA}_z| < 1$ cm was chosen in order to include more secondaries, and improve the statistical constraints on the fit. As can be seen, in the second bin there is a slight shoulder towards the negative side of 0, where the fitted material template exceeds the data, which is the biggest systematic discrepancy of the fits. This effect has been investigated, and since i) it is outside of the signal region and ii) it is within the uncertainties, it was concluded to be a negligible effect.

[39] Also, there are no secondary $^3\overline{\mathrm{He}}$ nuclei from material spallation, so the secondary correction is even less important.

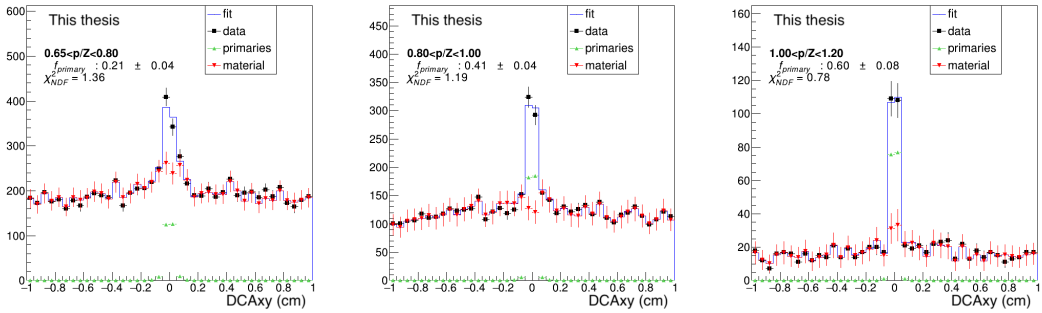


Figure 43: Template fits for determining the primary fraction of ^{3}He in the first 3 momentum bins (above this momentum the primary fraction goes to 1), for a $|\mathrm{DCA}_z| < 1$ cm cut. The fits were performed using the TFractionFitter method available in ROOT.

3.3 Results

After all the corrections are applied, we can now obtain the final $^3\overline{\mathrm{He}}/^3\mathrm{He}$ and the corresponding $\sigma_{\mathrm{inel}}(^3\overline{\mathrm{He}})$, which are shown in figure 44. The measurement is in agreement with the parameterization used in Geant4 at a significance of slightly above 1σ. The lowest momentum bin shows a hint at a steeper rise than the parameterization. The second bin is shown as an upper limit since the uncertainties reached below 0, which would be an unphysical value for the cross section.

This represents the first measurement of $\sigma_{\mathrm{inel}}(^3\overline{\mathrm{He}})$.

The measurement of $\sigma_{\mathrm{inel}}(^3\overline{\mathrm{He}})$ done in Pb–Pb collisions using the TOF-to-TPC method is shown for comparison in figure 45. The much increased statistics available for the Pb–Pb data sample results in much reduced statistical uncertainty. The two measurements deliver consistent results in the overlapping momentum region.

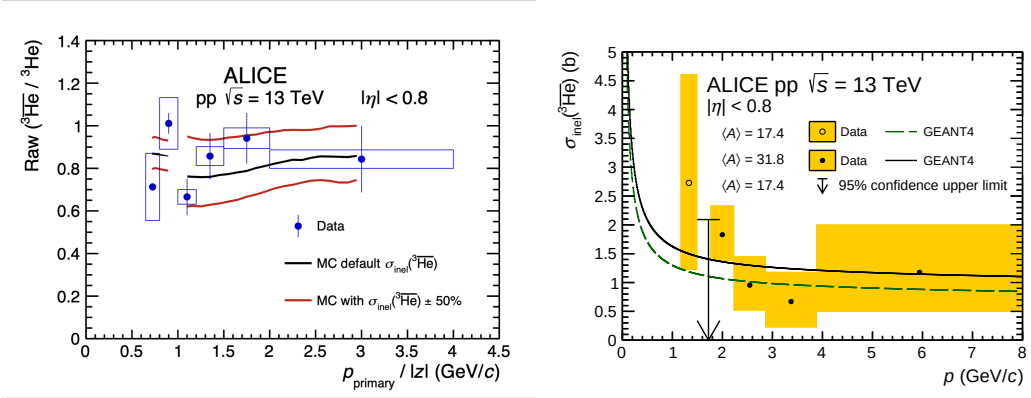


Figure 44: (Left) $^3\overline{\mathrm{He}}/^3\mathrm{He}$ measured in pp collisions at $\sqrt{s}$ =13 TeV, as a function of the particle momentum at the primary vertex. Statistical uncertainties are shown as lines, and systematic uncertainties are shown as boxes. The discontinuity at p/Z = 1 GeV/c is due to the additional requirement of a TOF hit, thus requiring tracks to traverse more material. (Right) $\sigma_{\mathrm{inel}}(^3\overline{\mathrm{He}})$ as measured using the antiparticle-to-particle method in pp collisions at $\sqrt{s}$ =13 TeV, as a function of the antinuclei momentum at annihilation. The uncertainties include both statistical and systematic uncertainties. Open points are from the analysis using the TPC only for particle identification, while closed points require a matching hit in the TOF in addition to the TPC, which therefore has a different averaged material value. The lines show the parameterization used in Geant4.

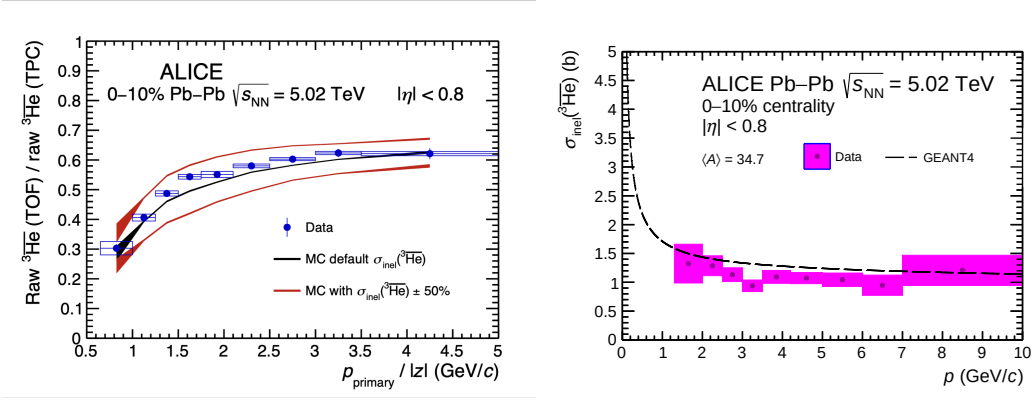


Figure 45: (Left) TOF-to-TPC ratio for $^3\overline{\text{He}}$ in Pb–Pb collisions at $\sqrt{s_{NN}}$ =5.02 TeV, as a function of the particle momentum at the primary vertex. Statistical uncertainties are shown as bars, and systematic uncertainties are shown as boxes. The colored lines are the same ratio in Monte Carlo simulations with varied $\sigma_{\text{inel}}(^3\overline{\text{He}})$. (Right) $\sigma_{\text{inel}}(^3\overline{\text{He}})$ as measured using the TOF-to-TPC method in Pb–Pb collisions at $\sqrt{s_{NN}}$ =5.02 TeV, as a function of the antinuclei momentum at annihilation. The uncertainties include both statistical and systematic uncertainties. The line shows the parameterization used in Geant4. Figures taken from [110].

4 Measurement of the antitriton inelastic cross section

4.1 Physics motivation and overview of the analysis method

The measurement of $\sigma_{\text{inel}}(^3\overline{\text{H}})$ does not have the same astrophysical motivation as the measurement of $\sigma_{\text{inel}}(^3\overline{\text{He}})$, since $^3\overline{\text{H}}$ is an unstable nucleus with a half-life of $\approx$ 12.3 years. Instead, the main motivation for this measurement is the comparison to the $^3\overline{\text{He}}$ inelastic cross section. This could shine light on any isospin dependence of the annihilation probability of antinuclei. Such an effect might also elucidate how the strong force interacts with isospin, in a potentially more sensitive way than observing neutrons, since they are much harder to detect due to not being charged. And while the current statistical uncertainties are unable to resolve any difference, the two measurements provide a proof of concept that this dependence can be measured by means of comparing the inelastic cross sections of $A = 3$ antinuclei.

4.2 Accessible momentum range of the measurement

Due to the single charge of $^3\overline{\text{H}}$, there are a few noteworthy differences in the particle identification in comparison to $^3\overline{\text{He}}$. The first and most important difference is that it is not clearly identifiable in the TPC alone at high momenta. This can be

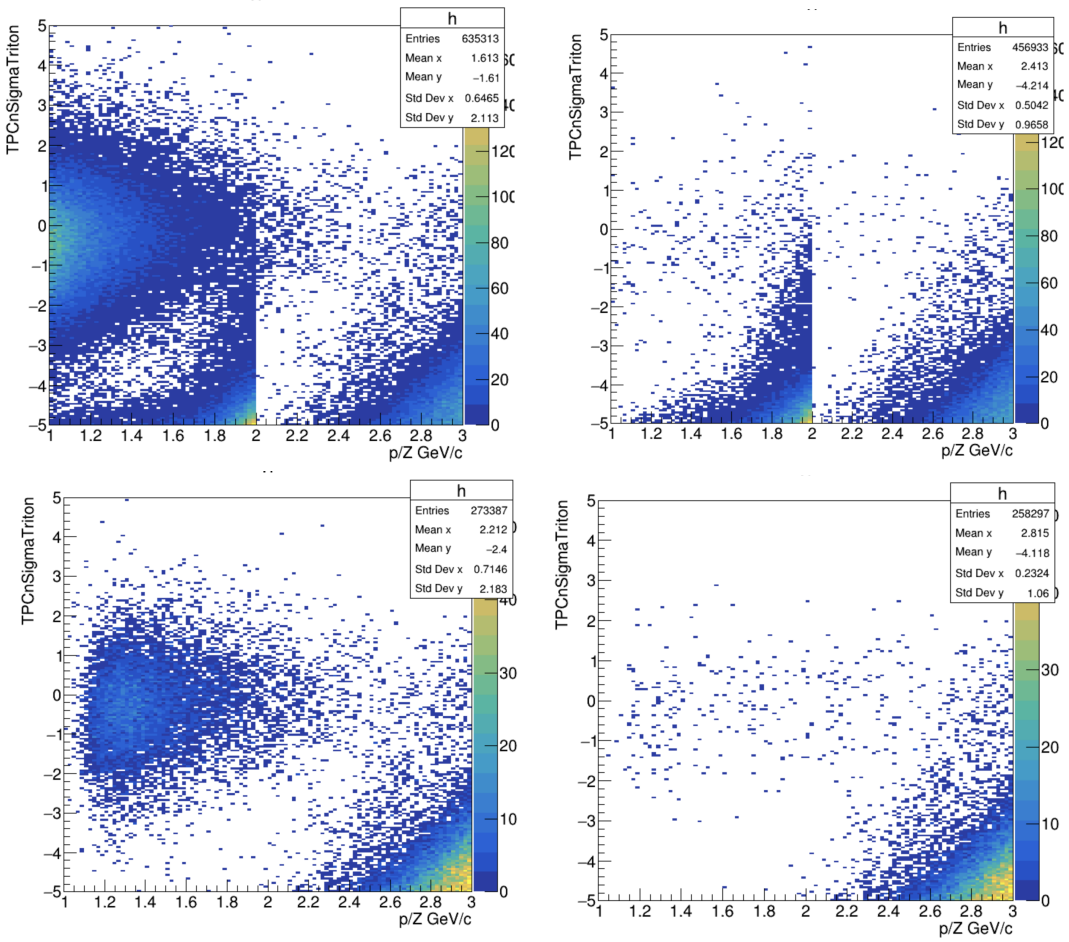


Figure 46: $n\sigma_{\mathrm{TPC}}$ vs momentum plots for tritons. A cut on the m_{TOF} is applied above 2 GeV/c in all figures. (Top left) the original distribution without an additional cut on either DCA or m_{TOF}. (Top right) the distribution after a cut of $|\mathrm{DCA}_{xy}| < 1\ mm$ and $|\mathrm{DCA}_z| < 1\ mm$ is applied. (Bottom left) the distribution after the cut on m_{TOF} is extended to momenta as low as 1 GeV/c. (Bottom left) the distribution after both the DCA and m_{TOF} cuts were applied.

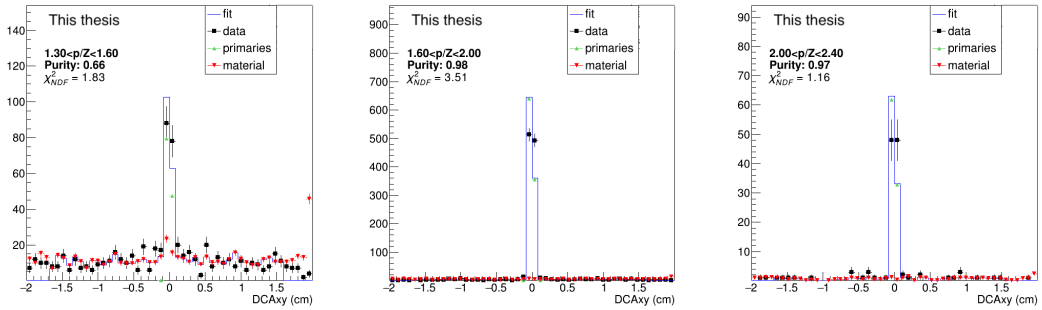


Figure 47: Template fits to the DCA distribution of ^{3}H, to account for the contributions from secondary nuclei from spallation processes. The primary fraction is evaluated as $f_p = \int_{-0.1cm}^{0.1cm} \text{fit}_{\text{signal}} d\text{DCA} / \int_{-0.1cm}^{0.1cm} \text{data}\, d\text{DCA}$. The results are shown for each momentum bin.

seen in figure 18, which shows that the expected energy loss for (anti)^{3}H merges with the bands from other particles at about 1.5 GeV. The considerations for the identification are shown in figure 46, which shows how the TOF cut is able to remove the contamination up to a momentum of ≈ 2.4 GeV/c, while the DCA cut removes much of the secondary contribution at low momentum. Additionally, by comparing the top and bottom panels on the right side of figure 46, which show the effect of the TOF cut after the DCA cut is applied, we can see that the additional requirement of the TOF removes all the contamination at low momentum, while preserving a large fraction of the signal. Furthermore, the fact that the the TOF is required means that the particles have to traverse more material, and thus the ratio becomes more sensitive to the inelastic cross section. Thus, the TOF is used in the whole momentum range for the measurement of the $^3\overline{\text{H}}$ /^{3}H ratio.

4.3 Secondary correction

Similarly as for $^3\overline{\text{He}}$, the $^3\overline{\text{H}}$ /^{3}H ratio still needs to be corrected for the remaining secondary nuclei from material spallation. This is done using template fits, according to the method described in 2.2.3. The fits are shown in figure 47. It can be seen that the contribution is negligible in the second and third bin. In the first bin, the contribution from secondaries is well constrained. The resulting primary fraction is shown in the bottom of the figure. The uncertainty of the primary fraction is added to the systematic uncertainties on the $^3\overline{\text{H}}$ /^{3}H ratio in quadrature.

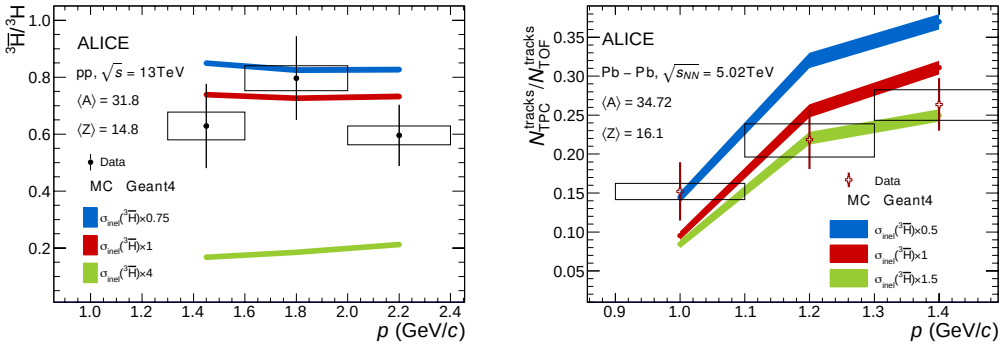


Figure 48: (Left) $^3\overline{\mathrm{H}}$ /^{3}H ratio as a function of momentum, with statistical uncertainties as bars and systematic uncertainties as boxes. The colored lines represent Monte Carlo simulations with varied inelastic cross sections. (Right) $^3\overline{\mathrm{H}}$ TOF-to-TPC ratio as a function of momentum, with statistical uncertainties as bars and systematic uncertainties as boxes. The colored lines represent Monte Carlo simulations with varied inelastic cross sections.

4.4 Results

In this section, the measurements of $\sigma_{\mathrm{inel}}(^3\overline{\mathrm{H}})$ are presented. The left side of figure 48 shows the $^3\overline{\mathrm{H}}$ /^{3}H ratio as measured in pp collisions, and the left side of figure 49 shows the resulting inelastic cross section measurement with the open circles. The measurement is consistent with the parameterization used in Geant4 within a significance of 2 σ, but shows a hint at a systematically larger vale for $\sigma_{\mathrm{inel}}(^3\overline{\mathrm{H}})$. The right side of figure 48 shows the TOF/TPC ratio of $^3\overline{\mathrm{H}}$ in Pb – Pb collisions at $\sqrt{s_{\mathrm{NN}}} = 5.02$ TeV[40] and the corresponding measurement of $\sigma_{\mathrm{inel}}(^3\overline{\mathrm{H}})$ is shown on the left of figure 49 as full circles. The measurements are compared with the results for $^3\overline{\mathrm{He}}$ in the right panel of figure 49, all scaled to the same average material, which shows that the results for $^3\overline{\mathrm{H}}$ and $^3\overline{\mathrm{He}}$ are consistent within uncertainties. This means that within the current uncertainties, the annihilation cross sections are consistent with isospin symmetry. Improvements on the statistical precision of these measurements will help constrain this assumption further using the data from the upcoming Run 3 and Run 4 campaigns at the LHC.

[40]These were not obtained as part of this thesis, but were obtained for the same publication as the cross section in Pb–Pb collisions (publication is in preparation).

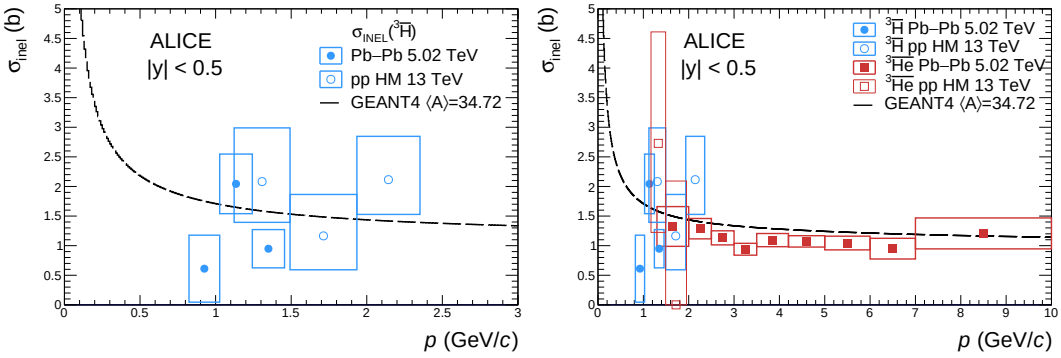


Figure 49: (Left) the resulting measurement of $\sigma_{\text{inel}}(^3\overline{\text{H}})$ using the antibaryon-to-baryon method ($\overline{\text{B}}$/B) and the TOF-to-TPC method, on the average ALICE material. The colored boxes show the total uncertainty (stat^2+ syst.^{2}). The line shows the parameterization as used in Geant4. (Right) comparison of the $\sigma_{\text{inel}}(^3\overline{\text{He}})$ and $\sigma_{\text{inel}}(^3\overline{\text{H}})$ measurements.

5 Antinuclei in the cosmos

Antinuclei are some of the rarest stable objects in cosmic rays, in fact, no compound antinuclei have ever been conclusively observed in cosmic rays. But it is this exact fact that makes them such promising candidates for the search of new physics beyond the Standard Model. Whereas for other particle species the signal-to-background ratio might be minuscule for any new effect, antinuclei production is so rare in standard model processes that any new physics might produce signals orders of magnitude greater than what can be explained with our current knowledge. While no conclusive observation of antinuclei in cosmic rays has been published, the AMS-02 Collaboration has repeatedly reported potential signals of antihelium [117, 118, 119], motivating a renewed push of research interest into cosmic-ray antinuclei.

The goal of this section is to discuss possible exotic sources of antinuclei in our galaxy focusing on WIMP dark matter and extragalactic WIMP dark matter. For antideuterons primordial black holes are also discussed as a possible source. These are compared to antinuclei produced in high-energy cosmic-ray collisions with the interstellar medium, which in the respective rest frame is an analogous process to the one used to produce antinuclei at accelerators. In the lab frame the collision is heavily boosted, which affects the produced spectra. Crucially, the new measurements of the inelastic cross sections of antihelium laid out in Section 3, and the first low-energy measurements of the antideuteron–matter inelastic cross section laid out in [105], are for the first time incorporated in such studies. The discussion

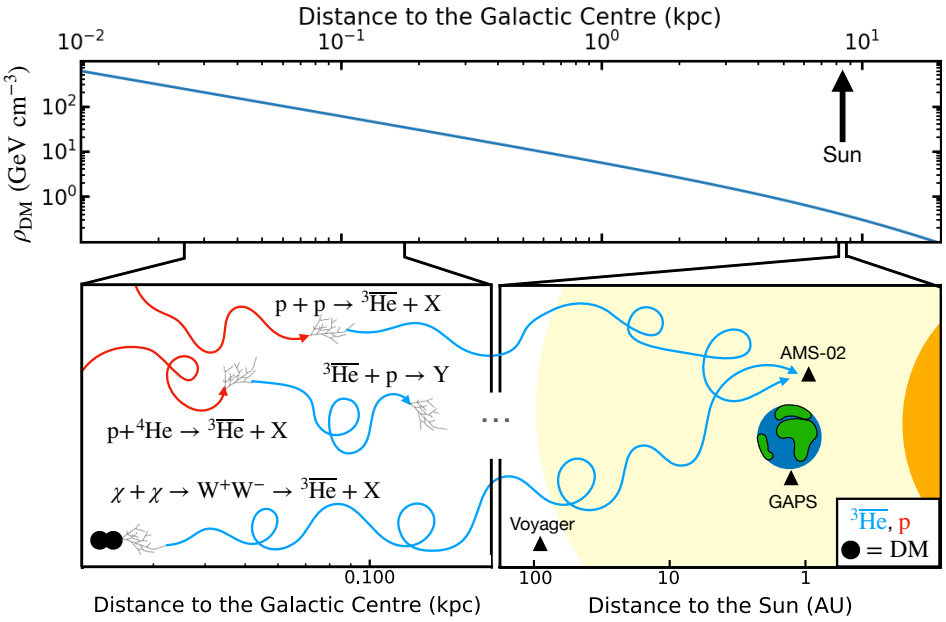


Figure 50: Illustrated story of the journey which antinuclei undertake before being observed near earth. Red lines shown high energy cosmic ray protons, Blue lines shown ${}^{3}\overline{\text{He}}$. The antinuclei get created all throughout the galaxy, and in the galactic centre antinuclei from dark matter is the most concentrated, due to the higher dark matter density. Similarly, antinuclei from high energy cosmic rays are created all over the galaxy. The created antinuclei then travel through the interstellar medium, some of them annihilating along the way. The ones which do make it to earth then are affected by the solar magnetic field, before reaching detectors near earth. All these processes need to be understood in order to be able to interpret an antinuclei signal in cosmic rays.

therefore focuses in particular on propagating these measurements to obtain the experimental uncertainites from inelastic interactions on the antinuclei flux near earth. This journey from creation to observation for antinuclei is illustrated in figure 50.

In order to study the two sources we employ the GALPROP framework [120]. This framework propagates particles through our galaxy, simulating various effects such as diffusion, convection and also inelastic processes. The resulting fluxes near earth are then presented for both antideuterons and $^3\overline{\text{He}}$, for different dark matter masses and profiles. Finally, current and planned experiments for detecting antinuclei in cosmic rays are discussed. The antinuclei fluxes from high-energy cosmic-ray collisions shown in this thesis as comparisons to the fluxes from possible dark-matter sources are taken from [121] and [113], for antideuteron and $^3\overline{\text{He}}$ respectively.

5.1 Sources of antinuclei in the cosmos

Antinuclei are some of the rarest stable particles in our galaxy, since very few abundantly occurring processes will produce them in any detectable amount [122, 123]. This is in contrast to nuclei, which are the most abundant stable particles within our galaxy. Indeed, nuclei up to Iron have been observed by a variety of methods: in the spectral lines of stars, in cosmic rays by the AMS collaboration [124] and of course on earth. A large amount of the light matter nuclei (up to Lithium) was produced during Big Bang Nucleosynthesis (BBN) [74], while all heavier nuclei were produced during stellar nucleosynthesis [125]. This process involves fusing hydrogen nuclei to create the necessary energy inside a star to counteract its own gravitational pull, creating helium in the process. This continues for most of the lifetime of the star, until its reserves of hydrogen run low. Without the sustained temperature and pressure provided by hydrogen fusion, the star's core will become inert and contract under gravity. Meanwhile, fusion will start in the outer layers of the star, where residual hydrogen is still found. This causes those layers to expand and cool, and the star forms what is called a red giant [125] or red supergiant [125]. Over time, the core will contract and heat up[41], until the conditions allow for even heavier elements (helium and sometimes carbon) to start fusing to create energy [125]. During this process, elements up to iron are created through nuclear fusion, and heavier elements can be created through slow neutron capture processes [125]. This process accounts for the production of roughly half of the elements heavier than iron [125]. When this source of energy becomes insufficient, the red giant's will implode and expel its outer shell,

[41] Red supergiants may have sufficient pressure immediately to commence helium fusion in their core. For more information on stellar information please refer to [125].

creating a planetary nebula. Red supergiants will explode in a supernovae, expelling huge amounts of energy and matter. In this process, rapid neutron capture occurs, producing the other half of elements heavier than iron [126].
However, due to the asymmetry of matter and antimatter in our galaxy, neither BBN nor stellar nucleosynthesis is thought to be a dominant source for antinuclei. Antimatter produced during BBN is likely to have annihilated propagating through the galaxy from the Big Bang until today. This can be shown by a back of the envelop calculation. Assuming an antinucleus with an annihilation cross section of $\approx$1b and a momentum of $\gtrapprox$ 0.1 GeV/n, the fraction surviving until this day is given by $N/N_0 = \exp(-\sigma\, n \beta\, c\, t)$, where n is the average matter density in the regions traversed. Taking $n = 1\text{cm}^{-3}$ and using $\beta = p/\gamma m$ one finds that only about $e^{-100} \approx 10^{-44}$ of the initial population would still be left today. And in order for stellar antinucleosynthesis to occur, anti-starts – or at least large clouds of antimatter – would have to exists. Any such regions would by default have to come in come in contact with the matter dominated regions which predominantly make up our galaxy. In those overlap regions, significant amounts of annihilations would cause a visible gamma ray signal [122]. No signal of this kind has been reported, although if such regions were small enough, they would appear as point sources to current instruments and thus make up a part of the currently unidentified point sources within our galaxy [127]. Recent work has claimed that such antimatter regions may have formed during the big bang and survived to this day [128, 58], making up $\approx$ 20 of the roughly 1000 unidentified point sources. However, these studies also note the necessity for the antimatter regions to have formed in places where the proton density is $O(10^{-8})$ of the cosmic average. The authors do not provide a viable mechanism by which this could have occurred.
We therefore have to look to other processes which could produce antinuclei. Due to baryon number conservation, all such processes are likely to produce at least an equal amount of light nuclei as well. However, since nuclei are far more abundant than antinuclei, these processes will only contribute a negligible amount to the total nuclei flux in our galaxy, while they might dominate the antinuclei flux. This extremely high expected signal-to-background ratio is the reason why antinuclei are considered such a promising probe into new physics.

5.1.1 High-energy cosmic-ray collisions

The most well-known source for antinuclei in cosmic rays — and the only one which does not require new physics or as of yet undiscovered objects — are collisions of high-energy cosmic rays with the interstellar medium. Such collisions, akin to collisions at particle accelerators, will produce antinuclei by converting the available mass–energy from the collision into (anti)nucleons which then coalesce (see section 1.5.1 for a more detailed discussion on antinuclei production). In order to predict

the production of antinuclei in such high energy collisions we need to know the differential production cross section of the antinuclei in question, for each collision which can occur, and we need to know which collisions those are, i.e. we need to know the composition of cosmic rays and of the interstellar medium, as a function of energy. For both the interstellar gas and cosmic rays, the composition is ≈90% protons, ≈9% Helium-4 and <1% heavier nuclei. Thus, the source term for nuclei from such secondary collisions can be written as

$$q(\vec{r},p) = \sum_{CR=\mathrm{H,He}} \sum_{ISM=\mathrm{H,He}} n_{ISM}(\vec{r} \int dp'_{\mathrm{CR}} \beta_{\mathrm{CR}} c \frac{d\sigma(p,p'_{\mathrm{CR}})}{dp} n_{\mathrm{CR}}(\vec{r},p'_{\mathrm{CR}}) \tag{17}$$

, where $\sum_{CR=\mathrm{H,He}} \sum_{ISM=\mathrm{H,He}}$ denote the sums over the particle species in cosmic rays and the interstellar medium, $n_{ISM}(\vec{r})$ is the density of the interstellar gas at a given point, $n_{\mathrm{CR}}(\vec{r},p'_{\mathrm{CR}})$ is the density of cosmic rays at a given position and energy, and $\frac{d\sigma(p,p'_{\mathrm{CR}})}{dp}$ is the differential production cross section for an antinucleus, as a function of the momentum of the produced antinucleus p and the momentum of the incoming cosmic ray p'_{CR}. The particles in the interstellar medium are considered to be at rest in this calculation, which is a valid approximation since they move at very low speeds in comparison to the incoming cosmic rays[42].

The production cross section of antinuclei in such small collisions systems is suppressed at low energies due to the baryon number conservation, since it is necessary to produce at least 4 (6) new nucleons in order to produce antideuterons ($^3\overline{\mathrm{He}}$). The requirement for these additional nucleons means that the threshold of the required COM energy is about $\sqrt{s}_{\mathrm{th}} \approx 6(8)m_p$ for antideuterons ($^3\overline{\mathrm{He}}$). Given that the ISM target is at rest, all the energy must come from the incoming cosmic ray particle. This means that the frame of reference of the collision will be highly boosted in comparison to the galactic frame, and that the centre of mass energy will only rise $\propto \sqrt{E_{\mathrm{CR}}}$. In the case of $^3\overline{\mathrm{He}}$ this corresponds to a threshold energy of the incoming proton of $E_p \approx 31$ GeV. In order to estimate these cross sections, Monte Carlo event generators are used to create the proton and neutron spectra and distributions, and coalescence afterburners are then applied in order to estimate the production of antinuclei. In this work, the production cross sections by [129] and [130] are used, referred to hereinafter as Shukla et. al. For $^3\overline{\mathrm{He}}$ $\mathrm{O}(10^{11}-10^{12})$ events are needed to get a statistical precision on the % level on the total yield for a given incoming beam energy [129]. The resulting production cross sections for $^3\overline{\mathrm{He}}$ and antideuterons are shown in figure 51, where they are shown for a wide array of incoming beam energies.

[42] Interstellar gas particles can be expected to move at speeds of the order of the rotational velocity of the milky way, which is O(100 km/s) or $\mathrm{O}(\beta = 10^{-}4)$. This is much lower than the velocity of incoming protons at the threshold for antinuclei production, where $\mathrm{O}(\beta > 0.999)$.

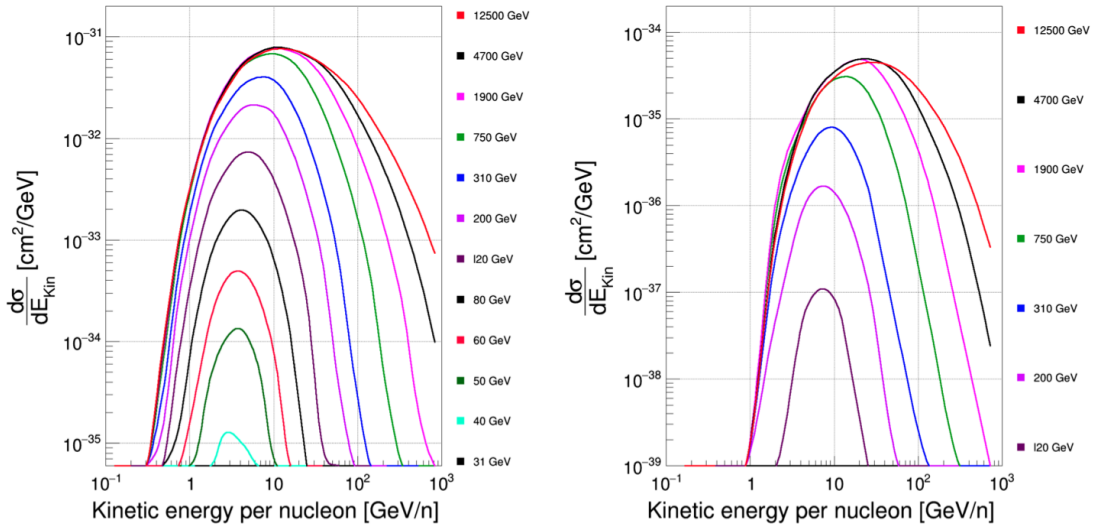


Figure 51: Production cross section for antideuterons (left) and $^3\overline{\text{He}}$ (right), as a function of the energy of the antinucleus produced, for a range of different projectile energies, taken from Shukla et. al. The $^3\overline{\text{He}}$ cross section includes the effect of antitritons which are produced and subsequently decay to $^3\overline{\text{He}}$.

As can be seen, it requires significantly above the threshold energy of $\sqrt{s}$ =31 GeV in ordet to produce any significant $^3\overline{\text{He}}$ flux[43].

The cross sections shown are constrained by data from a variety of accelerator experiments. The list of experiments used to constrain the production cross for antideuterons is shown in figure 52, while for $^3\overline{\text{He}}$ the data is very scarce for p-p collisions at low energies. In order to validate the production, the authors instead used their model to simulate pp collisions at $\sqrt{s} = 7$ TeV, in order to compare with ALICE data. The resulting fit is shown in figure 53, where the uncertainties are obtained by varying the coalescence momentum by 30%. It can be seen from figure 52, for $\sqrt{s} \gtrapprox 25$ GeV, there are only measurements at mid-rapidity. However, due to the highly boosted nature of the frame in CR collisions, antinuclei are likely to be produced at very forward rapidities. Thus, further experimental searches at forward rapidity are needed in order to better constrain antinuclei production in high energy CR collisions.

Once these cross sections are obtained, they need to be folded with the galactic cosmic ray spectrum at each point in space. This spectrum spans over more than 11 orders of magnitude if all particles are considered, and at least 6 orders of magnitude for protons. A compilation of available data on the cosmic ray spectrum can be

[43] It is the lowest energy considered for antideuterons since the same simulations were used to determine both sets of spectra in Shukla et. al.

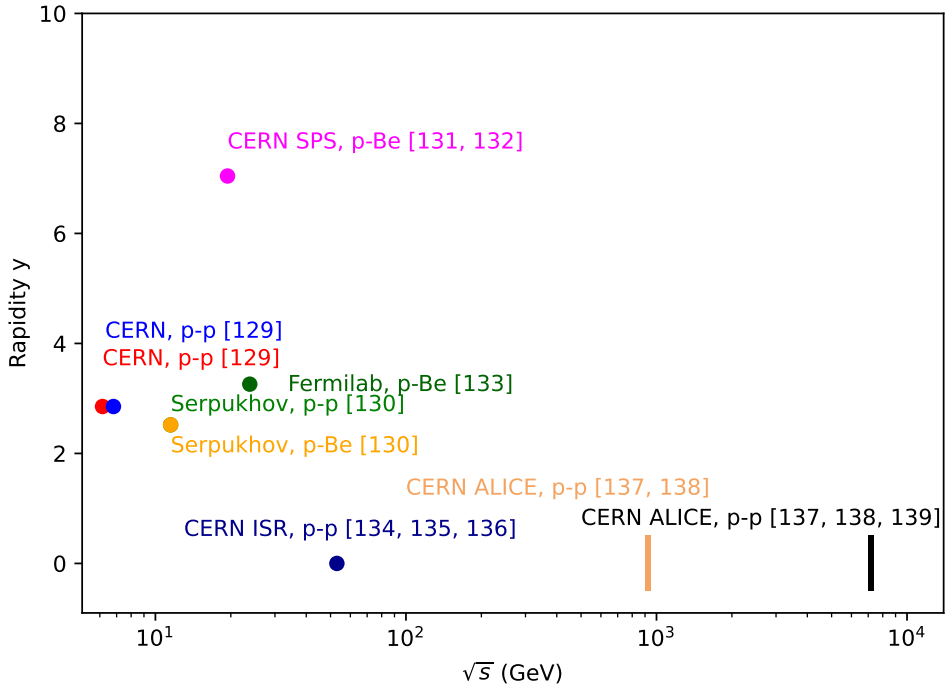


Figure 52: A list of experiments with measurements of (anti)deuteron production, as a function of rapidity and $\sqrt{s}$. The compilation is taken from table 2 in [130], based on data in [131, 132, 133, 134, 135, 136, 137, 138, 139, 140, 141].

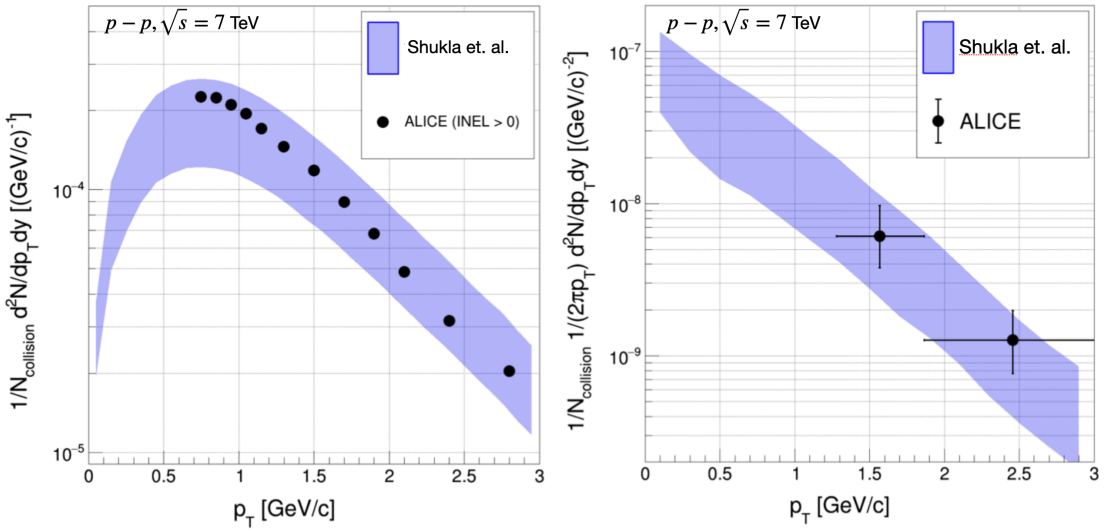


Figure 53: Comparison of the antideuteron (left) and $^3\overline{\text{He}}$ (right) spectra obtained by Shukla et. al. with ALICE data for $\sqrt{s} = 7$ TeV pp collisions.

found in figure 54. The implementation of this process in Galprop is done by implementing the cross section above, and thus calculating equation 17 at each point in the space/momentum grid employed in GALPROP. For a more detailed discussion of Galprop see section 5.3. Also shown in the left of this figure is the source term of antideuterons, as a function of both the incoming particle momentum and the momentum of the produced antideuteron. From this it can be seen that the most important momentum range to probe is 100-500 GeV/c.

5.1.2 Weakly interacting massive particles (WIMPs) dark matter

Some WIMP dark matter theories predict that WIMP annihilations can produce a significant amount of antinuclei [4, 2, 1]. Such theories are based on the assumption that dark matter is made of particles (hereinafter denoted χ), which during the big bang were in thermal equilibrium with SM particles. This requires that some SM processes were able to create χ. This can be understood kinematically from the available energy in such a process. If the SM particles colliding would have an energy which exceeds $\sqrt{s} = 2m_\chi$, they could create a dark matter particle pair. Similarly, the dark matter particles would have to be able to either decay or annihilate into SM particles, in order to maintain the equilibrium, as shown in figure 56. We shall first consider the scenario that the dominant mechanism of interaction for dark matter into SM particles was decau. If they would only decay, there would have to be some mechanism which reduces this decay rate by many orders of magnitude once the

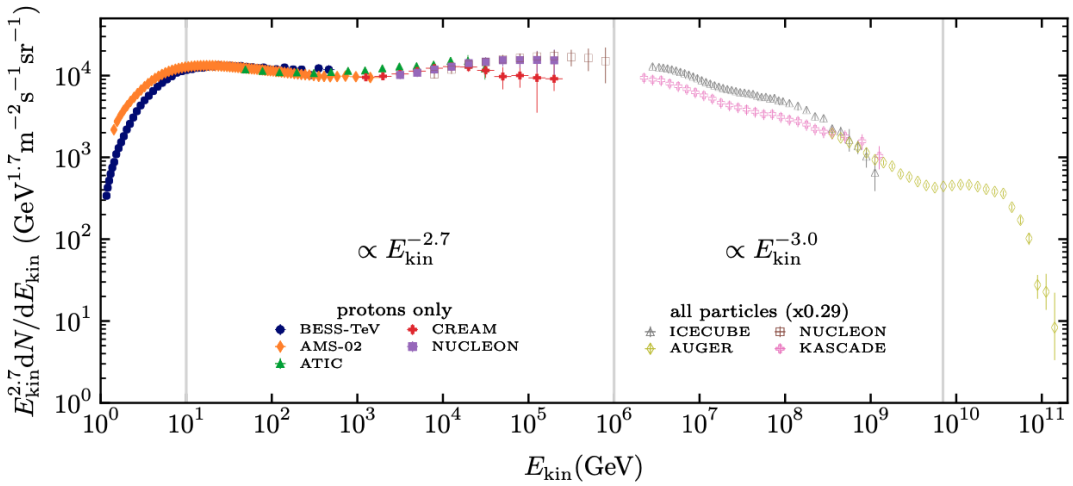


Figure 54: Cosmic ray particle spectra, for protons and all particles, from relevant experiments. Figure taken from [142].

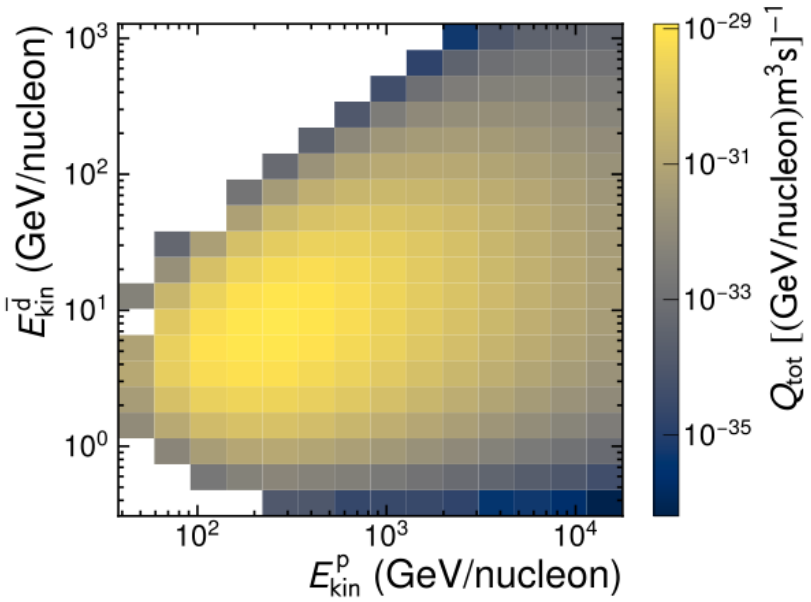


Figure 55: The source term of antideuteron from high energy cosmic ray collisions, as a function of the incoming proton energy and the outgoing antideuteron energy. The figure is taken from [121].

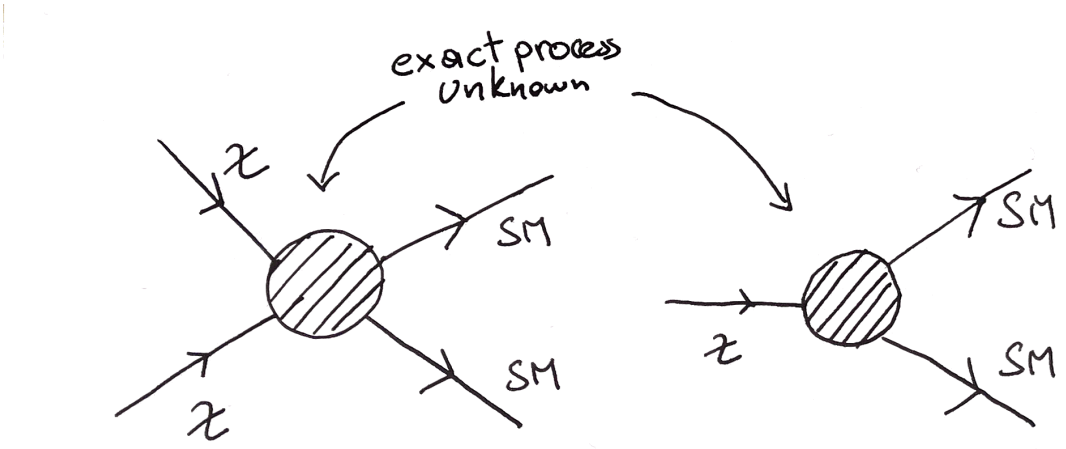


Figure 56: A schematic of dark matter pair annihilation into standard model particles (left) and of dark matter decay into standard model particles (right) for a WIMP particle. The exact process by which this would occur is not known, and therefore currently model dependent. Note that a scattering process between a dark matter and a standard model particle would look very similar to the diagram on the left, with the space and time axes inverted (i.e. change the arrow direction of the top dark matter and bottom standard model particle). However, this scattering might happen via a very different internal process, so the two cannot be directly related in a model independent way.

thermal equilibrium is broken and dark matter decoupled from baryonic matter, since otherwise dark matter would have continued to decay rapidly and almost none would be left today[44]. For dark matter annihilations no such effect is necessary, since the annihilation rate naturally decreases with the dark matter density squared (this will be explained in equation 18). Thus, as the universe expands, dark matter with a coupling into baryons through annihilation will naturally freeze out and its abundance from this point would remain almost constant. However, given that residual annihilations are still possible when two dark matter particles meet, any SM particles produced could be observed and shine a hint on its nature. It is this exact process which is looked for in cosmic ray antinuclei signals. A cold dark matter particle pair annihilating at rest has $\sqrt{s}= 2\mathrm{m}_{\chi}$. The net baryon number would be 0 in such a process, resulting in no further penalty for the production of multiple antinucleons. Per definition, WIMPs interact only weakly, and thus their initial annihilation would occur through a weak channel. Since the weak bosons couple to all other standard model particles, this enables the production of particles such as antinuclei.

The spectrum and yield of antinuclei produced in these annihilations has to be estimated based on known standard model processes. To this end, Monte Carlo event generators are employed [4, 123, 1], in which the initial state is the first state of standard model particles which is assumed to occur in the annihilation process, with a COM energy equal to twice the dark matter mass m_{χ}cookbook.The exact initial state of SM particles is not known, but commonly the channels $W^+W^-$and $\mathrm{b\bar{b}}$ are considered [123, 4]. These two form a convenient subset, as over the range of expected masses (10 GeV to about 1 TeV), they are consistently two of the more optimistic scenarios, and cover the different parameter space within these optimistic scenarios [1]. This can be seen from figure 57. Since event generators do not produce (anti)nuclei – but only the individual nucleons – the (anti)nuclei yields and spectra have to be calculated using the coalescence model. One particular annihilation channel has recently been proposed [144], which suggests a boost of the $^3\overline{\mathrm{He}}$ yield through an intermediate decay to $\overline{\Lambda}_{\overline{\mathrm{b}}}$. While the branching ratio for the process $\overline{\Lambda}_b \rightarrow {}^3\overline{\mathrm{He}} + X$ is not well constrained by data, the default tunes[45] of the event generators tends to underestimate this, and thus the amount of $^3\overline{\mathrm{He}}$ production (it also has an

[44] This would require a mechanism to destabilize dark matter particles in the very hot and dense medium which existed just after the big bang. During the period before dark matter decoupled – which is assumed to have occurred around the quark-gluon-plasma phase of the early universe, i.e. 10^{-12}s - 10^{-5} s after the big bang – the decay rate would have had to be much less than 10^{-5}s in order to achieve thermal equilibrium. In order to remain stable after decoupling, its lifetime would have to exceed the current lifetime of the universe, around 10^{17}s. In medium modifications of decay widths is a known effect [143], however, it is difficult to imagine a process which modifies the lifetime of such particles by at least 20 orders of magnitude.

[45] Tunes when used to talk to event generators are the specific settings which are used for the event generator to more accurately reproduce a given result, e.g. the proton spectra at a given energy.

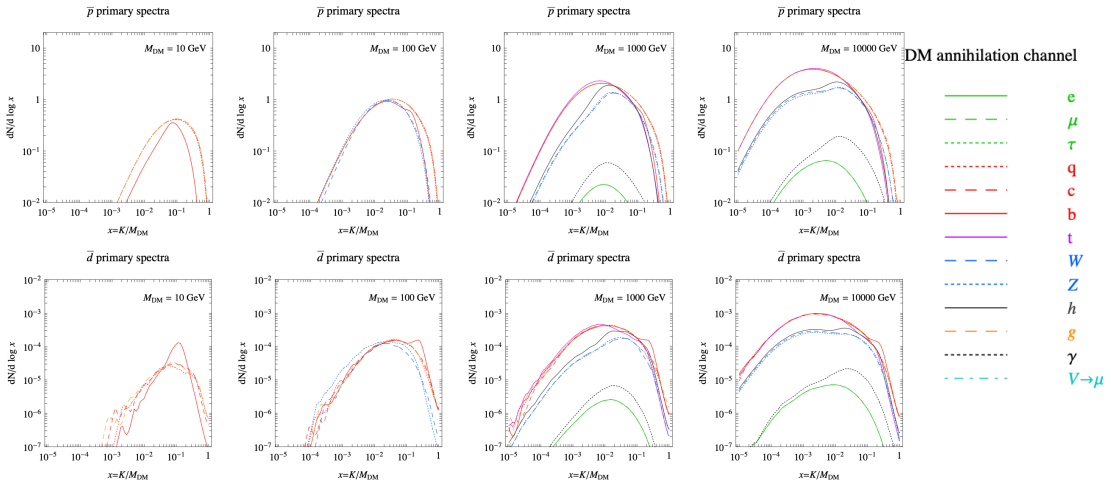


Figure 57: Antiproton (top) and antideuteron (bottom) spectra from dark matter annihilations as a function of the antinuclei kinetic energy per nucleon, normalized to a single annihilation event, for a wide variety of initial SM states. This figure is taken from [1].

impact on the antideuteron production, but far less, as can be seen in section 68 below). In particular, a discrepancy is observed between two commonly used event generators (Pythia [145] and EPOS [146]) of about a factor 3. In order to rectify this, a special setting of the Pythia event generator is used to reproduce the branching fraction close to the one of EPOS. This setting is referred to as the $\overline{\Lambda}_b$ tune in the following discussion. According to these results, there is an almost 10 fold increase in the resulting detectable $^3\overline{\text{He}}$ flux, in particular at high energies around 10 GeV/A. This is of particular interest since according to the authors, such an increase would cause a signal detectable by the AMS-02 experiment, with an event rate of about 1/year. The authors also consider the decay of $\overline{\Lambda}_b$ through light intermediator particles, which provides a slightly different spectrum.
So in addition to the spectra obtained using default event generators from [123, 4], the spectra incorporating the $\overline{\Lambda}_b$ decay are also considered as part of this thesis. All the relevant spectra from these processes for antideuterons and $^3\overline{\text{He}}$ are shown in figure 58.

Since decoupling from baryonic matter, the dark matter would have cooled with the expanding universe, and thus is assumed to be at a similar temperature as the

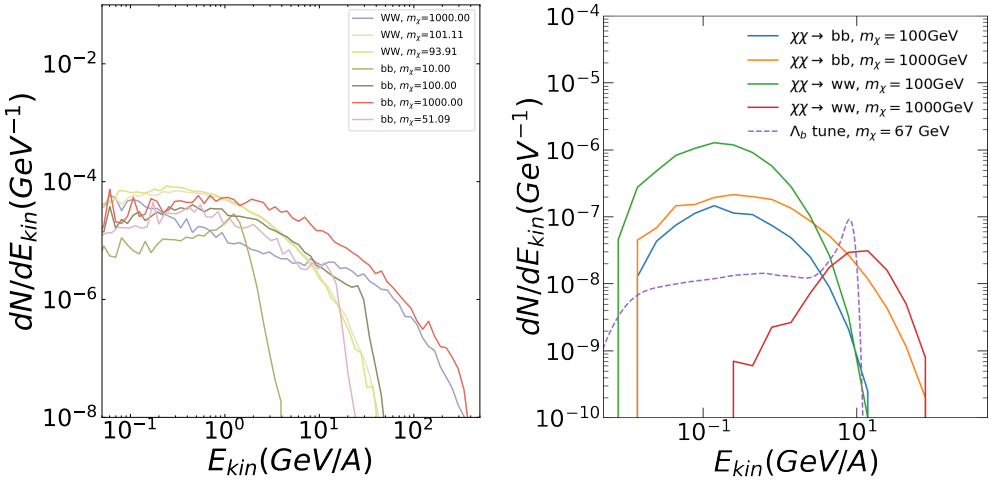


Figure 58: Antideuteron (left) and $^3\overline{\text{He}}$ (right) spectra from dark matter annihilations as a function of the antinuclei kinetic energy per nucleon, normalized to a single annihilation event. Spectra for $W^+W^-$and bb channels are taken from [4], $\overline{\Lambda}_b$ tune is taken from [144].

cosmic microwave background (CMB) today, of about 2.7K [147]. This is referred to as cold dark matter. Another consideration which supports cold dark matter is that the majority seems to be gravitationally bound within galaxies and galaxy clusters [57, 148, 149, 150]. As such, the COM frame is assumed to be the same as the galactic frame, and no boost from the initial velocities are necessary. This is convenient, since one can therefore simply take the spectrum of produced antinuclei per dark matter annihilation – which is obtained from applying a coalescence afterburner to the output of a Monte Carlo event generator – and multiply it by the local annihilation rate of dark matter. Thus, one can write the source term $q(\vec{r}, E)$ for WIMP dark matter as

$$q(\vec{r}, E) = \frac{1}{2}\left(\frac{\rho_\chi(\vec{r})}{m_\chi}\right)^2 < \sigma v > (1+\epsilon)\frac{dN}{dE}, \tag{18}$$

where the factor 1/2 comes from symmetry considerations for majorana dark matter[46], the term $\left(\frac{\rho_\chi(\vec{r})}{m_\chi}\right)^2$ is the square of the number density of the WIMP dark matter, which is then multiplied by the velocity averaged dark matter annihilation cross section $< \sigma v >$, giving the rate of dark matter annihilations for a given point in space. The term $1+\epsilon$ accounts for contributions from other particles which are produced

[46] See section 1.7.5 for a discussion on the difference between Majorana and Dirac dark matter.

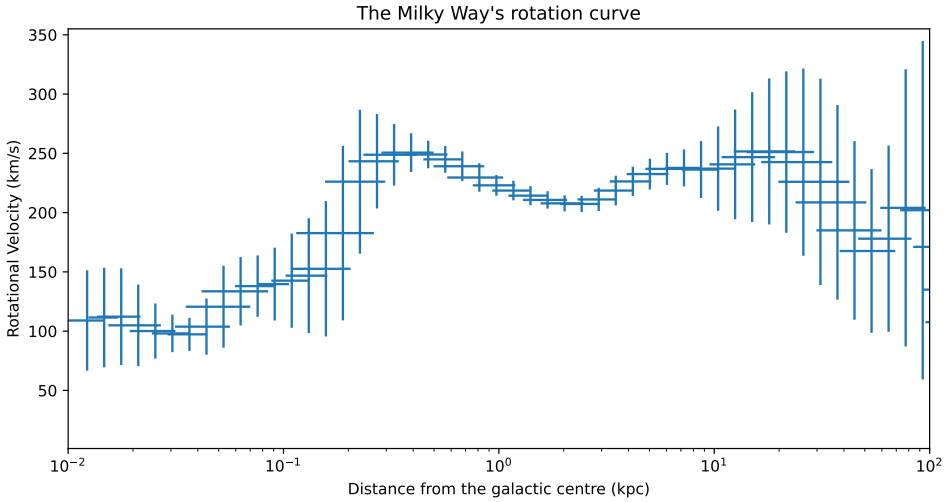


Figure 59: Rotation curve of stars in the Milky Way, as a function of distance from the galactic center. Reproduction of data reported in [78].

and subsequently decay into the antinucleus in question, at timescales longer than the consideration of the MC event generator. The value of ϵ is 0 for antideuterons and 1 for for $^3\overline{\mathrm{He}}$, to account for $^3\overline{\mathrm{H}}$. The final term of equation 18 is the spectrum of produced antinuclei normalised to a single dark matter annihilation. The terms of equation 18, their contraints and degeneracies are discussed below.

The dark matter density profile $\rho_\chi(\vec{r})$ affects both the total amount of antinuclei produced as well as their initial distribution. This parameter can be constrained from measurements of the Milky Way's rotation curve, similarly to how it is done for other galaxies. However, measuring the rotation curve of the Milky Way involves extra challenges, given that we are measuring from within. This is due to the fact that for other galaxies, measuring the difference in velocity through red/bluehisft at different positions is sufficient to measure the rotation curve, whereas for our own galaxies we need the measure both the 3d position and velocity of many stars. The most promising technique to do this is Very-Long-Baseline-Interferometry, which essentially uses telescope arrays spanning multiple continents as interferometers [151]. A more detailed discussion of measuring rotation curves can be found in [79, 78]. Our galaxy's rotation curve has been reported in [78], found by combining multiple existing measurements. It is reproduced in figure 59.

In order to fit such rotation curves, our galaxy is conventionally split into individual parts, each of which can be assumed to have a simpler shape. The usual

breakdown of these parts is shown in table 3, and further details can be found in [79]. The gravitational potentials of these parts can then be summed up linearly, and the rotational velocities caused by each such potential can be added in quadrature. In order to fit the contribution from dark matter, the shape of the dark matter distribution has to be chosen a priori, such that the exact parameters and normalization can then be obtained from the fit. This is an important point, since the total normalization of the dark matter profile is not well constrained. Rather, the relatively well constrained rotation curve in the proximity of the solar system results in the fact that the local dark matter density $\rho_\chi(\vec{r} = r_\odot) := \rho_\chi^\odot$ is much better constrained than the total normalization of the dark matter profile. Thus, the different dark matter profiles are constrained to their value at $r_\odot = 8.5$kpc[47], the estimated position of our sun.

Part	Shape	Extent	Total Mass
Central black hole	Point mass	< 0.1pc	3.6×10^6 M⊙
Buldge(s)	Spherical exponential	<1kpc	10^{11} M⊙
Flat disk	Constant flat disk	< 15kpc	$\approx 10^{10}$ M⊙
Dark matter halo	vaires	100s of kpc	10^{12} M⊙

Table 3: Individual axissymmetric parts of the Mikly Way used for fitting rotation curves. The distinction is made in order to simplify the fit, rather than a hard distinction within the actual galaxy. Non-axissymmetric components are neglected for rotation curves, based on the assumption that any effects would cancel out when averaged over the full rotation. The values for the total mass were taken from [79]. The extent column is approximate and given in order to help the reader visualise the distributions. Due to the distributions being exponential, they only asymptotically approach 0.

There are several profiles on the market, which achieve similar goodness-of-fit when fit to account for the dark matter component in the rotation curve [4], while also achieving the required normalisation at $r_\odot$. The ones used in this work are the Navarro-Frenk-White(NFW) profile [152], shown in equation 19

$$\rho_\chi^{NFW}(\vec{r}) = \frac{\rho_0}{(r/r_s)[1+(r/r_s)]^2}, \tag{19}$$

with scale radius r_s =24.42kpc, the Einasto profile [153], shown in equation 20

$$\rho_\chi^{Einasto}(\vec{r}) = \rho_0 \exp\left\{-\frac{2}{\alpha}\left[\left(\frac{r}{r_s}^\alpha - 1\right)\right]\right\}, \tag{20}$$

[47] The value is currently estimated to be 0.4GeVcm^{-}3 [150, 4, 79, 78, 74].

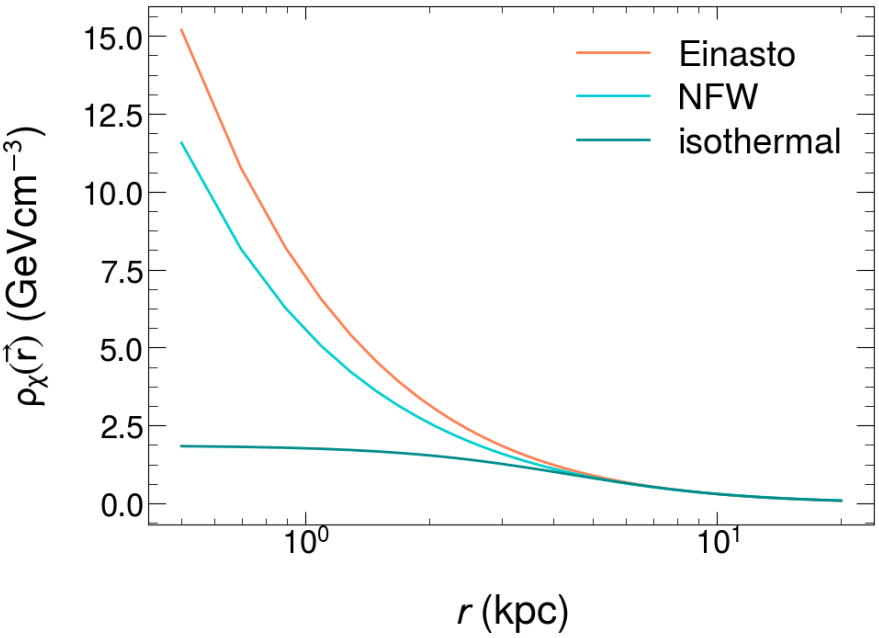


Figure 60: Dark matter density profiles used in this work, as a function of the distance to the galactic centre. The best fit values for each profile are taken from [4].

with α=0.17 and r_s=28.44kpc, and the much shallower isothermal profile [154] and the isothermal profile, shown in equation 21

$$\rho_\chi^{isothermal}(\vec{r}) = \frac{\rho_0}{r^2 + r_s^2}, \tag{21}$$

with r_s=4.38kpc. The profiles are plotted in figure 60, using best fit values taken from [4]. It can be seen that the isothermal profile has a very shallow rise towards the galactic center, while the Einasto profile rises very steeply. The NFW profile lies between the two[48], and is often used preferentially [2, 4, 123]. The stark difference between them is due to their origin. The isothermal profile is motivated purely by the fit to galactic rotation curves, while the NFW and Einasto profiles are motivated by the addition of numerical N-body simulations, which the isothermal profile struggles to replicate [155]. All these profiles assume spherical symmetry. Numerical simulations seem to prefer a triaxial ellipsoid, however, given the lack of data for the tidal motion of stars in the Milky Way, it is currently not possible to narrow down the shape more exactly than a simple spherically symmetric model. These three profiles cover most of the available parameter space for the dark matter profile.

[48] At very small radii, the NFW profile becomes larger than the Einasto profile.

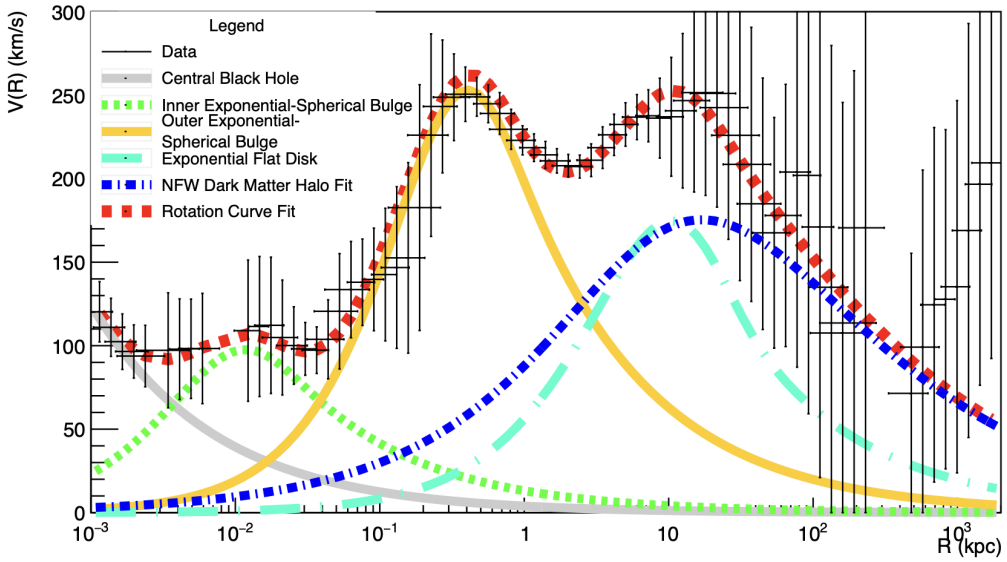


Figure 61: Fit of the rotation curve of the Milky Way, with a NFW profile. Figure is taken from [156], based on work in [149].

It is important to ask why the stark differences towards the center of the galaxy play such a reduced role that all three of these profiles are able to fit the data, and if such differences would therefore make any interpretation of an antinuclei flux from dark matter impossible. The answer to the first part of the question is twofold. Firstly, it is very challenging to measure the rotation curve of our own galaxy with high precision at positions far from the solar system, as can be seen from the uncertainties in figure 59. Secondly, the gravitational effect of the dark matter halo contributes mainly at distances larger than ≈ 2 kpc from the galactic center, where the presence of extra mass at the centre of our galaxy (from a steeper profile) is not as strongly felt. This can be seen from figure 61. The second question also has a fortunate answer: the effect of different profiles on a potential local flux of antinuclei from a dark matter source is rather small, as is discussed in section 5.6.

To summarize: the dark matter density profile in our galaxy is constrained by measurements of the Milky Way's rotation curve. Measuring the rotation curve is a non-trivial process, which involves measuring the 3d position of stars within our own galaxy. The most modern method to achieve this is Very-Long-Baseline-Interferometry (VLBI), which uses telescope arrays spanning continents as a giant interferometer. Once the rotation curve is measured, the effect from luminous matter is accounted for, and the remainder is assigned to the dark matter component. Due to the experimental uncertainties involved in measuring the velocity of far away

objects, this leaves a significant plausible parameter space for the shape of the dark matter profile towards the center of our galaxy.

The second term of equation 18 is the dark matter mass, m_χ. The dark matter mass is a free parameter, with possible values ranging from very light dark matter[49] below the eV range all the way to the WIMP dark matter discussed in this work, with plausible mass ranges from 10s of GeV to the TeV range. As discussed in section 1.7.2, the appeal of WIMP dark matter is that the expected weak cross section of such a particle in the very early universe would yield a population today of the same magnitude as we observe (a mathematical derivation can be found in [150] and is reproduced in section 1.7.2). It would also explain the lack of evidence for the production of dark matter at accelerators, since we might at this point not yet have reached the energies required to produce such particles. Finally, many extensions of the standard model naturally include such a particle, most notably super symmetry, which requires the neutralino, a particle which would fit the WIMP description [82]. This was a rather enticing argument at the inception of WIMPs in the 80s, however, by now the parameter space for supersymmetric theories has become very small [82], due to null observations at accelerators including the LHC. This has made the question of how to incorporate such a particle into the Standard Model more difficult, and thus increased the interest in alternative dark matter candidates, which are discussed in section 1.7.3.

Since the exact nature of dark matter remains a mystery, a priori a wide range of masses is possible. However, direct detection experiments have placed limits on the dark matter-matter interaction cross sections, as a function of the dark matter mass [90, 91] and a recent compilation of these limits is shown in figure 62. It is not possible to relate this interaction cross section with the dark matter self annihilation cross section $<\sigma_{ann} v>$ on general grounds, since they might depend on very different couplings. But it can help us make an informed decision on WIMP masses. As can be seen from figure 62, for masses over a few 10s of GeV, constraints become very strong, limiting the cross section to below a billionth of a pb. Upcoming next generation experiments, such as XENONnT [95] and Darkside20k [157], are expected to push these limits within reach of the neutrino coherent scattering background. If these experiments also do not see a signal, it would eliminate the possibility of background free detection using direct detection methods.

The chosen mass has a direct effect on all three remaining terms of equation 18: i) $\frac{1}{m_\chi^2}$, ii) $\frac{dN_{\bar{p},\bar{d},\overline{^3He}}}{dE}$ and iii)$<\sigma v>$. The effect on i) is trivial, and reduces the overall normalization of the antinuclei source term for higher m_χ. The mass' effect on ii) is based on the amount of energy available for the production of (anti)nuclei, as well as for their kinetic energy. For higher masses, the antinuclei yields increase non-trivially,

[49] A popular light dark matter model is the axion model [18].

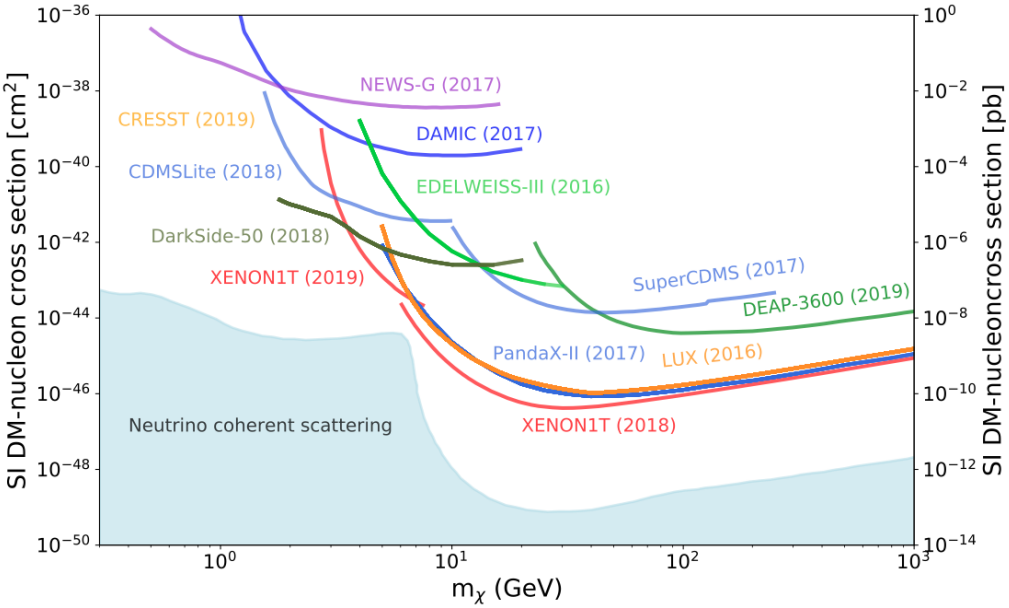


Figure 62: Limits from direct detection experiments on the dark matter - nucleon interaction cross section, as a function of the dark matter mass. The figure is taken from [158].

but slower then the inverse square reduction from the first term. Additionally, the extra energy available for higher masses translates into a spectrum peaked at higher momenta. This depends not only on the available energy, but also on the decay channel. The $\frac{dN_{\bar{p},\bar{d},^3\overline{He}}}{dE}$ spectra used for the antideuteron and $^3\overline{He}$ results shown in this chapter are shown in figure 58. The effect of m_χ on $<\sigma v>$ is mostly experimental, since $<\sigma v>$ is constrained from antiproton measurements.

Any dark matter annihilation process which can result in antideuterons must of course also produce antiprotons. However, contrary to heavier antinuclei, antiprotons are also copiously produced in other processes, due to the much lower energy threshold required for producing a single antinucleon, and the loss of the need to coalesce multiple antinucleons into a single compound antinucleus. This results in a significant and well constrained antiproton flux, which has been measured by the AMS collaboration [60, 59]. Thus, any model chosen must not produce a dark matter component for antiprotons which is incompatible with those measurements. These limits are expressed in terms of $<\sigma v>$ as a function of m_χ. This representation is chosen since ρ_χ can be measured independently, and $<\sigma v>$ varies much more slowly with m_χ than the other terms. The limits – which have been extracted by several groups [159, 160, 161, 162] and compiled by [57]– are shown in figure 63. Indicated in the figure is the maximum limit on $<\sigma v>$, as well as the thermal relic

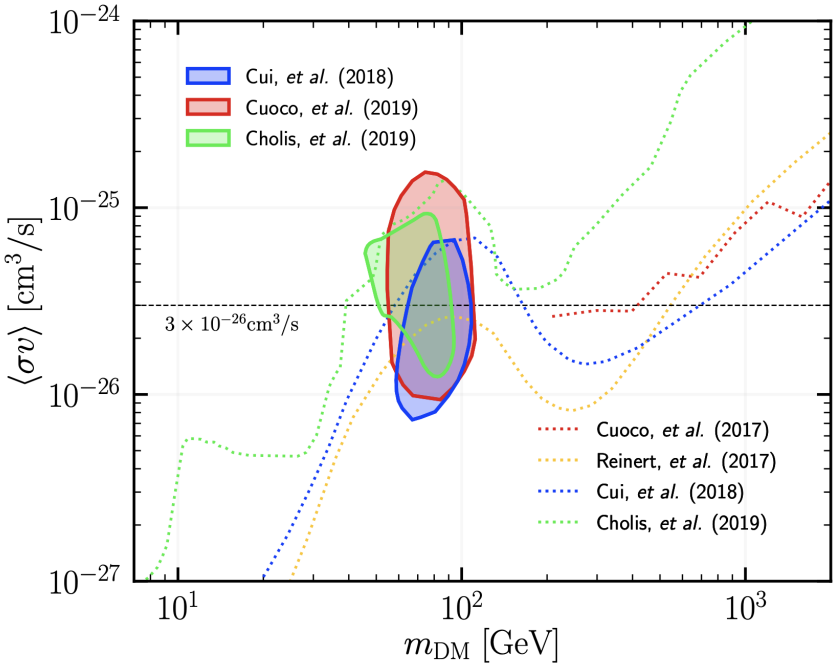


Figure 63: Limits on $<\sigma v>$ based on AMS antiproton data. Figure is taken from [57].

cross section ($\approx 1pb \times c$)[50].

Also indicated in this figure is the area in which a possible excess of antiprotons was observed in the $\overline{\rm p}$ spectrum measured by the AMS collaboration, which could hint at a dark matter particle within this mass range of 50-100GeV/c^2. The different areas correspond to analysis of the same AMS-02 data by different groups, using either a frequentist or a Bayesian approach [57]. It can be seen from the left hand side of the figure that for low dark matter masses, the limits lie significantly below the thermal value for this cross section. Thus, m_χ affects the constraints on $<\sigma v>$, particularly for low masses. It is also worth noting that these limits have to be extracted for a given dark matter density profile, and thus when exploring the maximum allowed antinuclei flux given the antiproton constraints, the choice of $\rho_\chi(\vec{r})$ is degenerate with the limits on $<\sigma v>$ set by the AMS antiproton limits.

To summarise: WIMP dark matter models predict that dark matter can annihilate and produce antinuclei. The resulting antinuclei source term depends on 4 things: i) the dark matter density profile, ii) the dark matter mass, iii) the dark matter self-annihilation cross section and iv) the produced spectrum of antinuclei, normalised

[50] See the derivation in section 1.7.2 for more details.

to a single dark matter decay. i) is constrained by looking at the rotation curve of our galaxy, ii) is a free parameter, iii) is constrained from above by antiproton measurements as a function of m_χ and iv) is calculated based on coalescence models, which depend on the total available energy and thus m_χ. Thus, there are a few notable degeneracies between the different terms of this source function. However, current constraints on these parameters are not stringent and leave open a large, reasonable parameter space which could result in a measureable antinuclei flux from a dark matter source, affirming antinuclei studies as a great tool for the indirect search for dark matter.

5.1.3 Extragalactic dark matter

Dark matter is not exclusively bound within galaxies, but is also present in larger cosmological structures, such as galaxy groups [149]. However, the profiles commonly used in order to fit the distribution of dark matter within our galaxy only take into account galactic dark matter, which can be inferred from the fact that such profiles go to 0 at large distances from the galactic centre. This is because to first order, the extragalactic component will vary over length scales bigger than our galaxy, so the gravitational potential caused by the extragalactic dark matter will be roughly constant within our galaxy, thus causing no active force which could be measured. However, such an additional flux of dark matter could indeed annihilate within our galaxy, thus providing an additional source for antinuclei. In this section the difference of this source to the galactic WIMP dark matter source will be qualitatively discussed. Previous work on the topic expects the extragalactic dark matter component to make up about 12% of the local dark matter abundance close to our solar system [149]. From this, it can be estimated that the extragalactic dark matter is responsible for no more than $\approx 20\%$ of the antinuclei flux near earth.

In order to determine whether the antinuclei flux caused by extragalactic dark matter follows the same assumptions as the galactic component, it is necessary to examine the differences between galactic and extragalactic dark matter. The first difference would be their velocity. Since the galactic component is bound and the extragalactic is not, the extragalactic component's velocity must exceed the escape velocity of the Milky Way, which lies at about 600km/s. This change in velocity may affect 2 terms in equation 18: the self annihilation cross section and the spectrum of produced antinuclei due to the boosted frame in which the collision takes place.
Starting with the effect on the self annihilation cross section, the difference might be due to the momentum dependence of the s-wave and p-wave contributions. The s-wave is velocity independent, while the p-wave contribution has a square dependence on the velocity. However, the speeds of 600km/s still only equate to a beta of 0.002, thus the contribution of the s-wave still dominates at these speeds,

resulting in no change in regards to galactic dark matter. In a similar fashion it can be shown that the effect of the increased speed on the produced antinuclei spectrum is negligible.

The effect which remains is that of the overall normalisation, which is influenced by the extragalactic component to ρ_χ. This extra component would have little to no effect on the rotation curve of our galaxy, and therefore causes a positive offset in comparison to the purely galactic case. The exact nature of this offset should to first order be roughly constant over our galaxy, however, the interaction of the extragalactic dark matter with our galaxy's gravitational pull would cause an increase in the local extragalactic dark matter density in comparison to another point within the local group. Thus, the main difference between the extragalactic dark matter and the galactic dark matter is the consideration of where the majority of annihilations would occur. Finally, we can conclude that since the overall normalisation for antinuclei fluxes from dark matter annihilations is constrained by the maximal allowed flux from antiprotons – as discussed in section 5.1.2 – the increase in flux due to an additional extragalactic dark matter component does not significantly impact expectations.

5.1.4 Primordial black holes

Another possible source of antinuclei in the cosmos are primordial black holes (PBHs). These objects would have formed very early in the universe, created from overdense regions shortly after the big bang. Their mass is therefore given by the particle horizon at the time of formation, $M_{\mathrm{PBH}} \approx c^3 t/G \approx 10^{15}(t/10^{-23}s)g$ [88, 163], where t is the time at their formation. These objects can have a large range in different masses, depending on their formation time. Since such low mass black holes would interact only gravitationally, they would meet the criteria for dark matter [121, 163]. However, as we shall see in this section, they cannot make up the dominant portion of dark matter in the galaxy.

Classically, it is impossible for anything - even light - to escape a black hole. However, as shown by [88], quantum mechanics predicts that black holes will indeed thermally emit (anti)particles, with a characteristic temperature $T = \frac{\hbar c^3}{8\pi G M k_B} \approxeq 1.06\left(\frac{M}{10^{13}g}\right)^{-1}\mathrm{GeV}k_b^{-1}$. This process can be understood as particles tunneling out of the black hole, or as virtual antiparticle-particle pairs being created and one partner tunneling through the event horizon into the black hole, preventing recombination. Both methods yield the same results. The lifetime of such black holes scales with their mass as $\tau_{\mathrm{PBH}} \propto M_{\mathrm{PBH}}^{-3}$, i.e. they evaporate faster the smaller they are. This results in PBHs emitting many (anti)particles almost simultaneously when they fully

evaporate at the end of their lifespan, a process akin to an explosion. The mass of currently evaporating PBHs is in the range of about $\approx 10^{15} g$, since lighter black holes would have already evaporated in the past, while heavier ones will only evaporate in the future. Such PBHs could produce antinuclei during the final stage of their evaporation.
The current abundance of PBHs in this mass range is most tightly constrained from γ-ray searches [127], to $\frac{\rho_{\mathrm{PBH}}}{\rho_{\mathrm{tot}}} < 10^{-26}(M_{\mathrm{PBH}}/10^{15} g)^{-5/2}$, which means that PBHs cannot make up all the dark matter in our galaxy. These limits include the extragalactic gamma ray background (for masses down to $10^{13} g$) and the galactic gamma ray spectrum (for masses of $\approx 10^{15} g$). Modification of the PBH lifetime due to an extra dimension in string theory could rectify this, allowing PBHs to make up 100% of dark matter [164].

In this thesis PBHs were considered as a possible source for antideuterons, using a PBH mass of $9.35 \times 10^{14} g$. For this mass, PBHs were found from antiproton constraints to make up no more than $f_{\mathrm{PBH}} = 4 \times 10^{-11}$ of all the dark matter in the galaxy. This corresponds to a local rate of PBH explosions of $2 \times 10^{-4}\, p\, c^{-3}\, y\, r^{-1}$. The source term of antideuterons from such events is given by equation 22

$$q(\vec{r}, p) = \frac{f_{\mathrm{PBH}} \rho_{\mathrm{CDM}}(\vec{r})}{M_{\mathrm{spectrum}}} \frac{dN}{dT}, \tag{22}$$

where M_{spectrum} is the typical mass of the PBHs considered, and ρ_{CDM} is the cold dark matter density profile, equivalent to the one used for WIMPs. The corresponding antideuteron spectrum per second $\frac{dN}{dT}$ is taken from [4], and is shown in figure 64.

5.2 Constraining the propagation of antinuclei through the galaxy

In the process of propagating thorough our galaxy, particles undergo several different effects. They get produced at various points in both space and time, for example most heavy nuclei are produced in supernovae [126]. As they then propagate from their source towards their eventual detection point near earth, they undergo diffusion effects, undergo elastically scattered and are diverted by the magnetic fields of the galaxy and individual celestial objects. They are also under the effect of bulk motion via convection effects. Finally, there are various effects which might cause a particle to disappear, mainly inelastic interactions with the interstellar medium, or breakup for unstable particles. All of these processes are characterised by the transport

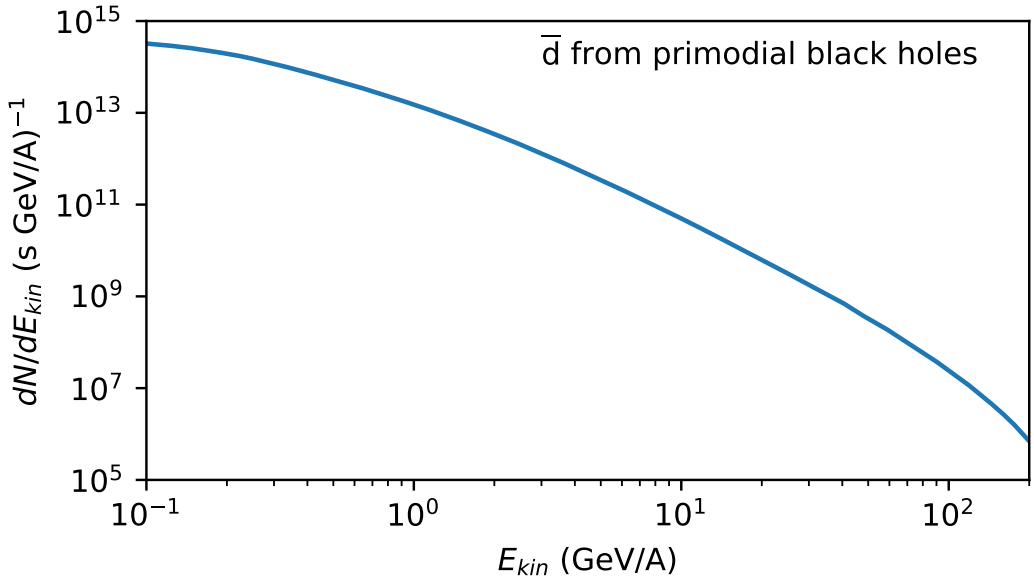


Figure 64: Spectrum of produced antideuterons per second, as a function of kinetic energy per nucleon, from a primordial black hole evaporation. Data from [4], provided in private communication.

equation [120], which is reproduced in equation 23

$$\frac{\partial \psi}{d t} = q(\mathbf{r}, p) + \mathbf{div}(D_{xx}\mathbf{grad}\psi - \mathbf{V}\psi) + \frac{\partial}{\partial p} p^2 D_{pp} \frac{\partial}{\partial p} \frac{\psi}{p^2} - \frac{\partial}{\partial p}\left[\psi \frac{d p}{d t} - \frac{p}{3}(\mathbf{div}\cdot\mathbf{V})\psi\right] - \frac{\psi}{\tau_f} - \frac{\psi}{\tau_r}, \tag{23}$$

where ψ is the time and space dependent flux of a given cosmic ray species, $q(\mathbf{r}, p)$ is the source term as a function of position and momentum, D_{xx} and D_{pp} are the spatial diffusion and diffusive re-acceleration coefficients, V is the convection velocity, and τ_f and τ_r are parameters characterising the annihilation and fragmentation rates, respectively. The relationship between the last term and the inelastic cross section of a cosmic ray species is given by equation 24

$$\frac{1}{\tau_r} = \beta c \left(n_{\mathrm{H}}(\vec{r}) \sigma^{^3\overline{\mathrm{He}}\mathrm{p}}_{\mathrm{inel}}(p) + n_{\mathrm{He}}(\vec{r}) \sigma^{^3\overline{\mathrm{He}}^4\mathrm{He}(p)}_{\mathrm{inel}} \right), \tag{24}$$

where, n_{H} is the number density of hydrogen gas (approximately 1 m^{-3}), n_{He} is the number density of helium gas (approximately 0.1 m^{-3}).

Equation 23 can be solved for a given set of parameters both analytically or numerically. Several tools exits in order to solve this equation, with the most well known being GALPROP (available under https://galprop.stanford.edu/) [120], Dragon [165] and PICARD [166]. In this work, GALPROP was used, which solves the transport equation numerically and will be explained in section 5.3. Galprop uses astrophysical measurements for the interstellar gas and cosmic ray source distributions, and employs nuclear physics measurements for interaction cross sections of particles and nuclei. Many different particle species can be en- or disabled in GALPROP, which affects the runtime of the simulations. For antinuclei from dark matter, other species need not be included, since the result is independent of other particle species. However, for antinuclei from secondary cosmic rays, other cosmic ray species can affect the total flux and therefore need to be considered.

It is important to note that only the first and final term of equation 23 – i.e. the source and loss terms – depend on the species of particle which is being considered. The other terms, which cover the actual propagation through the galaxy, depend solely on parameters which are common to all particle species. This can be understood as the same magnetic fields and bulk motion affecting all particles. Thus, these parameters can be constrained by fitting abundant cosmic ray species which are sensitive to a particular parameter, in order to constrain the propagation for all

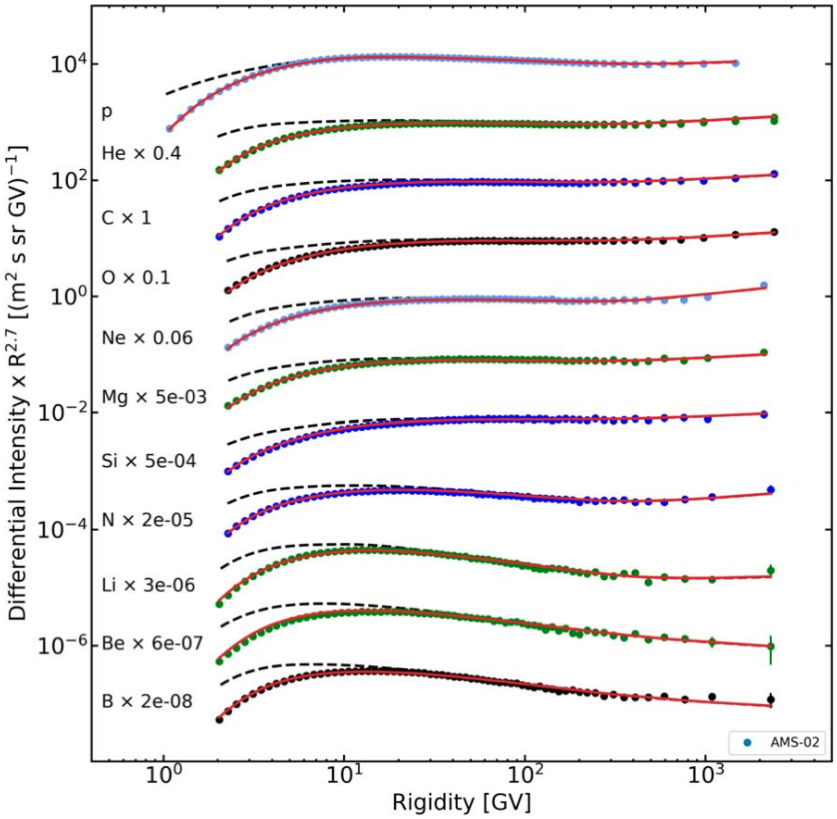


Figure 65: Fluxes of several cosmic ray nuclei, as measured by AMS-02, compared to the predictions of the best-fit values obtained by fitting several key species. Figure taken from [63]

species. This is particularly important for the propagation of antinuclei, which are extremely rare. These propagation parameters have been investigated and reported by e.g. Boscini [62, 63] and Cuoco [161]. The effectiveness of these fits can be seen by comparing predicted spectra of protons, antiprotons and heaver cosmic ray nuclei with the measurements done by AMS-02, which are shown in figure 65. The solid lines are the predictions from the Boscini model after solar modulation is applied, while the dashed lines are the predictions before solar modulation. It can be seen that the predictions work very well for large energies, and there is a smooth response at low energies, which is well understood based on the effects of the heliosphere. This shows that the propagation is well under control.

The effect at low energies is due to the effect of the heliosphere, which is not included in codes such as GALPROP. These codes can only simulate large scale effects,

and as such they output the particle fluxes outside of our solar system. Within our solar system, the solar magnetic field will affect incoming charged particles, and this needs to be accounted for. The solar mangnetic field is not constant, but rather it varies over an 11 year period [167]. Thus, the effect of the solar modulation is also time dependent and needs to be calculated for a specific scenario. In this thesis, a solar minimum is considered, in order to discern the most optimistic flux of low energy antinuclei. There are tools which treat this in great detail for cosmic rays, such as HELMOD [168], but there are currently no such tools on the market which are able to treat antinuclei. Thus, a simple force field model has been commonly used for this purpose in the literature [4, 123, 2]. The advantage of this model is its broad applicability, while its disadvantage is mainly a large uncertainty induced for low momentum particles [169]. The force field model is a simplified solution to the Parker equation [170], which treats the full extent of the problem including solar winds and turbulences. This complete treatment relies on knowledge of turbulences and boundary spectra of the particle species involved, and thus lies beyond the scope of this thesis and similar analyses [2, 4, 63]. The force field approximation reproduces the overall effect of solar modulation, although the exact values it produces are not exact at low energies [169]. It also relies only on a single parameter, the so called Fisk potential ϕ_F, and related the unmodulated flux F to the modulated flux F' according to equation 25, while modifying the corresponding kinetic energies according to equation 26

$$F'(E',\phi) = F(E)\frac{(E-Z\phi)^2-m^2}{E^2-m^2}, \tag{25}$$

$$E' = E - Z\phi, \tag{26}$$

where m denotes the mass of the cosmic ray species in question. For the analyses in this thesis, the Fisk potential is assigned a value of 0.4 GV.

It is important to note that some of the propagation parameters which are degenerate for one source are not necessarily so for another. In particular, the source from dark matter is strongly dependent on the height of the galaxy considered (since this increases the total amount of dark matter considered), rather than the ratio of the diffusion and the height, D_{xx}/z_h, which is the common factor for antinuclei from high-energy cosmic rays. This degeneracy for secondaries can be seen in table 4, where the aforementioned ratio is shown to be consistent between the two paramterizations. Since propagation parameters are constrained by nuclei following roughly the same source distribution as secondaries, this difference in sensitivity causes a much larger uncertainty in the possible fluxes for antinuclei from dark matter than

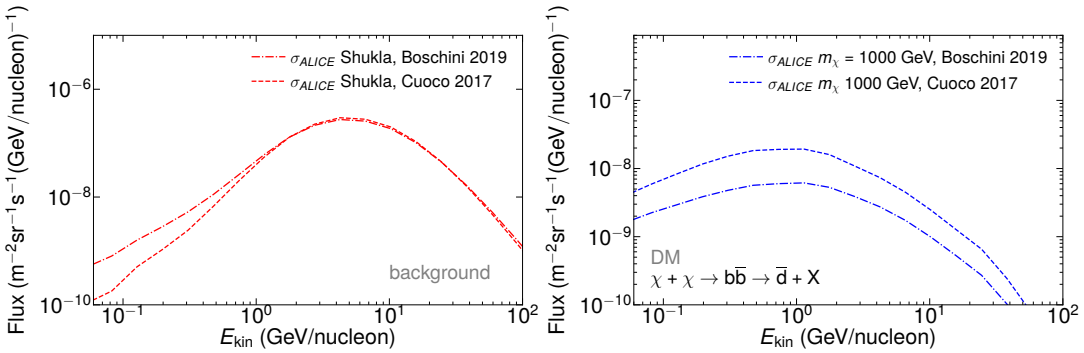


Figure 66: Comparison between the different GALPROP propagation parameters used in this work, for antideuterons from high energy cosmic ray collisions (left) and from dark matter annihilations (right).

for antinuclei fluxes from high-energy cosmic rays [121]. This is also shown in figure 66, where it can be seen that for a wide energy range, both different propagation parameterization used in this work give near identical antideuteron fluxes from high energy cosmic ray collisions, while for dark matter the difference is more than a factor 2. For antideuterons from high-energy cosmic rays the discrepancies between the two different parameterizations only become non-negligible at very low energies, where the propagation is less well constrained and complicated by the need to disentangle solar modulation effects.

At this point it is also important to note the composition of both cosmic rays and the interstellar medium. For the interstellar medium, its composition determines the targets for incoming cosmic rays. This is important both for the production of secondary antinuclei in high energy cosmic ray collisions, and also for the annihilation of antinuclei as they travel through our galaxy. Both the interstellar medium and baryonic cosmic rays share similar compositions: 90% protons and 9% ^{4}He [171]. The remaining elements is made up of heavier elements.

5.3 The Galprop framework

The technical details of the implementation of antinuclei propagation in GALPROP can be found in [112]. The following section aims to give the reader an understanding of the concepts considered.

As already discussed in section 5.2, the Galprop framework functions by solving the transport equation numerically (equation 23). It does so by finding a steady state solution, iterating in smaller and smaller timesteps until a stable solution is found. During each timestep, it iterates over a position and momentum grid, the former of which can either be expressed in 2 dimensions (r and z) or 3 (x, y, z). Since we

assume axial symmetry, the two are mathematically equivalent, so for the purpose of this work, the 2 dimensional method was chosen.

Galprop is configured by passing a set of parameters from an external text file. The important parameters are shown in table 4. Of particular note are the Galaxy half height z_h, and the diffusion parameter D_{xx}, since these two are degenerate for cosmic rays from non-exotic sources. The actual parameter which is being fixed is the ratio of the two. This is because for non-exotic sources, the number of sources doesn't change so any change in position is compensated by increased diffusion. For a dark matter source however, the height of the galaxy has direct implications for the number of dark matter sources, so this degeneracy is broken.

Parameter	Units	Best fit value from Boscini	Best Fit value from Cuoco
z_h	kpc	4	6.78
D_{xx}	cm^2s^{-1}	4.5×10^{28}	7.48×10^{28}

Table 4: Two of the parameters for the tuning of Galprop, which show the degeneracy between them.

It is important to note that the main parameter which affects a lot of propagation is the so called grammage, which is the amount of matter of the interstellar medium which particles have to traverse. This is the product of the density of the interstellar medium and the path length of the particles, and can be constrained by the ratio of primary to secondary cosmic rays, according to equation 27[51]

$$\psi_s/\psi_p = \frac{n\Delta z \sigma \beta c z_h}{2D_{xx}}, \tag{27}$$

where n is the density of matter in the interstellar medium, ψ_p and ψ_s are the primary and secondary fluxes, and σ is the production cross section of the secondary particles when the primary cosmic rays interact with the interstellar medium. This means that this ratio is simply the amount of matter traversed $\times$ the production cross section $\times \frac{z_h}{2D_{xx}}$, which shows the degeneracy for these parameters. The primary to secondary ratio is best constrained from the Boron-to-Carbon (B/C) ratio, since Carbon is expected to be produced mostly during stellar processes, while all Boron is produced in collisions of heavier nuclei with the ISM [124]. This ratio has been measured by the AMS collaboration to very high accuracy [124], with errors less than 3% up to rigidities of 100 GV.

[51] This is the simplified equation without losses, for more details see [172], section 7.1.

Antinuclei are not by default included in Galprop. Fortunately, the framework is capable of handling negative nuclei with antiprotons, therefore the extension was done by providing the mass of the antideuteron/antihelium, their inelastic cross sections on the interstellar medium, and their source functions. Separate entries were used for the secondary production from high-energy cosmic rays and from dark matter annihilations. The inelastic cross section had to be provided on a proton and helium target, which are significantly lighter than the average detector materials probed in the measurements shown in section 3, therefore the results had to be extrapolated to these lighter targets. The exact methods of the extrapolations are explained in section 5.4.

The source functions for antinuclei from either high-energy cosmic-ray collisions or from dark matter annihilations were included in GALPROP as a function of the distance from the galactic centre. For the dark matter part, this can be done simply by evaluating equation 18 described above for a specific radius and kinetic energy. However, for antinuclei from high-energy cosmic rays this is not possible, since the spectrum of cosmic rays at a given point enters into the equation. Therefore, the production cross sections for the relevant collision systems (pp, p–He, He–p, He–He) were implemented in GALPROP, and the interactions between those cosmic-ray species were calculated as described in [113], based on the production cross sections in [129].

5.4 Annihilations within our galaxy

As antinuclei travel through our galaxy, they might inelastically interact with matter in the interstellar medium. This can either be in the form of inelastic scattering[52] or annihilation, although of the two the latter is expected to be dominant. The result of these interaction is thus mostly the disappearance of the antinuclei. The produced particles are mostly pions, and thus not stable enough to detect them and maybe extract a signal from them. Some high-energy photons could also be produced, and such gamma rays are the target of specific sky surveys looking for large areas of anti-matter, which when coming into contact with matter should produce a detectable signal. However, a single annihilation would be undetectable at any significant

[52] Non-annihilating inelastic scattering of antinuclei on matter is expected to be very rare. An example of this would be the collision of $^{3}\overline{\mathrm{He}}$ with a ^{4}He nucleus which causes the ^{4}He nucleus to break up, and thus a drastically different momentum for the $^{3}\overline{\mathrm{He}}$. Since such particles would be lost to the tracking algorithm in the ALICE detector, these processes are included in the measurements of the inelastic cross section. However, in the galaxy such particles would not disappear and thus could in theory be detected (this is usually called tertiary production). Since the expected flux caused by this effect is several orders of magnitude lower than a signal, it is neglected for the purposes of this thesis.

distance. We can therefore conclude that the relevant result of annihilation is the disappearance of the antinucleus in question.

The loss of antinuclei in Galprop was taken into account by implementing the inelastic cross section. As antinuclei are propagated throughout our galaxy, the total amount of matter they interact with is calculated for each timestep, position and momentum grid point (see section 5.3 for details). In order to do so, both the distribution and the composition of the interstellar medium is required. The composition is known to a relatively high accuracy [171], and is dominated by hydrogen, which makes up ≈90% of the total mass in the interstellar medium. The remainder is mainly helium, making up ≈ 9% of the total mass. During each calculation step, the inelastic cross sections on the dominant species of the interstellar medium (hydrogen and helium) are used to calculate how many antinuclei are lost in each momentum bin. Therefore, it is necessary to evaluate the cross sections on these very light targets, rather than the heavy targets on which they were measured.

In order to extrapolate the results of the inelastic cross sections to light targets, the A scaling from Geant was applied. To achieve this, the deviation of the inelastic cross section from the default implemented in Geant was obtained for the mean material in ALICE, as described in section 3, and proportianlly applied to the antinucleus-proton cross section in Geant. This assumes that the relative scaling is the same regardless of the target nucleus, and an additional 8% uncertainty is assigned to allow for any deviation from this assumption. This value was achieved by comparing the A scaling used in Geant4 and in full Glauber calculations [110, 43]. For values outside the range of the measurements detailed in sections 3, the scaling factor at the last available momentum was used. The resulting cross sections are shown for both antideuterons and $^3\overline{\mathrm{He}}$ in figure 67. The Geant lines shown in these figures are based on Glauber model calculations, as discussed in section 1.4.4.

5.5 Antinuclei fluxes for different dark matter masses and annihilation channels

In this section the effects of different dark matter masses on antinuclei fluxes will be discussed. The fluxes are compared to a prediction for secondary antinuclei from high-energy cosmic ray collisions with the interstellar medium. In the lower panel on figure 69 and on the right side of figure 70, the transparency of the galaxy to antinuclei is shown. This is defined in equation 28 as the ratio of the obtained flux with a given non-zero inelastic cross section, to the flux obtained when all inelastic interactions are turned off. The dark matter self annihilation cross section used for the dark matter models shown in this chapter is $<\sigma v>= 2.7 \times 10^{-26}\mathrm{cm}^3\mathrm{s}^-1$, unless

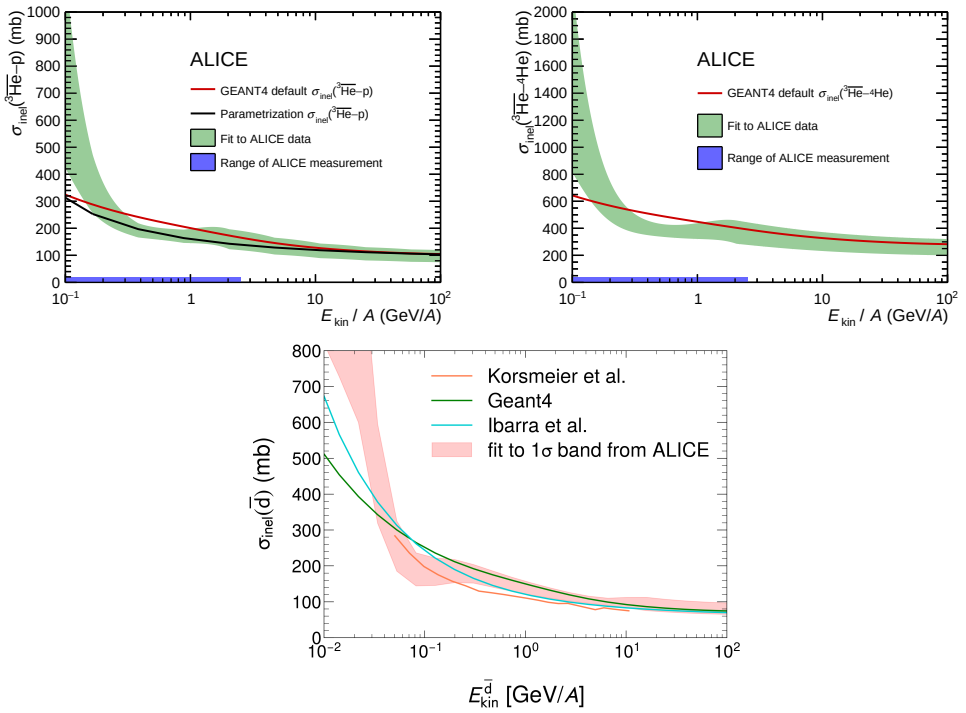


Figure 67: Scaled inelastic cross sections of $^3\overline{\text{He}}$ (top) on proton (left) and Helium-4 (right) targets and antideuterons on proton targets (bottom). The band shows the experimental uncertainty from the ALICE measurements [105, 110], plus an additional 8% uncertainty associated with the scaling from heavier targets (C, O, Al) to protons (H). The parameterization shown in the top left panel (labeled Korsmeier et al in the bottom panel) is taken from [2], and is based on scaling the total deuteron-antiproton cross section by the inelastic portion of the antiproton-proton cross section, and then scaling the obtained value by 3/2 to account for the extra nucleon in $^3\overline{\text{He}}$. The cross section in the bottom panel labeled Ibarra et. al. is taken from [4], and is based on taken 2 times the antiproton-proton inelastic cross section, as parameterized by [36]. See section 1.4.4 for a more detailed discussion on calculating inelastic cross sections.

otherwhise noted. This is compatible with the currently allowed limit, and also at the thermal value of the cross section, which is discussed in section 5.1.2.

$$\text{Transparency}(\sigma_{\text{inel}}) = \frac{\text{Flux}(\sigma_{\text{inel}})}{\text{Flux}(\sigma_{\text{inel}} = 0)}. \tag{28}$$

Several parameterizations of the inelastic cross sections were considered and are shown for the fluxes in this section. The colored bands represent the results obtained using the inelastic cross sections measured by ALICE, and the associated experimental uncertainties from this measurement. The solid lines denote the results obtained using the default inelastic cross sections implemented in Geant4.

5.5.1 Results for antideuterons

The antideuteron fluxes inside and outside of the solar system can be seen in figure 68. Of particular note is the signal to background ratio, i.e. the ratio between secondaries coming from cosmic-ray collisions and fluxes from dark matter. At low energies, for values of $m_\chi \lesssim 100$ GeV , the signal exceeds the secondaries by several orders of magnitude at energies energies below ca. 3 GeV/A. This reinforces low-energy antideuterons as a unique probe for indirect dark matter searches. At larger energies the spectral shape of the antideuteron fluxes from dark matter becomes very similar to the one expected for secondaries, and also the normalisation becomes very similar. This makes WIMP models with masses above ca. 1 TeV difficult to differentiate from secondary production, and thus loses the strength for probing such dark matter models.
The largest flux is achieved by the 10 GeV dark matter mass model, which is due to the increased normalisation due to the $1/m_\chi$ term. However, for such low dark matter masses, the used dark matter self annihilation cross section has been ruled out by antiproton limits, as can be seen in figure 63. Thus, the flux at 51 GeV would produce the largest allowed antideuteron flux.

For antideuterons, and additional channel was considered in addition to the usual $W^+W^-$and $b\bar{b}$ channels: a boosted production via the intermediate production of $\overline{\Lambda_b}$ and its subsequent decay, as described in [144]. This particular channel was only recently considered, and is expected to boost antinuclei yields. The validity of the approach rests on the fact that normal tunes of event generators under represent both the production of $\overline{\Lambda_b}$ and its branching fraction into antinuclei, however, this needs to be followed up with measurement to clearly determine the actualy size of this effect.
There are also two different background models considered for antideuterons, la-

beled Shukla et. al. based on [129], and Kachelriess et al. based on [52]. For more details see [121].

5.5.2 Results for $^3\overline{\mathrm{He}}$

In this section the results for antihelium-3 fluxes using different dark matter masses m_χ are shown and discussed. These masses range over 2 orders of magnitude from 10 GeV all the way to 2 TeV, all of which are valid hypotheses for WIMP masses. As can be seen in figure 69, the result is not just a difference in the overall normalization, but also in the shape of the produced spectrum. This is because the larger energy available with the higher mass translates into more kinetic energy in the final state particles, i.e. the produced antinuclei. It can also be seen that the increased production with increased mass does not compensate for the reduction in annihilation rate due to the lower number density[53], thus the magnitude of the flux decreases with increasing dark matter mass. Also shown in the bottom panel for each figure, is the transparency of the galaxy to $^3\overline{\mathrm{He}}$ defined in equation 28. It is promising that the predicted fluxes from $\overline{\Lambda}_b$ decays in figure 69 reach the AMS-02 sensitivities even without accounting for other uncertainties. For other channels, a boost of about 1-2 orders of magnitude is possible in the most optimistic scenario, as can be seen from table 5, which could potentially allow a signal in both the $b\overline{b}$ and W^+W^-channels for masses of around $m_\chi = 100$ GeV. And even a null observation would place more and more stringent limits on dark matter models, further tightening the available parameter space.

5.6 Results for different dark matter profiles

The effect of the different dark matter profiles is shown only on one channel and one dark matter mass, since it has similar effects on all channels/masses. The absolute normalization is degenerate with bounds from antiproton measurements, as was discussed in section 5.1.2. However, more insight can be gained from the bottom panels of figure 70, where the transparency is shown. The transparency of the Milky Way shows a significant shift between the three different profiles. This can be understood as the mean distance that antinuclei from dark matter have to traverse in order to get to earth. The more peaked the profile is towards the center, the longer the mean path. This in turn reduces the transparency. Thus, the transparency of the galaxy to antinuclei is lowest for the Einasto profile, which is the most peaked, as can be seen in figure 60. It is highest for the isothermal profile, which is relatively flat towards the centre of the Milky Way.

[53] This is the $1/m_\chi^2$ scaling seen in equation 18.

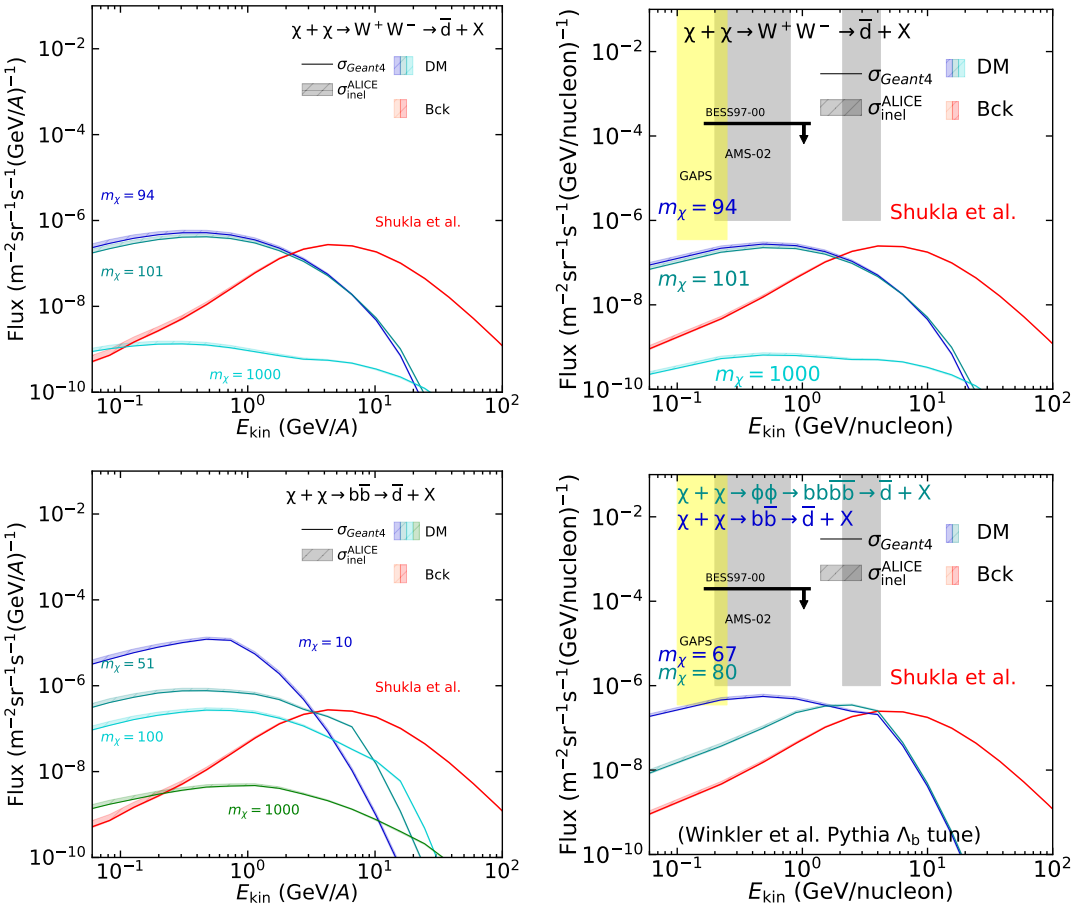


Figure 68: Expected antideuteron fluxes for different m_χ ranging from 10 GeV to 1 TeV, and from primordial black holes (PBHs). They are compared to an expected spectrum of secondary antideuterons from high-energy cosmic-ray collisions. The results are shown for the position of the solar system. The figures on the left show the results without solar modulation, and on the right with solar modulation included by means of a force field model, as is discussed in section 5.2. The results are also shown for different possible annihilation channels of dark matter, either through W^+W^-(top) or through $b\bar{b}$ (bottom).

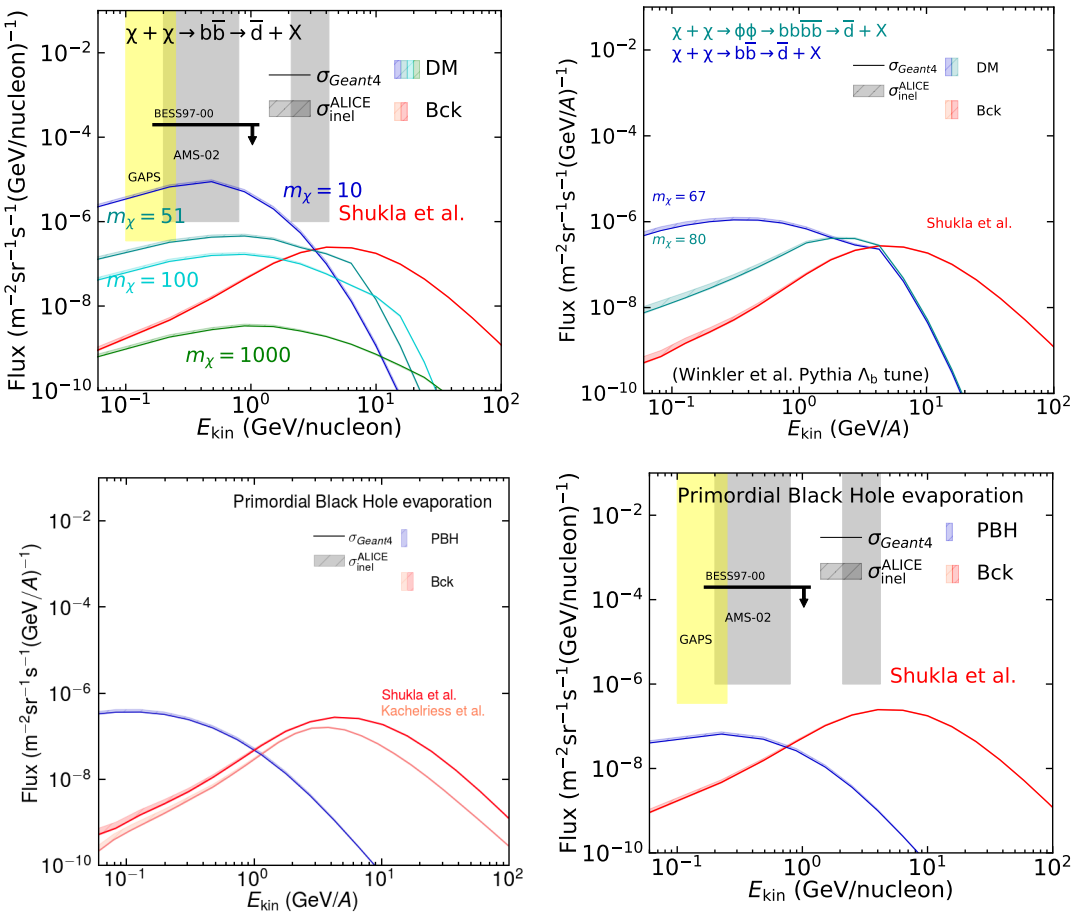


Figure 68: Expected antideuteron fluxes (cont.) dark matter annihilations through $\overline{\Lambda}_{\overline{b}} \rightarrow b\overline{b}$ and light mediators (top) and from primordial black holes (PBHs) (bottom). The figures on the left show the results without solar modulation, and on the right with solar modulation included by means of a force field model, as is discussed in section 5.2.

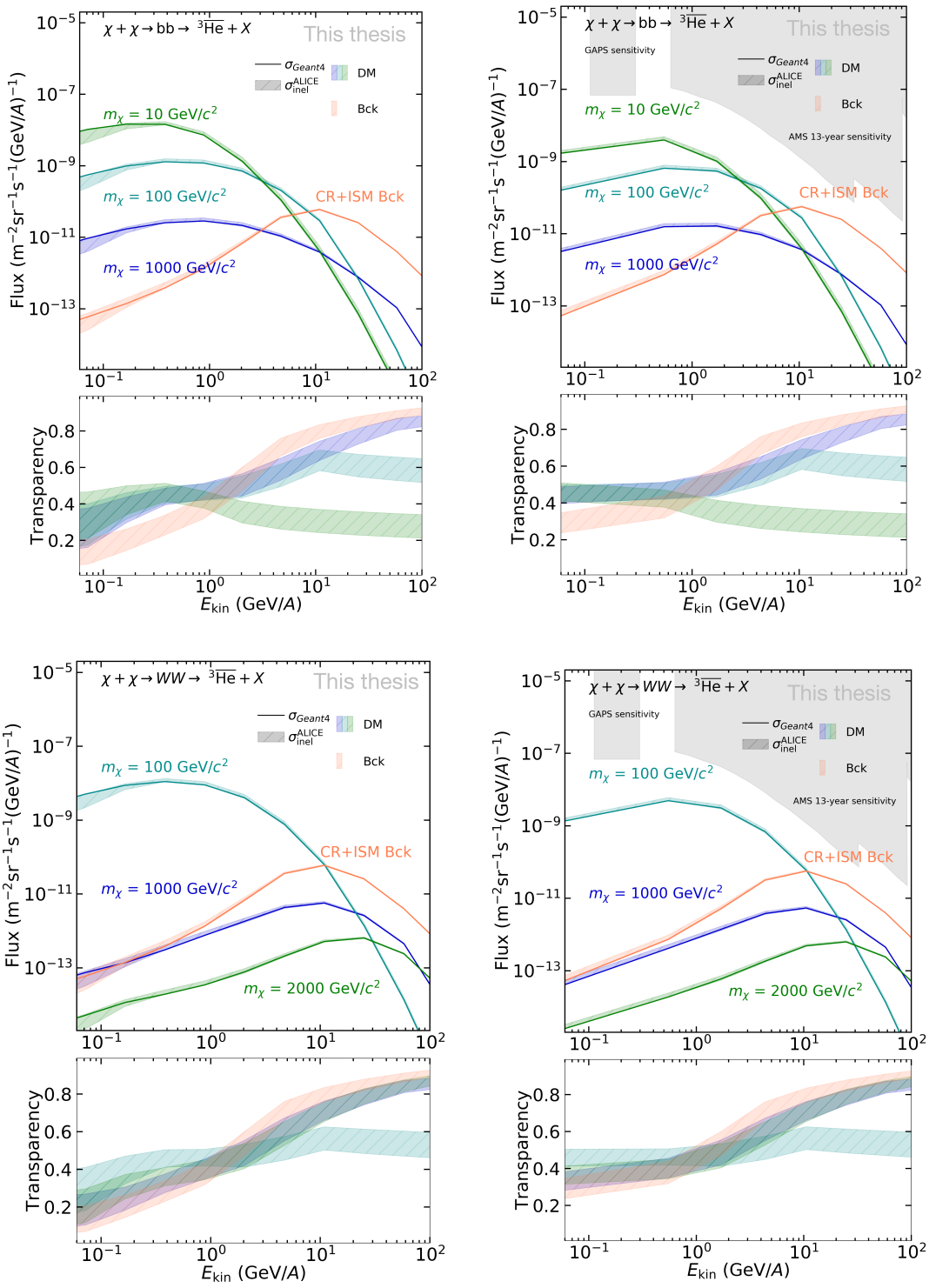


Figure 69: Expected $^3\overline{\text{He}}$ fluxes for different m_χ ranging from 1GeV to 2TeV. They are compared to an expected spectrum of secondary $^3\overline{\text{He}}$ from high energy cosmic ray collisions. The results are shown for the position of the solar system. The figures on the left show the results without solar modulation, and on the right with solar modulation included by means of a force field model, as is discussed in section 5.2. The results are also shown for different possible annihilation channels of dark matter, either through W^+W^-(top), through $b\bar{b}$ (bottom).

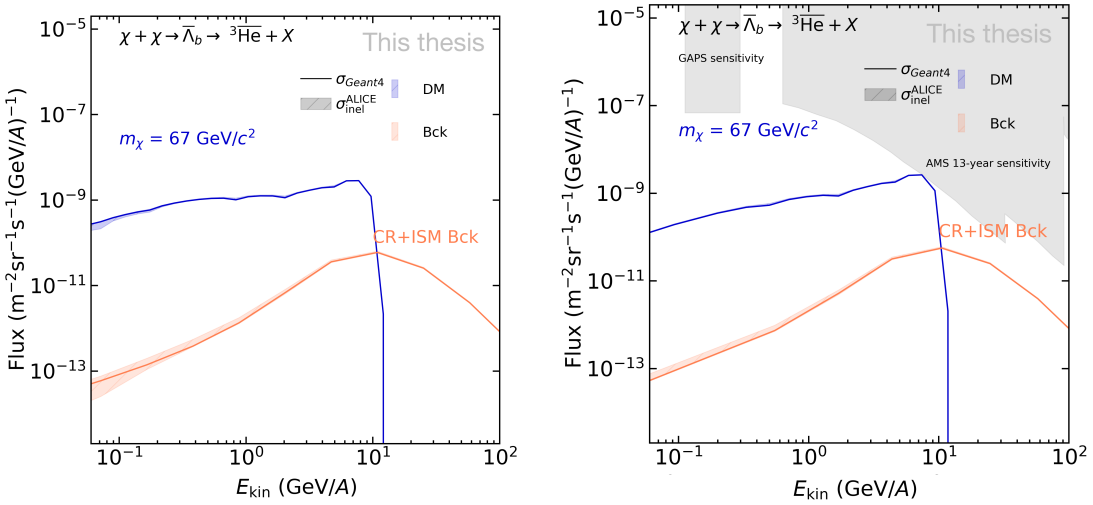


Figure 69: Expected $^3\overline{\text{He}}$ fluxes (cont.) from dark matter annihilations through $\overline{\Lambda}_b$ decays. They are compared to an expected spectrum of secondary $^3\overline{\text{He}}$ from high energy cosmic ray collisions. The results are shown for the position of the solar system. The figures on the left show the results without solar modulation, and on the right with solar modulation included by means of a force field model, as is discussed in section 5.2.

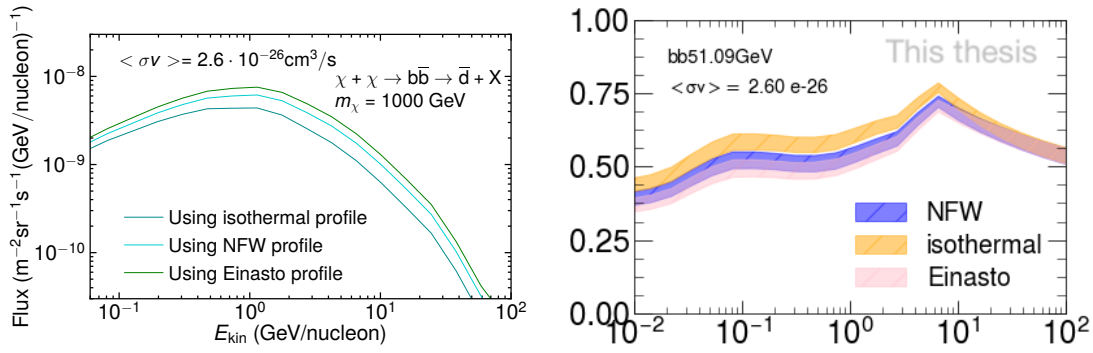


Figure 70: Antideuteron fluxes for different dark matter profiles (left) and the corresponding transparencies (right), for antideuterons from dark matter annihilation through the $b\bar{b}$ channel.

5.7 Discussion of the uncertainties on antinuclei fluxes and transparencies

Presented in this chapter are the experimental uncertainties on the effect of inelastic interactions on antinuclei fluxes in cosmic rays, as well as on the transparency of the galaxy to antinuclei from different sources. It is important to note that these uncertainties are now quantified based on experimental data for the first time, and that they uncertainties are much smaller than other uncertainties in the field, as can be seen by comparing the values given in table 5.

Source of effect	Effect for CR	Effect for DM	Source
Inelastic interactions $\overline{\mathrm{d}}$ ($^3\overline{\mathrm{He}}$)	±20% (15%)	±10% (15%)	This thesis, [121, 110]
Propagation parameters	≈20%	≈200%	This thesis, [121]
Production $\overline{\mathrm{d}}$ ($^3\overline{\mathrm{He}}$)	$^{+27}_{-42}$% (± 10-20x)	$^{+63}_{-70}$% (± 10-30x)	[121, 4, 2]
DM model uncertainties	N/A	≈ 1000%	[121]

Table 5: A list of the sizes of uncertainties involved in making predictions for antinuclei fluxes. The second and third column are describing the size of the effect on antinuclei from high energy cosmic ray collisions and from potential dark matter annihilations, respectively.

Another important uncertainty is the model dependence of the transparency, specifically the dark matter mass and annihilation channel dependence. This effect can be seen in the bottom panels of figure 69. When comparing the transparencies associated with different dark matter mass assumptions for the W^+W^-channel, the momentum dependence of the transparency at high energies varies greatly. For higher dark matter masses, the shape of the $^3\overline{\mathrm{He}}$ flux is more similar to the secondary flux than to the flux with the standard m_χ assumption of ≈100GeV/c^2. This results in a transparency which is very similar in both shape and magnitude to the one for secondaries. For the $b\overline{b}$ channel, the difference in m_χ causes a much reduced difference in spectral shape, and the transparencies change shape more slowly with increasing m_χ. In particular for the $b\overline{b}$ channel, a significant difference still remains at low energies, which are the most interesting for indirect dark matter searches. This effect can change the transparencies at high energies from ≈50% for $m_\chi = 100\mathrm{GeV}/c^2$ to almost 90% at 2 TeV/c^2.
Another parameter which affects the transparency is the dark matter profile considered. This effect can be seen in figure 70, which shows transparencies for antideuterons from dark matter with different dark matter profiles. It shows that there is an effect depending on the dark matter profile chosen, which can be understood as the mean path length the antinuclei travel before getting to earth. The more

peaked Einasto and NFW profiles have lower transparencies, since a larger amount of antinuclei is produced close to the centre of the galaxy (i.e. further away), and this the chance of antinuclei interacting inelastically increases. This effect causes a difference in the transparency between the profiles of about 10%.

5.8 Summary of propagation of antinuclei through the galaxy

From the results in this section several conclusions can be drawn. The most impactful are the novel experimental uncertainties on the effect of the inelastic cross section on antinuclei propagation, i.e. on the transparency. These uncertainites are of the order of 15% for antihelium, and 10% for antideuterons, and thus significantly below the uncertainites from other effects, dominantly the uncertainty on the production of these antinuclei. The second conclusion is that the exact shape of the dark matter profile is a minor component in determining the normalization of antinuclei, even before possible degeneracies with antiproton limits are taken into account. This means that even though the dark matter profile is a free choice in current models, the final antinuclei fluxes are not sensitive to this. The choice of the dark matter mass however has an important effect, both on the shape and the normalization of the resulting antinuclei spectrum. In particular for large WIMP masses, approaching or exceeding masses of 1 TeV, the shape of the spectrum becomes very similar to the shape of the secondary spectrum, which would make differentiation between them difficult. From the considered channels, only the Λ_b boosted channel significantly deviated from the others, and only for $^3\overline{\mathrm{He}}$, which however leaves open the possibility that other not thoroughly considered channels might influence the production of one antinucleus over another. If one were to speculate about the tentative antihelium events seen by the AMS collaboration, which are predominantly at high energies, they might originate from a heavy WIMP, with the $^3\overline{\mathrm{He}}$ production significantly boosted relative to antiproton and antideuteron productions, through some unknown mechanism. What is clear however, is that unraveling the mysteries of such a signal could do wonders for our understanding of antinuclei sources in our galaxy, and might even expose new physics.

5.9 Experiments to detect antinuclei in the cosmos

Given their rarity, antinuclei in cosmic rays are difficult to detect.

Detecting antinuclei in cosmic rays has to be done near the top of our atmosphere, since antinuclei would annihilate well before reaching any ground-based detector. This leaves either space bourne experiments or high-altitude balloon flights. Currently there are two promising experiments either currently or soon to be deployed: the Alpha Magnetic Spectrometer (AMS) [173] on the international space

station (ISS), and the General AntiParticle Spectrometer (GAPS) [148, 174], which is a planned balloon flight experiment. The two are shortly discussed below.

The experiment which currently has the best sensitivity for detecting antinuclei is AMS-02, which is a magnetic spectrometer on the international space station. As a magnetic spectrometer, AMS-02 is more sensitive to charge differences, and therefore more sensitive to $^3\overline{\text{He}}$ nuclei than to antideuterons, since the latter need to be distinguished from the significalty more abundant antiprotons. However, it is still a big surprise that AMS has reported potential signals consistent with multiple $^3\overline{\text{He}}$ nuclei, given that none of the currently available models predict a flux within the sensitivity of AMS, much less an order of magnitude above. These reports have cause a large amount of effort from both experimental and theoretical communities to come up with theories which might explain this signal, while also taking into account the lack of evidence for an antideuteron signal. It is currently unclear which process would produce such a large $^3\overline{\text{He}}$ flux without boosting the antideuteron flux in a similar amount, with some suggested options being a boost to $^3\overline{\text{He}}$ production via Λ_b decays [144].
The current generation of the AMS experiment – AMS-02 – has been studying cosmic rays since 2011, having analyzed over 200 billion cosmic-ray events. It consists of several detector systems, including a Time-of-Flight detector, a silicon tracker, a star tracker (to determine its orientation), a transition radiation detector, a permanent magnet to curve charged particle tracks, a Cherenkov detector and an electromagnetic calorimeter. AMS has delivered incredibly precise data on cosmic ray spectra of nuclei up to heavy elements, as well for electrons, positrons and antiprotons. In particular the antiproton spectra have been studies extensively for hints of WIMP dark matter decays, as was already discussed in section 5.1.2.
The "smoking gun" signal which AMS could detect from exotic physics such as dark matter would of course be an antinuclei signal. However, as can be seen from the fluxes in figure 69, it is not yet clear what source could feasibly reach AMS-02 sensitivities, although several models could do so within all their uncertainties. Therefore it is extremely interesting that AMS has repeatedly reported the observation of multiple possible high-energy $^3\overline{\text{He}}$ and $^4\overline{\text{He}}$ events [117, 118], but as of now these findings have not been published, only presented in talks. The results from one such talk are shown in figure 71. These events have kinetic energies per nucleon above 10 GeV/c. Should the observed signals indeed be from antihelium nuclei, it comes with a few puzzling questions. Why is the flux so much greater than expected? This increase is possible within uncertainties to be the result of high-energy cosmic-ray collisions, but only under the most favorable conditions. They are also significantly above the expected flux of most dark matter models, however as shown by the study of the $\overline{\Lambda}_b$ boosted $^3\overline{\text{He}}$ flux from dark matter annihilations, some dark matter models could fea-

sibly reproduce these results. One study has concluded that the only standard model process that could plausibly produce such a flux would be an antistar within 1 kpc of earth [122, 123]. This would however be very visible from gamma-ray observations, as the large amounts of antimatter–matter annihilations would produce a distinct signal in the gamma-ray spectrum. As such, a confirmation of the reported signals would suggest a source beyond the standard model. One possible explanation would be dark matter, where the production of antinuclei is boosted by channels not yet considered. One such example is the recent study on antinuclei production through the $\overline{\Lambda_b}$ channel [144]. The second question these findings raise is the scaling of the antinuclei production with each additional nucleon. The number of $^3\overline{\text{He}}$ to $^4\overline{\text{He}}$ events observed suggest a ratio close to 1:3, whereas for production in small systems at the LHC the penalty factor is 1:1000 [72]. The final question – and perhaps the easiest to answer – is why 10 possible $^3\overline{\text{He}}$ events have been observed while AMS has so far only seen 7 possible antideuteron events [119]. The most likely explanation for this question is simply that differentiating antideuterons from antiprotons is very difficult, as they have the same charge. The background from the antiproton signal might therefore simply cover the sensitivity to an antideuteron flux.

The current generation of the AMS experiment will hopefully continue to deliver data for years to come - and is even currently being upgraded in order to improve the accuracy of their antiproton measurements - however, planning for the next generation is already ongoing. This next generation experiment is called AMS-100, due to its planned acceptance of 100m^{2}sr [175]. It will be a satellite experiment located at Lagrange point 2 of the Sun–Earth system, using many of the same technologies and systems as the James Webb Space Telescope (JWST). AMS-100 would have a 1000 fold increase in acceptance compared to AMS-02, and be able to deal with rigidities up to 100 TV (AMS-02 up to 2 TV). It will also employ a greater magnetic field, using high-temperature superconductors [175]. As such, it is expected to deliver more precise measurements of antinuclei in cosmic rays, and thus to shine light on the questions posed by current measurements.

GAPS is a more specialised detector, focused less on measuring all kinds of cosmic rays but rather specializing on detecting annihilation events of antimatter. It works based on an outer "umbrella" of TOF detectors around a Si tracker, in order to identify such annihilation events. The setup is shown in figure 72. A novel technique is used to detect annihilations, called the "exotic atom" technique, which is outlines in figure 72. The antiparticle travelling through the detector will loose energy due to Bethe–Bloch ionization until it stops, at which point it will displace an electron in an atom to form an exotic atom with near unit probability. The radiative decay of such an exited atom can be uniquely matched to the components of the exotic atom

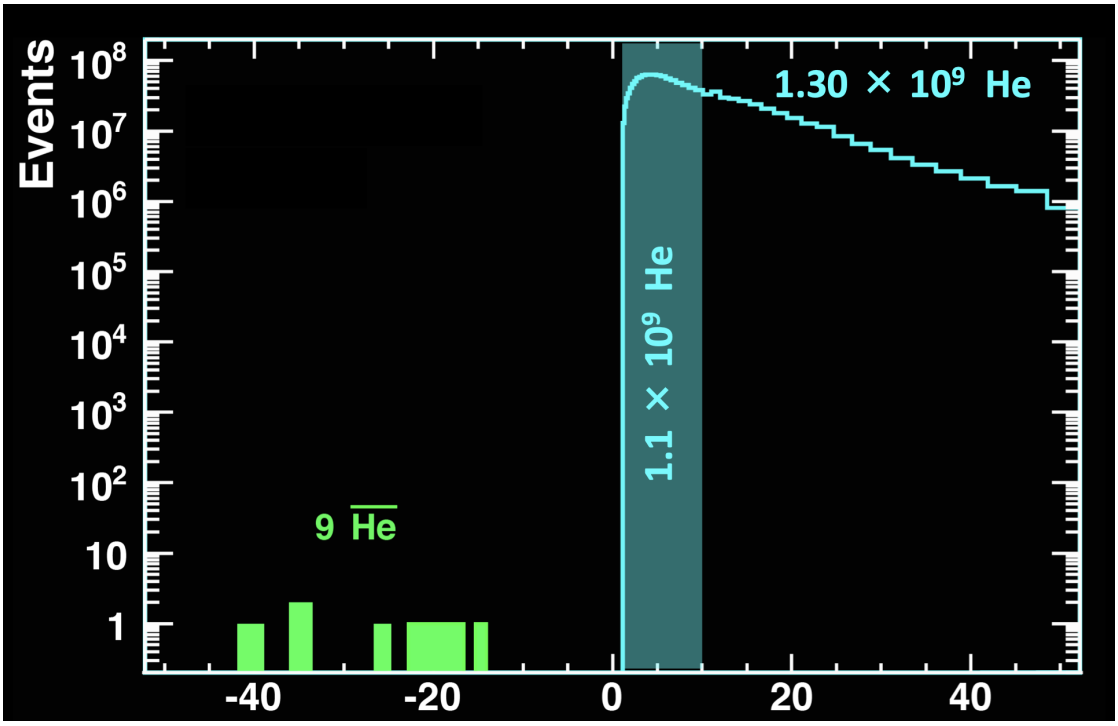


Figure 71: Plot of the rigidity resolution of AMS for comparing $^3\overline{\text{He}}$ and ^{3}He signals. 9 possible $^3\overline{\text{He}}$ events are shown. These findings have not yet been published and this figure is taken from a talk [119].

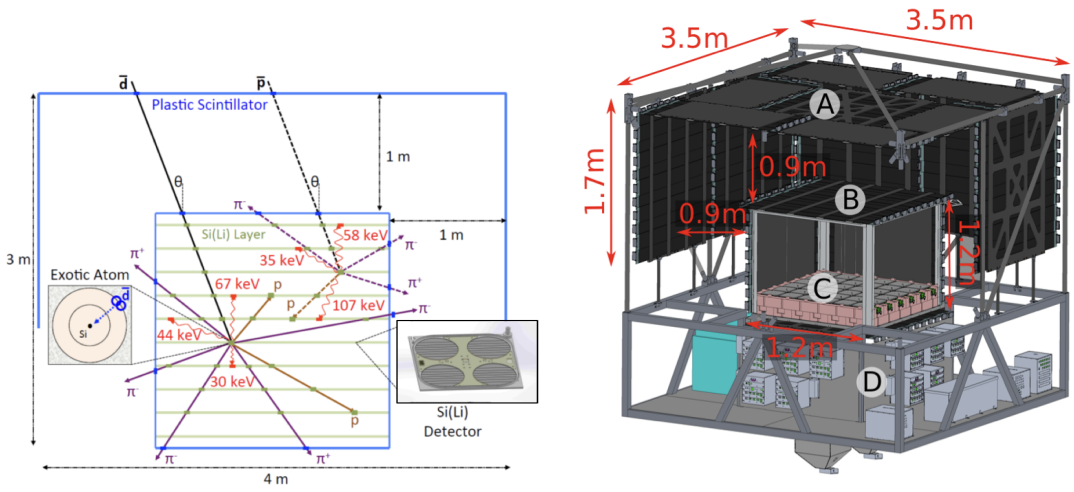


Figure 72: (Left) GAPS antiparticle detection method: antiparticles slow down and stop in the Si(Li) target, forming an exotic atom. Atomic X-rays will be emitted as it de-excites, followed by the pion (and proton) emission from nuclear annihilation. $\overline{\text{d}}/\overline{\text{p}}$ identification is based on (1) the stopping range, (2) the pion and proton multiplicity, (3) the atomic X-rays energies. Figure and caption taken from [174]. (Right) The GAPS detector, the central tracker (C) is surrounded by the inner ("cube", B) and outer ("umbrella", A) TOF layers. The readout electronics, flight computer, ballast and other support infrastructure are located underneath the tracker (D). Solar panels, cooling systems, antennae and thermal insulation are not shown for clarity. Figure and description taken from [148].

[148]. GAPS will fly over the south pole, where the effects from earth's magnetic field are minimal. The benefit of antinuclei detection via balloon bourne experiments over satellite bourne ones is the much reduced costs.

The main goal of GAPS is to measure low-energy antideuteron flux, or to improve on the current upper limit, and to follow up on the potential antihelium events seen by the AMS Collaboration. GAPS reach extends to lower energies than those probed by AMS, making such searches complementary. The expected sensitivity to antideuterons of GAPS is shown in figure 68, compared with AMS upper limits. As can be seen, the sensitivities are comparable, but GAPS reaches much lower momenta, while AMS covers a much larger momentum span. The shown antideuteron fluxes in figure 68 do not reach the GAPS sesitivities, however, within the uncertainties outlined in table 5, they can indeed reach the GAPS sensitivities. Therefore, a null observation by GAPS would help to constrain current models. GAPS is also acting as a pathfinder future balloon experiments by demonstrating such new technologies,

and their usefulness for specific searches.

6 Final remarks and outlook

The use the ALICE detector material as a target for measuring antinuclei annihilations by means of their inelastic cross sections has proven a fruitful way to conduct these otherwise challenging measurements. Yet the potential of these measurement techniques is far from exhausted. In this section I want to highlight what has already been achieved (not just by me in this thesis, but also by other works), and talk about the progress still to come.

6.1 Measurements of the inelastic cross sections of antinuclei

The full list of the inelastic cross section measurements using both the antiparticle-to-particle method and the TOF-to-TPC method are shown in figure 73. For antideuterons, this represents the first low energy measurement of the inelastic cross section, while for $^3\overline{\mathrm{He}}$ and $^3\overline{\mathrm{H}}$ it is the very first measurement of the inelastic cross sections ever. In the upcoming Run 3 and Run 4 data taking campaigns at the LHC, we will be able to drastically reduce the statistical uncertainties dominating for the $A = 3$ antinuclei, and hopefully extend this set of measurements to $A = 4$ antinuclei. Indeed, in Run 3 the expected increase in statistics for Pb–Pb collisions is a factor 100. Considering the penalty factor per additional nucleon in Pb–Pb collisions, this would result in statistical uncertainties for the measurement of the inelastic cross sections of $A = 4$ antinuclei only $\sqrt{3.5}$ times larger than the uncertainties on the $A = 3$ results already measured, making such measurements highly feasible. Additionally, by updating studies on the material budget and improving our secondary distributions in Monte Carlo, the statistical uncertainties are expected to be significantly reduced, so that hopefully we will be able to make precision measurements of these cross sections. Furthermore, there are plans to include a target material in the ALICE detector, in order to probe the annihilation of particles on different materials directly. With this exciting experimental development – and the ever improving understanding of the nature of the strong force due to femtoscopy measurements [176] we hope to inspire new theoretical work on the topic of antinuclei annihilations, and maybe finally even a theoretical framework to describe its low energy behavior.

6.2 Use of these measurements

In nuclear physics, the principal use of these cross sections is twofold. The first use is a more accurate description of antinuclei propagation using Geant4, once the Geant4 parameterizations are adjusted with these new results. Additionally, these measurements allow the assignment of an experimental uncertainty due to these

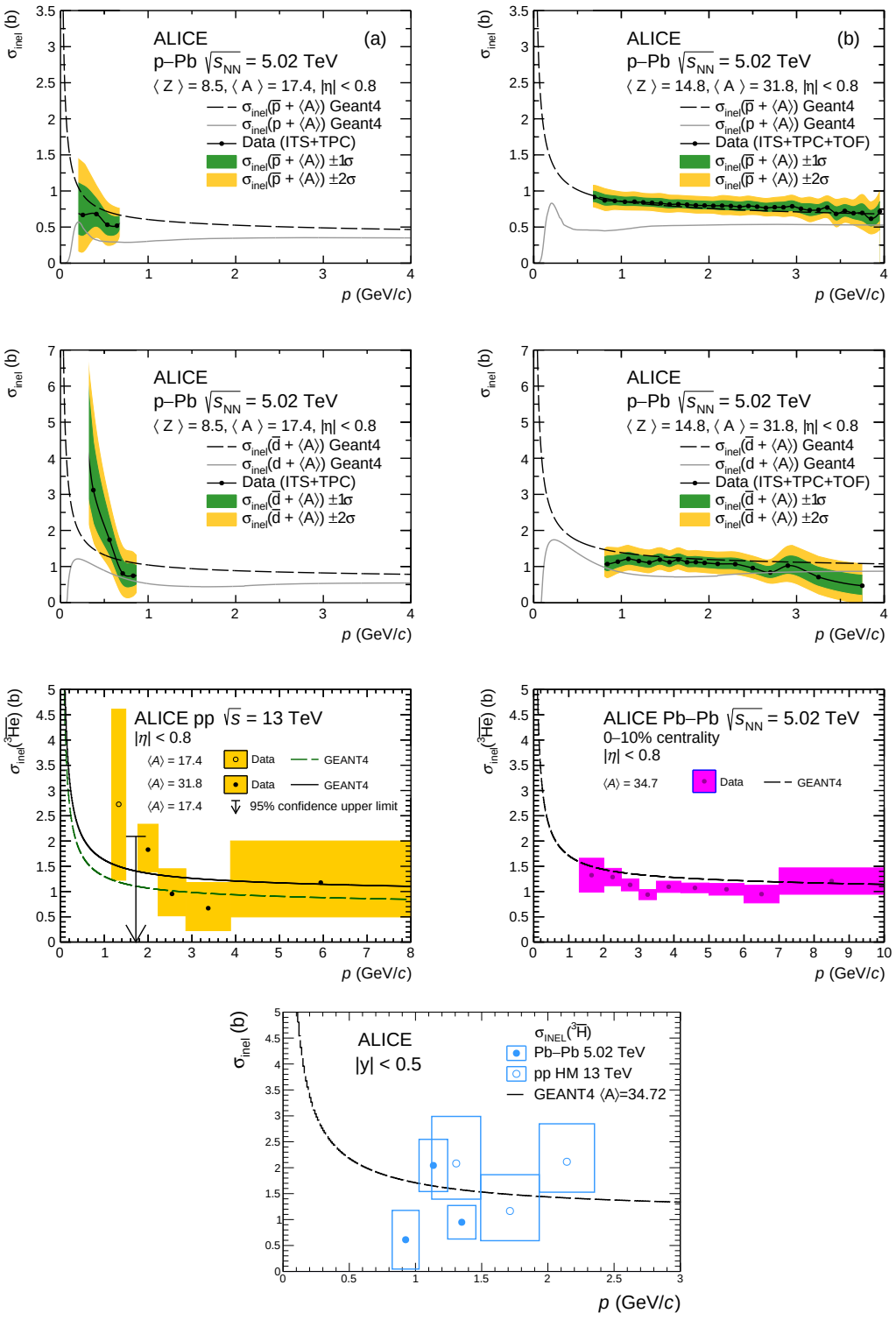


Figure 73: The inelastic cross section measurements for the antinuclei from $A = 1$ to $A = 3$, as measured by ALICE in [105, 110] and in an upcoming publication on $^3\overline{\mathrm{H}}$.

measurements. Ideally, this would allow the study of antinuclei production to lower momenta than is currently common practice [177, 178, 179, 180, 181, 182]. The second use is a new probe into the isospin dependence of the strong force, using two charged particles in $^3\overline{\text{He}}$ and $^3\overline{\text{H}}$. With future precision measurements, any possible discrepancy between these isospin partners will complement existing studies using the antiproton and antineutron inelastic cross sections [183].

But the main use of these measurements is in another field: astrophysical dark matter searches using antinuclei. The work done as part of this thesis has shown the effect of the annihilation on the expected antinuclei fluxes and determined an experimental uncertainty on the transparency of our galaxy to $^3\overline{\text{He}}$ from a variety of sources. The inelastic cross section can also be used by the experiments looking for $^3\overline{\text{He}}$, to calculate their own efficiency for detection.
We eagerly await the publication of the tentative $^3\overline{\text{He}}$ -like events seen by the AMS-02 experiment, and if confirmed hope that this work will help interpret such a remarkable flux of antinuclei.

6.3 Reevaluating physical and experimental effects on the cosmic antideuteron flux and its uncertainties

Finally, the cosmic antideuteron flux was reevaluated, in collaboration with theoreticians and astrophysicists from the GAPS experiment. This included a detailed discussion of sources (the dark matter sources were discussed in detail in section 5, for a more detailed discussion of the cosmic ray background, please see [121]), and propagation; as well as a discussion of the degeneracies between constraints of the two. This has highlighted the importance of a rigorous treatment of propagation, and of performing a full chain analysis when fitting data (such as the cosmic ray antiproton "excess"; the constraints coming from such fits are highly model dependent).

Current generation experiments seem to already be able to measure some antinuclei events, which presents an interesting challenge for theoretical models. Either way either current or next generation experiments should shine a light on cosmic ray antinuclei, and morph any discussion on the uncertainties affecting their fluxed from a theoretical exercise to an experimental necessity.

6.4 Outlook

In short, the future of antinuclei inelastic cross section measurement is one of improving upon these first measurements by measuring with higher precision, and many different target materials. Additionally, the $^{4}\overline{\mathrm{He}}$ is a final important piece for astrophysical studies. This will also allow testing the differences between the $^{3}\overline{\mathrm{He}}$ and $^{3}\overline{\mathrm{H}}$ inelastic cross sections, which can take into account isospin dependence and size effects.

And as antinuclei searches in space are getting ever closer to the detection of an antinuclei signal, the importance of nuclear physics studies as input for theoretical predictions becomes ever more important. The crown jewel would be the detection of an antinuclei signal far from expectations of high energy cosmic ray collisions, which would signal new and exciting physics in any case. And maybe even a first look into the nature of dark matter.

7 Appendix

7.1 Current status of the evidence for and against (but mostly against) the existence of anti-stars

As has been covered plenty already in this thesis, one of the biggest remaining mysteries in physics is the asymmetry between the amount of matter and antimatter present in our universe. It is thought that up to 95% of luminous matter consists of matter rather than antimatter. But how can it be known that another star is not entirely comprised of antimatter, given that the only difference in particles is their electric charge? The answer lies in the fact that even though structures within our galaxy and even universe are filled with only extremely low densities, they are not actually empty. It therefore stands to reason that if there were a region dominated by antimatter (even just a single anti-star, although a larger region seems more likely), such a region would eventually have to end and come in contact with a matter dominated region. In this volume of overlap, antimatter-matter annihilations would occur abundantly, resulting in a significant amount of high energy gamma rays. Such a specific and localized signal should be relatively easy to detect with dedicated gamma ray surveys, such as FermiLAT [127]. The lack of any evidence thereof suggests that there are no large antimatter dominated regions, and thus no anti-stars.

7.2 Why the statistical hadronization model is not used for calculating (anti)nuclei yields from WIMP dark matter annihilations

The statistical hadronization model (SHM) [184] is the idea that particles are produced in thermal equilibrium, and is able to predict the yields of particles over many order of magnitudes based on a single parameter: the temperature. However, the model does not predict the correlations in momentum space or the spectra of antinuclei. This causes several problems when attempting to use the SHM for the prediction of antinuclei from WIMP dark matter. The first is the fact that the spectra of produced antinuclei is very relevant for their propagation and for the signal to background ratio in this detection channel. Furthermore, the lack of any indication of the temperature of this process makes it highly challenging to predict the yields produced.

References

[1] M. Cirelli, G. Corcella, A. Hektor, G. Hütsi, M. Kadastik, P. Panci, M. Raidal, F. Sala, and A. Strumia, "PPPC 4 DM ID: a poor particle physicist cookbook for dark matter indirect detection," *Journal of Cosmology and Astroparticle Physics*, vol. 2011, pp. 051–051, mar 2011.

[2] M. Korsmeier, F. Donato, and N. Fornengo, "Prospects to verify a possible dark matter hint in cosmic antiprotons with antideuterons and antihelium," *Phys. Rev.*, vol. D97, no. 10, p. 103011, 2018.

[3] P. von Doetinchem *et al.*, "Cosmic-ray Antinuclei as Messengers of New Physics: Status and Outlook for the New Decade," 2 2020.

[4] A. Ibarra and S. Wild, "Prospects of antideuteron detection from dark matter annihilations or decays at AMS-02 and GAPS," *JCAP*, vol. 1302, p. 021, 2013.

[5] J. Schwichtenberg, *Physics from Symmetry*. Springer, 2018.

[6] E. Eichten, K. Gottfried, T. Kinoshita, J. Kogut, K. D. Lane, and T. M. Yan, "Spectrum of charmed quark-antiquark bound states," *Phys. Rev. Lett.*, vol. 34, pp. 369–372, Feb 1975.

[7] G. Parisi, R. Petronzio, and F. Rapuano, "A measurement of the string tension near the continuum limit," *Physics Letters B*, vol. 128, no. 6, pp. 418–420, 1983.

[8] "Quark confinement graphic." https://en.wikipedia.org/wiki/File:Quark_confinement.svg. Accessed: 2022-11-07.

[9] E. Noether, "Invariante variationsprobleme," *Nachrichten von der Gesellschaft der Wissenschaften zu Göttingen, Mathematisch-Physikalische Klasse*, vol. 1918, pp. 235–257, 1918.

[10] A. Pich, "CP violation; 1993 ed.," *ICTP Ser. Theor. Phys.*, vol. 10, pp. 14–42, 1993.

[11] J. H. Christenson, J. W. Cronin, V. L. Fitch, and R. Turlay, "Evidence for the 2π decay of the k_2^0 meson," *Phys. Rev. Lett.*, vol. 13, pp. 138–140, Jul 1964.

[12] A. Alavi-Harati, I. F. Albuquerque, T. Alexopoulos, M. Arenton, K. Arisaka, S. Averitte, A. R. Barker, L. Bellantoni, A. Bellavance, J. Belz, R. Ben-David, D. R. Bergman, E. Blucher, G. J. Bock, C. Bown, S. Bright, E. Cheu, S. Childress, R. Coleman, M. D. Corcoran, G. Corti, B. Cox, M. B. Crisler, A. R. Erwin, R. Ford, A. Glazov, A. Golossanov, G. Graham, J. Graham, K. Hagan, E. Halkiadakis, K. Hanagaki, S. Hidaka, Y. B. Hsiung, V. Jejer, J. Jennings, D. A. Jensen,

R. Kessler, H. G. E. Kobrak, J. LaDue, A. Lath, A. Ledovskoy, P. L. McBride, A. P. McManus, P. Mikelsons, E. Monnier, T. Nakaya, U. Nauenberg, K. S. Nelson, H. Nguyen, V. O'Dell, M. Pang, R. Pordes, V. Prasad, C. Qiao, B. Quinn, E. J. Ramberg, R. E. Ray, A. Roodman, M. Sadamoto, S. Schnetzer, K. Senyo, P. Shanahan, P. S. Shawhan, W. Slater, N. Solomey, S. V. Somalwar, R. L. Stone, I. Suzuki, E. C. Swallow, R. A. Swanson, S. A. Taegar, R. J. Tesarek, G. B. Thomson, P. A. Toale, A. Tripathi, R. Tschirhart, Y. W. Wah, J. Wang, H. B. White, J. Whitmore, B. Winstein, R. Winston, J.-Y. Wu, T. Yamanaka, and E. D. Zimmerman, "Observation of direct cp violation in k_s^0 decays," *Physical Review Letters*, vol. 83, pp. 22–27, jul 1999.

[13] R. Aaij and et.al., "First observation of cp violation in the decays of b_s^0 mesons," *Physical Review Letters*, vol. 110, may 2013.

[14] R. Aaij and et.al., "Observation of cp violation in charm decays," *Physical Review Letters*, vol. 122, may 2019.

[15] V. A. Kostelecký and N. Russell, "Data tables for lorentz and cp violation," *Reviews of Modern Physics*, vol. 83, pp. 11–31, mar 2011.

[16] A. Kostelecky, "The status of cpt," 1998.

[17] G. 't Hooft, "Computation of the quantum effects due to a four-dimensional pseudoparticle," *Phys. Rev. D*, vol. 14, pp. 3432–3450, Dec 1976.

[18] K. Choi, S. H. Im, and C. S. Shin, "Recent progress in the physics of axions and axion-like particles," *Annual Review of Nuclear and Particle Science*, vol. 71, pp. 225–252, sep 2021.

[19] D. A. Kirzhnits and A. D. Linde, "Macroscopic Consequences of the Weinberg Model," *Phys. Lett. B*, vol. 42, pp. 471–474, 1972.

[20] L. C. P. Van Hove, "Theoretical prediction of a new state of matter, the "quark-gluon plasma" (also called "quark matter")," 1987.

[21] P. Braun-Munzinger, V. Koch, T. Schäfer, and J. Stachel, "Properties of hot and dense matter from relativistic heavy ion collisions," *Physics Reports*, vol. 621, pp. 76–126, mar 2016.

[22] "Timeline of the universe." https://map.gsfc.nasa.gov/media/060915/index.html. NASA, Accessed: 2022-11-07.

[23] A. Ibarra, "Neutrinos and dark matter," *AIP Conference Proceedings*, vol. 1666, no. 1, p. 140004, 2015.

[24] K. M. Ferriè re, "The interstellar environment of our galaxy," *Reviews of Modern Physics*, vol. 73, pp. 1031–1066, dec 2001.

[25] F. Nicastro, S. Mathur, and M. Elvis, "Missing baryons and the warm-hot intergalactic medium," *Science*, vol. 319, pp. 55–57, jan 2008.

[26] V. Schönfelder, "Gamma ray astronomy and search for antimatter in the universe," *Hyperfine Interactions*, vol. 44, pp. 85–96, Mar 1989.

[27] R. Aaij and et. al., "Measurement of CP asymmetry in d0→k-k decays," *Physics Letters B*, vol. 767, pp. 177–187, apr 2017.

[28] M. Ahmadi, et. al., and T. A. Collaboration, "Investigation of the fine structure of antihydrogen," *Nature*, vol. 578, pp. 375–380, Feb 2020.

[29] A. D. Sakharov, "Violation of CP Invariance, C asymmetry, and baryon asymmetry of the universe," *Pisma Zh. Eksp. Teor. Fiz.*, vol. 5, pp. 32–35, 1967.

[30] G. R. Farrar and M. E. Shaposhnikov, "Baryon asymmetry of the universe in the minimal standard model," *Physical Review Letters*, vol. 70, pp. 2833–2836, may 1993.

[31] A. Santamaria, "Masses, mixings, yukawa couplings and their symmetries," *Physics Letters B*, vol. 305, no. 1, pp. 90–97, 1993.

[32] V. Q. Phong, P. H. Khiem, N. P. D. Loc, and H. N. Long, "Sphaleron in the first-order electroweak phase transition with the dimension-six higgs field operator," *Physical Review D*, vol. 101, jun 2020.

[33] A. Papaefstathiou, S. Plätzer, and K. Sakurai, "On the phenomenology of sphaleron-induced processes at the LHC and beyond," *Journal of High Energy Physics*, vol. 2019, dec 2019.

[34] J.-M. Richard, "Antiproton physics," *Frontiers in Physics*, vol. 8, jan 2020.

[35] B. El-Bennich, M. Lacombe, B. Loiseau, and S. Wycech, "Paris $n\overline{N}$ potential constrained by recent antiprotonic-atom data and $\overline{n}p$ total cross sections," *Phys. Rev. C*, vol. 79, p. 054001, May 2009.

[36] L. C. Tan and L. K. Ng, "Calculation of the equilibrium antiproton spectrum," *Journal of Physics G: Nuclear Physics*, vol. 9, p. 227, feb 1983.

[37] A. Galoyan, A. Ribon, and V. Uzhinsky, "Dynamics of Anti-Proton–Protons and Anti-Proton–Nucleus Reactions," *Nucl. Theor.*, vol. 35, pp. 194–202, 2016.

[38] A. Galoyan, "Dynamics of interactions of anti-protons and anti-nuclei with nuclei in Geant4," *PoS*, vol. BaldinISHEPPXXII, p. 049, 2015.

[39] T. Regge, "Introduction to complex orbital momenta," *Il Nuovo Cimento (1955-1965)*, vol. 14, pp. 951–976, Dec 1959.

[40] V. Flaminio, W. G. Moorhead, D. R. O. Morrison, and N. Rivoire, *Compilation of cross-sections*. Geneva: CERN, 1984. Updated version of CERN HERA 79-03; contains all data published up to the beginning of 1982.

[41] C. Amsler and F. Myhrer, "Low energy antiproton physics," *Annual Review of Nuclear and Particle Science*, vol. 41, no. 1, pp. 219–267, 1991.

[42] V. Franco and R. J. Glauber, "High-energy deuteron cross sections," *Phys. Rev.*, vol. 142, pp. 1195–1214, Feb 1966.

[43] V. Grichine, "Integral cross-sections of light nuclei in the glauber-gribov representation," *Nuclear Instruments and Methods in Physics Research Section B: Beam Interactions with Materials and Atoms*, vol. 427, pp. 60–62, 2018.

[44] V. Uzhinsky, J. Apostolakis, A. Galoyan, G. Folger, V. Grichine, V. Ivanchenko, and D. Wright, "Antinucleus–nucleus cross sections implemented in geant4," *Physics Letters B*, vol. 705, no. 3, pp. 235–239, 2011.

[45] S. P. Denisov *et al.*, "Measurements of anti-deuteron absorption and stripping cross sections at the momentum 13.3 GeV/c," *Nucl. Phys.*, vol. B31, pp. 253–260, 1971.

[46] F. G. Binon *et al.*, "Absorption cross-sections of 25 GeV/c antideuterons in Li, C, Al, Cu and Pb," *Phys. Lett.*, vol. 31B, pp. 230–232, 1970.

[47] V. Uzhinsky *et al.*, "Antinucleus-nucleus cross sections implemented in GEANT4," *Phys. Lett.*, vol. B705, pp. 235–239, 2011.

[48] S. Acharya *et al.*, "Production of ^{4}He and $^4\overline{\mathrm{He}}$ in Pb-Pb collisions at $\sqrt{s_{\mathrm{NN}}} =$ 2.76 TeV at the LHC," *Nucl. Phys.*, vol. A971, pp. 1–20, 2018.

[49] M. Kachelrieß, S. Ostapchenko, and J. Tjemsland, "Alternative coalescence model for deuteron, tritium, helium-3 and their antinuclei," *Eur. Phys. J. A*, vol. 56, no. 1, p. 4, 2020.

[50] K. Blum and M. Takimoto, "Nuclear coalescence from correlation functions," *Physical Review C*, vol. 99, apr 2019.

[51] S. Acharya and et. al., "Production of light (anti)nuclei in pp collisions at $$ \sqrt{s} $$ = 13 TeV," *Journal of High Energy Physics*, vol. 2022, jan 2022.

[52] M. Kachelriess, S. Ostapchenko, and J. Tjemsland, "Revisiting cosmic ray antinuclei fluxes with a new coalescence mode," 2020.

[53] L. Zhu, C. M. Ko, and X. Yin, "Light (anti-)nuclei production and flow in relativistic heavy-ion collisions," *Phys. Rev. C*, vol. 92, p. 064911, Dec 2015.

[54] C. D. Anderson, "The apparent existence of easily deflectable positives," *Science*, vol. 76, no. 1967, pp. 238–239, 1932.

[55] R. L. Golden, S. Horan, B. G. Mauger, G. D. Badhwar, J. L. Lacy, S. A. Stephens, R. R. Daniel, and J. E. Zipse, "Evidence for the existence of cosmic-ray antiprotons," *Phys. Rev. Lett.*, vol. 43, pp. 1196–1199, Oct 1979.

[56] E. A. Bogomolov, N. D. Lubyanaya, V. A. Romanov, S. V. Stepanov, and M. S. Shulakova, "A STRATOSPHERIC MAGNETIC SPECTROMETER INVESTIGATION OF THE SINGLY CHARGED COMPONENT SPECTRA AND COMPOSITION OF THE PRIMARY AND SECONDARY COSMIC RADIATION.," in *16th International Cosmic Ray Conference*, pp. 330–335, 1979.

[57] P. von Doetinchem, K. Perez, T. Aramaki, S. Baker, S. Barwick, R. Bird, M. Boezio, S. Boggs, M. Cui, A. Datta, F. Donato, C. Evoli, L. Fabris, L. Fabbietti, E. F. Bueno, N. Fornengo, H. Fuke, C. Gerrity, D. G. Coral, C. Hailey, D. Hooper, M. Kachelriess, M. Korsmeier, M. Kozai, R. Lea, N. Li, A. Lowell, M. Manghisoni, I. Moskalenko, R. Munini, M. Naskret, T. Nelson, K. Ng, F. Nozzoli, A. Oliva, R. Ong, G. Osteria, T. Pierog, V. Poulin, S. Profumo, T. Pöschl, S. Quinn, V. Re, F. Rogers, J. Ryan, N. Saffold, K. Sakai, P. Salati, S. Schael, L. Serksnyte, A. Shukla, A. Stoessl, J. Tjemsland, E. Vannuccini, M. Vecchi, M. Winkler, D. Wright, M. Xiao, W. Xu, T. Yoshida, G. Zampa, and P. Zuccon, "Cosmic-ray antinuclei as messengers of new physics: status and outlook for the new decade," *Journal of Cosmology and Astroparticle Physics*, vol. 2020, pp. 035–035, aug 2020.

[58] M. Hütten and D. Kerszberg, "TeV dark matter searches in the extragalactic gamma-ray sky," *Galaxies*, vol. 10, p. 92, aug 2022.

[59] F. Calore, M. Cirelli, L. DEROME, Y. Genolini, D. Maurin, P. Salati, and P. D. Serpico, "AMS-02 antiprotons and dark matter: Trimmed hints and robust bounds," *SciPost Physics*, vol. 12, may 2022.

[60] J. Heisig, M. Korsmeier, and M. W. Winkler, "Dark matter or correlated errors: Systematics of the AMS-02 antiproton excess," *Physical Review Research*, vol. 2, oct 2020.

[61] N. Xu, "An overview of STAR experimental results," *Nuclear Physics A*, vol. 931, pp. 1–12, nov 2014.

[62] M. J. Boschini *et al.*, "Solution of heliospheric propagation: unveiling the local interstellar spectra of cosmic ray species," *Astrophys. J.*, vol. 840, no. 2, p. 115, 2017.

[63] M. J. Boschini *et al.*, "Deciphering the Local Interstellar Spectra of Primary Cosmic-Ray Species with HelMod," *Astrophys. J.*, vol. 858, no. 1, p. 61, 2018.

[64] T. Massam, T. Müller, B. Righini, M. Schneegans, and A. Zichichi, "Experimental observation of antideuteron production," *Nuovo Cimento*, vol. 39, pp. 10–14, 1965.

[65] S. Acharya *et al.*, "Production of light (anti)nuclei in pp collisions at $\sqrt{s} = 13$ TeV," *JHEP*, vol. 01, p. 106, 2022.

[66] S. Acharya *et al.*, "Production of light (anti)nuclei in pp collisions at $\sqrt{s} = 5.02$ TeV," 12 2021.

[67] J. Adam *et al.*, "Production of light nuclei and anti-nuclei in pp and Pb-Pb collisions at energies available at the CERN Large Hadron Collider," *Phys. Rev.*, vol. C93, no. 2, p. 024917, 2016.

[68] S. Acharya *et al.*, "Production of deuterons, tritons, ^{3}He nuclei and their antinuclei in pp collisions at $\sqrt{s} = 0.9$, 2.76 and 7 TeV," *Phys. Rev.*, vol. C97, no. 2, p. 024615, 2018.

[69] Y.-G. Ma, "Observation of antimatter nuclei at rhic-star," *Journal of Physics: Conference Series*, vol. 420, p. 012036, mar 2013.

[70] K. Aamodt and et.al., "Midrapidity antiproton-to-proton ratio in pp collisons at $\sqrt{s} = 0.9$ and 7 tev measured by the alice experiment," *Phys. Rev. Lett.*, vol. 105, p. 072002, Aug 2010.

[71] E. Abbas and T. A. Collaboration, "Mid-rapidity anti-baryon to baryon ratios in pp collisions at $\sqrt{s} = 0.9/2.76$ and 7 tev measured by alice," *The European Physical Journal C*, vol. 73, p. 2496, Jul 2013.

[72] S. Acharya and et. al., "Multiplicity dependence of light (anti-)nuclei production in p–pb collisions at snn=5.02 tev," *Physics Letters B*, vol. 800, p. 135043, 2020.

[73] F. Zwicky *Helvetica Physica Acta*, vol. 6, pp. 110–127, 1933.

[74] R. L. Workman and Others, "Review of Particle Physics," *PTEP*, vol. 2022, p. 083C01, 2022.

[75] T. C. Planck vol. 641, p. A6, sep 2020.

[76] J. G. de Swart, G. Bertone, and J. van Dongen, "How dark matter came to matter," *Nature Astronomy*, vol. 1, mar 2017.

[77] J. P. Ostriker, P. J. E. Peebles, and A. Yahil, "The Size and Mass of Galaxies, and the Mass of the Universe," , vol. 193, p. L1, Oct. 1974.

[78] I. Ablimit, G. Zhao, C. Flynn, and S. A. Bird, "The Rotation Curve, Mass Distribution and Dark Matter Content of the Milky Way from Classical Cepheids," *Astrophys. J.*, vol. 895, no. 1, p. L12, 2020.

[79] Y. Sofue, "Rotation and mass in the milky way and spiral galaxies," *Publications of the Astronomical Society of Japan*, vol. 69, p. R1, dec 2016.

[80] J.-P. Kneib and P. Natarajan, "Cluster lenses," *The Astronomy and Astrophysics Review*, vol. 19, nov 2011.

[81] Koppelman, Helmer H. and Helmi, Amina, "Determination of the escape velocity of the milky way using a halo sample selected based on proper motion," *A&A*, vol. 649, p. A136, 2021.

[82] S. P. Martin, "A supersymmetry primer," 1997.

[83] H. Baer, K.-Y. Choi, J. E. Kim, and L. Roszkowski, "Dark matter production in the early universe: Beyond the thermal wimp paradigm," *Physics Reports*, vol. 555, pp. 1–60, 2015. Dark matter production in the early Universe: Beyond the thermal WIMP paradigm.

[84] T. Padmanabhan, *Structure formation in the universe*. Cambridge Univ. Press, 1999.

[85] R. D. Peccei and H. R. Quinn, "CP conservation in the presence of pseudoparticles," *Phys. Rev. Lett.*, vol. 38, pp. 1440–1443, Jun 1977.

[86] S. Weinberg, "A new light boson?," *Phys. Rev. Lett.*, vol. 40, pp. 223–226, Jan 1978.

[87] M. Danilov, "Review of sterile neutrino searches at very short-baseline reactor experiments," *Physica Scripta*, vol. 97, p. 094001, aug 2022.

[88] S. W. HAWKING, "Black hole explosions?," *Nature*, vol. 248, pp. 30–31, Mar 1974.

[89] M. VISSER, "ESSENTIAL AND INESSENTIAL FEATURES OF HAWKING RADIATION," *International Journal of Modern Physics D*, vol. 12, pp. 649–661, apr 2003.

[90] E. Aprile and et.al., "Xenon1t dark matter data analysis: Signal reconstruction, calibration, and event selection," *Phys. Rev. D*, vol. 100, p. 052014, Sep 2019.

[91] S. Akerib and et.al., "Extending light WIMP searches to single scintillation photons in LUX," *Physical Review D*, vol. 101, feb 2020.

[92] P. A. M. Dirac, "Quantised singularities in the electromagnetic field„" *Proceedings of the Royal Society of London. Series A, Containing Papers of a Mathematical and Physical Character*, vol. 133, no. 821, pp. 60–72, 1931.

[93] G. Collaboration, "Final results of gerda on the search for neutrinoless double-β decay," *Phys. Rev. Lett.*, vol. 125, p. 252502, Dec 2020.

[94] T. Bringmann, P. F. Depta, M. Hufnagel, and K. Schmidt-Hoberg, "Precise dark matter relic abundance in decoupled sectors," *Physics Letters B*, vol. 817, p. 136341, jun 2021.

[95] E. Aprile and et.al., "Search for new physics in electronic recoil data from xenonnt," *Phys. Rev. Lett.*, vol. 129, p. 161805, Oct 2022.

[96] J. Conrad and O. Reimer, "Indirect dark matter searches in gamma and cosmic rays," *Nature Physics*, vol. 13, pp. 224–231, Mar 2017.

[97] T. A. Collaboration, "The alice experiment at the cern lhc," *Journal of Instrumentation*, vol. 3, p. S08002, aug 2008.

[98] J. Alme, Y. Andres, H. Appelshäuser, S. Bablok, N. Bialas, R. Bolgen, U. Bonnes, R. Bramm, P. Braun-Munzinger, R. Campagnolo, P. Christiansen, A. Dobrin, C. Engster, D. Fehlker, Y. Foka, U. Frankenfeld, J. Gaardhøje, C. Garabatos, P. Glässel, C. G. Gutierrez, P. Gros, H.-A. Gustafsson, H. Helstrup, M. Hoch, M. Ivanov, R. Janik, A. Junique, A. Kalweit, R. Keidel, S. Kniege, M. Kowalski, D. Larsen, Y. Lesenechal, P. Lenoir, N. Lindegaard, C. Lippmann, M. Mager, M. Mast, A. Matyja, M. Munkejord, L. Musa, B. Nielsen, V. Nikolic, H. Oeschler,

E. Olsen, A. Oskarsson, L. Osterman, M. Pikna, A. Rehman, G. Renault, R. Renfordt, S. Rossegger, D. Röhrich, K. Røed, M. Richter, G. Rueshmann, A. Rybicki, H. Sann, H.-R. Schmidt, M. Siska, B. Sitár, C. Soegaard, H.-K. Soltveit, D. Soyk, J. Stachel, H. Stelzer, E. Stenlund, R. Stock, P. Strmeň, I. Szarka, K. Ullaland, D. Vranic, R. Veenhof, J. Westergaard, J. Wiechula, and B. Windelband, "The ALICE TPC, a large 3-dimensional tracking device with fast readout for ultra-high multiplicity events," *Nuclear Instruments and Methods in Physics Research Section A: Accelerators, Spectrometers, Detectors and Associated Equipment*, vol. 622, pp. 316–367, oct 2010.

[99] "Real-time data processing in the alice high level trigger at the lhc," *Computer Physics Communications*, vol. 242, pp. 25–48, 2019.

[100] *ALICE Time-Of-Flight system (TOF): Technical Design Report.* Technical design report. ALICE, Geneva: CERN, 2000.

[101] J. Adam *et al.*, "Determination of the event collision time with the ALICE detector at the LHC," *Eur. Phys. J. Plus*, vol. 132, no. 2, p. 99, 2017.

[102] K. Aamodt *et al.*, "Midrapidity antiproton-to-proton ratio in pp collisions at $\sqrt{s} = 0.9$ and 7 TeV measured by the ALICE experiment," *Phys. Rev. Lett.*, vol. 105, p. 072002, 2010.

[103] S. Agostinelli *et al.*, "GEANT4–a simulation toolkit," *Nucl. Instrum. Meth. A*, vol. 506, pp. 250–303, 2003.

[104] J. Allison *et al.*, "Recent developments in Geant4," *Nucl. Instrum. Meth. A*, vol. 835, pp. 186–225, 2016.

[105] S. Acharya *et al.*, "Measurement of the low-energy antideuteron inelastic cross section," *Phys. Rev. Lett.*, vol. 125, no. 16, p. 162001, 2020.

[106] V. Franco and R. J. Glauber, "High-energy deuteron cross sections," *Phys. Rev.*, vol. 142, pp. 1195–1214, Feb 1966.

[107] D. Morton, Q. Wu, and G. Drake, "Nuclear charge radius for he3," *Physical Review A - PHYS REV A*, vol. 73, 03 2006.

[108] E. Abbas and et.al., "Mid-rapidity anti-baryon to baryon ratios in pp collisions at $\sqrt{s} = 0.9,\ 2.76$ and 7 TeV measured by ALICE," *The European Physical Journal C*, vol. 73, jul 2013.

[109] J. H. Lambert, *Photometria sive de mensura et gradibus luminis, colorum et umbrae by Lambert, Johann Heinrich.* Augustae Vindelicorum : sumptibus viduae Eberhardi Klett typis Chistophori Petri Detleffsen, 1760.

[110] S. Acharya *et al.*, "First measurement of the absorption of $^3\overline{\mathrm{He}}$ nuclei in matter and impact on their propagation in the galaxy," 2 2022.

[111] "Performance of the ALICE experiment at the CERN LHC," *International Journal of Modern Physics A*, vol. 29, p. 1430044, sep 2014.

[112] "Modelling of Antihelium-3 Cosmic-Ray Propagation," 2022.

[113] "Validation of the ALICE material budget between TPC and TOF detectors," 2022.

[114] R. Barlow, "Systematic errors: Facts and fictions," in *Conference on Advanced Statistical Techniques in Particle Physics*, pp. 134–144, 7 2002.

[115] H. Hahn, E. Forsyth, H. Foelsche, M. Harrison, J. Kewisch, G. Parzen, S. Peggs, E. Raka, A. Ruggiero, A. Stevens, S. Tepikian, P. Thieberger, D. Trbojevic, J. Wei, E. Willen, S. Ozaki, and S. Lee, "The rhic design overview," *Nuclear Instruments and Methods in Physics Research Section A: Accelerators, Spectrometers, Detectors and Associated Equipment*, vol. 499, pp. 245–263, 03 2003.

[116] A. Collaboration, "Measurement of $^3\overline{\mathrm{He}}$ hadronic interaction cross-section in pb-pb collisions," 2021. ALICE internal Analysis note, ANA-1106.

[117] S. Ting, "The first five years of the alpha magnetic spectrometer on the international space station."

[118] J. Sokol, "Sam ting's last tease," *Science*, vol. 356, no. 6335, pp. 240–241, 2017.

[119] S. Lu, "Cosmic ray antideuteron search with alpha magnetic spectrometer (ams)," *Munich Insitute for Particle and Astrophysics - Worshop on antinuclei in cosmic rays 2022*, 2022.

[120] A. W. Strong, I. V. Moskalenko, and V. S. Ptuskin, "Cosmic-Ray Propagation and Interactions in the Galaxy," *Annual Review of Nuclear and Particle Science*, vol. 57, pp. 285–327, Nov. 2007.

[121] L. Šerkšnytė *et al.*, "Reevaluation of the cosmic antideuteron flux from cosmic-ray interactions and from exotic sources," *Phys. Rev. D*, vol. 105, no. 8, p. 083021, 2022.

[122] V. Poulin, P. Salati, I. Cholis, M. Kamionkowski, and J. Silk, "Where do the ams-02 antihelium events come from?," *Phys. Rev. D*, vol. 99, p. 023016, Jan 2019.

[123] A. Coogan and S. Profumo, "Origin of the tentative AMS antihelium events," *Physical Review D*, vol. 96, oct 2017.

[124] M. Aguilar and et. al., "Precision measurement of the boron to carbon flux ratio in cosmic rays from 1.9 gv to 2.6 tv with the alpha magnetic spectrometer on the international space station," *Phys. Rev. Lett.*, vol. 117, p. 231102, Nov 2016.

[125] D. D. Clayton, *Principles of stellar evolution and nucleosynthesis*. University of Chicago Press, 1983.

[126] E. M. Burbidge, G. R. Burbidge, W. A. Fowler, and F. Hoyle, "Synthesis of the elements in stars," *Rev. Mod. Phys.*, vol. 29, pp. 547–650, Oct 1957.

[127] T. C. FermiLAT, "Incremental Fermi Large Area Telescope Fourth Source Catalog," , vol. 260, p. 53, June 2022.

[128] T. Bringmann and C. Weniger, "Gamma ray signals from dark matter: Concepts, status and prospects," *Physics of the Dark Universe*, vol. 1, no. 1, pp. 194–217, 2012. Next Decade in Dark Matter and Dark Energy.

[129] A. Shukla, A. Datta, P. von Doetinchem, D.-M. Gomez-Coral, and C. Kanitz, "Large-scale simulations of antihelium production in cosmic-ray interactions," *Physical Review D*, vol. 102, sep 2020.

[130] D.-M. Gomez-Coral, A. M. Rocha, V. Grabski, A. Datta, P. von Doetinchem, and A. Shukla, "Deuteron and antideuteron production simulation in cosmic-ray interactions," *Physical Review D*, vol. 98, jul 2018.

[131] A. N. Diddens, W. Galbraith, E. Lillethun, G. Manning, A. G. Parham, A. E. Taylor, T. G. Walker, and A. M. Wetherell, "Particle production in proton-proton collisions at 19 and 24 gev/c," *Il Nuovo Cimento (1955-1965)*, vol. 31, pp. 961–973, Mar 1964.

[132] V. V. Abramov *et al.*, "High p_T Deuteron and Anti-deuteron Production in pp and p a Collisions at 70-GeV," *Sov. J. Nucl. Phys.*, vol. 45, p. 845, 1987.

[133] W. Bozzoli, A. Bussière, G. Giacomelli, E. Lesquoy, R. Meunier, L. Moscoso, A. Muller, F. Rimondi, and S. Zylberajch, "Production of d, t, 3he, d, t and 3he by 200 gev protons," *Nuclear Physics B*, vol. 144, no. 2, pp. 317–328, 1978.

[134] J. W. Cronin, H. J. Frisch, M. J. Shochet, J. P. Boymond, P. A. Piroué, and R. L. Sumner, "Production of hadrons at large transverse momentum at 200, 300, and 400 gev," *Phys. Rev. D*, vol. 11, pp. 3105–3123, Jun 1975.

[135] A. Bussiére, G. Giacomelli, E. Lesquoy, R. Meunier, L. Moscoso, A. Muller, F. Rimondi, S. Zucchelli, and S. Zylberajch, "Particle production and search for long-lived particles in 200–240 gev/c proton-nucleon collisions," *Nuclear Physics B*, vol. 174, no. 1, pp. 1–15, 1980.

[136] B. Alper, H. Bgild, P. Booth, F. Bulos, L. Carroll, G. von Dardel, G. Damgaard, B. Duff, F. Heymann, J. Jackson, G. Jarlskog, L. Jonsson, A. Klovning, L. Leistam, E. Lillethun, G. Lynch, G. Manning, M. Prentice, D. Quarrie, and J. Weiss, "Large angle production of stable particles heavier than the proton and a search for quarks at the cern intersecting storage rings," *Physics Letters B*, vol. 46, no. 2, pp. 265–268, 1973.

[137] W. M. Gibson, A. Duane, H. Newman, H. Ogren, S. Henning, G. Jarlskog, R. Little, T. Sanford, S. L. Wu, H. BØggild, B. G. Duff, K. Guettler, M. N. Prentice, S. J. Sharrock, and B.-S.-M. Collaboration, "Production of deuterons and antideuterons in proton-proton collisions at the cern isr," *Lettere al Nuovo Cimento (1971-1985)*, vol. 21, pp. 189–194, Feb 1978.

[138] M. Albrow, D. Barber, P. Benz, B. Bošnjaković, J. Brooks, C. Chang, A. Clegg, F. Erné, P. Kooijman, F. Loebinger, N. McCubbin, P. Murphy, A. Rudge, J. Sens, A. Sessoms, J. Singh, and J. Timmer, "Search for stable particles of charge 1 and mass deuteron mass," *Nuclear Physics B*, vol. 97, no. 2, pp. 189–200, 1975.

[139] E. Serradilla Rodríguez, *Producción de núcleos de deuterio y antideuterio en el experimento Alice del LHC*. PhD thesis, UCM, Madrid, Dept. Phys., UCM, Madrid, Dept. Phys., 2014.

[140] S. Acharya and et. al., "Production of deuterons, tritons, ^{3}He nuclei, and their antinuclei in pp collisions at $\sqrt{s} = 0.9$, 2.76, and 7 tev," *Phys. Rev. C*, vol. 97, p. 024615, Feb 2018.

[141] T. A. Collaboration, "Production of light nuclei and anti-nuclei in pp and pb-pb collisions at energies available at the cern large hadron collider," *Phys. Rev. C*, vol. 93, p. 024917, Feb 2016.

[142] T. Pöschl, *Modeling of the Galactic Cosmic-Ray Antiproton Flux and Development of a Multi-Purpose Active-Target Particle Telescope for Cosmic Rays*. Dissertation, Technische Universität München, München, 2022.

[143] F. Riek, R. Rapp, Y. Oh, and T.-S. H. Lee, "Medium modifications of themml:math xmlns:mml="http://www.w3.org/1998/math/MathML" display="inline"mml:mrowmml:mi/mml:mi/mml:mrow/mml:mathmeson in nuclear photoproduction," *Physical Review C*, vol. 82, jul 2010.

[144] M. W. Winkler and T. Linden, "Dark matter annihilation can produce a detectable antihelium flux through $\overline{\Lambda_b}$ decays," *Physical Review Letters*, vol. 126, mar 2021.

[145] C. Bierlich, S. Chakraborty, N. Desai, L. Gellersen, I. Helenius, P. Ilten, L. Lönnblad, S. Mrenna, S. Prestel, C. T. Preuss, T. Sjöstrand, P. Skands, M. Utheim, and R. Verheyen, "A comprehensive guide to the physics and usage of pythia 8.3," 2022.

[146] K. Werner, L. Karpenko, M. Bleicher, and T. Pierog, "The Physics of EPOS," *EPJ Web Conf.*, vol. 52, p. 05001, 2013.

[147] D. J. Fixsen, "The temperature of the cosmic microwave background," *The Astrophysical Journal*, vol. 707, p. 916, nov 2009.

[148] R. Bird and et. al., "Gaps: Searching for dark matter using antinuclei in cosmic rays," 2019.

[149] A. N. Baushev, "EXTRAGALACTIC DARK MATTER AND DIRECT DETECTION EXPERIMENTS," *The Astrophysical Journal*, vol. 771, p. 117, jun 2013.

[150] V. Trimble, "Existence and nature of dark matter in the universe," *Annual Review of Astronomy and Astrophysics*, vol. 25, no. 1, pp. 425–472, 1987.

[151] P. Charlot, C. S. Jacobs, D. Gordon, S. Lambert, A. de Witt, J. Böhm, A. L. Fey, R. Heinkelmann, E. Skurikhina, O. Titov, E. F. Arias, S. Bolotin, G. Bourda, C. Ma, Z. Malkin, A. Nothnagel, D. Mayer, D. S. MacMillan, T. Nilsson, and R. Gaume, "The third realization of the international celestial reference frame by very long baseline interferometry," *Astronomy &amp Astrophysics*, vol. 644, p. A159, dec 2020.

[152] J. F. Navarro, C. S. Frenk, and S. D. M. White, "The structure of cold dark matter halos," *The Astrophysical Journal*, vol. 462, p. 563, may 1996.

[153] D. Merritt, A. W. Graham, B. Moore, J. Diemand, and B. Terzić, "Empirical models for dark matter halos. i. nonparametric construction of density profiles and comparison with parametric models," *The Astronomical Journal*, vol. 132, pp. 2685–2700, jan 2006.

[154] R. Jimenez, L. Verde, and S. P. Oh, "Dark halo properties from rotation curves," *Monthly Notices of the Royal Astronomical Society*, vol. 339, pp. 243–259, feb 2003.

[155] H.-N. Lin and X. Li, "The dark matter profiles in the milky way," *Monthly Notices of the Royal Astronomical Society*, vol. 487, pp. 5679–5684, jun 2019.

[156] F. Seiterle, "Evaluation of an extragalactic dark matter component to the galactic antinuclei flux from dark matter," 2022.

[157] C. E. Aalseth and et. al., "DarkSide-20k: A 20 tonne two-phase LAr TPC for direct dark matter detection at LNGS," *The European Physical Journal Plus*, vol. 133, mar 2018.

[158] P. A. Zyla and et. al., "Review of Particle Physics," *Progress of Theoretical and Experimental Physics*, vol. 2020, 08 2020. 083C01.

[159] I. Cholis, T. Linden, and D. Hooper, "A robust excess in the cosmic-ray antiproton spectrum: Implications for annihilating dark matter," *Phys. Rev. D*, vol. 99, p. 103026, May 2019.

[160] M.-Y. Cui, X. Pan, Q. Yuan, Y.-Z. Fan, and H.-S. Zong, "Revisit of cosmic ray antiprotons from dark matter annihilation with updated constraints on the background model from AMS-02 and collider data," *Journal of Cosmology and Astroparticle Physics*, vol. 2018, pp. 024–024, jun 2018.

[161] A. Cuoco, J. Heisig, L. Klamt, M. Korsmeier, and M. Krämer, "Scrutinizing the evidence for dark matter in cosmic-ray antiprotons," *Physical Review D*, vol. 99, may 2019.

[162] A. Cuoco, J. Heisig, M. Korsmeier, and M. Krämer, "Constraining heavy dark matter with cosmic-ray antiprotons," *Journal of Cosmology and Astroparticle Physics*, vol. 2018, pp. 004–004, apr 2018.

[163] S. Hawking, "Gravitationally Collapsed Objects of Very Low Mass," *Monthly Notices of the Royal Astronomical Society*, vol. 152, pp. 75–78, 04 1971.

[164] L. A. Anchordoqui, I. Antoniadis, and D. Lüst, "Dark dimension, the swampland, and the dark matter fraction composed of primordial black holes," *Phys. Rev. D*, vol. 106, p. 086001, Oct 2022.

[165] C. Evoli, D. Gaggero, A. Vittino, G. D. Bernardo, M. D. Mauro, A. Ligorini, P. Ullio, and D. Grasso, "Cosmic-ray propagation with DRAGON2: I. numerical solver and astrophysical ingredients," *Journal of Cosmology and Astroparticle Physics*, vol. 2017, pp. 015–015, feb 2017.

[166] R. Kissmann, "PICARD: A novel code for the galactic cosmic ray propagation problem," *Astroparticle Physics*, vol. 55, pp. 37–50, mar 2014.

[167] C. S. Jørgensen, C. Karoff, V. Senthamizh Pavai, and R. Arlt, "Christian horrebow's sunspot observations – i. life and published writings," *Solar Physics*, vol. 294, p. 77, Jun 2019.

[168] M. Boschini, S. Della Torre, M. Gervasi, G. La Vacca, and P. Rancoita, "Propagation of cosmic rays in heliosphere: The helmod model," *Advances in Space Research*, vol. 62, no. 10, pp. 2859–2879, 2018. Origins of Cosmic Rays.

[169] L. J. Gleeson and W. I. Axford, "Solar Modulation of Galactic Cosmic Rays," , vol. 154, p. 1011, Dec. 1968.

[170] O. Stawicki, H. Fichtner, and R. Schlickeiser, "The Parker propagator for spherical solar modulation," , vol. 358, pp. 347–352, June 2000.

[171] G. Gloeckler and J. Geiss, "Composition of the local interstellar medium as diagnosed with pickup ions," *Advances in Space Research*, vol. 34, no. 1, pp. 53–60, 2004. To the Edge of the Solar System and Beyond.

[172] A. W. Strong, I. V. Moskalenko, T. A. Porter, G. Jóhannesson, E. Orlando, S. W. Digel, and A. E. Vladimirov, "Galprop version 54: Explanatory supplement," *Users Guide, Sep*, 2011.

[173] M. A. et al., "Precision measurement of the proton flux in primary cosmic rays from rigidity 1 gv to 1.8 tv with the alpha magnetic spectrometer on the international space station," *Physical Review Letters*, vol. 114, p. 171103, 2015.

[174] E. Vannuccini and et. al., "Gaps, low-energy antimatter for indirect dark-matter search," 2018.

[175] S. Schael, A. Atanasyan, J. Berdugo, T. Bretz, M. Czupalla, B. Dachwald, P. von Doetinchem, M. Duranti, H. Gast, W. Karpinski, T. Kirn, K. Lübelsmeyer, C. Maña, P. Marrocchesi, P. Mertsch, I. Moskalenko, T. Schervan, M. Schluse, K.-U. Schröder, A. Schultz von Dratzig, C. Senatore, L. Spies, S. Wakely, M. Wlochal, D. Uglietti, and J. Zimmermann, "Ams-100: The next generation magnetic spectrometer in space – an international science platform for physics and astrophysics at lagrange point 2," *Nuclear Instruments and Methods in Physics Research Section A: Accelerators, Spectrometers, Detectors and Associated Equipment*, vol. 944, p. 162561, 2019.

[176] ALICE Collaboration, "Towards the understanding of the genuine three-body interaction for p—p—p and p—p—," 2022.

[177] S. Acharya and et.al., "Production of 4he and 4he in pb–pb collisions at snn=2.76tev at the lhc," *Nuclear Physics A*, vol. 971, pp. 1–20, 2018.

[178] S. Acharya *et al.*, "Measurement of the (anti-)^{3}He elliptic flow in Pb–Pb collisions at $\sqrt{s_{\rm NN}} = 5.02$ TeV," *Phys. Lett. B*, vol. 805, p. 135414, 2020.

[179] S. Acharya *et al.*, "(Anti-)deuteron production in pp collisions at $\sqrt{s} = 13$ TeV," *Eur. Phys. J. C*, vol. 80, no. 9, p. 889, 2020.

[180] S. Acharya *et al.*, "Multiplicity dependence of (anti-)deuteron production in pp collisions at $\sqrt{s} = 7$ TeV," *Phys. Lett.*, vol. B794, pp. 50–63, 2019.

[181] S. Acharya *et al.*, "Measurement of deuteron spectra and elliptic flow in Pb-Pb collisions at $\sqrt{s_{\rm NN}} = 2.76$ TeV at the LHC," *Eur. Phys. J.*, vol. C77, no. 10, p. 658, 2017.

[182] S. Acharya *et al.*, "Multiplicity dependence of light (anti-)nuclei production in p-Pb collisions at $\sqrt{s_{\rm NN}} = 5.02$ TeV," *Phys. Lett. B*, vol. 800, p. 135043, 2020.

[183] A. Bianconi, E. L. Rizzini, V. Mascagna, and L. Venturelli, "Enhancement of annihilation cross sections by electric interactions between the antineutron and the field of a large nucleus," *The European Physical Journal A*, vol. 50, dec 2014.

[184] F. Becattini, "An introduction to the statistical hadronization model," 2009.

List of Figures

1 The particles of the standard model of particle physics. There are 3 generations of quarks and leptons, which differ from previous generations only in their mass. Quarks are split into up-like quarks, with a $+\frac{2}{3}$ charge, and down-like quarks with a $1\frac{1}{3}$ charge. Leptons are split between charged leptons with charge $q = -1$ and neutrinos, which carry no electromagnetic or color charge, and are very light. There are 4 gauge bosons for the 3 fundametal forces which the standard model describes: the gluon (g) for the strong force, the photon (γ) for the electromagnetic force, and the W and Z bosons for the weak force. Additionally, there is the scalar higgs boson, which is responsible for the mechanism which gives other particles their mass. 3

2 Color confinement by string fragmentation. As the antiquark-quark pair moved away from each other, more and more energy is stored in the color flux tube between them. Eventually, there is sufficient energy to create a new quark-antiquark pair, and thus truncate the flux tube. This process continues until the (anti)quarks run out of sufficient energy to create new quark-antiquark pairs. The quarks can then hadronise. The figure is taken from [8]. 4

3 Timeline of the universe, starting from the Big Bang [22]. 7

4 First order Feynman diagrams showing the annihilations of elementary particles. Top row: quark-antiquark annihilation through the strong (left), electromagnetic (middle) and weak (right) force. Bottom row: lepton-antilepton annihilation through the electromagnetic (left) and weak (right) force. 11

5 Schematic of $p\bar{p}$ annihilation into 3 mesons, done by rearranging the valence quarks but without annihilating any quark-antiquark pair. . . 12

6 Annihilation channels for antiproton-proton. The solid lines represent quarks and the dashed lines represent a gluonic string (which can then decay via string fragmentation, as shown in figure 2). Curled lines represent $\bar{q}q$ annihilations. The diagrams thus represent: a) 3 antiquark-quark annihilations; b) a single antiquark-quark annihilation into 2 mesons and a gluon string; c) corresponds to a quark-antiquark and string annihilation, with the creation of 2 quark-antiquark strings. Diagrams e) and f) can produce exotic mesons. Figure taken from [38]. 14

7 A comparison of antiproton-proton inelastic cross section data with the model used in Geant4 [37]. Points are experimental data as described in [40], the blue line represents the model. See text for details. 15

8 Antiproton-nucleus annihilation for different materials, taken from [44]. 16

9 Statistical hadronisation model fits, with three different implementations, to the light flavour hadron yields in central (0-10%) Pb–Pb collisions at $\sqrt{s_{NN}}$= 2.76 TeV. The upper panel shows the fit results together with the data, whereas the middle panel shows the difference between model and data normalised to the model value and the lower panel the difference between model and data normalised to the experimental uncertainties. Figure and caption taken from [48]. 18

10 Production yield $\mathrm{d}N/\mathrm{d}y$ normalised by the spin degeneracy as a function of the mass number for inelastic pp collisions, minimum-bias p-Pb and central Pb-Pb collisions. The empty boxes represent the total systematic uncertainty while the statistical errors are shown by the vertical bars. The lines represent fits with an exponential function. Figure taken from [72]. 23

11 Computer simulations of the distribution of galaxies within our universe, with hot dark matter (left) and cold dark matter (right), compared to the observed distribution (middle). Figure is taken from [23]. 26

12 Transition of dark matter from thermal equilibrium to freeze out. Both the decoupling temperature (where dark matter stops being in thermal equilibrium with luminous matter) and the freeze out temperature (when the rate of expansion has dropped the annihilation rate to negligible amounts, so that the comoving density can be considered constant) are indicated on the schematic. Figure is based on the figure in [83]. 28

13 Collection of candidate dark matter models over a wide mass range. The most prominent candidates are WIMP dark matter, axion dark matter and sterile neutrinos. Primordial black hole dark matter is not shown on this plot. Figure taken from [83]. 29

14 Thermally averaged annihilation cross section for WIMP dark matter as a function of the dark matter mass as it is required to reproduce the measured present-day abundance of dark matter. The left y-axis shows the values for Dirac dark matter, while the right y-axis shows the values for Majorana dark matter, showing the difference of a factor 2. Taken from [94]. 33

15 Schematic representation of the ALICE detector and its subdetector systems, during the Run 2 data taking period (2015-2018). 36

16 A schematic of the ALICE Inner Tracking System. The three layer groups (SPD, SSD, SDD) are marked. 38

17 Left: Schematic of the field cage of the TPC detector [98]. Right: Schematic of the reconstruction mechanism for tracks in the TPC [99]. 39

18 Specific energy loss in the TPC as a function of the rigidity p/z. Due to their masses, particles can be differentiated according to equation 12. This shows the identifying power of the TPC for low momentum particles. 40
19 The TOF detector of the ALICE experiment. 41
20 Left: Measurement of the track velocity β_{TOF} as a function of the reconstructed momentum of the particle associated to the track, from the TOF detector in pp collisions at $\sqrt{s} = 13$ TeV. β_{TOF} is classically measured as length of the track divided by the time-of-flight. Right: Performance figure showing the TOF used for the identification of $^3\overline{\mathrm{He}}$ nuclei. 42
21 Schematic of the data structures within ALICE. The data is split by run periods, then by event, and within the event by tracks. 43
22 Particle identification procedure for $^3\overline{\mathrm{He}}$ (left) and ^{3}He (right), showing the distribution of $n\sigma_{\mathrm{TPC}}$ for the momentum bins in the TPC only part of the analysis. The green line is the fitted signal, the red line is to fit the contamination towards negative $n\sigma_{\mathrm{TPC}}$. The black line shows the combined fit. 46
23 Plots of the $n\sigma_{\mathrm{TPC}}$ distribution for $^3\overline{\mathrm{He}}$ (left) and ^{3}He (right), for the momentum bins in the TPC+TOF only part of the analysis, i.e. after a cut on m^2_{TOF} is applied. The green line is the fitted signal. 47
23 (Continued) Plots of the $n\sigma_{\mathrm{TPC}}$ distribution for $^3\overline{\mathrm{He}}$ (left) and ^{3}He (right), for the momentum bins in the TPC+TOF only part of the analysis, i.e. after a cut on m^2_{TOF} is applied. The green line is the fitted signal. 48
24 Particle identification procedure for $^3\overline{\mathrm{H}}$ (left) and ^{3}H (right), showing the $n\sigma_{\mathrm{TPC}}$ distribution for each momentum bin, after a cut on m^2_{TOF} is applied. The green lines represent the fitted signal, and the black lines the fitted signal+background. 49
25 (Anti)nuclei spectra for ^{3}He $^3\overline{\mathrm{He}}$. Blue points show ^{3}He while the red points show $^3\overline{\mathrm{He}}$. Statistical uncertainties are shown as errorbars while systematic uncertainties are shown as boxes. These spectra are not yet corrected for secondary particles from material spallation. . . 50
26 Extracted primary ^{3}He yields in each analysis bin as a function of the value of the cut on |DCAz|. Due to the variations in the first bin, an 8% uncertainty was assigned. 51
27 Example DCA_{xy} distributions of particles from primary and secondary particles in Monte Carlo simulations. The particle shown here is $^3\overline{\mathrm{He}}$ with a $|\mathrm{DCA}_z|<1$ cm requirement. 52

28 DCA_{xy} distributions of ^{3}He candidates without any cut on ITS hists (left) and after a hit in one of the two first layers of the ITS is required (right). The reduction in the number of candidates is mainly in the sidebands, and therefore from secondaries. 52

29 Comparison of different methods for determining the primary fraction from the template fits, shown in the second bin of the $^3\overline{\text{He}}$ analysis, with a $|DCA_z|$<1cm cut. (Left) Fit using the TFractionFitter. (Middle) Default templates scaled according to the weights assigned by the TFractionFitter, but without changing their shapes. (Right) Fits performed by scaling the material templates to the region outside $|DCA_{xy}|$ < 0.1 cm. The solid line represents the data and the histogram points are the fitted material template. See text for more details. 54

30 Normalized secondary particle yieds as a function of primary particles fired obtained from a toy Monte Carlo simulation of a particle beam on materials mimicking the LHC beampipe in ALICE and the beampipe + ITS support structure. The resulting secondary deuterons and ^{3}He are shown as a function of the primary particle fired, where the results are roughly scaled by the primary particles relative abundance. 55

31 Cumulative material budget of the ALICE detector, as a function of radius from the beampipe, taken from [105]. The solid red line is the value for straight tracks which hit the centre of the TOF sector, while the dashed blue line is the average value over azimuthal angle. 57

32 Ratio of antiprotons to protons produced at mid-rapidity as a function of beam rapidity. At LHC energies the value approaches unity, demonstrating that at such high energies antimatter and matter are produced in almost equal amounts. Figure taken from [108]. 59

33 Bin by bin plots of the $^3\overline{\text{He}}/^3$He ratio as a function of the varied inelastic cross section in Monte Carlo simulations, together with the one measured in data. The fitted line is an exponential fit according to the Lambert-Beer law 15, and is used to extract the cross section scaling factor. 61

34 Bin by bin plots of the $^3\overline{\text{H}}/^3$H ratio as a function of the varied inelastic cross section in Monte Carlo simulations, together with the one measured in data. The fitted line is an exponential fit according to the Lambert-Beer law 15, and is used to extract the cross section scaling factor. 62

35 TPC/TOF ratio for $^3\overline{\mathrm{He}}$ as a function of the varied inelastic cross section, for one momentum bin. Figure taken from [110]. The dashed green curve is the a fit of the Lambert-Beer law (equation 15) to the values of the TPC/TOF ratio obtained from MC simulations with varied inelastic cross section (black crosses). The blue datapoint is the ratio in data, and the pink point is the corresponding measurement of the inelastic cross section. 63
36 Schematic representation for how the correction for the energy loss of antinuclei – and the corresponding systematic uncertainty – is applied to the measurements of the inelastic cross sections. In order to map from the scaling factor to the inelastic cross section, the default parameterization used in Geant4 is employed. 64
37 Local A and Z values (left) and density (right) of the ALICE detector material ad mid-rapidity as a function of the radial distance from the interaction point. 65
38 Uncertainty on the ALICE material budget between the TPC and TOF detectors, as found by comparing the yields in the TPC to the ones in the TOF for pions from K^0_s decays (red) and protons from Λ decays (black). The uncertainty is determined by comparing the measured ratio to ones obtained from detailed Monte Carlo simulations of the ALICE detector with varied material budgets, using Geant3 (left) and Geant4 (right). Figures taken from [113]. 67
39 Evaluation of the systematic uncertainty due to track cuts, for $^3\overline{\mathrm{He}}$ (left) and $^3\overline{\mathrm{H}}$ (right). The same analysis was re-performed over 100 times with random permutations of "tight", "default", and "loose" cuts on each considered parameter. 69
40 Uncertainty on the antiparticle-to-particle ratio introduced by varying the elastic cross sections by 30% (left) and the inelastic matter cross section by 10% (right). Since the cross section for $^3\overline{\mathrm{H}}$ and $^3\overline{\mathrm{He}}$ are the same in Geant4, these values are valid for both species. 70
41 The antiproton inelastic cross section on the average ALICE detector material, taken from [105]. The black line and dots show the datapoints, while the green and yellow bands show the 1 and 2 sigma total uncertainties (stat^2+syst^2). The dashed line is the parameterization for this cross section in Geant4, which is fitted to data. 71

42 Ratio of the antiproton-to-proton ratios (left) and antideuteron-to-deuteron ratios (right) as a function of momentum, obtained in high multiplicity pp collisions and in pPb collisions, compared to the expected difference from the different collision energies (dashed red line). The agreement with the red line shows that this analysis technique is consistent across different collision systems, as expected. . . 72

43 Template fits for determining the primary fraction of ^{3}He in the first 3 momentum bins (above this momentum the primary fraction goes to 1), for a $|\mathrm{DCA}_z| < 1$ cm cut. The fits were performed using the TFractionFitter method available in ROOT. 75

44 (Left) $^3\overline{\mathrm{He}}/^3\mathrm{He}$ measured in pp collisions at $\sqrt{s}$ =13 TeV, as a function of the particle momentum at the primary vertex. Statistical uncertainties are shown as lines, and systematic uncertainties are shown as boxes. The discontinuity at $p/Z = 1$ GeV/c is due to the additional requirement of a TOF hit, thus requiring tracks to traverse more material. (Right) $\sigma_{\mathrm{inel}}(^3\overline{\mathrm{He}})$ as measured using the antiparticle-to-particle method in pp collisions at $\sqrt{s}$ =13 TeV, as a function of the antinuclei momentum at annihilation. The uncertainties include both statistical and systematic uncertainties. Open points are from the analysis using the TPC only for particle identification, while closed points require a matching hit in the TOF in addition to the TPC, which therefore has a different averaged material value. The lines show the parameterization used in Geant4. 76

45 (Left) TOF-to-TPC ratio for $^3\overline{\mathrm{He}}$ in Pb–Pb collisions at $\sqrt{s_{NN}}$ =5.02 TeV, as a function of the particle momentum at the primary vertex. Statistical uncertainties are shown as bars, and systematic uncertainties are shown as boxes. The colored lines are the same ratio in Monte Carlo simulations with varied $\sigma_{\mathrm{inel}}(^3\overline{\mathrm{He}})$. (Right) $\sigma_{\mathrm{inel}}(^3\overline{\mathrm{He}})$ as measured using the TOF-to-TPC method in Pb–Pb collisions at $\sqrt{s_{NN}}$ =5.02 TeV, as a function of the antinuclei momentum at annihilation. The uncertainties include both statistical and systematic uncertainties. The line shows the parameterization used in Geant4. Figures taken from [110]. 77

46 $n\sigma_{\mathrm{TPC}}$ vs momentum plots for tritons. A cut on the m_{TOF} is applied above 2 GeV/c in all figures. (Top left) the original distribution without an additional cut on either DCA or m_{TOF}. (Top right) the distribution after a cut of $|\mathrm{DCA}_{xy}| < 1\ mm$ and $|\mathrm{DCA}_z| < 1\ mm$ is applied. (Bottom left) the distribution after the cut on m_{TOF} is extended to momenta as low as 1 GeV/c. (Bottom left) the distribution after both the DCA and m_{TOF} cuts were applied. 78

47 Template fits to the DCA distribution of ^{3}H, to account for the contributions from secondary nuclei from spallation processes. The primary fraction is evaluated as $f_p = \int_{-0.1cm}^{0.1cm} \text{fit}_{\text{signal}} d\text{DCA} / \int_{-0.1cm}^{0.1cm} \text{data}\ d\text{DCA}$. The results are shown for each momentum bin. 79

48 (Left) $^3\overline{\text{H}}$ /^{3}H ratio as a function of momentum, with statistical uncertainties as bars and systematic uncertainties as boxes. The colored lines represent Monte Carlo simulations with varied inelastic cross sections. (Right) $^3\overline{\text{H}}$ TOF-to-TPC ratio as a function of momentum, with statistical uncertainties as bars and systematic uncertainties as boxes. The colored lines represent Monte Carlo simulations with varied inelastic cross sections. 80

49 (Left) the resulting measurement of $\sigma_{\text{inel}}(^3\overline{\text{H}})$ using the antibaryon-to-baryon method ($\overline{\text{B}}$/B) and the TOF-to-TPC method, on the average ALICE material. The colored boxes show the total uncertainty (stat^2+ syst.^{2}). The line shows the parameterization as used in Geant4. (Right) comparison of the $\sigma_{\text{inel}}(^3\overline{\text{He}})$ and $\sigma_{\text{inel}}(^3\overline{\text{H}})$ measurements. 81

50 Illustrated story of the journey which antinuclei undertake before being observed near earth. Red lines shown high energy cosmic ray protons, Blue lines shown $^3\overline{\text{He}}$. The antinuclei get created all throughout the galaxy, and in the galactic centre antinuclei from dark matter is the most concentrated, due to the higher dark matter density. Similarly, antinuclei from high energy cosmic rays are created all over the galaxy. The created antinuclei then travel through the interstellar medium, some of them annihilating along the way. The ones which do make it to earth then are affected by the solar magnetic field, before reaching detectors near earth. All these processes need to be understood in order to be able to interpret an antinuclei signal in cosmic rays. 82

51 Production cross section for antideuterons (left) and $^3\overline{\text{He}}$ (right), as a function of the energy of the antinucleus produced, for a range of different projectile energies, taken from Shukla et. al. The $^3\overline{\text{He}}$ cross section includes the effect of antitritons which are produced and subsequently decay to $^3\overline{\text{He}}$ 86

52 A list of experiments with measurements of (anti)deuteron production, as a function of rapidity and $\sqrt{s}$. The compilation is taken from table 2 in [130], based on data in [131, 132, 133, 134, 135, 136, 137, 138, 139, 140, 141]. 87

53 Comparison of the antideuteron (left) and $^3\overline{\text{He}}$ (right) spectra obtained by Shukla et. al. with ALICE data for $\sqrt{s} = 7$ TeV pp collisions. 88

54 Cosmic ray particle spectra, for protons and all particles, from relevant experiments. Figure taken from [142]. 89
55 The source term of antideuteron from high energy cosmic ray collisions, as a function of the incoming proton energy and the outgoing antideuteron energy. The figure is taken from [121]. 89
56 A schematic of dark matter pair annihilation into standard model particles (left) and of dark matter decay into standard model particles (right) for a WIMP particle. The exact process by which this would occur is not known, and therefore currently model dependent. Note that a scattering process between a dark matter and a standard model particle would look very similar to the diagram on the left, with the space and time axes inverted (i.e. change the arrow direction of the top dark matter and bottom standard model particle). However, this scattering might happen via a very different internal process, so the two cannot be directly related in a model independent way. 90
57 Antiproton (top) and antideuteron (bottom) spectra from dark matter annihilations as a function of the antinuclei kinetic energy per nucleon, normalized to a single annihilation event, for a wide variety of initial SM states. This figure is taken from [1]. 92
58 Antideuteron (left) and $^3\overline{\mathrm{He}}$ (right) spectra from dark matter annihilations as a function of the antinuclei kinetic energy per nucleon, normalized to a single annihilation event. Spectra for $W^+W^-$and $b\bar{b}$ channels are taken from [4], $\overline{\Lambda}_b$ tune is taken from [144]. 93
59 Rotation curve of stars in the Milky Way, as a function of distance from the galactic center. Reproduction of data reported in [78]. 94
60 Dark matter density profiles used in this work, as a function of the distance to the galactic centre. The best fit values for each profile are taken from [4]. 96
61 Fit of the rotation curve of the Milky Way, with a NFW profile. Figure is taken from [156], based on work in [149]. 97
62 Limits from direct detection experiments on the dark matter - nucleon interaction cross section, as a function of the dark matter mass. The figure is taken from [158]. 99
63 Limits on $<\sigma v>$ based on AMS antiproton data. Figure is taken from [57]. 100
64 Spectrum of produced antideuterons per second, as a function of kinetic energy per nucleon, from a primordial black hole evaporation. Data from [4], provided in private communication. 104

65 Fluxes of several cosmic ray nuclei, as measured by AMS-02, compared to the predictions of the best-fit values obtained by fitting several key species. Figure taken from [63] 106
66 Comparison between the different GALPROP propagation parameters used in this work, for antideuterons from high energy cosmic ray collisions (left) and from dark matter annihilations (right). 108
67 Scaled inelastic cross sections of $^3\overline{\mathrm{He}}$ (top) on proton (left) and Helium-4 (right) targets and antideuterons on proton targets (bottom). The band shows the experimental uncertainty from the ALICE measurements [105, 110], plus an additional 8% uncertainty associated with the scaling from heavier targets (C, O, Al) to protons (H). The parameterization shown in the top left panel (labeled Korsmeier et al in the bottom panel) is taken from [2], and is based on scaling the total deuteron-antiproton cross section by the inelastic portion of the antiproton-proton cross section, and then scaling the obtained value by 3/2 to account for the extra nucleon in $^3\overline{\mathrm{He}}$The cross section in the bottom panel labeled Ibarra et. al. is taken from [4], and is based on taken 2 times the antiproton-proton inelastic cross section, as parameterized by [36]. See section 1.4.4 for a more detailed discussion on calculating inelastic cross sections. 112
68 Expected antideuteron fluxes for different m_χ ranging from 10 GeV to 1 TeV, and from primordial black holes (PBHs). They are compared to an expected spectrum of secondary antideuterons from high-energy cosmic-ray collisions. The results are shown for the position of the solar system. The figures on the left show the results without solar modulation, and on the right with solar modulation included by means of a force field model, as is discussed in section 5.2. The results are also shown for different possible annihilation channels of dark matter, either through W^+W^-(top) or through $b\bar{b}$ (bottom). 115
68 Expected antideuteron fluxes (cont.) dark matter annihilations through $\overline{\Lambda}_{\overline{b}} \rightarrow b\bar{b}$ and light mediators (top) and from primordial black holes (PBHs) (bottom). The figures on the left show the results without solar modulation, and on the right with solar modulation included by means of a force field model, as is discussed in section 5.2. 116

69 Expected $^3\overline{\mathrm{He}}$ fluxes for different m_χ ranging from 1GeV to 2TeV. They are compared to an expected spectrum of secondary $^3\overline{\mathrm{He}}$ from high energy cosmic ray collisions. The results are shown for the position of the solar system. The figures on the left show the results without solar modulation, and on the right with solar modulation included by means of a force field model, as is discussed in section 5.2. The results are also shown for different possible annihilation channels of dark matter, either through W^+W^-(top), through $b\bar{b}$ (bottom). 117

69 Expected $^3\overline{\mathrm{He}}$ fluxes (cont.) from dark matter annihilations through $\overline{\Lambda}_b$ decays. They are compared to an expected spectrum of secondary $^3\overline{\mathrm{He}}$ from high energy cosmic ray collisions. The results are shown for the position of the solar system. The figures on the left show the results without solar modulation, and on the right with solar modulation included by means of a force field model, as is discussed in section 5.2. 118

70 Antideuteron fluxes for different dark matter profiles (left) and the corresponding transparencies (right), for antideuterons from dark matter annihilation through the $b\bar{b}$ channel. 118

71 Plot of the rigidity resolution of AMS for comparing $^3\overline{\mathrm{He}}$ and ^{3}He signals. 9 possible $^3\overline{\mathrm{He}}$ events are shown. These findings have not yet been published and this figure is taken from a talk [119]. 123

72 (Left) GAPS antiparticle detection method: antiparticles slow down and stop in the Si(Li) target, forming an exotic atom. Atomic X-rays will be emitted as it de-excites, followed by the pion (and proton) emission from nuclear annihilation. $\bar{d}/\bar{p}$ identification is based on (1) the stopping range, (2) the pion and proton multiplicity, (3) the atomic X-rays energies. Figure and caption taken from [174]. (Right) The GAPS detector, the central tracker (C) is surrounded by the inner ("cube", B) and outer ("umbrella", A) TOF layers. The readout electronics, flight computer, ballast and other support infrastructure are located underneath the tracker (D). Solar panels, cooling systems, antennae and thermal insulation are not shown for clarity. Figure and description taken from [148]. 124

73 The inelastic cross section measurements for the antinuclei from $A = 1$ to $A = 3$, as measured by ALICE in [105, 110] and in an upcoming publication on $^3\overline{\mathrm{H}}$ 127

List of Tables

1 Constant values for determining the fir parameter R_A used in the Geant4 Glauber approximation for antinucleus-nucleus collisions [44]. 17
2 Values for the average atomic mass number of the ALICE detector material $< A >$, for different analysis methods. They are evaluated according to equation 16. 65
3 Individual axissymmetric parts of the Mikly Way used for fitting rotation curves. The distinction is made in order to simplify the fit, rather than a hard distinction within the actual galaxy. Non-axissymmetric components are neglected for rotation curves, based on the assumption that any effects would cancel out when averaged over the full rotation. The values for the total mass were taken from [79]. The extent column is approximate and given in order to help the reader visualise the distributions. Due to the distributions being exponential, they only asymptotically approach 0. 95
4 Two of the parameters for the tuning of Galprop, which show the degeneracy between them. 109
5 A list of the sizes of uncertainties involved in making predictions for antinuclei fluxes. The second and third column are describing the size of the effect on antinuclei from high energy cosmic ray collisions and from potential dark matter annihilations, respectively. 119